Finite Element Methods for the Time Dependent Simulation of Viscoelastic Fluid Flows

by

Michael Joseph Szady

B.S.E., Chemical Engineering, Princeton University (1990)
M.S.Ch.E.P., Massachusetts Institute of Technology (1992)

Submitted to the Department of Chemical Engineering
in partial fulfillment of the requirements for the degree of

Doctor of Philosophy

at the

MASSACHUSETTS INSTITUTE OF TECHNOLOGY

June 1996

Author .....
Department of Chemical Engineering
May 30, 1996

Certified by .....
Robert C. Armstrong
Professor of Chemical Engineering
Thesis Supervisor

Certified by .....
Robert A. Brown
Professor of Chemical Engineering
Thesis Supervisor

Accepted by .....
Robert E. Cohen
Graduate Officer, Department of Chemical Engineering

Two new numerical methods were constructed based on these observations: the EVSS-Gradient (EVSS-G) and the Discrete-EVSS-G (DEVSS-G) methods. The EVSS-G formulation is similar to the EVSS formulation except that it uses an independent interpolation of the velocity gradient instead of the rate-of-strain tensor in the constitutive equation and bilinear basis functions for the stress variable instead of biquadratic basis functions. The DEVSS-G formulation begins similar to the EVSS-G formulation except the elastic stress is not substituted into the constitutive equations resulting in a simpler formulation for complex, nonlinear constitutive models such as the CR-FENE model.

The linear stability of the EVSS-G/FEM and DEVSS-G/FEM was tested on the planar Couette geometry and both significantly improve the numerical stability compared to the original EVSS/FEM. For the EVSS-G/FEM no upper bound was found up to at least $De = 200.0$ while the DEVSS-G/FEM was stable up to at least $De = 100.0$. Nonlinear stability calculations for the planar Couette geometry were also computed to confirm these results. There is little doubt the stability goes even higher; the calculations were stopped only due to the extremely long computational times required to show stability at very high De.

The accuracy, convergence with mesh refinement and robustness of the algorithms were demonstrated by the solution of various two-dimensional, steady-state benchmark problems such as the flow between eccentric rotating with a UCM model and the flow through an infinite periodic linear array of cylinders in a channel with the CR-FENE model. The algorithms have also been applied to numerous other problems by members of our research group at MIT. The new methods will extend fairly easily to three-dimensional flows where the application of trilinear stress approximations will considerably simplify the calculations.

Fully nonlinear time dependent calculations were studied for the planar Couette flow for the UCM and CR-FENE models and for flow through an infinite periodic linear array of cylinders for the CR-FENE model. However, the extension of the fully implicit time integration from the linear stability calculations was found to be infeasible; it is estimated that the latter problem would take approximately 3,600 hours (150 days) of CPU time to take 600 time steps using an HP9000 Series 735 workstation. The θ-method, a semi-implicit time integration method, was implemented. It uses three substeps to march forward in time; the amount of work necessary for all three substeps is less than the amount required for one fully implicit step (approximately a factor fifteen savings on an operations count basis). The variables are divided into groups (here, one set is elliptic and the other is hyperbolic) where in the first step, the elliptic group is solved implicitly and the other explicitly. This order is reversed in the second step and, finally, the third step repeats the first step. An attempt to implement this approach in the EVSS-G framework revealed that the time derivative of the rate-of-strain tensor found in the constitutive equation causes the failure of this method. The DEVSS-G/FEM does not have this term and can be successfully formulated in the θ-method. It is for this reason that the DEVSS-G/FEM is recommended for all further viscoelastic flow calculations. The startup calculations for planar Couette flow gave the expected exponential form of the stress variables. The startup flow calculations through an infinite linear periodic array of cylinders showed

no time dependent solutions up to a $We = 3.0$; all calculations converged to the steady-state solutions found using the steady-state version of the DEVSS-G/FEM.

This is the first implementation of a decoupled, iterative solver for viscoelastic flow calculations. The calculations for the flow through a linear periodic array of cylinders took roughly 18 minutes per time step (for time steps on the order of $10^{-1} - 10^{-2}$ relaxation times) on the HP9000 Series 735 workstation for approximately 40,000 unknowns. On a Cray-C90, the calculations took approximately 90 seconds per time step. Thus, this is a feasible method to calculate two-dimensional, time dependent viscoelastic flow simulations.

The time dependent finite element algorithm developed in this thesis using the DEVSS-G formulation of the viscoelastic flow equations and the θ-method to integrate forward in time can now be used with confidence that the resulting numerical solutions will be an accurate representation of the equations being solved. This numerical algorithm can be used as a tool to help develop an understanding of the causes of viscoelastic flow instabilities (instabilities that occur even when the Re is negligible). Axisymmetric extrusion flows could be perfect situation for the examination of two-dimensional time dependent flows, as they ar known to exist experimentally and the steady-state flow has been characterized numerically (Salamon, 1995).

Thesis Supervisor: Robert C. Armstrong
Title: Professor of Chemical Engineering

Thesis Supervisor: Robert A. Brown
Title: Professor of Chemical Engineering

Acknowledgements

There are many people whom I would like to thank for making this thesis possible. I wish to thank my advisors, professors Robert Brown and Robert Armstrong for their guidance, constructive criticism and support during the course of this research. Their extensive knowledge in the fields of viscoelastic fluid mechanics and numerical methods contributed greatly to this work and also to my professional development. I would also like to thank my thesis committee members, professors Klavs Jensen and Anthony Patera. I am indebted to Dr. Paul Northey who initially started this research and Dr. David Bornside for the development of several computational tools without which this thesis would have difficult to complete. I would like to acknowledge the National Science Foundation, the Office of Naval Research and the Defense Research Projects Agency for providing financial support for this research and the MIT Supercomputer Facility, the Pittsburgh National Supercomputer Center and E.I. DuPont de Nemours company for providing computational resources.

I would like to thank my fellow members of the Bob and Bob research group - Paul, Aparna, Todd, Jeff, Lars, Howard, Radha, Talid, Alice and Hua - whose helpful discussions have helped immensely in this research. I would like to thank the support staff, Arline, Carol, Nancy, Elaine and Janet, for taking care of me during my time at MIT.

I am lucky to have met some wonderful friends over the years: Colin Wolden, LLoyd Johnston, Rick Batycky, and Russ Allgor. I would also like to thank all those members of the MIT Ruckin' Beavers rugby club who have given me an athletic outlet for my joys and frustrations, especially, Hal Ackler, Chevy, Jon Suber, Spanky, and Greg.

I would like to thank my parents and my brothers for their support and encouragement. Without you pushing me through all the years, mom and dad, I would not be where and who I am today. Finally, I would like to thank my bride-to-be Ivana Clayton for her love, encouragement and support during the last few years of my graduate work.

Contents

List of Figures

List of Tables

Chapter 1

Introduction

"The only interesting fields of science are the ones where you still don't know what you're talking about."

– I.I. Rabi

Natural polymers such as those found in wood, cotton and silk have long been a part of people's lives. In the twentieth century, synthetic polymers also have become extensively utilized to the point where they have become a dominant part of our everyday existence. Polymers are used in everything from plastic containers, to light switches, to the entire body of an automobile.

Research in polymer chemistry had its beginnings in the 1920's (Hiemenz, 1984), but the investigation of polymer rheological properties has been intensely studied only more recently. Polymer melts and solutions are not governed by the equations of motion for Newtonian fluids such as water; the simple proportional relationship between stress and the rate-of-strain on the fluid, that is the basis of the Newtonian constitutive equation, is lost. These non-Newtonian fluids require a more complicated dependence between the stress and the rate-of-strain on each fluid element. A direct result of this fact is that there are very few analytical solutions to the equations of motion for non-Newtonian fluid flow, even for inertialess flows where the equations are

linear, but these cannot be solved without a constitutive equation which is nonlinear. Therefore, numerical solutions are required.

The simplest non-Newtonian fluid is the generalized Newtonian fluid where the viscosity of the fluid is allowed to depend on the shear-rate (e.g., the Carreau-Yasuda or power law model). There are many industrially important processes where the non-Newtonian viscosity is the dominant effect, and there are many examples of closed-form solutions for models of this type (Bird *et al.*, 1987). However, this fluid model cannot describe normal stresses, elastic or time-dependent effects; these fluids are sometimes called inelastic. The second case of non-Newtonian fluid models are called viscoelastic models because they attempt to describe viscous and elastic effects which also include the normal stress effects. Viscoelastic models usually require numerical solutions of the flow equations for all but the simplest of flow geometries.

While there have been numerous and successful numerical solutions of Newtonian and generalized Newtonian flows, until recently, this was not true of viscoelastic flow simulations. The lack of reliable numerical solutions presents various problems for the engineer interested in designing polymer processing equipment. By contrast, the application of simulations of Newtonian or generalized Newtonian fluid mechanics to the design of manufacturing equipment has been very successful. Typical examples of the influence of these types of numerical examples can be found in Sharratt (1990). The calculations have been used to determine that baffles to decrease the bypass of fluid in a nitration reaction would have a negligible effect due the tangential velocity in the reactor which had been neglected in an initial "back of the envelope" calculation. It has also been used to study the general mixing patterns in stirred tank reactors with the change of impellers which is used in conjunction with published correlations to help optimize the mixing in vessels. However, most fluids in the chemical processing industries are viscoelastic; they are largely rheologically complex polymer melts or solutions. Because of the lack of good simulation tools, industrial development has relied more on the experience of the engineer with various materials and empirical relationships gleaned from experimental data based on trial-and-error experimentation. The goal of much research in non-Newtonian fluid mechanics is to predict *a priori*

the features of the polymer flow in a given flow geometry so as to optimize the process. With reliable numerical simulations, engineers may use computer simulations to increase the probability of a successful design, rather than the time consuming and expensive construction and execution of repetitive experiments. Thus, numerical simulation of the steady-state and transient flows of viscoelastic polymer melts and solutions has many potential applications in the design, optimization and control of processing equipment for a variety of manufacturing and materials processing industries. In the simplest formulations, modeling of these flows requires the solution of the equations of mass and momentum conservation for an incompressible liquid simultaneously with a constitutive equation for the deviatoric stress tensor due to the viscoelastic behavior of the fluid. Finite element methods have been developed for the solution of this equation set for all the reasons that make these methods popular for the analysis of Newtonian flows: complex geometries are easily incorporated, nonuniform meshes can be employed to distribute the computational power to regions of the domain where the solution changes rapidly, and the boundary conditions for free-surface flows can be systematically incorporated into the numerical approximation. Even with the large knowledge base built upon Newtonian flow problems, the numerical analysis of viscoelastic flow problems governed by differential constitutive equations has emerged as a distinctly difficult problem (Brown *et al.*, 1986). The largest difficulty centers around the additional equations required to describe the viscoelastic flow properties of the fluid. These additional equations are of hyperbolic type while the momentum and continuity equations are of elliptic type for Newtonian flows. Accordingly, families of new mixed finite element methods have been developed for the calculation of the velocity, pressure and deviatoric stress fields in viscoelastic flows that specifically account for the mixed elliptic/hyperbolic nature of the equation set.

However, even with these advances, the numerical solution of the equations of motion for a fully nonlinear transient, three-dimensional flow is still beyond the capabilities of the current generation of super computers, such as the Cray C90, much less the extremely complicated geometries found in industrial processes. This limita-

tion necessitates the simplification of the calculations to two-dimensional geometries. Furthermore, experimentalists also have been examining flows through simple geometries to understand better the characteristics of viscoelastic liquids. At low De and negligible Re (De and Re are dimensionless measures of flow characteristics) so that the flow is basically inertialess, good agreement exists between experiments and the steady-state numerical simulations (see for example, Baaijens, 1995, Larson, 1992 and Rajagopalan *et al.*, 1992). As the flow rates in the experiments are increased, flow transitions are observed to transient and/or three-dimensional states even for simple flow geometries. Examples include the extrusion of silicone gums (Piau *et al.*, 1992), flow in Taylor Couette devices (Baumert and Muller, 1995 and Larson, 1992), flow through abrupt contractions (Boger, 1987 and McKinley, 1990), flow in parallel plate and cone-in-plate rheometers (McKinley *et al.*, 1991 and 1995), flow past a single cylinder in a channel (McKinley, 1990 and Oztekin *et al.*, 1995) and flow through a square array of cylinders (Chmielewski and Jayaraman, 1993). These experimental flow transitions include changes from steady-state to transient, symmetric to asymmetric and/or two-dimensional to three-dimensional flow. A new need has arisen due to the preponderance of experimental data: numerical techniques capable of predicting the appearance of time dependent flow transitions and calculating the new solutions resulting from these bifurcations. To obtain a numerical method capable of solving these time dependent problems is the main goal of this thesis.

Mixed finite element methods for the numerical solution of the momentum, continuity and constitutive equations involve approximations for the velocity, pressure and deviatoric stress fields and discretization of these equations by appropriate weighted residual methods. Issues in the development of these methods include the relationships between the choice of the weighted residual method for each differential equation and the mathematical type of the equations, as well as the connection between the weighted residual methods and the choice of polynomial spaces for the finite element approximations.

First, the mathematical type of the partial differential equations to be solved is important; partial differential equations can be elliptic, parabolic or hyperbolic.

The essential difference is the method of information transport; hyperbolic equations transport information along streamlines at a finite speed, whereas elliptic equations transport information in all directions at infinite speed. Parabolic equations are a mixture of these two types in that some information is transported like an elliptic equation and some like a hyperbolic equation. The choice of the weighted residual method used to solve each differential equation must take into account the mathematical type of the equation (Johnson, 1987). For inertialess flows, the velocity equations are elliptic; the stress equations are hyperbolic; and the equation for pressure is a constraint on the velocity equations. The final two issues are related to the connection between the weighted residual method and the choice of the polynomial spaces for the finite element approximations. The polynomial spaces chosen for the variables in the set of equations must be compatible and consistent when substituted into the discretized equations. Compatibility of approximations essentially means that the discrete problem is well posed as $h \rightarrow 0$, h being a characteristic size for the finite element mesh. A numerical method is consistent when the exact solution can be substituted into the discretization of the problem and yields the exact solution as the answer.

Guidance in these various choices has come from several directions: the theory of the mathematical type of the equation set (Rutkevich, 1970 and 1972; Joseph *et al.,* 1985), the development of mathematical proofs for the existence of solutions for small De (Renardy, 1985) and the development of rigorous convergence proofs for finite element approximations in this limit (Baranger and Sandri, 1991a and 1991b).

The numerical method is characterized by three features: numerical convergence, robustness, and temporal stability of the numerical solution. In an acceptable numerical scheme, the error approaches zero as the characteristic size of the mesh approaches zero (Carey & Oden, 1983) which is the definition of convergence. The solution is compared with solutions calculated by other methods to determine the accuracy of the method. Robustness is essentially the ability of the numerical method to solve a variety of flow problems accurately. There are two types of temporal stability to consider: the physical stability of the equations themselves and the numerical stability

of the numerical technique. The equations are physically unstable if the magnitude of the solution goes to infinity as time goes to infinity; otherwise, it is stable. The temporal numerical linear stability of a numerical method is determined by randomly perturbing the linearized equations of motion and the constitutive equations around the steady-state solution. The behavior of the physical system (stable or unstable) must be the same for the numerical method for it to be considered stable; i.e., if the continuous problem is stable, then the numerical method must be also *and* if the continuous solution is unstable, then the numerical method must mimic this instability. If the numerical method fails to do this, then it is unstable.

Through the use of these assessments of the numerical method and much numerical experimentation, there has been considerable progress in the development of numerically stable and accurate mixed finite elements for viscoelastic flows. The formulations of most mixed finite element methods for numerical simulation of viscoelastic flows governed by differential constitutive equations are based on separate finite element approximations and weighted residual methods for the velocity and pressure fields associated with the momentum and continuity equations, and for the extra elastic stress, which is governed by the constitutive equation. The rationale for these formulations is based on artificially splitting the momentum and continuity equations from the constitutive equation. For an incompressible fluid, the momentum and continuity equations compose an elliptic saddle point problem for the velocity and pressure fields, whereas the constitutive equations are a set of first-order hyperbolic equations for the components of the stress tensor. In recent years, several mixed finite element methods have been developed for the solution of these problems; these include the mixed method of Marchal and Crochet (1987), the Explicitly Elliptic Momentum Equation (EEME) method of King *et al.* (1988), and the Elastic-Viscous Split-Stress (EVSS) method of Rajagopalan *et al.* (1990b). The spectral (*hp*-) finite element methods developed by Khomami and coworkers also deserve mention. Each is based on different formulations of the original equation set and on different finite element approximations and weighted residual techniques. Each method has been demonstrated computationally to give convergent solutions for the calculation

of smooth, steady-state flows; and comparisons between the methods are beginning to shed light on what parts of the algorithm are crucial for numerical stability and accuracy. Even with the tremendous progress in the last few years, there still are issues that must be resolved before optimal and robust numerical methods for large classes of calculations are available. The new mixed methods presented in this thesis are based on computational observations of the limits of existing methods and on heuristic ideas about the cause for these difficulties.

Several features of the algorithm are particularly important. As mentioned above these are the choices of the finite element approximations to velocity, pressure and stress fields and the selection of weighted residual methods for discretization of the momentum, continuity and constitutive equations. We follow the basic approach implemented in the EVSS method of Rajagopalan *et al.* (1990b) to solve the elliptic saddle point problem for velocity and pressure by using the standard Galerkin weak form and compute the elastic stress tensor from the constitutive equation by using numerical methods appropriate for hyperbolic equations: streamline upwinding (SU; Brooks and Hughes, 1982), the streamline upwind Petrov-Galerkin (SUPG; Brooks and Hughes, 1982) and the Galerkin least-squares/Douglas-Wang (GLS/DW; Baaijens, 1992; Douglas & Wang, 1989; and Leborgne, 1992) methods are used here.

Calculations for model flows, such as the flow between eccentric rotating cylinders, the flow through an undulating tube, and the flow around a sphere in a tube, have been demonstrated to be convergent with mesh refinement for the simplest viscoelastic constitutive equations, the upper-convected Maxwell (UCM) and Oldroyd-B equations, and for moderate values of the Deborah number. The first two solutions have been compared to calculations using spectral-finite element (Beris *et al.*, 1987) and spectral-finite difference methods (Pilitsis & Beris, 1989) to establish the accuracy of the calculations. The accuracy of the calculation of any given flow appears to be limited only by the resolution of thin boundary and internal layers in the stress that develop adjacent to solid boundaries and in strong extensional flows. The boundary layers next to streamlines on which $\boldsymbol{v} = \mathbf{0}$ are particularly important in this research. These thin layers result because of the singular nature of the constitutive equations in

the limit where the velocity field vanishes, as at a stationary, no-slip surface. In this limit, the constitutive equations reduce from hyperbolic conservation laws to ordinary differential equations in time defined at each point on the zero velocity streamline or boundary. This singularity of the hyperbolic equations is emphasized in this thesis.

Solutions for typical flows using any of these current methods show that the stress field requires far more resolution than the velocity field; also, the present methods appear to have mathematical compatibility constraints that couple the approximations for velocity and stress so as to be inefficient for computing very accurate stress fields. The current methods are also computationally inefficient and seem impractical for extensions into three dimensional flow geometries. Although some time-dependent calculations have been developed based on both the EEME (Northey *et al.*, 1990) and the EVSS formulations (Brown *et al.*, 1993), the utility of these algorithms has been limited by convergence problems for flows with high De. Moreover, the temporal accuracy and stability of the discrete equations which result from the spatial discretizations are open issues. Another goal of this thesis is to examine this issue for two of the current mixed finite element methods, EEME and EVSS. It is demonstrated that these methods are indeed temporally unstable. Therefore, time-dependent calculations performed with either of these methods could produce spurious solutions which are independent of the actual equations being solved.

The elastic-viscous split stress-gradient (EVSS-G) method is introduced to overcome the time-dependent shortcomings of the EEME/FEM and EVSS/FEM, as it is temporally stable. Another new method, the discrete elastic-viscous split stress-gradient (DEVSS-G) method is also introduced; this method has the advantage of a simpler formulation for complex constitutive equations such as the CR-FENE model than for the EVSS-G/FEM while still maintaining the steady-state and time-dependent characteristics of the EVSS-G/FEM.

The outline of the remainder of this thesis will be discussed briefly. The mathematical modeling of viscoelastic flows is reviewed in Chapter 2, beginning with the conservation of mass and momentum. This introduces the need for a constitutive equation to define fully the mathematical problem; the simplest constitutive equa-

tion is the Newtonian fluid model which forms the basis of classical hydrodynamics. The rheological properties of polymers are described to indicate the necessity for more complicated constitutive equations. Three will be highlighted in this thesis, namely, the upper convected Maxwell (UCM), the Oldroyd-B, and the Chilcott-Rallison form of the finitely extensible nonlinear elastic (CR-FENE) dumbbell equations. The mathematical type of the equation set for viscoelastic flows will also be briefly discussed.

The computational method used in this research for the spatial discretization is the finite element method while finite differences are used for the temporal discretization. In general, for elliptic equations, the Galerkin method is used to solve the problem numerically. For elliptic equations with constraints of which the Stokes problem is an example, mixed finite element methods have been introduced in which the Galerkin method is required to conform with a consistency condition in the approximation of the variables known as the LBB or inf-sup condition. For hyperbolic equations, a number of different techniques are summarized including the variations of streamline upwinding and total variation diminishing methods. Three will be examined in the calculations reported here: streamline upwinding (SU), the streamline upwind-Petrov Galerkin (SUPG) method, and the Galerkin-least squares (GLS) method.

The viscoelastic flow equations are reformulated to make the mathematical type of the various equations explicit in Chapter 4. The different formulations are EEME, viscous, EVSS, EVSS-G and DEVSS-G. Each of these are solved by artificially splitting the momentum and continuity equations from the stress equations and then are solved according to their mathematical type. The finite element formulation of these methods is discussed next. The finite element method is only used for the spatial discretization; for the time discretization, finite differences are used. For the linear stability problem, first and second order Adams-Moulton methods are used, as they are implicit and guarantee stability of the time discretization. A predictor-corrector method consisting of a second order Adams-Bashforth predictor followed by a second order Adams-Moulton corrector is introduced. The method of local mesh refinement is analyzed next; this is followed by a discussion on the technique used for bandwidth minimization, the Gibbs-Poole-Stockmayer (GPS) method (Gibbs *et al.* 1976a).

The stability of inertialess planar Couette flow of a UCM fluid to two dimensional disturbances was chosen as a model problem to examine the temporal stability of the numerical methods. This flow has a known closed-form solution and the analysis of its stability to infinitesimal disturbances can be found in closed form. The linear stability analysis shows that the real part of the exponential growth rate is always negative; therefore, the flow is linearly stable (Gorodtsov & Leonov, 1969). Since the actual solution is always stable, the numerical solution should also exhibit temporal linear stability. If the numerical calculation is not stable, then the discretization of the equations must have introduced an instability. Since this is a time dependent problem, the instability could have been introduced in either the spatial or the temporal discretization. To avoid the possibility of the temporal discretization causing the instability, fully implicit Adams-Moulton time integrators of first or second order in time are used. These two classes of methods are known to be A-stable or unconditionally stable for all temporal step sizes; thus, any observed numerical instability indicates that the spatial discretization is causing the instability. This indicates that the spatial discretization introduces an eigenvalue that causes the discretized equation to grow in time. For this instability to appear only in the temporal stability analysis, the eigenvalue must be complex, as the steady-state solution only depends on the real part of the eigenvalue. In Chapter 5, the EEME/FEM and EVSS/FEM are shown to exhibit this behavior (give convergent and accurate steady-state results, but is nonetheless linearly unstable). This is due to (what we believe are) incompatibilities in the constitutive equation on streamlines with zero velocity. Two new methods are introduced, EVSS-G/FEM and DEVSS-G/FEM, to correct the inconsistencies and are shown to be temporally stable and exhibit the correct dynamical behavior for all computed solutions in accordance with the analytical solution.

The characteristics of the EVSS-G/FEM and DEVSS-G/FEM for computing steady-state flows are examined in Chapter 6. The accuracy, convergence with mesh and robustness of these methods are shown through the application to several different flow geometries. The EVSS-G/FEM computations include the following geometries: eccentric cylinders, an infinite periodic linear array of cylinders in a channel,

the wavy-wall channel, and an infinite two-dimensional square array of cylinders. The DEVSS-G/FEM is compared to the EVSS-G/FEM for the flow of a CR-FENE model in a linear array of cylinders in a channel and shown to be essentially identical.

In Chapter 7, the new numerical methods introduced in this thesis are applied to linear stability problems with no known closed-form solutions. The first is the planar Couette flow of a CR-FENE model. This flow is shown to be numerically stable for all values of De and the decay rate is similar to that of a UCM fluid when the effective Deborah number is based on the shear-rate dependent relaxation time for the CR-FENE model rather than the zero-shear-rate. The second flow examined is that of an infinite periodic linear array of cylinders in a channel. This flow was shown to be stable up to at least $We = 0.9$.

In Chapter 8 the simulation of nonlinear, time dependent viscoelastic flows is addressed. The fully implicit time integration methods are shown to be too costly to implement on the computers of today. This leads to the study of semi-implicit methods of time integration wherein some variables are handled implicitly and others are handled explicitly. Two different types are studied in detail: the first consists of a sequential solution of blocks of equations, as examined in Northey (1991), and the second is based on operator splitting methods, as reviewed in Glowinski & Periaux (1992). The former method can be set in a Picard iteration scheme to increase the accuracy of the solution because in the limit of an infinite number of iterations, the fully implicit method is recovered. These types of methods are shown to fail in Chapter 8. The second semi-implicit scheme, the θ-method, consists of dividing the time interval into three substeps, but at each substep some of the variables are solved implicitly while the rest are solved explicitly; this then flips for the second step, etc. This method has had some success in computational fluid dynamics and has recently been applied to viscoelastic flows by Singh and Leal (1993) and Saramito (1994). For the EVSS-G formulation, the θ-method results in the time derivative of the velocity gradient term dropping out of the discretized equations. Thus the discretized equation being solved is different from the original equation being solved. On the other hand, the DEVSS-G formulation does not contain this term and is amenable to this scheme.

Therefore, combined with the additional simplicity in the formulation of the DEVSS-G/FEM, this becomes the preferred method. Calculation of the startup of flow is described in two different flow geometries: planar Couette flow and the flow through an infinite periodic array of cylinders in a channel; both examine the CR-FENE fluid. For the simple shear flow example, the lack of inertia results in the velocity, pressure, and velocity gradient (algebraic variables) instantaneously reaching, after one time step, their steady-state values. The stress variables exponentially increase to their steady-state solutions. In the periodic cylinder geometry, overshoots are observed and all De examined yield a steady-state solution at long times. Nonlinear stability analyses were performed for these two flow geometries also; both were found to be stable to perturbations up to 10% of the stress variables maximum value. Finally, the conclusions of this thesis are summarized in Chapter 8.

Chapter 2

Mathematical Modelling of Viscoelastic Fluid Flows

"The mountains flowed before the Lord."

– The prophetess Deborah from Deborah's song, Judges 5:5.

The flow of many fluids can be described mathematically by a set of partial differential equations which determine the relationships between the velocities, pressure, stresses, temperature, and body forces. These equations are derived by conserving mass, momentum, energy, and species. In this research, all flows will be isothermal without chemical reactions; hence, only the equations of conservation of mass and momentum need to be examined. In addition to these two equations, a constitutive equation is necessary to evaluate the stresses.

This chapter will outline the information necessary to model viscoelastic fluids mathematically. First, the conservation equations, or the equations of change, are presented. This is followed by some examples of the qualitative differences between Newtonian and non-Newtonian fluids. The mathematical models interrelating stress and deformation in viscoelastic fluids, constitutive equations, are described next; here, all will be of the differential type. The reader is referred to Bird *et al.* (1960) for the

derivations of the transport equations and to Bird *et al.* (1987) for the rheological properties of polymers and constitutive equations.

2.1 Governing Equations

The fluid density, ρ, will be taken to be a constant resulting in the well known case of an incompressible fluid. Then, the conservation of mass equation is written as follows:

$$\nabla \cdot \boldsymbol{v} = 0, \tag{2.1}$$

where $\mathbf{v}$ is the fluid velocity. The conservation of momentum equation is written in the notation of Bird *et al.* (1987) as:

$$\frac{\partial}{\partial t}\rho\boldsymbol{v} = -(\nabla \cdot \rho\boldsymbol{v}\boldsymbol{v}) - (\nabla \cdot \boldsymbol{\pi}) + \boldsymbol{F}, \tag{2.2}$$

where $\boldsymbol{\pi}$ is a second-order tensor which relates the transfer of momentum through molecular motions of the fluid and $\boldsymbol{F}$ is a body force per unit mass, e.g., gravity or an electrostatic force. Substituting the continuity equation, eq. (2.1), into the momentum equation gives

$$\rho\frac{\partial \boldsymbol{v}}{\partial t} + \rho\boldsymbol{v} \cdot \nabla\boldsymbol{v} = -\nabla\cdot\boldsymbol{\pi} + \boldsymbol{F}. \tag{2.3}$$

The substantial derivative is defined as

$$\frac{D}{Dt} \equiv \frac{\partial}{\partial t} + \boldsymbol{v} \cdot \nabla, \tag{2.4}$$

and represents the time rate of change in a coordinate system translating along with the fluid; i.e., a Lagrangian coordinate system. Substituting eq. (2.4) into the momentum equation yields

$$\rho\frac{D\boldsymbol{v}}{Dt} = -\nabla \cdot \boldsymbol{\pi} + \boldsymbol{F}. \tag{2.5}$$

The continuity equation and the equation of motion, eqs. (2.1) and (2.5), are exact for any incompressible fluid. However, these equations cannot be solved in closed form without an additional constitutive relation for the total stress tensor, $\boldsymbol{\pi}$.

The total stress tensor is split into two parts

$$\boldsymbol{\pi} = p\boldsymbol{I} + \boldsymbol{\tau}, \tag{2.6}$$

where p is the thermodynamic pressure[1], $\boldsymbol{I}$ is the identity tensor, and $\boldsymbol{\tau}$ is the extra or deviatoric stress which depends upon the rheology of the fluid.

Substituting eq. (2.6) into the momentum equation gives

$$\rho\frac{D\boldsymbol{v}}{Dt} = -\boldsymbol{\nabla}p - \boldsymbol{\nabla}\cdot\boldsymbol{\tau} + \boldsymbol{F}. \tag{2.7}$$

This form of the momentum equation, the continuity equation and a constitutive equation for $\boldsymbol{\tau}$ defines the mathematical statement of the field equations for the velocity.

The equation of motion, eq. (2.7), and the continuity equation, eq. (2.1), are made dimensionless by using a characteristic length L, velocity V and time T. Using L/V as the time scale, the dimensionless forms of the conservation of momentum and the continuity equation are

$$Re\left(\frac{\partial\boldsymbol{v}}{\partial t} + \boldsymbol{v}\cdot\nabla\boldsymbol{v}\right) = -\boldsymbol{\nabla}p - \boldsymbol{\nabla}\cdot\boldsymbol{\tau} + \boldsymbol{g}, \tag{2.8}$$

$$\boldsymbol{\nabla}\cdot\boldsymbol{v} = 0, \tag{2.9}$$

where the pressure is scaled by $\eta_0 V/L$, η_0 is the zero-shear-rate viscosity, Re is the Reynolds number and $\boldsymbol{g}$ is the dimensionless body force. The Reynolds number is

[1]The pressure is defined through a thermodynamic equation of state $p = p(\rho, T)$, i.e., the same function as that used in thermal equilibrium (Bird *et al.*, 1987).

dimensionless and is defined as

$$Re \equiv \frac{\rho V^2/L}{\eta_0 V/L^2} = \frac{\rho V L}{\eta_0}, \tag{2.10}$$

and scales the ratio of inertial to viscous forces. For $Re \ll 1$, inertial forces are negligible and the viscous and elastic forces are balanced by the pressure gradient.

The simplest constitutive equation defines a Newtonian fluid and is referred to as Newton's law of viscosity. It simply states that stress is linearly proportional to the rate-of-strain

$$\boldsymbol{\tau} = -\eta\dot{\boldsymbol{\gamma}}, \tag{2.11}$$

where

$$\dot{\boldsymbol{\gamma}} = \boldsymbol{\nabla v} + (\boldsymbol{\nabla v})^T \tag{2.12}$$

is the rate-of-strain tensor and η is the (constant) viscosity of the fluid. This gives the well-known Navier-Stokes equations for incompressible fluids

$$Re\left(\frac{\partial \boldsymbol{v}}{\partial t} + \boldsymbol{v}\cdot\boldsymbol{\nabla v}\right) = -\boldsymbol{\nabla} p + \boldsymbol{\nabla}^2\boldsymbol{v} + \boldsymbol{g}. \tag{2.13}$$

When Re is negligible, as will be assumed in the remainder of this thesis, eq. (2.13) reduces to the Stokes equation

$$-\boldsymbol{\nabla}^2\boldsymbol{v} + \boldsymbol{\nabla} p - \boldsymbol{g} = 0. \tag{2.14}$$

2.2 Rheology of Viscoelastic Fluids

Viscoelastic fluids not only differ from Newtonian fluids quantitatively in the form of the constitutive equation but also qualitatively (Bird *et al.*, 1987). Ten examples of viscoelastic behavior of polymers are shown in Figures 2-1 and 2-2, which is taken from Bird & Curtiss (1984). There are three main reasons for these differences between Newtonian and viscoelastic fluids: shear-rate-dependent viscosities, normal stresses, and 'elastic' effects. The first does not directly cause any of the effects seen in Figures

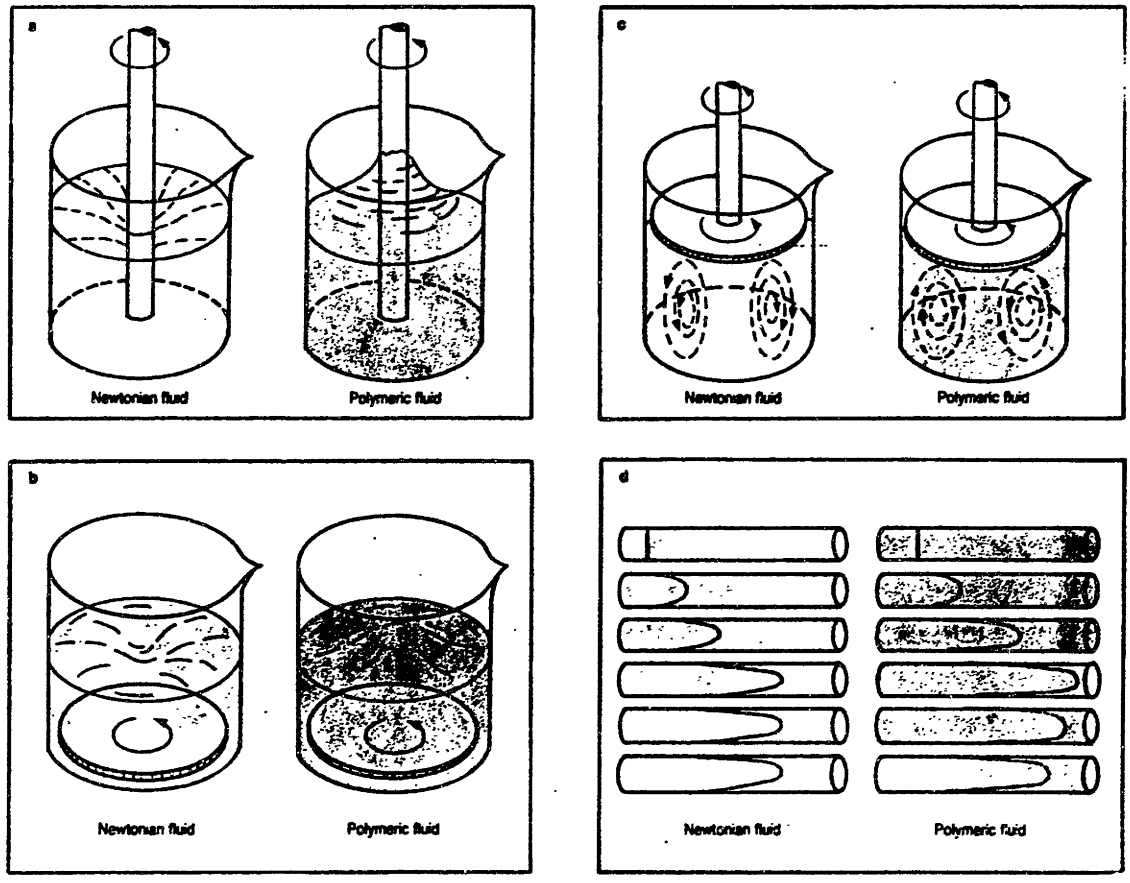

Figure 2-1: Characteristic viscoelastic behavior (Bird & Curtiss, 1984). These four experiments indicate how the behavior of polymeric liquids is different from that of Newtonian liquids. The experiments are described in the text. a) rotating rod; b) rotating disk on bottom; c) rotating disc on top; d) pump turned off.

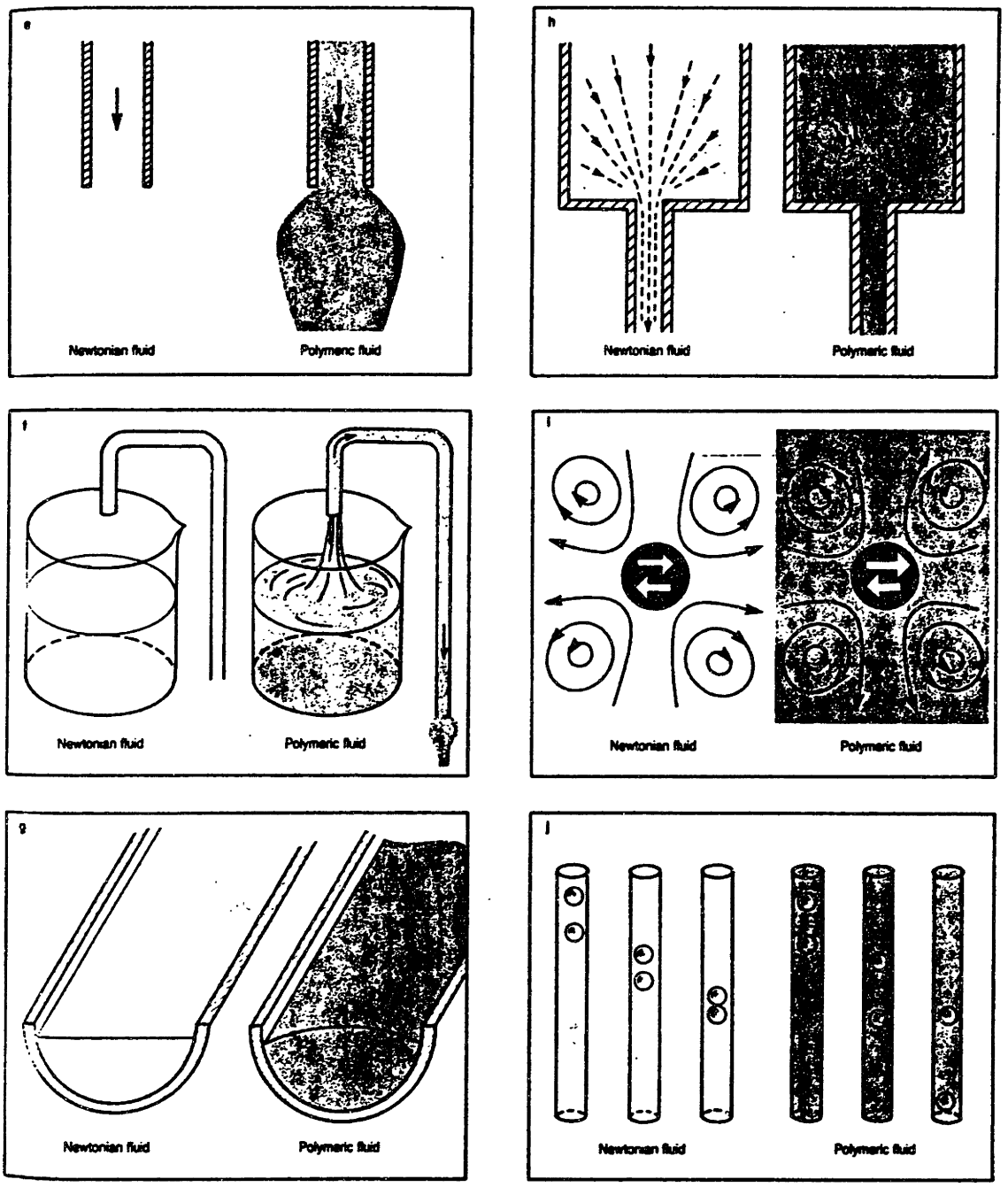

Figure 2-2: Characteristic viscoelastic behavior (Bird & Curtiss, 1984). These six experiments indicate how the behavior of polymeric liquids is different from that of Newtonian liquids. The experiments are described in the text. e) die-swell; f) siphon across a gap; g) flow down a trough; h) sudden contraction; i) transversely oscillating cylinder; j) two spheres falling along centerline of a cylinder.

2-1 and 2-2, but is an important difference nonetheless. There are two normal stress differences in unidirectional shear flow - the first normal stress difference defined as $(\tau_{11} - \tau_{22})$ and the second normal stress difference $(\tau_{22} - \tau_{33})$ where 1, 2, and 3 are coordinate directions along the direction of the fluid velocity, the direction of velocity variation, and the neutral direction, respectively (Bird *et al.,* 1987). Newtonian fluids have zero normal stresses in shearing flow. The extra tensile contributions from these normal stresses are along the streamlines or "1" direction. The polymer molecules are aligned and stretched along the streamlines, but the polymers want to relax to a randomly oriented state; this gives rise to the extra stress term. Elastic forces cause secondary flows that are generally in an opposite direction to secondary forces caused by inertial forces (Bird *et al.,* 1987). They also give rise to memory effects; i.e., the fluid behavior at time t_1 depends on the flow history $t_0 \leq t < t_1$, where, generally, $t_0 \rightarrow -\infty$.

Several of the experiments shown in Figures 2-1 and 2-2 can be explained due to normal stresses. The spinning rod experiment is shown in Figure 2-1a where the polymeric fluid crawls up the rod, and a rotating disc at the bottom of the container shows the same type of effect in that the polymer rises above the disk as shown in Figure 2-1b. This phenomena is equivalent to rod climbing, but without a rod. In both experiments the streamlines are closed circles and the extra tension due to the first normal stress difference forces the fluid inwards against the centrifugal force and upwards against gravity (Bird *et al.,* 1987). This type of stress is often called a hoop stress. The flow of a viscoelastic flow down an inclined trough results in a slightly convex surface, as shown in Figure 2-2g. The extra tension in this example is in the direction normal to the fluid surface. The gradient of the velocity is largest at the walls; thus the fluid will be pulled down there and bulge at the center of the trough (Bird *et al.,* 1987).

There are several experiments which show the formation of secondary flows from elastic effects rather than inertial forces. The direction of rotation of the vortex is inward toward the center of the beaker instead of outward for the viscoelastic fluid when the rotating disc is on top of the fluid (see Figure 2-1c). The reversal of the flow

direction is due to the presence of the normal stresses opposing the centrifugal forces which push the fluid outward as in the Newtonian case (Bird *et al.,* 1987). Polymer fluids move toward a transversely oscillating cylinder along the line of oscillation (see Figure 2-2i); this flow reversal is identical to the rotating lid (Bird *et al.,* 1987).

The remaining qualitative differences are due to combinations of the differences mentioned earlier between the two types of fluids. Figure 2-1d shows how the non-Newtonian fluid recoils after a pump is shut off in a tube. This shows the fading memory effect of the viscoelastic fluid; the stretched polymers in the fluid recoil from a stretched to a relaxed state. As shown in Figure 2-2e, polymers swell significantly after exiting from a tube. Again, the normal stresses give rise to an additional tension which is no longer counterbalanced by the walls; thus, the fluid contracts axially and expands radially. The amount of die swell could also depend on the length to diameter ratio of the die due to the fading memory of the fluid. If the fluid is forced from a large reservoir through a die which is small in diameter and short in length, then the fluid will remember its previous state in the reservoir and expand upon leaving the die (Bird *et al.,* 1987). A viscoelastic fluid will maintain a siphon across a gap whereas the Newtonian fluid will not (see Figure 2-2f). The streamline orientation and elongation of the polymer molecule creates the large axial stresses necessary to keep the siphon working (Bird *et al.,* 1987). The formation of vortices in the sudden contraction geometry is shown in Figure 2-2h. The cause of this difference is not presently known. Figure 2-2j shows two spheres falling along the centerline of a cylinder. The polymeric fluid can cause the spheres to move together as in the Newtonian fluid or when the spheres are separated beyond a critical distance they will separate over time. This may be due to the presence of a 'negative' wake.

A parameter that quantifies the non-Newtonian behavior of the fluid is the Deborah number, De, which is defined as

$$De \equiv \frac{\lambda}{L/V}, \tag{2.15}$$

where λ is the relaxation time of the fluid. The time constant of the fluid used in

the definition of De can be the zero-shear-rate relaxation time of the fluid λ_0 or some λ_1 from a viscoelastic model. De scales as the characteristic time scale for the fluid (relaxation time) to the characteristic time scale of the flow (residence time, reciprocal forced frequency, etc.). For $De \to 0$ the fluid behaves like a Newtonian fluid whereas for $De \to \infty$ the fluid behaves as a Hookean solid. As De approaches unity, elastic effects in the flow become significant. As an example, the relaxation time of water is $\sim 10^{-13}$ seconds at room temperature. For normal flow situations, De is practically zero; however, if it were possible to observe the flow of water over time scales of order 10^{-13}, then viscoelastic effects would be significant as $De \sim 1$.

2.3 Viscoelastic Constitutive Equations

In the previous section, the qualitative differences between Newtonian and viscoelastic fluids were examined; now, the quantitative differences will be discussed by introducing various constitutive equations of differential type. The mixed boundary-value problem governing the transient flow of an incompressible viscoelastic liquid described by a prototypical differential constitutive model is written here in terms of the dimensionless velocity ($\boldsymbol{v}(\boldsymbol{x})$), pressure ($p(\boldsymbol{x})$) and deviatoric stress ($\boldsymbol{\tau}(\boldsymbol{x})$) fields as

$$Re\left(\frac{\partial \boldsymbol{v}}{\partial t} + \boldsymbol{v}\cdot\boldsymbol{\nabla}\boldsymbol{v}\right) = -\boldsymbol{\nabla}p - \boldsymbol{\nabla}\cdot\boldsymbol{\tau} + \boldsymbol{g}(\boldsymbol{x}), \tag{2.16}$$

$$\boldsymbol{\nabla}\cdot\boldsymbol{v} = 0, \tag{2.17}$$

$$\boldsymbol{\tau} + h(tr\boldsymbol{\tau}; De)\left(\frac{\boldsymbol{\tau}}{f(tr\boldsymbol{\tau}; De)}\right)_{(1)} = -\dot{\boldsymbol{\gamma}} - De\beta\left(\frac{\dot{\boldsymbol{\gamma}}}{f(tr\boldsymbol{\tau}; De)}\right)_{(1)}, \tag{2.18}$$

where the subscript $\boldsymbol{\tau}_{(1)}$ defines the upper convected derivative of the tensor $\boldsymbol{\tau}$ as

$$\boldsymbol{\tau}_{(1)} \equiv \frac{\partial \boldsymbol{\tau}}{\partial t} + \boldsymbol{v}\cdot\boldsymbol{\nabla}\boldsymbol{\tau} - (\boldsymbol{\nabla}\boldsymbol{v})^T\cdot\boldsymbol{\tau} - \boldsymbol{\tau}\cdot(\boldsymbol{\nabla}\boldsymbol{v}), \tag{2.19}$$

and $\boldsymbol{g}(\boldsymbol{x})$ is the body force acting on the liquid. The Reynolds number and the Deborah number are defined by eqs. (2.10) and (2.15), respectively, using the same velocity, length and time scales as in Section 2.1; the stress is made dimensionless

using the scale $\eta_0 V/L$. In the formulation of the constitutive equation, eq. (2.18), the parameter β is equal to the ratio of the viscosity of a Newtonian solvent (η_s) to the zero-shear-rate viscosity of the composite solution ($\eta_0 = \eta_s + \eta_p$), where η_p is the polymer contribution to the zero-shear-rate viscosity.

Polymer fluids, as discussed qualitatively in the previous section, possess a memory of the past which decays in time. This dependence on past rates-of-strain is better approximated if a number of relaxation times λ_i (and, thus, a number of De_i) are used; the stresses for individual relaxation times can be added together using the principle of superposition to form a multi-mode model where each relaxation time has an independent parameter β_i. Small relaxation times control short-time responses while large relaxation times control long-time, asymptotic behavior.

The functions $f(tr\boldsymbol{\tau}; De)$ and $h(tr\boldsymbol{\tau}; De)$ in eq. (2.18) are specific for different viscoelastic constitutive models. The simplest models are recovered by setting $f = 1$ and $h = De$ to yield the Oldroyd-B model

$$\boldsymbol{\tau} \equiv \boldsymbol{\tau}_p + \boldsymbol{\tau}_s, \tag{2.20}$$

$$\boldsymbol{\tau}_s = -\beta\dot{\boldsymbol{\gamma}}, \tag{2.21}$$

$$\boldsymbol{\tau}_p + De\boldsymbol{\tau}_{p(1)} = -(1-\beta)\dot{\boldsymbol{\gamma}}, \tag{2.22}$$

where $\boldsymbol{\tau}_p$ is the polymer contribution to the deviatoric stress and $\boldsymbol{\tau}_s$ is the Newtonian solvent contribution to the stress. In addition, setting $\beta = 0$, a solventless polymeric fluid, gives the upper-convected Maxwell (UCM) model

$$\boldsymbol{\tau}_p + De\boldsymbol{\tau}_{p(1)} = -\dot{\boldsymbol{\gamma}}. \tag{2.23}$$

The Oldroyd-B model can be derived using the kinetic theory of dilute polymer solutions (Bird *et al.*, 1987). The polymer solution is modelled as Hookean dumbbells (the polymer) in a Newtonian solvent. The UCM model can be derived from a network model for concentrated polymer solutions and melts.

The UCM model has been used in numerous calculations due to its simplicity

and because it models many viscoelastic effects; however, there are several important deficiencies of this model which must be noted. Neither shear-rate-dependence of the viscosity nor overshoot of the normal stress are predicted for the start-up of steady shear flow; both effects are seen in real fluids. More importantly, in elongational flows, the normal stresses go to infinity at a finite strain-rate which is clearly aphysical (also true for the Oldroyd-B model). Both this model and the Oldroyd-B model may be ill-posed near a singularity such as the salient and reentrant corners in the sudden contraction geometry (Coates, 1992a, Coates *et al.,* 1992b and Salamon 1995); although some evidence to contrary is present in the literature (Davies & Devlin, 1993, Hinch 1993, and Renardy 1994). Finally, there is only a single time constant; although this can be eliminated by introducing a series of independent modes.

Many other differential constitutive equations have been introduced through the usage of micromechanical theories (Larson 1988). These introduce extra terms which attempt to correct the deficiencies in the UCM and Oldroyd-B models; accordingly, the terms have physical interpretations. However, they all rely on the upper convective derivative of stress to impart the basic viscoelastic behavior; therefore, it becomes essential to understand the UCM model *before* using more advanced constitutive equations in numerical simulations. The use of the UCM equations initially will be emphasized in this research.

The more complicated constitutive equation which will be examined in this thesis is the Chilcott-Rallison finitely extensible nonlinear elastic (CR-FENE) dumbbell model (Chilcott & Rallison, 1988). This model eliminates the infinite normal stresses at finite strain rates by limiting the extent to which the dumbbell can be elongated. The constitutive equation for the CR-FENE model is defined in terms of the configuration tensor $\boldsymbol{A}$ which is the ensemble average of the second moment (i.e., dyad) of the end-to-end vector for the dumbbell ($\langle \mathbf{QQ} \rangle$) scaled with the square of the equilibrium radius of gyration of a Gaussian chain and can be written as follows:

$$De\boldsymbol{A}_{(1)} + f(R)(\boldsymbol{A} - \boldsymbol{I}) = 0, \tag{2.24}$$

where $\boldsymbol{I}$ is the identity tensor and

$$f(R) = \frac{1}{1-R^2/L^2}, \tag{2.25}$$

$$R^2 = tr(\boldsymbol{A}), \tag{2.26}$$

where L is the dimensionless contour length scaled with the equilibrium radius of gyration and $tr(\boldsymbol{A})$ is a measure of the linear dimension of the polymer chain length scaled with the equilibrium radius of gyration. The maximum chain length ($\langle \mathbf{QQ} \rangle_{max}$) is given by L^2. To convert the momentum equation into the variables of the constitutive equation the following three equations can be used:

$$\boldsymbol{\sigma} = -p_{CR}\boldsymbol{I} + \dot{\boldsymbol{\gamma}} + \frac{1-\beta}{De} f(R)\boldsymbol{A}, \tag{2.27}$$

$$p\boldsymbol{I} = p_{CR}\boldsymbol{I} - \frac{1-\beta}{De} f(R)\boldsymbol{I}, \tag{2.28}$$

$$\boldsymbol{\tau}_p = -\frac{(1-\beta)}{De} f(R)[\boldsymbol{A} - \boldsymbol{I}], \tag{2.29}$$

where p_{CR} is a modified pressure. The constitutive equation in terms of $\boldsymbol{\tau}_p$ is then

$$\boldsymbol{\tau}_p + \frac{De}{f(R)}\boldsymbol{\tau}_{p(1)} - \frac{(1-\beta)}{f(R)}\dot{\boldsymbol{\gamma}} = \mathbf{0}. \tag{2.30}$$

Writing the constitutive equation in terms of eq. (2.18) yields the two functions $f(tr\boldsymbol{\tau}; De) = 1$ and $h(tr\boldsymbol{\tau}; De) = \frac{De}{f(R)}$. In the limit $L = \infty$, the Oldroyd-B equation is recovered; if, in addition, $\beta = 0$, the UCM model is recovered.

For confined flows, the differential equations eqs. (2.16), (2.17) and (2.22) or (2.24) require boundary conditions to be specified where appropriate. The velocity components are specified along solid boundaries, where the usual assumptions of no-slip and no-penetration conditions are applied so that both components of the velocity vanish there. Appropriate inlet and outlet boundary conditions are applied for the velocity field; whereas the stress field only has boundary conditions on inflow boundaries. All of the flows to be considered here are spatially periodic in one-dimension so that the periodic boundary condition replaces the inlet and outlet boundary conditions.

2.4 Mathematical Type

Partial differential equations (PDEs) can be characterized by their mathematical type. It will be seen in Chapter 3 that the mathematical type of a PDE has important implications for the steady-state and time-dependent formulations of the numerical method used to solve the equation. The classification of PDEs is important for the implementation of boundary conditions to make the boundary-value problem well-posed and is treated in most texts on PDEs such as Carrier & Pearson (1976) and John (1982). The mathematical type derives its importance from the fact that it determines the mechanism whereby information is transmitted through the domain Ω.

Consider the general, constant coefficient second-order partial differential equation for the scalar $u(x, y)$ on Ω,

$$Au_{xx} + 2Bu_{yx} + Cu_{yy} + Du_x + Eu_y + Fu + G = 0, \tag{2.31}$$

where A, B, C, D, E, F and G are constants. The mathematical type of the equation is determined by the specification of Cauchy data (u and its normal derivative) on an arbitrary curve Γ which is defined by $\xi(x, y) = 0$ which is a member of the set of curves, $\xi(x, y)$ =constant. Defining a new coordinate system from the definition of another set of curves, $\eta(x, y)$ =constant, which are not tangent to ξ in Ω (i.e., $\xi_x\eta_y - \xi_y\eta_x \neq 0$), the type of the equation can be found by determining whether or not the Cauchy boundary data on Γ guarantees a unique solution. Expanding u in a Taylor series about Γ (the series can be shown to have a unique solution by the Cauchy-Koweleski Theorem (Carrier & Pearson, 1976 and John, 1982)) and changing independent variables from (x, y) to (ξ, η) results in an equation for $u_{\xi\xi}$:

$$\left\{ A\left(\frac{\xi_x}{\xi_y}\right)^2 + 2B\left(\frac{\xi_x}{\xi_y}\right) + C \right\} u_{\xi\xi} + f(u, u_{\xi\eta}, \ldots) = 0. \tag{2.32}$$

It can be seen that only the coefficients of the highest order terms will determine the solvability of the Cauchy problem; the mathematical type of an equation is governed

by the highest order differential operator in the equation.

If $B^2 - AC > 0$, there exist two real curves, or characteristics, where the Cauchy data are insufficient to specify $u(x, y)$ resulting in an ill-posed problem. Equations of this type are known as hyperbolic. Information is transferred forward in time along the characteristic in a wave-like form. The initial conditions are specified at the inflow boundary for and are convected through the domain to the outflow boundary. This is similar to the information transport in a plug flow reactor.

If $B^2 - AC = 0$, there exists only one characteristic; again, the Cauchy problem is not solvable. An initial condition at the inflow boundary for the variable resulting in the characteristics is needed. Equations of this type are known as parabolic. Information propagates as in the hyperbolic case in the direction associated with the real characteristic and is shared instantaneously in the other direction. The effect of the initial condition decays exponentially until, after finite time, it is no longer important; whereas, in hyperbolic equations the initial conditions are important for all time. This is similar to the startup of a continuous, stirred tank reactor (CSTR) in which the information is transported in time and shared instantaneously in the spatial directions.

If $B^2 - AC < 0$, there are no real roots so no characteristics exist. The equation is thus well-posed for the Cauchy data and is used as the boundary conditions. The speed of propagation of information is infinite; every point in the domain is coupled to every other and instantaneously reacts to any changes in the domain. This is similar to the spatial information transport in a CSTR.

The type analysis can be generalized to a system of nth order PDEs by rewriting the equations as a set of first order PDEs (Carrier and Pearson, 1976). As an example, take a system of equations in $\Re^2$ with x and y as coordinate directions. The PDE can be written as

$$\boldsymbol{A}\frac{\partial u}{\partial x} + \boldsymbol{B}\frac{\partial u}{\partial y} = \boldsymbol{C}. \tag{2.33}$$

The type of the system of equations is still determined by the characteristic slopes,

$\alpha = \partial x/\partial y$, which are found by evaluating the expression

$$det[\boldsymbol{A} - \frac{\partial x}{\partial y}\boldsymbol{B}] = 0. \tag{2.34}$$

Real characteristics are associated with hyperbolicity; imaginary characteristics are associated with ellipticity.

The mathematical type of the viscoelastic flow equations are complicated by the fact that the type can change depending on values of parameters in the equations. The equation of motion is elliptic for the inertialess limit. With inertia the equations can change type from elliptic to hyperbolic and back again in various areas of the domain and at various times (Joseph *et al.*, 1985). An elliptic saddle point problem is formed when the momentum equation is coupled with the continuity equation (Carey & Oden, 1986). This type of problem leads to various constraints on the numerical method used to solve the system of equations (see Section 3.2). The addition of the constitutive equation further complicates the matter, since by itself it is a hyperbolic equation set.

For inertialess flow, Rutkevich (1970; 1972) was the first to study the mathematical type of the equation set defining the UCM model. The importance of this analysis and the subsequent study by Joseph *et al.* (1985) lies in the observation that the equation set is of mixed mathematical type. The linearized equation set for steady-state, two-dimensional flow is a set of six first order partial differential equations for the canonical variables formed by the two velocity components, the three deviatoric stress components, and the pressure. This equation set has mixed type, i.e., some variables have elliptic character and others are hyperbolic. The six characteristics, α, are given by

$$\alpha_1 = +i, \tag{2.35}$$

$$\alpha_2 = -i, \tag{2.36}$$

$$\alpha_3 = v_x/v_y, \tag{2.37}$$

$$\alpha_4 = v_x/v_y, \tag{2.38}$$

$$\alpha_5 = [\lambda_1 \tau_{yx} - \sqrt{det(\lambda_1 \boldsymbol{\tau} - \eta_0 \boldsymbol{I})}]/(\eta_0 - \lambda_1 \tau_{yy}), \tag{2.39}$$

$$\alpha_6 = [\lambda_1 \tau_{yx} - \sqrt{det(\lambda_1 \boldsymbol{\tau} - \eta_0 \boldsymbol{I})}]/(\eta_0 - \lambda_1 \tau_{yy}). \tag{2.40}$$

The first two characteristics are imaginary (elliptic type); the second two characterisitics are real (hyperbolic type); the final two characteristics can be either real or imaginary depending on the tensor $\boldsymbol{\chi} \equiv \lambda_1 \boldsymbol{\tau} - \eta_0 \boldsymbol{I}$. If $\boldsymbol{\chi}$ is negative-definite, then the determinant is negative, complex roots exist and the characteristics are imaginary (elliptic type). If $\boldsymbol{\chi}$ is positive semi-definite, then the determinant is greater than or equal to zero, real roots exist, and the characteristics are real (hyperbolic type).

Joseph *et al.* (1985) associated the characteristics with the corresponding equations for the UCM fluid being solved. The two real streamwise characteristics ($\alpha_{3,4}$) are associated with the constitutive equation; the two purely imaginary characteristics ($\alpha_{1,2}$) are associated with the incompressibility constraint; and the remaining two characteristics are associated with the vorticity or momentum equation. The change of type of the equations is associated with the constitutive model (for inertialess fluids).

The flow of the Oldroyd-B fluid with no inertia is governed by the following equations:

$$-\eta_s \boldsymbol{\nabla}^2 \boldsymbol{v} + \boldsymbol{\nabla} \cdot \boldsymbol{\tau}_p + \boldsymbol{\nabla} p = \boldsymbol{0}, \tag{2.41}$$

$$\boldsymbol{\nabla} \cdot \boldsymbol{v} = \boldsymbol{0}, \tag{2.42}$$

$$\boldsymbol{\tau}_p + \lambda_1 \boldsymbol{\tau}_{p(1)} = -\eta_p \dot{\boldsymbol{\gamma}}. \tag{2.43}$$

The characteristics α, for a two-dimensional flow, are given by the equation

$$(1 + \alpha^2)^2(-v_x + \alpha v_y)^3 = 0. \tag{2.44}$$

This results in three real (hyperbolic) characteristics which are associated with the three component equations of the stress tensor and four imaginary (elliptic) characteristics which are associated with the momentum and continuity equations. The

addition of the elliptic solvent term in the momentum equation, $\eta_s \nabla^2 \boldsymbol{v}$, has a singular effect on the mathematical type of the equation set. The number of canonical variables has been increased from six to seven, and the type of the momentum equation is now independent of the tensor $\boldsymbol{\chi}$. Furthermore, the equations are now always elliptic (see Section 4.1 for further information).

The type analysis affects the formulation of numerical methods in several key areas. First, it indicates that the momentum and continuity equations remain essentially an elliptic saddle point problem while the constitutive equations retain their hyperbolic character. This suggests splitting the variables into two types where different numerical methods can be used on each. The momentum and continuity equations can be solved by a Stokes solver for nonhomogeneous data (the divergence of the polymer stress); the constitutive equations can be solved by an appropriate solver for hyperbolic equations as if the velocity field were given data. This point will be amplified in Chapters 3 and 4. Second, the boundary conditions appropriate for each variable are determined in the type analysis. Finally, in Chapter 4 the viscoelastic fluid flow equations are reformulated in order to show explicitly the mathematical type of the equations; this has allowed the development of several numerical methods that are accurate, convergent, robust, and temporally stable.

Chapter 3

Finite Element Methods

"Nerzhin, his lips tightly drawn, was inattentive to the point of rudeness: he did not even bother to ask what exactly Verenyov had written about this arid branch of mathematics in which he himself had done a little work for one of his courses. Suddenly he felt sorry for Verenyov. [Functional analysis] belonged to the stratosphere of human thought. It might conceivably turn out to be of some use in the twenty-fourth century, but for the time being...

I care not for the sun and stars,
I see but man in torment."

– Alexander Solzhenitsyn from The First Circle

The viscoelastic flow equations, eqs. (2.16 – 2.18), have analytical solutions for only a small set of flow problems. In general, a numerical solution must be sought, wherein the dependent variables - velocity, stress and pressure - are discretized using a numerical method. The finite element method (FEM)[1] has had much success not only in Newtonian fluid dynamics problems, but also in many other fields of engineering, including solid mechanics for which it was originally derived. The FEM is the best method for approximating arbitrarily shaped domains and retains large flexibility for the resolution of boundary layers using local mesh refinement. Finite element analysis

[1]There is no single finite element method; in fact, it is a family of different methods which include the Rayleigh-Ritz method, the Galerkin method and the Petrov-Galerkin method.

is the method of choice in this research for solving the stationary viscoelastic equations. Issues in the development of the finite element method to solve the viscoelastic flow equations include the mathematical type of the equations, the compatibility of the approximations to the variables and the consistent discretization of the equations. First, the solution of elliptic problems via the FEM is discussed in Section 3.1. Mixed methods are examined in Section 3.2 with particular emphasis on the Stokes' problem. Since the constitutive equations are hyperbolic, the application of the FEM to hyperbolic equations is discussed in Section 3.3. The upwinding methods in current use for advection-diffusion problems also are discussed. The reader is referred to other references (Becker *et al.*, 1981; Carey & Oden, 1983; Carey & Oden, 1984; Carey & Oden, 1986 and Johnson, 1987) for further information on the FEM.

3.1 FEM for Elliptic Equations

The FEM belongs to the class of weighted residual methods. The basic idea is to relax the continuity of the solution of the original differential equations (the strong form) to allow a more general solution using an integral formulation which is known as the weak or variational form of the problem. This derivation follows methods derived from variational principles for elliptic differential equations. The domain of the solution is divided into simple subdomains, usually triangles or quadrilaterals (which are not necessarily of equal size), and the solution is constructed from an approximation over the set of the individual elements.

The FEM is best illustrated by considering an example formed from the elliptic linear operator, L, defined on the domain Ω with boundary Γ:

$$Lu = f, \tag{3.1}$$

with homogeneous Dirichlet boundary conditions $u = 0$ on Γ. The function $f(x)$ may be simply considered as inhomogeneous data. This form is known as the *Euler-*

Lagrange equation of the appropriate variational form:

$$(Lu - f, v) = 0. \tag{3.2}$$

At this point, the introduction of Sobolev function spaces will make a discussion of the FEM theory more precise (Carey & Oden, 1986). If the norm of the function $g(\boldsymbol{x})$ satisfies the condition

$$\|g\| \equiv (g, g)^{1/2} \equiv \int_\Omega g^2 d\Omega < \infty, \tag{3.3}$$

then $g(\boldsymbol{x})$ is defined as being square-integrable, $g(\boldsymbol{x}) \in L_2(\Omega)$, where Ω is the domain. For any integer m, the Sobolev spaces $g(\boldsymbol{x}) \in H^m(\Omega)$ are defined as

$$H^m(\Omega) = \{g(\boldsymbol{x}) \in L_2(\Omega); D^s g \in L_2(\Omega), s = 1, \ldots, m\}, \tag{3.4}$$

where D^m is all mth-order partial derivatives of $g(\boldsymbol{x})$. The implication of this definition is that all mth-order derivatives of $g(\boldsymbol{x})$ are square integrable. The norm for H^m is defined as

$$\|g\|_m^2 \equiv \int_\Omega \left\{[D^m g]^2 + [D^{m-1} g]^2 + \ldots + g^2\right\} d\Omega. \tag{3.5}$$

The inner product associated with the mth-Sobolev space is defined as

$$(a, b)_m \equiv \int_\Omega [D^m(a) D^m(b) + D^{m-1}(a) D^{m-1}(b) + \ldots + ab] d\Omega. \tag{3.6}$$

The requirement that the solution u satisfies the boundary condition ($u = 0$ on Γ) further restricts the Sobolev space such that $u \in H_\Gamma^{2m}$ where H_Γ^{2m} is the space of all functions that satisfy the boundary conditions, for example, $u = 0$ on Γ, and have finite energy in the $2m$ norm.

In eq. (3.1), the operator L can be viewed as a transformation of the space H_Γ^{2m} onto H^0 (assuming $f \in H^0$). The use of functional analysis determines if L is a one-to-one transformation, i.e., if L is invertible. Then for each f there is one and only one u, and this guarantees the existence and uniqueness of u. The mathematical

representation of the necessary and sufficient condition for uniqueness is

$$\|u\|_{2m} \leq C\|f\|_0, \tag{3.7}$$

where C is a constant.

The variational form of eq. (3.1) is written as

$$I(v) = (Lv, v) - 2(f, v) \qquad \forall v, \tag{3.8}$$

where $(\cdot, \cdot)$ is the inner product as defined in eq. (3.6) for $m = 0$. Note that v has to satisfy $v = 0$ on Γ.j The solution to the Euler-Lagrange equation corresponds with the minimization of the quadratic functional $I(v)$ or the setting of eq. (3.8) to zero (Carey & Oden, 1983). This is the weak or Galerkin form of the problem. The solution also no longer has to satisfy the differential equation exactly at every point in the domain, but rather simply that the error or residual of the solution weighted with an appropriate function is small when integrated over the domain. The solution no longer corresponds to a minimum, but rather to a stationary point. This allows the requirement of L being either positive-definite or symmetric to be relaxed. Galerkin's method approximates this stationary point by requiring the residual $(Lu - f)$ to be orthogonal to the set of functions v.

The finite element method replaces the infinite dimensional function space H^1_Γ with a set of finite-dimensional subspaces $S^h \subset H^1_\Gamma$. The functions, $v^h \in S^h$, are known as the trial functions and are determined as

$$v^h(\mathbf{x}) = \sum_{j=1}^{N} a_j \phi_j(\mathbf{x}), \tag{3.9}$$

where N is the number of subelements into which the domain has been divided, $\{a_j\}$ are the nodal values of the function $\{v^h(\boldsymbol{x})\}$ and $\{\phi_j(\boldsymbol{x})\}$ are the basis functions of the subspace S^h. The nodal values are unknown and are found as the solution of the finite element equations which is simply the solution of a set of nonlinear algebraic equations.

The basis functions are an important aspect to the FEM. They are defined so that they are nonzero only over a small portion of the domain, i.e., they have local support. This results in a discretized equation set whose component matrices are sparse and banded. A banded, sparse matrix is advantageous computationally because the number of arithmetic operations and storage requirements are much less than that for a dense matrix (Golub and Van Loan, 1989). The functions v^h in this thesis will be taken to be bilinear or biquadratic Lagrangian polynomials. In the Galerkin finite element method the trial functions are taken to be the same as the weighting functions.

The implementation of the Galerkin method requires the residual $(Lu^h - f)$ to be orthogonal to u^h and thus S^h (as u^h is made up of basis functions for S^h). Requiring the residual and the basis functions for S^h to be orthogonal in the inner product meets this requirement

$$\int_\Omega [Lu^h - f]\phi_k^h d\Omega = 0 \qquad k = 2, \ldots, N. \tag{3.10}$$

The weak form is not applied to any nodes where there is an essential boundary condition (here taken to be at $k = 1$). Equation (3.10) and the essential boundary conditions make up a set of N algebraic equations in N unknowns which can be solved by inverting the matrix of coefficients for the steady-state equations.

In order to determine how good the obtained numerical solution using the finite element method is, it is necessary to define the expected error in this solution. The energy norm is a natural way to describe the error in the FEM in that the finite-element weak formulation minimizes the error in this norm (Becker *et al.,* 1981; Carey & Becker, 1983 and Carey & Oden, 1986). It can be shown that

$$K\|v\|_1^2 \geq a(v,v) \geq \sigma\|v\|_1^2, \tag{3.11}$$

where, in terms of the weak form of eq. (3.1),

$$a(v,v) = (Lv,v) = (f,v), \tag{3.12}$$

where $(\cdot,\cdot)$ is the inner product defined by eq. (3.6) and K and σ are both positive constants. The first half of the inequality shows that the error is bounded; the second half is a statement of the ellipticity of the operator L contained in the energy norm. Both of these are sufficient to show existence and uniqueness of the weak solution. Interpolation theory is used to show that the rate of convergence of the interpolant, ω^h, of v is

$$a(e^h, e^h) \leq Ch^{2k}\|f\|_\Omega^2, \tag{3.13}$$

where $e^h = (v - \omega^h)$ is an upper bound for the error in the FEM, C is a constant, h is a characteristic mesh spacing, and $k-1$ is the order of the polynomial interpolant which is equal to the order of the Lagrangian polynomial basis function. This inequality requires that the error in ω^h and, hence, Galerkin's method to vanish at a rate of h^{2k} in the limit of infinite refinement. This leads to the definition of the energy norm

$$\|e\|_E \equiv \left(\int_\Omega [(e')^2 + e^2]dx\right)^{1/2}. \tag{3.14}$$

The rate of convergence of the finite element method can be derived in terms of the powers of the interpolating power of the polynomial used to approximate the variable as (Becker *et al.*, 1981)

$$\|e\|_E \leq Ch^{k-1}. \tag{3.15}$$

Convergence to the order of the interpolating polynomial is called optimal.

All of the convergence results depend on the ellipticity condition, eq. (3.11). When this condition fails, as in hyperbolic equations, Galerkin's method also fails and produces spurious results unrelated to the exact solution. This will be examined further in Section 3.3.

3.2 Stokes' Flow

Finite element methods for the inertialess (Re=0) Newtonian flow problem, or Stokes' problem, are well developed (Carey & Oden, 1986). Because of the relevance of this

problem as the $De = 0$ limit of the viscoelastic problem, it is worthwhile to examine this analysis in some detail. The equations of motion are

$$-\mu\nabla^2\boldsymbol{v} + \nabla p = \boldsymbol{F}, \tag{3.16}$$

$$\nabla \cdot \boldsymbol{v} = 0, \tag{3.17}$$

and we assume that the flow satisfies the boundary condition $\boldsymbol{v} = \mathbf{0}$ on the boundary of the domain Γ, where μ is the viscosity, $\boldsymbol{v}$ is the velocity, p is the thermodynamic pressure, and $\boldsymbol{F}$ is the body force, typically gravity. This mathematical problem is similar to the one studied in the previous section; the only difference is the presence of the continuity equation; eq. (3.17) acts as a constraint on eq. (3.16). This constraint limits the space of allowable functions used in Galerkin's method to a Sobolev subspace defined as

$$K = \{\boldsymbol{v} \in H^1_\Gamma | \nabla \cdot \boldsymbol{v} = \mathbf{0}\}. \tag{3.18}$$

Applying the method outlined in the previous section, the problem would now be to minimize the functional defined as

$$J(\boldsymbol{v}) \equiv \int_\Omega \{\frac{\mu}{2}\nabla\boldsymbol{v} : \nabla\boldsymbol{v} - \boldsymbol{F} \cdot \boldsymbol{v}\} d\Omega, \tag{3.19}$$

which simply measures the total energy of the system. The variational form of the problem minimizes J over all velocities belonging to the functional space, K, i.e., satisfying incompressibility. It is usually difficult first to find and then to prove that various functions belong to constrained functional spaces so this type of problem is typically solved through the introduction of a Lagrange multiplier.

The introduction of a Lagrange multiplier into the constrained minimization problem results in a direct equivalence between the multiplier and the pressure. Thus, the continuity equation can be considered as a constraint and is solved with respect to the pressure basis functions (Carey & Oden, 1986). The constrained optimization problem becomes, therefore, a two field problem to find a stationary value at some

point $(\boldsymbol{u}, p) \in H^1_\Gamma \otimes Q$ such that

$$\int_\Omega (\mu \boldsymbol{\nabla v} : \boldsymbol{\nabla u} - p \boldsymbol{\nabla} \cdot \boldsymbol{v} - \boldsymbol{F} \cdot \boldsymbol{v}) d\Omega = \boldsymbol{0} \qquad \forall\, v \in H^1_\Gamma, \tag{3.20}$$

$$\int_\Omega (q \boldsymbol{\nabla} \cdot \boldsymbol{u}) d\Omega = \boldsymbol{0} \qquad \forall\, q \in Q, \tag{3.21}$$

where $Q = L_2(\Omega)$. In Carey & Oden (1986), it is proven that this is equivalent to solving the original Stokes' problem.

The solution generated is not a minimum in the space $H^1_\Gamma \otimes Q$, but is a saddle point. The existence of this saddle point is satisfied by the chosen Lagrangian polynomials for v^h and q^h if it can be proved that L is elliptic and a consistency condition for $\boldsymbol{v}$ and p is satisfied. This consistency condition states that

$$\sup_{v \in H^1_\Gamma} \frac{\int_\Omega q \boldsymbol{\nabla} \cdot \boldsymbol{v} d\Omega}{\|\boldsymbol{v}\|_1} \geq C \|q\|_0 \qquad \forall\, q \in Q, \tag{3.22}$$

where $C > 0$ is a constant. This constraint is known as the inf-sup or Ladyzhenskaya-Brezzi-Babuska (LBB) condition (Babuska, 1973; Brezzi, 1974; Carey & Oden, 1983, Carey & Oden, 1986 and Ladyzhenskaya, 1969). It requires boundedness of the variational operator and restricts the choices for the approximating spaces for velocity and pressure, S^h and P^h. One set of basis functions which has been found to conform to the LBB condition (and will be used throughout this thesis) is biquadratic approximations for velocity and bilinear approximations for pressure (Carey & Oden, 1986).

Violation of the LBB condition results in a weak solution that is not unique. If the numerical method used to solve the problem uses an inconsistent approximation for $(\boldsymbol{v}, p)$, then the solution will be seriously degraded by spurious oscillations and wiggles. It also has been proven that if the LBB condition is satisfied, then optimal convergence properties for Galerkin's method will be attained. The use of biquadratic velocities and bilinear pressures results in errors that will satisfy (Carey & Oden, 1986)

$$\|\boldsymbol{u} - \boldsymbol{u}_h\|_1 \leq C h^2 (\|\boldsymbol{u}\|_3 + \|p\|_2), \tag{3.23}$$

$$\|p - p_h\|_0 \leq Ch^2(\|\boldsymbol{u}\|_3 + \|p\|_2), \tag{3.24}$$

where C is a constant independent of the mesh size parameter, h.

3.3 Hyperbolic Equations

The Galerkin FEM works extremely well as long as it is applied to problems with elliptic operators. However, most differential viscoelastic constitutive equations are hyperbolic in terms of the stress, as emphasized earlier in Section 2.4. Galerkin's method can be applied to hyperbolic equations; however, the ellipticity condition is not satisfied and the equations do not have a variational form. The convergence rate of Galerkin's method is only $O(h^{k-1})$ which is suboptimal (Johnson, 1987). Also, it was shown by Johnson *et al.* (1984) that unless the solution is everywhere "smooth," interpreted mathematically in terms of the solution $\boldsymbol{v}(\boldsymbol{x})$ satisfying $\boldsymbol{v}(\boldsymbol{x}) \in H^2(\Omega)$, Galerkin's method is unstable and the solution contains spurious oscillations. Other methods have been derived to augment the stability of Galerkin's method for hyperbolic equations; below, these techniques are described in reference to the UCM model, eq. (2.23).

3.3.1 Cause of Oscillations in Galerkin's Method

The source of the spurious oscillations in Galerkin's method when applied to hyperbolic equations can be seen by the examination of the scalar, one-dimensional hyperbolic problem (Leborgne, 1993):

$$u\phi' = f, \tag{3.25}$$

with $\phi(0) = 0$ and where u and f are given. The upwind finite difference form of the first derivative is

$$\phi'(x) = \frac{\phi(x) - \phi(x-h)}{h}. \tag{3.26}$$

The Galerkin finite element discretization is equivalent to the second-order centered one-dimensional finite difference discretization. Applying this discretization to eq. (3.26) yields

$$\phi' = \frac{\phi(x+h) - \phi(x-h)}{h} - \frac{h}{2}\frac{\phi(x+h) - 2\phi(x) + \phi(x-h)}{h^2}, \tag{3.27}$$

which indicates that the discrete problem actually solves a problem that has an elliptic operator. The equivalent differential equation is

$$u\phi' - \kappa\phi'' = f, \tag{3.28}$$

where $\kappa = uh/2$. The essential boundary condition is still present, but a second 'implicit' boundary condition, needed for the second-order derivative, is not defined in the problem statement because the original equation only has a first-order derivative. This second boundary condition is of natural or Neumann type, $\phi' = 0$. This second boundary condition can lead to an unexpected boundary layer which is only present in the numerical solution, not in the original continuous problem being solved.

This boundary layer phenomena is illustrated using eq. (3.28) with specific boundary conditions, namely, $\phi(0) = 1$ and $\phi(1) = 0$, where $u > 0$ and $\kappa > 0$ and are both constants in eq. (3.28). The closed-form solution is

$$\phi(t) = \frac{e^{\mathrm{Pe}} - e^{\mathrm{Pe}x}}{e^{\mathrm{Pe}} - 1}, \tag{3.29}$$

where Pe$= u/\kappa$. The discretization of eq. (3.28) is

$$u\frac{\phi_{i+1} - \phi_{i-1}}{2h} - \kappa\frac{\phi_{i+1} - 2\phi_i + \phi_{i-1}}{h^2} = f_i. \tag{3.30}$$

The mesh Peclet or the Courant-Friedrichs-Lewy (CFL) number is

$$\mathrm{Pe}_h = \frac{uh}{2\kappa}. \tag{3.31}$$

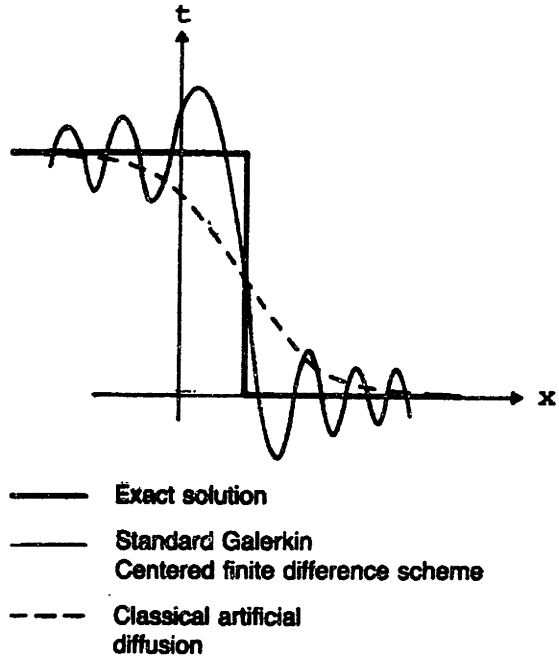

Figure 3-1: Behavior of the Galerkin method and the artificial diffusion method for a solution with a discontinuity (reproduced from Johnson (1987)).

The solution to the discretized equation is

$$\phi_i = c_1 + c_2 \left(\frac{1 + \mathrm{Pe}_h}{1 - \mathrm{Pe}_h} \right)^i , \tag{3.32}$$

where c_1 and c_2 are determined by the boundary conditions at ϕ_0 and ϕ_n. The scheme will contain an oscillatory solution when $\mathrm{Pe}_h > 1$. Thus, in order to prevent oscillations either h must be made small or κ must be made large. Obviously, this becomes impractical if, by definition of the problem, $\kappa \ll 1$. There will be no control of errors near sharp gradients or discontinuities, and spurious oscillations will develop (see Fig. 3-1).

3.3.2 Low Accuracy, Stabilized Methods

The spurious oscillations introduced by Galerkin's method are unacceptable. Several different methods have been introduced to improve the stability of the numerical algorithm. This section examines the simplest and lowest order methods: classical

artificial diffusion (AD) and streamline upwinding (SU). Both methods involve the addition of a term to the original equations and are thus classically inconsistent or, in terms of the definition given in Chapter 1, consistent to order h. Two additional low order methods which have been extensively examined for numerical calculations using the Euler equations ($Re \gg 1$ or $\mu = 0$) are total variation diminishing (TVD) and monotone methods. These will be discussed in the next section.

The AD method attempts to regularize the solution by adding to the equation(s) a second-order term of the form

$$-\nabla \cdot \left(\boldsymbol{\beta}(h) \cdot \nabla \boldsymbol{u}^h\right),$$

where $\boldsymbol{\beta}$ is the artificial diffusivity tensor whose magnitude is $O(h)$. The term is supposed to be small enough such that the overall solution structure is not changed, but, at the same time, the elliptic term is large enough to regularize the equation so that Galerkin's method will work (the ellipticity condition will be satisfied; thus, guaranteeing the existence of a unique solution). The stability of the method is indeed improved, but the overall accuracy of the method can be no greater than $O(h)$ because the added term is a first-order perturbation of the original equation so this method is classically inconsistent or consistent to the first order in h. Furthermore, the tensor $\boldsymbol{\beta}$ is isotropic which leads to excessive diffusion in all directions (Brooks & Hughes, 1982). This is contrary to the nature of hyperbolic equations, which pass information only along the characteristics, not all directions. The AD method contains significant diffusion across these characteristics, which can be considered as streamlines, that will smooth sharp gradients. Figure 3-1 shows an example of this crosswind diffusion. This method will not be used in computations in this thesis.

Making $\boldsymbol{\beta}$ anisotropic such that crosswind diffusion is minimized helps alleviate this problem. SU (Brooks & Hughes, 1982) defines $\boldsymbol{\beta}$ in the notation of King *et al.* (1988) as

$$\boldsymbol{\beta} \equiv \frac{De}{2} \frac{\boldsymbol{v}\boldsymbol{v}}{|\boldsymbol{v} \cdot \boldsymbol{v}|} \left[(v_x h_x)^2 + (v_y h_y)^2\right]^{1/2}, \tag{3.33}$$

where (v_x, v_y) are the components of the velocity at the center of a quadrilateral

element and (h_x, h_y) are the sizes of the element in the x- and y-directions. This method is streamwise parabolic, eliminates the crosswind diffusion and is stable. The crosswind diffusion can be introduced when it is applied to systems of equations as discussed by Brooks & Hughes (1982). The drawback is the $O(h)$ accuracy of the method itself. This method will be used in later computations, but will be shown to be inaccurate or require excessive mesh refinement at high De compared to the higher order methods discussed below.

3.3.3 Numerical Methods from Hyperbolic Conservation Equations

The methods to be described in this section have been utilized mostly in connection with codes solving compressible flow equations especially for high Re flow where the viscous terms of the Navier-Stokes equation, eq. (2.13), are neglected. This equation of motion is often referred to as the Euler equation and is part of a set of hyperbolic equations (inclusion of the energy equation and an equation of state for the pressure is needed) in which an overall quantity such as the entropy is conserved. These types of equations are sometimes referred to as conservation laws. In these equations, shocks often form which are simply discontinuities in the solution; these discontinuities are modelled numerically as extremely steep gradients. The viscoelastic flow equations being solved in this thesis are hyperbolic and can have steep gradients which cause oscillations in Galerkin's method. It may be possible to utilize some of the numerical concepts from the solution of conservation laws to solve the viscoelastic flow equations.

First, several categories defining the types of numerical methods for conservation laws will be given. The basic characteristics revolve around a concept known as the total variation of a function which is defined over the time interval $[0, T]$ as

$$TV(\boldsymbol{u}) = \limsup_{\epsilon \to 0} \frac{1}{\epsilon} \int_0^T \int_{-\infty}^{\infty} |\boldsymbol{u}(\boldsymbol{x} + \epsilon, t) - \boldsymbol{u}(\boldsymbol{x}, t)| d\boldsymbol{x} dt + \limsup_{\epsilon \to 0} \frac{1}{\epsilon} \int_0^T \int_{-\infty}^{\infty} |\boldsymbol{u}(\boldsymbol{x}, t + \epsilon) - \boldsymbol{u}(\boldsymbol{x}, t)| d\boldsymbol{x} dt. \tag{3.34}$$

For a hyperbolic conservation law, the continuous equations are total variation decreasing (TVD) or

$$TV\left(u(x,t+\epsilon)\right) \leq TV\left(u(x,t)\right), \tag{3.35}$$

where $\epsilon \geq 0$. Therefore, any numerical method used to solve the conservation law reliably also must be TVD

$$TV(U^{n+1}) \leq TV(U^n), \tag{3.36}$$

where n and $n+1$ indicate increasing discrete time levels. TVD equations and numerical methods have the property of monotonicity preservation, i.e., if the initial condition U_j^0 is monotone, then so is U_j^n. This means that oscillations *cannot* be present in the numerical solution if they are not present in the initial condition. Obviously, Galerkin's method is neither monotonicity preserving nor TVD, since spurious oscillations can occur; both the AD and SU methods are monotonicity preserving and TVD. Another property of a numerical method or a solution is L_1-contracting which states that

$$\|\boldsymbol{u}(\cdot,t_2)\|_1 \leq \|\boldsymbol{u}(\cdot,t_1)\|_1, \qquad \textit{for } t_2 \geq t_1. \tag{3.37}$$

It is also true that if a numerical method or a solution to the conservation law is L_1-contracting, then it is TVD also. It can be shown that the one-dimensional, first-order finite difference upwind scheme (both AD and SU) is both L_1-contracting and TVD, if the CFL condition is satisfied. Finally, a numerical method, represented as $U_j^{n+1} = \mathcal{F}(U^n; j)$, is monotone if for two sets of initial data, where

$$V_j^0 \geq U_j^0 \qquad \forall\, j, \tag{3.38}$$

then the numerical solutions satisfy the following property:

$$V_j^n \geq U_j^n \qquad \forall\, j \qquad \Longrightarrow \qquad V_j^{n+1} \geq U_j^{n+1} \qquad \forall\, j. \tag{3.39}$$

To prove that a method is monotone, it is necessary to show that

$$\frac{\partial \mathcal{F}(U^n; j)}{\partial U_i^n} \geq 0 \qquad \forall\, i, j, U^n. \tag{3.40}$$

In essence this is stating that if the value of U_i^n is increased, then the value of U_j^{n+1} cannot decrease. The property of monotonicity is the most restrictive of the properties just discussed; the order of the properties being monotone $\subset$ L_1-contracting $\subset$ TVD $\subset$ monotonicity preserving.

For monotone methods, it was proven in Crandall & Majda (1980) that the numerical solution for a conservation law computed with a consistent monotone method with a sufficiently small, fixed ratio $\Delta t/\Delta x$ converges to the entropy solution as $\Delta t \to 0$. This would seem to make the monotone class of numerical methods very attractive for use in the computation of viscoelastic flow, especially considering the ease of checking a numerical method to ensure that it is indeed monotone using eq. (3.40). However, the use of monotone methods is severely restricted by the following theorem: a monotone method is at most first-order accurate. The proof of this theorem relies on the examination of the modified equation actually solved by the numerical method (for an example see the discussion regarding the cause of oscillations in Galerkin's method in Section 3.3.1) and was first proved by Harten *et al.* (1976). By examining the local truncation error of the numerical method applied to the discretized equations and expanding in a Taylor series, a monotone method actually solves the second-order, advective-diffusive partial differential equation

$$u_t + f_x(u) = k\frac{\partial}{\partial x}\left(\beta(u)u_x\right), \tag{3.41}$$

instead of the first-order, hyperbolic PDE given by $k = \Delta t = 0$. Monotonicity preservation implies $\beta(u) > 0$. Since the modified equation is an $O(k)$ perturbation of the original problem, the solution can be no better than an $O(k)$ approximation to the solution. This restriction is similar to that of the AD and SU methods so that monotone methods will not be used for computations in this thesis.

Since the monotone methods are limited to first-order accuracy, 'high resolution'

methods have been developed over the last decade. These methods are loosely defined as being second-order or higher accurate on smooth solutions and result in well resolved, non-oscillatory discontinuities and are mostly total variation diminishing. The idea behind 'high resolution' methods is to utilize a high order method, but to modify it such that the amount of numerical dissipation is increased in the neighborhood of very sharp gradients and/or discontinuities. In order to have nonoscillatory behavior near these sharp gradients, the method must be monotonicity preserving, as mentioned above. The type of method which can be developed is limited by the fact that a *linear*, monotonicity preserving method is at most first-order accurate. The proof, originally by Godunov (1959), is fairly simple in that all it requires is that any linear, monotonicity preserving method is monotone; at which point, the result follows from the above restriction on monotone methods to only first-order accuracy. Thus, any 'high resolution' method must be nonlinear which means that the solution of linear problems by these numerical methods are *nonlinear*.

In order to clarify what this means, an example will be shown using the second-order Lax-Wendroff finite difference formula which is

$$U_j^{n+1} = U_j^n - \nu(U_{j+1}^n - U_{j-1}^n) + \frac{1}{2}\nu^2(U_{j+1}^n - 2U_j^n + U_{j-1}^n), \tag{3.42}$$

where, $\nu = ak/h$ is the Courant number or the cell Peclet number. To attempt to make a 'high resolution' numerical method, an artificial viscosity, Q, is added to the Lax-Wendroff method

$$U_j^{n+1} = U_j^n - \nu(U_{j+1}^n - U_{j-1}^n) + \frac{1}{2}\nu^2(U_{j+1}^n - 2U_j^n + U_{j-1}^n) + kQ(U_{j+1}^n - 2U_j^n + U_{j-1}^n), \tag{3.43}$$

where the final term is an $O(k)$ perturbation of the Lax-Wendroff method, eq. (3.42). If Q is a constant, then this is a linear method in U. The competition between the added dissipation and the dispersion of the method leads to oscillations (LeVeque, 1990). If the added artificial viscosity is made to depend on the data, $Q = Q(U^n; j)$, then the method is nonlinear. This is true even if the problem being solved is linear because the nonlinearity comes from the perturbation term of the method and will

always be present. This makes the analysis of these schemes difficult, not to mention the extra computational time required to solve the system of nonlinear equations. Basically, the goal of high resolution schemes are to use a high order method whenever the solution is smooth and then switch to a first order, monotone method whenever sharp gradients arise. This type of scheme would still allow the use of linear methods for the solution of linear problems.

The high resolution methods discussed here are based on the first-order monotone Godunov's method as a starting point. The basis of this method relies on the fact that an upwind method can only be applied correctly if the direction of upwinding is known (otherwise, it may be possible to actually be downwinding rather than upwinding). The simplest method to determine the upwinding direction is to find the eigenvalues of the problem and then to upwind in the correct direction depending on the sign of the eigenvalue. For a linear problem this can be done by simply diagonalizing the velocity matrix; however, for a nonlinear problem this requires the diagonalization of the Jacobian matrix which can be difficult and time-consuming (if the Jacobian depends on time, this will have to done at each time step). Godunov's method proposes to solve the Riemann problem at each time step instead. The Riemann problem is the solution of a conservation law given piecewise constant data with a single discontinuity. Godunov's method consists of the following steps:

1. Given the data $\{U_j^n\}$, construct $\tilde{u}^n(x, t_n) =$ piecewise constant,
2. Solve the conservation law exactly to get $\tilde{u}^n(x, t_{n+1})$, the Riemann problem,
3. Compute cell averages to get U_j^{n+1}.

The computation of the cell averages is determined by the equation

$$U_j^{n+1} = U_j^n - \frac{k}{h}\left[f\left(u^*(U_j^n, U_{j+1}^n)\right) - f\left(u^*(U_{j-1}^n, U_j^n)\right)\right], \tag{3.44}$$

where f is the flux across each cell or element boundary. Although Godunov's method is not usually implemented in this fashion, it is indicative of the solution process (LeVeque, 1990). The solution of the exact Riemann problem is not necessary to the algorithm; the exact solution is averaged over each element in the next step which

can introduce fairly large numerical errors. Thus, approximate Riemann solvers have been suggested; the most popular of which is the Roe solver (LeVeque, 1990). The solution of the exact Riemann problem $\tilde{u}^n(x, t_{n+1})$ is replaced by $\hat{u}^n(x, t_{n+1})$, where this is the solution of a constant coefficient, linear system of conservation laws given piecewise data or the solution of the Riemann problem given by

$$\hat{u}_t + \hat{A}(u_l, u_r)\hat{u}_x = 0, \tag{3.45}$$

where, u_l, u_r are the left and right grid points used for the cell average to find U_j^{n+1}, respectively. The matrix $\hat{A}$ is determined by imposing three conditions (LeVeque, 1990):

1. $\hat{A}(u_l, u_r)(u_r - u_l) = f(u_r) - f(u_l)$, where f is the flux of eq. (3.45),
2. $\hat{A}(u_l, u_r)$ is diagonalized by using its real eigenvalues $\hat{\lambda}_i$,
3. $\hat{A}(u_l, u_r) \to f'(\bar{u})$ smoothly as $u_l, u_r \to \bar{u}$, where $\bar{u}$ is the location of the discontinuity in the cell.

The first condition requires the approximate solver to be conservative; it also requires the solver to be consistent if u_l, u_r are separated by only one discontinuity. The second condition ensures the approximate Riemann problem is hyperbolic and solvable. Finally, the third condition guarantees the approximate solution is at least $O(h)$ on smooth solutions. To find a general structure for $\hat{A}$ is impractical, the structure is usually found for each specific application. The first condition only requires the solution to be conservative in some variable, not necessarily the one for the continuous equations; for the Euler equations, this method results in an entropy-violating solutions which essentially means the solution will not solve for rarefaction waves correctly. This has led to the development of E-schemes (entropy satisfying) by Osher (1984). Since the result is still first-order accurate, details will not be discussed here.

The purpose of introducing the Godunov/Roe solver was to set up the basis through which nonlinear, 'high resolution' numerical methods are made. The simplest is the flux-limiter method in which a high-order flux is chosen for smooth areas of the solution and a low-order flux is chosen for areas with discontinuities or sharp

gradients. This hybridization of two fluxes looks like

$$F(U^n; j) = F_L + \phi(U^n; j)\,[F_H(U^n; j) - F_L(U^n; j)]\,, \tag{3.46}$$

where, $\phi(U^n; j)$ is the flux limiter function, F_L is the low-order flux and F_H is the high-order flux. This method does have trouble at extrema points where the solution is still smooth so the high order method is wanted, but in order for the method to be TVD, ϕ must be set to zero and the first-order accurate flux used. This was proven by Osher & Chakravarthy (1984) as the theorem: TVD methods are at most first-order in the neighborhood of extrema points. Now, these methods are first-order in regions of sharp gradients *and* in regions of maxima and minima of the numerical solution. The concept of flux-corrected transport (Sweby, 1984) is essentially this method with F_H viewed as an anti-diffusive flux that corrects for the overly diffuse, low-order term F_L. This type of method has been applied to viscoelastic flow problems by Baaijens(1994).

A more general method is known by the term, slope-limiter. This type of method generalizes Godunov's method by using a higher order approximation than the piecewise constant to solve the Riemann problem. These were introduced in a series of papers by van Leer (1973, 1974, 1977a, 1977b, 1979) in which the approximation for $\tilde{u}^n$ is made piecewise linear through the construction

$$\tilde{u}^n(x, t_n) = U_j^n + \sigma_j^n(x - x_j) \qquad \text{on cell} \qquad [x_{j-1/2}, x_{j+1/2}], \tag{3.47}$$

where σ_j^n is the slope in cell j based on U^n. In Godunov's method, $\sigma_j^n = 0 \;\; \forall\; n, j$. At this point, the method is simply the Lax-Wendroff method; a linear, second-order method. To ensure the solution is TVD, the slope-limiter concept is introduced through the definition of the slope from eq. (3.47)

$$\sigma_j^n = \left(\frac{U_{j+1}^n - U_j^n}{h}\right)\Phi_j, \tag{3.48}$$

where Φ_j is the slope limiter. These schemes were called MUSCL schemes (Monotone Upstream-centered Scheme for Conservation Laws) by van Leer (1973, 1974, 1977a,

1977b, 1979). One of the simplest slope-limiters is the minmod type

$$\sigma_j^n = \frac{1}{h}\text{minmod}(U_{j+1}^n - U_j^n, U_j^n - U_{j-1}^n), \tag{3.49}$$

where, the minmod function is defined as

$$\begin{aligned} \text{minmod}(a,b) &\equiv \begin{cases} a, & \text{if } |a| < |b| \text{ and } ab > 0; \\ b, & \text{if } |b| < |a| \text{ and } ab > 0; \\ 0, & \text{if } ab \leq 0, \end{cases} \\ &= \frac{1}{2}\left(\text{sgn}(a) + \text{sgn}(b)\right) \min\left(|a|, |b|\right). \end{aligned} \tag{3.50}$$

Note that the slope is set to zero if $U_{j+1}^n - U_j^n$ and $U_j^n - U_{j-1}^n$ are of opposite signs (goes through an extrema between the two cells); this is geometrically required to satisfy the conditions for a TVD method (Goodman & Le Veque, 1988). Slope limiters can be written as a flux-limiter to show the interchangeability of the ideas as

$$\begin{aligned} \phi(\theta) &\equiv \begin{cases} 0, & \text{if } \theta \leq 0; \\ \theta, & \text{if } 0 \leq \theta \leq 1; \\ 1, & \text{if } \theta \geq 1, \end{cases} \\ &= \max\left(0, \min(1, \theta)\right), \end{aligned} \tag{3.51}$$

where

$$\theta_j^n = \frac{U_j^n - U_{j-1}^n}{U_{j+1}^n - U_j^n}. \tag{3.52}$$

There are many more examples of slope (or flux) limiters which will not be discussed here; the reader is referred to Sweby (1984) and LeVeque (1990). These ideas were applied to viscoelastic problems by Rekers (1995). Further generalizations of Godunov's scheme result in higher order methods. The construction of $\tilde{u}^n$ by piecewise quadratic functions result in the piecewise parabolic method (PPM) introduced by Colella and Woodward (1984). Higher order approximations have been proposed by Harten and coworkers (Harten *et al.*, 1987 and Harten & Osher, 1987) in the essentially non-oscillatory (ENO) schemes. These higher order methods are based on the central idea of the slope limiters, i.e., compare the linear interpolants on a cell based

on the left and the right and use the lesser value which results in a nonoscillatory method in the sense that the total variation of the numerical results are no greater than the total variation of the discrete data. Several methods of implementing this idea to the ENO schemes have been proposed, but they essentially follow the same methodology. The simplest variant is to take a three point divided difference based on $\{W^n_{j-2}, W^n_{j-1}, W^n_j\}$ and $\{W_{j-1}, W_j, W_{j+1}\}$. The least oscillatory result is accepted and the next difference is calculated and so on.

These methods appear to satisfy our goal of obtaining high order methods which will obtain better results than the SU method of the previous section. However, a theorem has been proved by Goodman and LeVeque (1985) which states that, except in some trivial cases, any numerical method which is TVD in two-dimensions or higher is at most first-order accurate. This is extremely disappointing because all of the major applications with which we are interested in solving the viscoelastic flow equations are in two or three dimensions. It is stated in LeVeque(1990) that TVD methods in one dimension have been combined with a concept called operator splitting (see Chapter 8 for a more complete discussion). The numerical results are better than first-order accurate and appear to be essentially nonoscillatory. Despite this numerical evidence, it was decided not to pursue these methods further in this thesis due to the lack of proof that the method definitely will be of higher accuracy than the first-order SU method.

3.3.4 Higher Accuracy, Stabilized Methods

The finite element techniques discussed in the previous two sections have improved stability relative to the Galerkin FEM, but the cost of this stability is *accuracy.* Here three additional methods will be introduced which all have higher accuracy as well as improved stability. These are the streamline upwind Petrov-Galerkin (SUPG) (Brooks and Hughes, 1982), the Galerkin least squares (GLS) (Baaijens, 1992; Franca *et al.,* 1992; Hughes *et al.,* 1989 and Leborgne, 1992) and the Douglas-Wang(DW) (Douglas & Wang, 1989) methods.

The SUPG method was the first method to show improved accuracy over the AD

and SU methods. It was introduced by Brooks and Hughes (1982) and proved convergent by Johnson *et al.* (1984) for linear hyperbolic equations. Rather than perturb the governing equation, the weighting function in the weighted residual method is modified; unequal trial and weighting functions in the weighted residual context are known as Petrov-Galerkin methods (Carey & Oden, 1986). The addition of diffusion along the streamlines is effectively added to the weighting function by the modification:

$$\Psi^\tau = \Phi^\tau + \frac{h}{\|\boldsymbol{\beta}^h\|}\boldsymbol{\beta}^h \cdot \boldsymbol{\nabla}\Phi^\tau, \tag{3.53}$$

where h is a characteristic element size and $\boldsymbol{\beta}^h$ is the velocity field from the equations of motion. Normalization of the velocity field is introduced to guarantee that the gradient contribution to the weighting function remains $O(1)$, regardless of the magnitude of the velocity. The accuracy of the method was shown by Johnson *et al.* (1984) to be

$$|||u^h - u||| \leq Ch^{k-1/2}, \tag{3.54}$$

where the mesh-dependent norm $|||\cdot|||$ is defined as

$$|||v^h||| \equiv h^{1/2}\|\boldsymbol{\beta}^h \cdot \boldsymbol{\nabla}v^h\|_0 + \|v^h\|_0 + \int_\Gamma \left((v^h)^2 \boldsymbol{n} \cdot \boldsymbol{\beta}^h\right) d\Gamma. \tag{3.55}$$

The displacement error is one-half order below optimal, and the zero norm for the gradients in the streamwise direction is optimal. Furthermore, point sources decay with rate $exp(-d/h^{1/2})$ in the cross-stream direction and with rate $exp(-d/h)$ in the upstream direction (Johnson *et al.*, 1984). Thus, numerical error and any other perturbations should be limited to a region $O(h^{1/2})$ around a characteristic with almost no upstream propagation.

The continuity restrictions necessary for the convergence of the SUPG method are not as severe as required by Renardy's existence proof for the existence of a solution to the hyperbolic problem. Johnson *et al.* (1984) showed that SUPG converges for linear first-order hyperbolic equations as long as the dependent variable, $\{\sigma_{ij}\}$, is in the space of functions with square integrable streamwise derivatives, $\sigma_{ij} \in H^1_{\Psi}(\Omega)$, defined

analogously to $H^1(\Omega)$, so that $\boldsymbol{v}\cdot\nabla\sigma_{ij} \in L^2(\Omega)$. There is no guarantee of continuity of the cross-stream derivative of σ_{ij}. It is interesting that the SU method does guarantee smoothness of the derivatives of the stress in all directions, i.e., $\sigma_{ij} \in H^1(\Omega)$, by introducing a second-order operator in the constitutive equation and cross-stream diffusion. The SUPG method has been further upgraded to handle steep gradients via shock-capturing methods (Hughes *et al.*, 1986 and Hughes & Mallet, 1986).

The SUPG method captures jump discontinuities or large gradients in the exact solution in a thin numerical layer; however, the solution has been observed to result in oscillations inside of this thin numerical boundary layer. This is due to the fact that it is not a TVD method as discussed in the last section. Discontinuity or shock capturing was introduced by Hughes *et al.* (1986) and Hughes & Mallet (1986) to decrease these oscillations. The weighting function for the discontinuity function is now (Johnson, 1987)

$$\Psi^\tau = \Phi^\tau + \frac{h}{\|\boldsymbol{\beta}^h\|}\boldsymbol{\beta}^h \cdot \nabla\Phi^\tau + \bar{\delta}\bar{\boldsymbol{\beta}}^h \cdot \nabla\Phi^\tau, \tag{3.56}$$

where

$$\bar{\boldsymbol{\beta}}^h = \frac{\boldsymbol{\beta}^h \cdot \nabla\boldsymbol{u}^h}{|\nabla\boldsymbol{u}^h \cdot \nabla\boldsymbol{u}^h|}\nabla\boldsymbol{u}^h, \tag{3.57}$$

and $\bar{\delta} \sim O(h/\bar{\boldsymbol{\beta}}^h)$. Basically, $\bar{\boldsymbol{\beta}}$ is the projection of $\boldsymbol{\beta}^h$ from eq. (3.53) onto $\nabla\boldsymbol{u}^h$. As $\bar{\boldsymbol{\beta}}^h$ depends on the velocity, $\boldsymbol{u}^h$, the method is nonlinear even if the problem to be solved is linear. Because of this nonlinearity, this technique was not used in this thesis, but should be considered when the accuracy of the stress boundary layers is important or there are very large gradients in the solution which are requiring excessive mesh refinement.

Recently, GLS methods are receiving attention for solving convection dominated transport problems (Franca *et al.*, 1992 and Hughes *et al.*, 1989) and for the calculation of viscoelastic flows (Baaijens, 1992 and Leborgne, 1992). These methods has been proved convergent for linear hyperbolic equations (Leborgne, 1992). In these weighted residual methods, the weak form generated by Galerkin's method is augmented by the term generated by a least squares approximation, weighted by a factor

that depends on the mesh. The purpose of the added component of the residual equation is to give numerical stability to the otherwise unstable Galerkin formulation, while not destroying the consistency of the discretization. The GLS formulation developed by Leborgne (1992) for linear hyperbolic equations is applied to the constitutive equations. A steady-state hyperbolic operator acting on the stress tensor $\boldsymbol{\sigma}$ can be defined for the UCM constitutive equation, eq. (2.23), as

$$L(\boldsymbol{\sigma}) \equiv \boldsymbol{\sigma} + De\left[\boldsymbol{v}\cdot\boldsymbol{\nabla}\boldsymbol{\sigma} - (\boldsymbol{\nabla}\boldsymbol{v})^T\cdot\boldsymbol{\sigma} - \boldsymbol{\sigma}\cdot(\boldsymbol{\nabla}\boldsymbol{v})\right]. \tag{3.58}$$

The weighting function is formed by adding the basis function to the least squares residual for the operator in eq. (3.58) as

$$\begin{aligned}\Psi^\tau &\equiv \Phi^\tau + \delta\left(L(\Phi^\tau)\right),\\ &= \Phi^\tau + \delta\left(\Phi^\tau + De\left[\boldsymbol{v}\cdot\boldsymbol{\nabla}\Phi^\tau - (\boldsymbol{\nabla}\boldsymbol{v})^T\cdot\Phi^\tau - \Phi^\tau\cdot(\boldsymbol{\nabla}\boldsymbol{v})\right]\right),\end{aligned} \tag{3.59}$$

where the scalar δ is defined as

$$\delta \equiv \frac{\left[(v_x h_x)^2 + (v_y h_y)^2\right]^{1/2}}{2\|\boldsymbol{v}\|}, \tag{3.60}$$

and the components of the velocity and the element size are defined as in eq. (3.33). The GLS method has been implemented with the restriction that $\delta \leq 1/24$ as argued by Franca *et al.* (1992).

Another recent method that is similar to the GLS method is the Douglas-Wang (DW) method (Douglas & Wang, 1989). For hyperbolic equations, the GLS and DW methods are identical. However, in the formulation of mixed problems, it was shown in Leborgne (1992) that the DW method should exhibit better convergence properties due to a difference in sign on the added least-squares term. In this research the GLS/DW method is applied only to the hyperbolic constitutive equations and not the entire mixed problem; thus, the GLS and DW methods are equivalent.

3.3.5 Convection of Tensorial Quantities Using SUPG

The SUPG method as introduced by Brooks and Hughes (1982) was for a scalar advection-diffusion problem; it was not introduced to be used to solve the viscoelastic fluid flow problem (Leborgne, 1992). There are some difficulties in extending this method to viscoelastic constitutive equations of which the user should be aware. If we examine the Galerkin formulation of a general constitutive equation

$$(\boldsymbol{\tau} + \boldsymbol{u} \cdot \boldsymbol{\nabla}\boldsymbol{\tau} + \boldsymbol{A}(\boldsymbol{\tau}), \boldsymbol{\tau}') = (\boldsymbol{F}, \boldsymbol{\tau}'), \tag{3.61}$$

where $\boldsymbol{A}(\boldsymbol{\tau})$ is a general tensor term and $\boldsymbol{\tau}'$ is the weighting function. The SU method as introduced by Raithby (1976) simply perturbs this equation by adding the term

$$\delta(\boldsymbol{u} \cdot \boldsymbol{\nabla}\boldsymbol{\tau}, \boldsymbol{u} \cdot \boldsymbol{\nabla}\boldsymbol{\tau}') = \delta\boldsymbol{\nabla} \cdot (\boldsymbol{u} \otimes \boldsymbol{u} \cdot \boldsymbol{\nabla}\boldsymbol{\tau}, \boldsymbol{\tau}'), \tag{3.62}$$

where $\delta = O(h)$. This additional term controls the transport of the advection term, $\boldsymbol{u} \cdot \boldsymbol{\nabla}\boldsymbol{\tau}$ through an elliptic term involving the advection term (Leborgne, 1992).

The SUPG method attempts to control this process, but in the classically consistent method by changing the weighting function. Writing the SUPG method in the same form as eq. (3.61) gives

$$(\boldsymbol{\tau} + \boldsymbol{u} \cdot \boldsymbol{\nabla}\boldsymbol{\tau} + \boldsymbol{A}(\boldsymbol{\tau}), \boldsymbol{\tau}' + \delta(\boldsymbol{u} \cdot \boldsymbol{\nabla}\boldsymbol{\tau}')) = (\boldsymbol{F}, \boldsymbol{\tau}'). \tag{3.63}$$

Now, expand, integrate the δ terms by parts and examine only the resulting δ terms

$$-\delta(\boldsymbol{u} \cdot \boldsymbol{\nabla}\boldsymbol{\tau}, \boldsymbol{\tau}') - \delta\left(\boldsymbol{u} \cdot \boldsymbol{\nabla}\boldsymbol{A}(\boldsymbol{\tau}), \boldsymbol{\tau}'\right) - \delta\left(\boldsymbol{\nabla} \cdot (\boldsymbol{u} \otimes \boldsymbol{u} \cdot \boldsymbol{\nabla}\boldsymbol{\tau}), \boldsymbol{\tau}'\right). \tag{3.64}$$

The first and third terms are identical to the SU method; the problem arises with the second term. It represents the transport of the quantity $\boldsymbol{A}(\boldsymbol{\tau})$ in an unknown direction; this hyperbolic term is not controlled by a diffusive stabilization term (Leborgne, 1992). The question now arises: when does this transport cause the SUPG method to fail? The second term does not guarantee that the SUPG method will fail; it

only indicates that it is possible to have problems if a modified mesh Peclet number, Pe_m, corresponding to this term becomes too large. This is identical to the failure of Galerkin's method for hyperbolic equations – once Pe_m becomes too large, the stability of the method is lost. This could account for the reported problems with the SUPG method in viscoelastic flow calculations where a singularity is involved (Marchal & Crochet, 1987 and Debae *et al.*, 1994).

Chapter 4

Reformulations of the Viscoelastic Governing Equations

"Philosophy is written in this very great book which is continuously open in front of our eyes (I mean the universe), but it cannot be understood if one does not first learn the language, and know the characters in which it is written. It is written in mathematical language , and the characters are triangles, circles, and other geometric figures..."

– Galileo Galilei from Saggiatore, 1623

Two issues to consider in the FEM are the connection between the weighted residual method and the choice of the polynomial spaces for the approximation of the variables. The compatibility of the method requires that the numerical method be well-posed as the characteristic mesh size goes to zero. If it is possible to substitute the exact solution into the discretization and yield the exact solution as the answer, then the method will be called classically consistent. If the resulting answer is exact only to the order of the method, then it will be called consistent to that order. A third issue is the stability which is determined by the boundedness of the solution and its stability to small perturbations. There are two types of temporal stability to consider: the physical stability of the equations themselves and the numerical stability of the numerical technique. The equations are physically unstable if the magnitude of the

solution goes to infinity as time goes to infinity; otherwise, it is stable. The temporal numerical stability of a numerical method is determined by randomly perturbing the linearized equations of motion around the steady-state solution. If the magnitude of the perturbation decays in time, then the solution is stable; if it grows in time, then it is unstable. For a time dependent problem, compatibility, consistency and numerical stability are necessary in order to show that the numerical method is convergent as the mesh is refined.

Until recently, the numerical methods for solving the viscoelastic flow equations failed above a critical De that often decreased with increasing mesh refinement, indicating the methods were *not* convergent. This led to studies of the equations themselves and their mathematical type (see Section 2.4) by Rutkevich (1970 and 1972) and Joseph *et al.* (1985). It was found that the equations were not always elliptic, i.e., they could change type. This has led to the reformulation of the governing viscoelastic flow equations with the goal of explicitly specifying the mathematical type of the equations; generally, the momentum and continuity equations are elliptic saddle point problems and the constitutive equations are hyperbolic partial differential equations. The methods to be discussed in this research are the Explicitly Elliptic Momentum Equation (EEME), Viscous, Elastic-Viscous Split Stress (EVSS), Elastic-Viscous Split Stress - Gradient (EVSS-G) and Discrete Elastic-Viscous Split Stress - Gradient (DEVSS-G) finite element methods; the latter two are introduced in this thesis. The discussion will be for the special case of inertialess flow, i.e., $Re = 0$; the incorporation of inertia poses no formulational difficulties as shown in Rajagopalan *et al.* (1990b). Also, the methods are described for the solution of the UCM, Oldroyd-B and CR-FENE models in Section 4.1 - 4.5 while the finite element formulations are given in Section 4.6; for further information the reader is referred to Brown *et al.* (1993) and Rajagopalan *et al.* (1990b).

Once the spatial portions of the differential equations are discretized by finite elements, the time-dependent viscoelastic equations are reduced to a set of differential-algebraic equations (DAE's). For a two-dimensional flow, the differential equations include the three stress field variables and the two velocity variables if inertia is in-

cluded (i.e., $Re \neq 0$). The algebraic equations include the three interpolated velocity gradient variables, the continuity equation which defines the pressure, and the velocity variables (if no inertia is present). Finite difference approximations are used to integrate these DAE's in time (Brenan *et al.,* 1989); integration methods to be used in this research are discussed in Section 4.7. Further information regarding fully implicit and semi-implicit schemes will be discussed in Chapter 8. The method used to implement the local mesh refinement is discussed in Section 4.8. Finally, bandwidth minimization is discussed in section 4.9.

4.1 Explicitly Elliptic Momentum Equation (EEME) Formulation

The EEME formulation was derived in the finite element context by King *et al.* (1988) using the form of the UCM equations that Renardy (1985) derived to prove existence and uniqueness of the solution. The tensor $\boldsymbol{\chi}$ from Section 2.4 in the discussion of the mathematical type of the UCM equations is negative-definite. This is used to guarantee the ellipticity operator of the momentum equation.

The inertialess UCM equations are written as

$$\boldsymbol{\nabla}\cdot\boldsymbol{\tau} + \boldsymbol{\nabla}p = \mathbf{0}, \tag{4.1}$$

$$\boldsymbol{\nabla}\cdot\boldsymbol{v} = \mathbf{0}, \tag{4.2}$$

$$\boldsymbol{\tau} + De\boldsymbol{\tau}_{(1)} + \dot{\boldsymbol{\gamma}} = \mathbf{0}. \tag{4.3}$$

The EEME formulation is written by taking the divergence of the constitutive equation

$$\boldsymbol{\nabla}\cdot\boldsymbol{\tau} + De\boldsymbol{\nabla}\cdot\left[\boldsymbol{v}\cdot\boldsymbol{\nabla}\boldsymbol{\tau} - (\boldsymbol{\nabla}\boldsymbol{v})^T\cdot\boldsymbol{\tau} - \boldsymbol{\tau}\cdot\boldsymbol{\nabla}\boldsymbol{v}\right] + \boldsymbol{\nabla}\cdot\dot{\boldsymbol{\gamma}} = \mathbf{0}. \tag{4.4}$$

A modified pressure, q, is introduced as

$$q = p + De\boldsymbol{v}\cdot\boldsymbol{\nabla}p. \tag{4.5}$$

Both of these equations are substituted into the momentum equation, eq. (4.1), and upon rearrangement yields

$$\nabla\cdot(\boldsymbol{\chi}\cdot\nabla\boldsymbol{v}) + De(\nabla\boldsymbol{v})\cdot(\nabla\cdot\boldsymbol{\tau}) + \nabla q = \mathbf{0}, \tag{4.6}$$

where, as before, $\boldsymbol{\chi}$ is the tensor

$$\boldsymbol{\chi} \equiv De\boldsymbol{\tau} - \boldsymbol{I}. \tag{4.7}$$

For a steady-state, inertialess flow, $\boldsymbol{\chi}$ is always negative-definite which ensures the ellipticity of the term $\nabla\cdot(\boldsymbol{\chi}\cdot\nabla\boldsymbol{v})$; therefore, the momentum equation is an elliptic partial differential equation. The continuity and constitutive equation are unchanged from eq. (4.2) and eq. (4.3), respectively.

The EEME formulation was extended to the Oldroyd-B model by Rajagopalan *et al.* (1990b) which, upon application of the methodology to the flow equations, eqs. (4.1), (4.2) and (2.22), results in the following form for the momentum equation:

$$\begin{aligned}\nabla\cdot[(De\boldsymbol{\tau}_p - \boldsymbol{I})\cdot\nabla\boldsymbol{v}] + De\nabla\boldsymbol{v}\cdot(\nabla\cdot\boldsymbol{\tau}_p) + \nabla q \\ - De\beta\left[(\nabla\boldsymbol{v})\cdot(\nabla^2\boldsymbol{v}) + \boldsymbol{v}\cdot\nabla(\nabla^2\boldsymbol{v})\right] = \mathbf{0},\end{aligned} \tag{4.8}$$

where the third-order derivative of the velocity is due to the singular effect of the solvent viscosity (see Section 2.4). The third-order derivatives are removed by introducing the vorticity

$$\boldsymbol{\omega} = \nabla \times \boldsymbol{v}. \tag{4.9}$$

This is substituted into the momentum equation noting that $\nabla^2\boldsymbol{v} = -\nabla\times\boldsymbol{\omega}$ to give

$$\begin{aligned}\nabla\cdot[(De\boldsymbol{\tau}_p - \boldsymbol{I})\cdot\nabla\boldsymbol{v}] + De\nabla\boldsymbol{v}\cdot(\nabla\cdot\boldsymbol{\tau}_p) + \nabla q \\ - De\beta[(\nabla\boldsymbol{v})\cdot(\nabla\times\boldsymbol{\omega}) + \boldsymbol{v}\cdot\nabla(\nabla\boldsymbol{\omega})] = \mathbf{0}.\end{aligned} \tag{4.10}$$

The vorticity is found by a least-squares interpolation of the the velocity field using

bilinear basis functions

$$\boldsymbol{\omega} - (\boldsymbol{\nabla} \times \boldsymbol{v}) = \mathbf{0}. \tag{4.11}$$

The last two equations are combined with the continuity equation, eq. (4.2), and the constitutive equation, eq. (2.22).

4.2 Viscous Formulation

The addition of solvent viscosity to the UCM viscoelastic flow equations gives the Oldroyd-B viscoelastic flow equations and introduces the term $\beta\dot{\boldsymbol{\gamma}}$ to the momentum equation which singularly changes the mathematical type of the equation set (see Section 2.4). Rewriting the equation set in terms of the viscous or Newtonian solvent and elastic or polymer portions of the deviatoric stress tensor gives

$$\boldsymbol{\tau} \equiv \boldsymbol{\tau}_p + \boldsymbol{\tau}_s. \tag{4.12}$$

The Newtonian solvent contribution can be written as

$$\boldsymbol{\tau}_s = -\beta\dot{\boldsymbol{\gamma}}, \tag{4.13}$$

where $\dot{\boldsymbol{\gamma}}$ is the dimensionless rate-of-strain tensor and β is defined as the ratio between the Newtonian solvent viscosity, η_s, and the total zero-shear-rate viscosity for the fluid, η_0 which is the sum of the solvent η_s and polymer η_p viscosities. In terms of the variable $\boldsymbol{\tau}_p$, the momentum and constitutive equations for the Oldroyd-B model become

$$-\beta\boldsymbol{\nabla}^2\boldsymbol{v} + \boldsymbol{\nabla}\cdot\boldsymbol{\tau}_p + \boldsymbol{\nabla}p = \mathbf{0}, \tag{4.14}$$

$$\boldsymbol{\nabla}\cdot\boldsymbol{v} = \mathbf{0}, \tag{4.15}$$

$$\boldsymbol{\tau}_p + De\boldsymbol{\tau}_{p(1)} + (1-\beta)\dot{\boldsymbol{\gamma}} = \mathbf{0}, \tag{4.16}$$

where the dependent variables are $(\boldsymbol{v}, p, \boldsymbol{\tau}_p)$. The ellipticity of the momentum equation is guaranteed by the solvent viscosity multiplying the Laplacian operator; this has been called the viscous form by Rajagopalan *et al.* (1990b) and also was used by Debbaut & Crochet (1986) and Keunings (1986).

This formulation does succeed in reintroducing the elliptic operator to the momentum equation; however, the equation is singular for $\beta \to 0$. The case, $\beta = 0$, corresponds to the UCM constitutive equation and results in the loss of the ellipticity in the momentum equation. Not only is this true for vanishing β, but also for $\beta \ll 1$, the ellipticity in the $\beta\nabla^2\boldsymbol{v}$ term is not always recognized by the numerical approximation as being elliptic. In other words, even though the equation still technically has elliptic character, it is overwhelmed by the other terms in eq. (4.14). This result led to the search for a transformation which would work in the limit of small β.

4.3 Elastic-Viscous Split Stress (EVSS) Formulation

Rajagopalan *et al.* (1990b) reconsidered a transformation which was first introduced by Mendelson *et al.* (1982) for a second-order fluid, which is algebraic, and then by Crochet *et al.* (1984) for differential constitutive models. This splitting will remove the β from the elliptic term in the momentum equation of the viscous method, eq. (4.14). This formulation is based on defining the elastic stress tensor $\boldsymbol{\Sigma}$ as

$$\boldsymbol{\Sigma} \equiv \boldsymbol{\tau} + \dot{\boldsymbol{\gamma}} = \boldsymbol{\tau}_p + (1-\beta)\dot{\boldsymbol{\gamma}}. \tag{4.17}$$

Substituting eq. (4.17) into the momentum and Oldroyd-B viscoelastic flow equations, eqs. (4.1), (4.2) and (2.22), yields

$$-\nabla^2\boldsymbol{v} + \nabla\cdot\boldsymbol{\Sigma} + \nabla p = \mathbf{0}, \tag{4.18}$$

$$\nabla\cdot\boldsymbol{v} = \mathbf{0}, \tag{4.19}$$

$$\boldsymbol{\Sigma} + De\boldsymbol{\Sigma}_{(1)} - De(1-\beta)\dot{\boldsymbol{\gamma}}_{(1)} = \mathbf{0}, \tag{4.20}$$

where the dependent variables are $(\boldsymbol{v}, p, \boldsymbol{\Sigma})$. The Laplacian operator in eq. (4.18) ensures that this equation is explicitly elliptic in $\boldsymbol{v}$, given a stress field $\boldsymbol{\Sigma}$. The mathematical type of the transformed equation set, eqs. (4.18), (4.19) and (4.20), has the same structure as the Oldroyd-B model [17] and can be artificially split into an elliptic saddle point problem consisting of the momentum and continuity equations, eqs. (4.18) and (4.19), and the hyperbolic differential equations for the constitutive equation in terms of the elastic stress tensor, eq. (4.20).

The use of this change of variables introduces the upper convected derivative of the rate-of-strain tensor into the constitutive equation which includes second derivatives in space of the velocity as well as time derivatives of the velocity gradient. Special attention must be given to the approximation of this term. In order to prove the existence of a solution in transient flows for the Oldroyd-B model, Guillope & Saut (1989) determined that it was necessary to have a velocity basis which is twice differentiable or $\boldsymbol{v} \in H^2$. If this is true, then the term $\dot{\boldsymbol{\gamma}}_{(1)}$ is well-defined and the constitutive equation is integrated to obtain $\boldsymbol{\Sigma}$. If the velocity field is interpolated by a biquadratic Lagrangian finite element approximation ($\boldsymbol{v} \in H^1$), then the second derivatives in the $\dot{\boldsymbol{\gamma}}_{(1)}$ term will contain singularities which will cause numerical instabilities. This was noted by several workers who tried this method (Apelian *et al.*, 1988, Beris *et al.*, 1984, Crochet *et al.*, 1984, Fortin & Zine, 1986 and Mendelson, 1982); all integrated this term by parts resulting in the weak form of the constitutive equation with the boundary integrals being integrated as data or as part of the equation set. These methods lead to spurious, mesh-sized oscillations, probably because integration by parts is usually performed on the main variable in the equation not on a term that can be considered as inhomogeneous data.

The breakthrough of the EVSS method is the new treatment of the term $\dot{\boldsymbol{\gamma}}$; Rajagopalan *et al.* (1990b) interpolated this term by a least-squares approximation

$$\dot{\boldsymbol{\gamma}} - (\boldsymbol{\nabla v}) - (\boldsymbol{\nabla v})^T = \mathbf{0}. \tag{4.21}$$

This approximation of the rate-of-strain tensor remains well-posed under differentia-

tion for a Lagrangian finite element approximation after subsequent substitution into eq. (4.20). This is similar to the recovery of the stresses from the displacements in nonlinear elasticity problems introduced in the 1970s by Oden and coworkers (Oden & Brauchli, 1971 and Oden & Reddy, 1971) and Hinton & Campbell (1974).

Numerical results with the EVSS method (Rajagopalan *et al.*, 1990b) show that introduction of the interpolation of the rate-of-strain tensor eliminates the mesh-sized oscillations present in earlier attempts using the elastic-viscous split stress transformation (see Section 4.6.3).

4.4 Elastic-Viscous Split Stress - Gradient (EVSS-G) Formulation

The formulation of the EVSS-G method for an Oldroyd-B fluid (Brown *et al.*, 1993 and Szady *et al.*, 1995) is similar to the formulation of the EVSS method given in the previous section. The elastic stress tensor defined by eq. (4.17) is substituted into the the momentum and constitutive equations to yield the transformed equations, eqs. (4.18 - 4.20). The difference in the formulations lies in the approximation used to make the upper convected derivative of the rate-of-strain tensor well-posed. As discussed in Brown *et al.* (1993) and Szady *et al.* (1995) and will be discussed further in Chapter 5, the differential constitutive equation is singular along curves where the velocity field vanishes and eq. (4.20) reduces to an algebraic relation between the elastic stress and the velocity gradient

$$\boldsymbol{\Sigma} - De\left[(\boldsymbol{\nabla v})^T\cdot\boldsymbol{\Sigma} + \boldsymbol{\Sigma}\cdot(\boldsymbol{\nabla v})\right] = De(1-\beta)\left[(\boldsymbol{\nabla v})^T\cdot\dot{\boldsymbol{\gamma}} + \dot{\boldsymbol{\gamma}}\cdot(\boldsymbol{\nabla v})\right]. \qquad (4.22)$$

The EVSS-G formulation is based on the idea of a compatibility constraint existing between the approximations to the stress and the velocity gradient due to the degeneracy of the differential equation set to an algebraic equation set along zero streamlines. This is a heuristic argument that is similar to that of Taylor & Hood (1973) in the introduction of the finite element used to solve the Navier-Stokes equa-

tions. The quantity interpolated by least-squares is now taken to be the velocity gradient instead of the rate-of-strain tensor $\dot{\gamma}$ and can be defined as

$$\boldsymbol{G} - \boldsymbol{\nabla v} = \mathbf{0}. \tag{4.23}$$

The full reasoning behind this choice will be explained in Chapter 5. Eq. (4.23) is substituted into the constitutive equation (4.20) for *all* appearances of the velocity gradient which yields

$$\begin{aligned} &\boldsymbol{\Sigma} + De\left[\frac{\partial \boldsymbol{\Sigma}}{\partial t} + \boldsymbol{v}\cdot\boldsymbol{\nabla}\boldsymbol{\Sigma} - (\mathbf{G})^T\cdot\boldsymbol{\Sigma} - \boldsymbol{\Sigma}\cdot\mathbf{G}\right] \\ &\quad - De(1-\beta)\left[\frac{\partial\left[\mathbf{G}+(\mathbf{G})^T\right]}{\partial t} + \boldsymbol{v}\cdot\boldsymbol{\nabla}\left[\mathbf{G}+(\mathbf{G})^T\right]\right. \\ &\quad \left. - \left[\mathbf{G}+(\mathbf{G})^T\right]\cdot\left[\mathbf{G}+(\mathbf{G})^T\right]\right] = \mathbf{0}. \end{aligned} \tag{4.24}$$

This methodology can easily be extended to other constitutive equations.

For the CR-FENE model, due to the nonlinearity of the trace of the connectivity tensor appearing in the equation, the definition of the elastic stress tensor has to be modified as was done in Lunsmann *et al.* (1993) to

$$\hat{\boldsymbol{\Sigma}} \equiv \frac{(1-\beta)}{De} f(R)(\boldsymbol{I} - \boldsymbol{A}) + (1-\beta)\dot{\gamma}. \tag{4.25}$$

In terms of the polymeric stress tensor $\boldsymbol{\tau}_p$ this becomes

$$\hat{\boldsymbol{\Sigma}} \equiv \boldsymbol{\tau}_p + (1-\beta)\dot{\gamma} + \frac{(1-\beta)}{De} f(R)\boldsymbol{I}. \tag{4.26}$$

This modification accounts for the presence of the polymeric stress tensor in the definition of the term $f(R)$. The constitutive equation for the EVSS-G method for the CR-FENE constitutive equation is then

$$\hat{\boldsymbol{\Sigma}} + De\left(\frac{\hat{\boldsymbol{\Sigma}}}{f(R)}\right)_{(1)} - De(1-\beta)\left(\frac{\boldsymbol{G}+(\boldsymbol{G})^T}{f(R)}\right)_{(1)} = \mathbf{0}. \tag{4.27}$$

In terms of the modified elastic stress tensor, the EVSS-G/CR-FENE constitutive equation is similar to the Oldroyd-B constitutive equation; the difference being the division of the convected derivative variables by $f(R)$ which makes the dumbbell finitely extensible. It should also be remembered that the pressure in the momentum equation for CR-FENE equations is the modified pressure p_{CR} as given by eq. (2.28).

The CR-FENE model is an example of a constitutive equation that requires significant modifications to the original definition of the elastic stress tensor in order to fit into the EVSS-type framework. Furthermore, experience with this or any other constitutive equation does not guarantee that another constitutive equation can be modified in a similar manner. The FENE-P model and the Gmela model are two examples of constitutive equations the former is similar to the CR-FENE equation in formulation while the Gmela model is different.

4.5 Discrete Elastic-Viscous Split Stress - Gradient (DEVSS-G) Formulation

The DEVSS-G formulation is similar to the mixed finite element method introduced by Guenette and Fortin (1995), but it differs in the same manner as that between the EVSS and EVSS-G methods. The derivation begins similar to the EVSS and EVSS-G methods in that the definition of an elastic stress tensor, eq. (4.17), is introduced. However, instead of substituting into both eqs. (2.8) and (2.22), the elastic stress is substituted *only* into eq. (2.8) to give eq. (4.18). Now, let

$$\boldsymbol{\Sigma} = \boldsymbol{\tau} + \left[\boldsymbol{G} + (\boldsymbol{G})^T\right] = \boldsymbol{\tau}_p + (1-\beta)\left[\boldsymbol{G} + (\boldsymbol{G})^T\right], \tag{4.28}$$

where the rate-of-strain tensor is approximated by the least-squares interpolated velocity gradient rather than the velocity field from the momentum equation. Substitute eq. (4.28) into eq. (4.18) to yield

$$-\nabla^2\boldsymbol{v} + \nabla\cdot\left[\boldsymbol{G} + (\boldsymbol{G})^T\right] + \nabla\cdot\boldsymbol{\tau} + \nabla p = \boldsymbol{0}. \tag{4.29}$$

In the continuous sense this is simply adding and subtracting the Laplacian of the velocity field to the momentum equation. It is in the *discrete* case that there is a difference between $\nabla \boldsymbol{v}$ and $\left[\boldsymbol{G} + (\boldsymbol{G})^T\right]$; the first is discontinuous while the second is continuous. Eq. (4.29) can also be written in terms of the polymeric stress, eqs. (4.12) and (4.13) (this is similar to the substitution resulting in the right hand side of eq. (4.28). Then the use of the least-squares approximation for the velocity gradient yields the DEVSS-G equations for the Oldroyd-B model

$$-\nabla^2 \boldsymbol{v} + (1-\beta)\nabla\cdot\left[\boldsymbol{G} + (\boldsymbol{G})^T\right] + \nabla\cdot\boldsymbol{\tau}_p + \nabla p = \boldsymbol{0}, \tag{4.30}$$

$$\nabla\cdot\boldsymbol{v} = \boldsymbol{0}, \tag{4.31}$$

$$\boldsymbol{\tau}_p + De\left[\frac{\partial \boldsymbol{\tau}_p}{\partial t} + \boldsymbol{v}\cdot\nabla\boldsymbol{\tau}_p - (\boldsymbol{G})^T\cdot\boldsymbol{\tau}_p - \boldsymbol{\tau}_p\cdot\boldsymbol{G}\right] - (1-\beta)\left[\boldsymbol{G} + (\boldsymbol{G})^T\right] = \boldsymbol{0}, \tag{4.32}$$

$$\boldsymbol{G} - \nabla\boldsymbol{v} = \boldsymbol{0}. \tag{4.33}$$

For the CR-FENE model, start with eq. (4.30) and substitute eqs. (2.28) and (2.29) to change the momentum equation into the variables of the constitutive equation and then simplify

$$-\nabla^2 \boldsymbol{v} + (1-\beta)\nabla\cdot\left[\boldsymbol{G} + (\boldsymbol{G})^T\right] - \frac{(1-\beta)}{De}\nabla\cdot[f(R)\boldsymbol{A}] + \nabla p_{CR} = 0. \tag{4.34}$$

The continuity equation and the velocity gradient equation are the same as for the Oldroyd-B constitutive equation, eqs. (4.31) and (4.33). The constitutive equation is unchanged from eq. (2.24).

The convected derivative of the rate-of-strain tensor, $\dot{\gamma}_{(1)}$, is *not* introduced into the equation set for the DEVSS-G formulation; in the EVSS and the EVSS-G methods, this term is present. The convected derivative becomes troublesome to interpret in transient flow; the least-squares interpolation of the rate-of-strain tensor or the velocity gradient tensor define the variable algebraically (with no time derivative). However, a time derivative of this variable appears in the constitutive equation. The interpretation of this type of operation is unclear and appears not to have been addressed in the literature before. The DEVSS-G method eliminates this problem

altogether by not introducing the term into the constitutive equations. This is one major advantage of the method. Another is the simplicity involved in the derivation of the method for very complex, nonlinear constitutive models like the CR-FENE model where the DEVSS-G methodology is significantly easier to derive than for the EVSS and EVSS-G methods.

4.6 Finite Element Formulations

The computational domain Ω is divided into quadrilateral elements $\{\Omega_i\}$ on which the equations of motion are discretized using classical finite element methods for the velocity ($\boldsymbol{v}^h$), pressure (p^h), stress ($\boldsymbol{T}^h$) and interpolation variable ($\boldsymbol{G}^h$), where the stress ($\boldsymbol{T}^h$) can signify the elastic stress ($\boldsymbol{\Sigma}^h$), the polymeric stress ($\boldsymbol{\tau_p}^h$) or the configuration tensor ($\boldsymbol{A}^h$) and the interpolation variable ($\boldsymbol{G}^h$) can signify the vorticity (ω^h), the rate-of-strain tensor ($\dot{\boldsymbol{\gamma}}^h$) or the velocity gradient ($\boldsymbol{G}^h$). The superscript h for these variables indicates the dependence of the approximation on the finite element mesh, where h is a characteristic mesh size. The variables are expanded using low order Lagrangian finite elements, either bilinear or biquadratic since quadrilateral elements are used. The EEME/FEM, Viscous/FEM, EVSS/FEM, EVSS-G/FEM and DEVSS-G/FEM are based on discretizing the equations of motion using methods appropriate for the elliptic saddle point problem (e.g., eqs. (4.18) and (4.19)), for the hyperbolic constitutive equation (e.g., eq. (4.24)) and for the least-squares interpolation of the interpolation variable, eq. (4.23).

The finite element approximations for the four-field equations satisfy

$$(\boldsymbol{v}^h, p^h, \boldsymbol{T}^h, \boldsymbol{G}^h) \subset (V^h, P^h, E^h, G^h),$$

where (V^h, P^h, E^h, G^h) are the spaces of the the finite element approximations to the velocity, pressure, constitutive equation variable and interpolation variable, respectively. Lagrangian biquadratic polynomials ($Q_2(\Omega)$) are used to approximate the velocity and the constitutive equation variable (only in the EEME/FEM, Viscous/FEM and EVSS/FEM) while Lagrangian bilinear polynomials ($Q_1(\Omega)$) are used for the pres-

sure, constitutive equation variable (only in the EVSS-G/FEM and DEVSS-G/FEM), vorticity, rate-of-strain tensor and velocity gradient.

4.6.1 EEME/FEM

The EEME/FEM method is based on solving eqs. (4.6) and (4.2) as an elliptic saddle point problem for $(\boldsymbol{v}^h, q^h)$. The elliptic saddle point problem is discretized using Galerkin's method with finite element basis functions proved to be compatible and convergent for the solution of the governing equations of motion in the Newtonian-Stokes flow limit (Carey & Oden, 1986). The constitutive equation, eq. (4.3), is integrated by using one of the stabilization methods discussed in Section 3.3. The equation set is a three-field problem, $\{\boldsymbol{v}^h, q^h, \boldsymbol{\tau}^h\} \in \{Q_2, Q_1, Q_2\}$. The finite element formulation is given by the following set of equations:

$$\begin{aligned}
&\int_\Gamma \Phi_j^v \boldsymbol{n}\cdot\left[(De\boldsymbol{\tau}^h - \boldsymbol{I})\cdot(\boldsymbol{\nabla v}^h)\right]\cdot\boldsymbol{e}_k d\Gamma \\
&\quad - \int_\Omega \boldsymbol{\nabla}\Phi_j^v\cdot\left[(De\boldsymbol{\tau}^h - \boldsymbol{I})\cdot(\boldsymbol{\nabla v}^h)\right]\cdot\boldsymbol{e}_k d\Omega \\
&\quad - \int_\Omega \Phi_j^v\left[(De\boldsymbol{\tau}^h - \boldsymbol{I})\cdot(\boldsymbol{\nabla v}^h):\boldsymbol{\nabla e}_k\right] d\Omega \qquad (4.35)\\
&\quad - \int_\Omega \left\{\Phi_j^v\left[De(\boldsymbol{\nabla v}^h)\cdot(\boldsymbol{\nabla}\cdot\boldsymbol{\tau}^h) + \boldsymbol{\nabla}q^h\right]\cdot\boldsymbol{e}_k\right\} d\Omega = 0, \qquad k = 1,\ 2,
\end{aligned}$$

$$\int_\Omega [\boldsymbol{\tau}^h + De\boldsymbol{\tau}_{(1)}^h + \dot{\boldsymbol{\gamma}}^h]:\boldsymbol{e}_m\boldsymbol{e}_n\Psi_j^\tau d\Omega = 0, \qquad m,\ n = 1,\ 2, \qquad (4.36)$$

$$\int_\Omega (\boldsymbol{\nabla}\cdot\boldsymbol{v}^h)\Phi_j^q d\Omega = 0, \qquad (4.37)$$

where $(\boldsymbol{v}^h, q^h, \boldsymbol{\tau}^h)$ are finite element approximations to the respective canonical variables, $k, m, n = x, y$ or r, θ or r, z depending on whether the coordinate system of the problem is Cartesian, cylindrical or axisymmetric, respectively, $(\boldsymbol{e}_i, \boldsymbol{e}_j)$ are the unit vectors in the coordinate system and h is the characteristic element size. Also, $\boldsymbol{e}_k$ is the kth base vector of the coordinate system and $\boldsymbol{n}$ is the outward pointing normal on the boundary, Γ, of the domain, Ω. Φ_j^v, Φ_j^q and Ψ_j^τ are the basis functions corresponding to the velocity, modified pressure and stress, respectively. Note that

Ψ_j^τ is given by eq. (3.53) for the SUPG method and by eq. (3.59) for the GLS/DW method. For the SU method, $\Psi_j^\tau = \Phi_j^\tau$ which is the Galerkin method and the perturbation term from Section 3.3.2 with $\boldsymbol{\beta}$ given by eq. (3.33) is added to eq. (4.36). In the momentum equation, only the explicitly elliptic term $\boldsymbol{\nabla}\cdot(\boldsymbol{\chi}\cdot\boldsymbol{\nabla}\boldsymbol{v})$ has been integrated by parts. Since the velocity test functions are zero on no-slip boundaries and the integrand of the line integral sums to zero along adjacent element faces, only the inflow and outflow boundaries can be non-zero. However, the periodicity of the problems considered here makes the line integrals in the momentum equation zero at the inflow/outflow boundaries. The pressure is recovered by solving the hyperbolic equation eq. (4.5) in a post processing routine similar to what is done to calculate the stream function (King, 1987).

This formulation results in a method which stable for high De and convergent with mesh refinement (King *et al.*, 1988). The accuracy of the method was checked against the spectral element method of Beris *et al.* (1986) for flow in eccentric cylinders and showed excellent agreement.

The EEME/FEM for the Oldroyd-B method also consists of applying Galerkin's method to the momentum and continuity equations followed by the application of the upwinding method to the constitutive equation. Finally, the second-order derivatives of the vorticity are integrated by parts in the momentum equation and explicitly interpolated in a variational sense using a bilinear basis set. The coefficients in the expansion are determined through a least-squares interpolation of the velocity field. The equation set is a four field problem, $\{\boldsymbol{v}^h, q^h, \boldsymbol{\tau}^h, \boldsymbol{\omega}^h\} \in \{Q_2, Q_1, Q_2, Q_3\}$. The resulting set of of equations for the finite element formulation are

$$
\begin{aligned}
&\int_\Gamma \Phi_j^v \boldsymbol{n}\cdot\left[(De{\boldsymbol{\tau}_p}^h - \boldsymbol{I})\cdot(\boldsymbol{\nabla}\boldsymbol{v}) + De\beta\boldsymbol{v}^h(\boldsymbol{\nabla}\times\boldsymbol{\omega}^h)\right]\cdot\boldsymbol{e}_k d\Gamma \\
&\quad - \int_\Omega \boldsymbol{\nabla}\Phi_j^v\cdot\left[(De{\boldsymbol{\tau}_p}^h - \boldsymbol{I})\cdot(\boldsymbol{\nabla}\boldsymbol{v}^h) + De\beta\boldsymbol{v}^h(\boldsymbol{\nabla}\times\boldsymbol{\omega}^h)\right]\cdot\boldsymbol{e}_k d\Omega \\
&\quad - \int_\Omega \Phi_j^v\left[(De{\boldsymbol{\tau}_p}^h - \boldsymbol{I})\cdot(\boldsymbol{\nabla}\boldsymbol{v}^h) + De\beta\boldsymbol{v}^h(\boldsymbol{\nabla}\times\boldsymbol{\omega}^h)\right]^T : \boldsymbol{\nabla}\boldsymbol{e}_k d\Omega \qquad (4.38) \\
&\quad + \int_\Omega \Phi_j^v\left[De(\boldsymbol{\nabla}\boldsymbol{v}^h)\cdot(\boldsymbol{\nabla}\cdot{\boldsymbol{\tau}_p}^h) + \boldsymbol{\nabla}q^h + De\beta(\boldsymbol{\nabla}\boldsymbol{v}^h)\cdot(\boldsymbol{\nabla}\times\boldsymbol{\omega}^h)\right]\cdot\boldsymbol{e}_k d\Omega \\
&\quad = 0, \qquad k = 1,\ 2,
\end{aligned}
$$

$$\int_\Omega [\boldsymbol{\tau}_p{}^h + De\boldsymbol{\tau}_{p(1)}^h + \dot{\boldsymbol{\gamma}}^h] : \boldsymbol{e}_m \boldsymbol{e}_n \Psi_j^\tau d\Omega = 0, \qquad m,\ n = 1,\ 2, \tag{4.39}$$

$$\int_\Omega (\boldsymbol{\nabla} \cdot \boldsymbol{v}^h) \Phi_j^q d\Omega = 0, \tag{4.40}$$

$$\int_\Omega \left[\boldsymbol{\omega}^h - (\boldsymbol{\nabla} \times \boldsymbol{v}^h)\right] \Phi_j^\omega d\Omega = 0, \tag{4.41}$$

where Φ_j^ω is the basis function corresponding to the vorticity.

Calculations for the corrugated-tube geometry were shown to be convergent with mesh and agreed with the spectral element results of Pilitsis & Beris (1989) over a wide range of De for $\beta = 0.85$. Calculations in the eccentric cylinder geometry were also performed and were convergent for low values of De for most values of β. It was noticed that at a fixed De, as β increased, the solution deteriorates through the appearance of mesh-size oscillations. These oscillations disappear with mesh refinement and are a result of the inability of the method to deal with the third-order derivative as it becomes more important in the calculation.

In summary the EEME method is a good method for computing viscoelastic flows near the UCM limit. As the third order terms in the momentum equation begin to dominate, which can occur when the contribution from the solvent is large, difficulties occur. When large amounts of inertia are included in the calculations, it also becomes difficult to numerically resolve the ellipticity of the EEME operator without significant mesh refinement; furthermore, the numerical formulation may fail to reflect the mathematical type of the momentum equation which should remain elliptic for all values of Re and De. Finally, the EEME form of the momentum equation becomes extremely difficult to derive for more complex forms of constitutive equations such as the CR-FENE model, if the form exists at all.

4.6.2 Viscous/FEM

This is a three-field problem, $\{\boldsymbol{v}^h, p^h, \boldsymbol{\tau}_p^h\} \in \{Q_2, Q_1, Q_2\}$. The momentum and continuity equations are discretized by Galerkin's method, and the constitutive equation is discretized by an upwinding method as for the EEME/FEM. The finite element

formulation is given by the following set of equations:

$$\begin{aligned}
&\int_\Gamma \Phi_j^v \boldsymbol{n}\cdot(\boldsymbol{\nabla v}^h)\cdot\boldsymbol{e}_k d\Gamma \\
&\quad - \int_\Omega \beta\left[\boldsymbol{\nabla}\Phi_j^v\cdot(\boldsymbol{\nabla v}^h)\cdot\boldsymbol{e}_k + \Phi_j^v(\boldsymbol{\nabla v}^h)^T : \boldsymbol{\nabla e}_k\right] d\Omega \qquad (4.42)\\
&\quad - \int_\Omega \Phi_j^v(\boldsymbol{\nabla}\cdot{\boldsymbol{\tau}_p}^h + \boldsymbol{\nabla}p^h)\cdot\boldsymbol{e}_k d\Omega = \mathbf{0}, \qquad k = 1,\ 2,
\end{aligned}$$

$$\int_\Omega \left[{\boldsymbol{\tau}_p}^h + De\boldsymbol{\tau}_{p(1)}^h + (1-\beta)\dot{\boldsymbol{\gamma}}^h\right] : \boldsymbol{e}_m\boldsymbol{e}_n\Psi_j^\tau d\Omega = \mathbf{0}, \qquad m,\ n = 1,\ 2, \qquad (4.43)$$

$$\int_\Omega(\boldsymbol{\nabla}\cdot\boldsymbol{v}^h)\Phi_j^q d\Omega = \mathbf{0}. \qquad (4.44)$$

A proof of the existence of weak solutions with the Oldroyd-B model was given by Renardy *et al.* (1987). Using a similar approach, Baranger & Sandri (1991a and 1991b) and Sandri (1994) developed a rigorous convergence proof for finite element approximations in the limit of small De and $h \to 0$. Although this formulation is formally correct for the Oldroyd-B fluid, the elliptic operator in eq. (4.14), $-\beta\nabla^2\boldsymbol{v}$ will become singularly small as the Deborah number is increased and the role of the elastic part of the stress increases. In fact, Rajagopalan *et al.* (1990b) has shown that mixed finite element methods based on the viscous formulation perform poorly as the De is increased and as η_s is decreased to zero. This empirical result demonstrates the lack of robustness of the analysis of Baranger and Sandri (1991b), in the sense that their proof is valid in the limits $h \to 0$ and $De \ll 1$ and the numerical calculations evaluate the usefulness of the method outside this limit.

4.6.3 EVSS/FEM

The finite element calculation is formulated as a four-field problem, $\{\boldsymbol{v}^h, p^h, \boldsymbol{\Sigma}^h, \dot{\boldsymbol{\gamma}}^h\} \in \{Q_2, Q_1, Q_2, Q_1\}$. Again, the momentum and continuity equations are discretized by Galerkin's method, the constitutive equations are discretized as in the EEME/FEM via an upwinding formulation, and the rate-of-strain tensor equations are discretized

by a least-squares interpolation. The weak form of an Oldroyd-B fluid is written as

$$
\begin{aligned}
&-\int_\Gamma \Phi_j^v \boldsymbol{n}\cdot(\boldsymbol{\nabla v}^h)\cdot\boldsymbol{e}_k d\Gamma \\
&\quad+\int_\Omega \left[\boldsymbol{\nabla}\Phi_j^v\cdot(\boldsymbol{\nabla v}^h)\cdot\boldsymbol{e}_k+\Phi_j^v(\boldsymbol{\nabla v}^h)^T{:}\boldsymbol{\nabla e}_k\right] d\Omega, \\
&\quad-\int_\Gamma \left(\Phi_j^v \boldsymbol{n}\cdot(\boldsymbol{\Sigma}^h+p^h\boldsymbol{I})\cdot\boldsymbol{e}_k\right) d\Gamma \\
&\quad+\int_\Omega \boldsymbol{\nabla}\Phi_j^v\cdot(\boldsymbol{\Sigma}^h+p^h\boldsymbol{I})\cdot\boldsymbol{e}_k d\Omega=0, \qquad k=1,\ 2,
\end{aligned}
\tag{4.45}
$$

$$
\int_\Omega \left[\boldsymbol{\Sigma}^h+De\boldsymbol{\Sigma}_{(1)}^h-De(1-\beta)\dot{\boldsymbol{\gamma}}_{(1)}^h\right]{:}\boldsymbol{e}_m\boldsymbol{e}_n\Psi_j^\Sigma d\Omega=0, \qquad m,\ n=1,\ 2, \tag{4.46}
$$

$$
\int_\Omega(\boldsymbol{\nabla}\cdot\boldsymbol{v}^h)\Phi_j^p d\Omega=0, \tag{4.47}
$$

$$
\int_\Omega \left[\dot{\boldsymbol{\gamma}}^h-(\boldsymbol{\nabla v}^h)-(\boldsymbol{\nabla v}^h)^T\right]{:}\boldsymbol{e}_m\boldsymbol{e}_n\Phi_j^G d\Omega=0, \qquad m,\ n=1,\ 2. \tag{4.48}
$$

The third term in eq. (4.45) is a boundary integral that arises through the application of the divergence theorem to the terms $\boldsymbol{\nabla}\cdot\boldsymbol{\Sigma}$ and $\boldsymbol{\nabla}p$ which is simply a total stress $\boldsymbol{n}\cdot\boldsymbol{\pi}$ boundary condition. This term usually arises in connection with free surface flows; due to the periodic nature of all flows considered in this thesis, this term is always zero.

For the eccentric cylinder geometry and Oldroyd-B equation, the EVSS/FEM indicates that for $0 \leq \beta \leq 1$, it yields a smoother solution than either the EEME or viscous formulations. It was noted that in the limit $\beta \to 0$, the EEME/FEM was slightly better than EVSS/FEM. The accuracy of the method was checked with the spectral element results of Pilitsis & Beris (1989) for the flow of an Oldroyd-B fluid through a corrugated tube and showed excellent agreement.

The EVSS method is valid over the entire range $0 \leq \beta \leq 1$ which makes it more robust than either the EEME or viscous formulations. The method also can easily be applied to a wide variety of constitutive equations either with or without solvent viscosity and to multi-mode models. The extension to the solution of free surface flows is simple, because of the explicit presence of the total stress boundary condition.

4.6.4 EVSS-G/FEM

The EVSS-G/FEM is a four-field problem, $\{\boldsymbol{v}^h, p^h, \boldsymbol{\Sigma}^h, \boldsymbol{G}^h\} \in \{Q_2, Q_1, Q_1, Q_1\}$. Note: The elastic stress now is interpolated *bilinearly* not biquadraticly as in the EEME/FEM, Viscous/FEM and EVSS/FEM. The momentum and continuity equations are the same as in the EVSS/FEM and are given by eqs. (4.45) and (4.47), respectively. The constitutive equations are discretized as before by an upwinding method for the hyperbolic equations and the velocity gradient equations are discretized by a least-squares interpolation. The weak form of these two equations is written as

$$\int_\Omega \Big[\boldsymbol{\Sigma}^h + De\boldsymbol{\Sigma}^h_{(1)} - De(1-\beta)\left(\boldsymbol{G}^h + (\boldsymbol{G}^h)^T\right)_{(1)}\Big] : \boldsymbol{e}_m\boldsymbol{e}_n\Psi^\Sigma_j d\Omega = 0, \qquad m,\ n = 1,\ 2, \tag{4.49}$$

$$\int_\Omega (\boldsymbol{G}^h - \boldsymbol{\nabla}\boldsymbol{v}^h) : \boldsymbol{e}_m\boldsymbol{e}_n\Phi^G_j d\Omega = 0, \qquad m,\ n = 1,\ 2. \tag{4.50}$$

In the 1970s, the stress variables were recovered from the displacements in nonlinear elasticity problems in a similar manner to eq. (4.50) (Oden & Brauchli, 1971, Oden & Reddy, 1971 and Hinton & Campbell, 1974). The interpolation functions gave smoother results than the previously used reconstructions from the original discontinuous basis functions for the displacements. Thus, while there is no mathematical proof that the EVSS-G method resolves an incompatibility in the discretized equations, it is loosely based on similar ideas from the elasticity literature.

The weak form of the equations can also be written using the standard inner product defined on Ω, $(\cdot,\cdot)$, and the line integral inner product defined on the boundary Γ, $\langle\cdot,\cdot\rangle$, which were defined in Chapter 3. As an example, the momentum equation given by eq. (4.45) can be written as

$$(\boldsymbol{\nabla}\boldsymbol{\Phi}^v_j, \boldsymbol{\nabla}\boldsymbol{v}^h) - (\boldsymbol{\nabla}\boldsymbol{\Phi}^v_j, \boldsymbol{\Sigma}^h + p^h\boldsymbol{I}) - \left\langle \boldsymbol{\Phi}^v_j, \mathbf{n}\cdot(\boldsymbol{\nabla}\boldsymbol{v}^h + \boldsymbol{\Sigma}^h + p^h\boldsymbol{I})\right\rangle_{\partial\Omega} = \mathbf{0}, \qquad \forall\ \boldsymbol{\Phi}^v_j \in V^h(\Omega), \tag{4.51}$$

This notation is introduced to make the equations in the following discussion simpler.

The differences between the equations of the EVSS/FEM and EVSS-G/FEM can be seen by a comparison of the constitutive equation in which every term of the upper convected derivatives is shown in the inner product notation from the preceding paragraph. The EVSS/FEM is as follows:

$$\begin{aligned}
&\left(\boldsymbol{\Psi}_j^{\Sigma}, \left[\boldsymbol{\Sigma}^h + De\left(\frac{\partial \boldsymbol{\Sigma}^h}{\partial t} + \boldsymbol{v}^h \cdot \boldsymbol{\nabla}\boldsymbol{\Sigma}^h - (\boldsymbol{\nabla}\boldsymbol{v}^h)^T \cdot \boldsymbol{\Sigma}^h - \boldsymbol{\Sigma}^h \cdot \boldsymbol{\nabla}\boldsymbol{v}^h\right)\right]\right) \\
&\quad - De(1-\beta)\left(\boldsymbol{\Psi}_j^{\Sigma}, \left[\frac{\partial \dot{\boldsymbol{\gamma}}^h}{\partial t} + \boldsymbol{v}^h \cdot \boldsymbol{\nabla}\dot{\boldsymbol{\gamma}}^h - (\boldsymbol{\nabla}\boldsymbol{v}^h)^T \cdot \dot{\boldsymbol{\gamma}}^h - \dot{\boldsymbol{\gamma}}^h \cdot \boldsymbol{\nabla}\boldsymbol{v}^h\right]\right) \qquad (4.52) \\
&\quad = \mathbf{0}, \qquad \forall\, \boldsymbol{\Psi}_j^{\Sigma} \in E^h(\Omega),
\end{aligned}$$

where $\boldsymbol{\nabla}\boldsymbol{v}^h$ is evaluated from the momentum equation and $\dot{\boldsymbol{\gamma}}^h$ is taken from the least-squares interpolation of $\boldsymbol{\nabla}\boldsymbol{v}^h$. In the EVSS-G/FEM, the velocity gradient tensor is interpolated by eq. (4.50) and is substituted into the constitutive equation for *every* occurrence of the velocity gradient. The EVSS-G/FEM constitutive equation is then

$$\begin{aligned}
&\left(\boldsymbol{\Psi}_j^{\Sigma}, \left[\boldsymbol{\Sigma}^h + De\left(\frac{\partial \boldsymbol{\Sigma}^h}{\partial t} + \boldsymbol{v}^h \cdot \boldsymbol{\nabla}\boldsymbol{\Sigma}^h - (\boldsymbol{G}^h)^T \cdot \boldsymbol{\Sigma}^h - \boldsymbol{\Sigma}^h \cdot \boldsymbol{G}^h\right)\right]\right) \\
&\quad - De(1-\beta)\left(\boldsymbol{\Psi}_j^{\Sigma}, \left[\frac{\partial(\boldsymbol{G}^h + (\boldsymbol{G}^h)^T)}{\partial t} + \boldsymbol{v}^h \cdot \boldsymbol{\nabla}(\boldsymbol{G}^h + (\boldsymbol{G}^h)^T)\right.\right. \qquad (4.53) \\
&\quad \left.\left. - 2(\boldsymbol{G}^h)^T \cdot \boldsymbol{G}^h - \boldsymbol{G}^h \cdot \boldsymbol{G}^h - (\boldsymbol{G}^h)^T \cdot (\boldsymbol{G}^h)^T\right]\right) = \mathbf{0}, \qquad \forall\, \boldsymbol{\Psi}_j^{\Sigma} \in E^h(\Omega).
\end{aligned}$$

This gives a consistent interpolation of the velocity gradient for every term in the upper convected derivative of the rate-of-strain tensor. The lowering of the elastic stress interpolation from biquadratic to bilinear results in a consistent approximation (bilinear) in all terms in the constitutive equation.

For the CR-FENE model, the EVSS-G equations are formulated analogously where the momentum equations (with the modified pressure p_{CR} and elastic stress $\hat{\boldsymbol{\Sigma}}$), the continuity equations and the velocity gradient interpolation equations are given by eqs. (4.45), (4.47) and (4.50), respectively. The weak form of the constitutive

equations are

$$\int_\Omega \left\{ \hat{\boldsymbol{\Sigma}}^h + De\left(\frac{\hat{\boldsymbol{\Sigma}}^h}{f(R)}_{(1)}\right) \right. \tag{4.54}$$
$$\left. - De(1-\beta)\left\{ \frac{\boldsymbol{G}^h}{f(R)} + \left(\frac{\boldsymbol{G}^h}{f(R)}\right)^T \right\}_{(1)} \right\} : \boldsymbol{e}_m \boldsymbol{e}_n \Psi_j^\Sigma d\Omega = 0, \qquad m,\ n = 1,\ 2,$$

In the expanded form the CR-FENE constitutive equation looks like

$$\left(\boldsymbol{\Psi}_j^{\hat{\Sigma}}, \left[\hat{\boldsymbol{\Sigma}}^h + De\left(\frac{\partial \frac{\hat{\boldsymbol{\Sigma}}^h}{f(R)}}{\partial t} + \boldsymbol{v}^h \cdot \boldsymbol{\nabla} \frac{\hat{\boldsymbol{\Sigma}}^h}{f(R)} - \frac{1}{f(R)} (\boldsymbol{G}^h)^T \cdot \hat{\boldsymbol{\Sigma}}^h - \frac{1}{f(R)} \hat{\boldsymbol{\Sigma}}^h \cdot \boldsymbol{G}^h \right) \right] \right)$$
$$- De(1-\beta)\left(\boldsymbol{\Psi}_j^{\hat{\Sigma}}, \left[\frac{\partial \left(\frac{\boldsymbol{G}^h}{f(R)} + (\frac{\boldsymbol{G}^h}{f(R)})^T \right)}{\partial t} + \boldsymbol{v}^h \cdot \boldsymbol{\nabla} \left(\frac{\boldsymbol{G}^h}{f(R)} + (\frac{\boldsymbol{G}^h}{f(R)})^T \right) \right.\right.$$
$$\left.\left. - \frac{2}{f^2(R)} (\boldsymbol{G}^h)^T \cdot \boldsymbol{G}^h \frac{1}{f^2(R)} \boldsymbol{G}^h \cdot \boldsymbol{G}^h - \frac{1}{f^2(R)} (\boldsymbol{G}^h)^T \cdot (\boldsymbol{G}^h)^T \right] \right) \tag{4.55}$$
$$= 0, \qquad \forall\, \boldsymbol{\Psi}_j^{\hat{\Sigma}} \in E^h(\Omega).$$

4.6.5 DEVSS-G/FEM

The DEVSS-G/FEM equations also are formulated exactly as the EVSS-G/FEM equations. The continuity equation and the velocity gradient equations are still given by eqs. (4.47) and (4.50), respectively. The weak form of the momentum and constitutive equations for an Oldroyd-B fluid are

$$- \int_\Gamma \Phi_j^v \boldsymbol{n} \cdot (\boldsymbol{\nabla} \boldsymbol{v}^h) \cdot \boldsymbol{e}_k d\Gamma$$
$$+ \int_\Omega \left[\boldsymbol{\nabla} \Phi_j^v \cdot (\boldsymbol{\nabla} \boldsymbol{v}^h) \cdot \boldsymbol{e}_k + \Phi_j^v (\boldsymbol{\nabla} \boldsymbol{v}^h)^T : \boldsymbol{\nabla} \boldsymbol{e}_k \right] d\Omega$$
$$- (1-\beta) \int_\Omega \Phi_j^v \boldsymbol{\nabla} \cdot \left(\boldsymbol{G}^h + (\boldsymbol{G}^h)^T \right) \cdot \boldsymbol{e}_k d\Omega \tag{4.56}$$
$$- \int_\Gamma \Phi_j^v \boldsymbol{n} \cdot (\boldsymbol{\Sigma}^h + p^h \boldsymbol{I}) \cdot \boldsymbol{e}_k d\Gamma$$
$$+ \int_\Omega \boldsymbol{\nabla} \Phi_j^v (\boldsymbol{\Sigma}^h + p^h \boldsymbol{I}) \cdot \boldsymbol{e}_k d\Omega = 0, \qquad k = 1,\ 2,$$
$$\int_\Omega \left[\boldsymbol{\Sigma}^h + De \boldsymbol{\Sigma}_{(1)}^h \right. \tag{4.57}$$

$$- De(1-\beta)\left(\boldsymbol{G}^h + (\boldsymbol{G}^h)^T\right)\Big]:\boldsymbol{e}_m\boldsymbol{e}_n\Psi_j^{\Sigma}d\Omega = 0, \qquad m,\ n = 1,\ 2.$$

The expanded form of the constitutive equation is

$$\left(\boldsymbol{\Psi}_j^{\tau_p}, \left[\boldsymbol{\tau}_p{}^h + De\left(\frac{\partial \boldsymbol{\tau}_p{}^h}{\partial t} + \boldsymbol{v}^h\cdot\nabla\boldsymbol{\tau}_p{}^h - (\boldsymbol{G}^h)^T\cdot\boldsymbol{\tau}_p{}^h - \boldsymbol{\tau}_p{}^h\cdot\boldsymbol{G}^h\right)\right]\right) \tag{4.58}$$
$$- De(1-\beta)\left(\boldsymbol{\Psi}_j^{\tau_p}, \left[\boldsymbol{G}^h + (\boldsymbol{G}^h)^T\right]\right) = 0, \qquad \forall\ \boldsymbol{\Psi}_j^{\Sigma_p} \in E^h(\Omega).$$

Note that the upper convected derivative of the rate-of-strain tensor does not appear in the constitutive equations.

For the CR-FENE model the weak forms of the momentum and constitutive equations are given in terms of the connectivity tensor $\boldsymbol{A}$

$$\begin{aligned}
&-\int_\Gamma \Phi_j^v \boldsymbol{n}\cdot(\nabla\boldsymbol{v}^h)\cdot\boldsymbol{e}_k d\Gamma \\
&\quad + \int_\Omega \left[\nabla\Phi_j^v\cdot(\nabla\boldsymbol{v}^h)\cdot\boldsymbol{e}_k + \Phi_j^v(\nabla\boldsymbol{v}^h)^T{:}\nabla\boldsymbol{e}_k\right] d\Omega \\
&\quad - (1-\beta)\int_\Omega \Phi_j^v \nabla\cdot\left(\boldsymbol{G}^h + (\boldsymbol{G}^h)^T\right)\cdot\boldsymbol{e}_k d\Omega \qquad (4.59)\\
&\quad - \frac{(1-\beta)}{De}\int_\Gamma \Phi_j^v \boldsymbol{n}\cdot[f(R)\boldsymbol{A}^h + p^h\boldsymbol{I}]\cdot\boldsymbol{e}_k d\Gamma \\
&\quad + \frac{(1-\beta)}{De}\int_\Omega \nabla\Phi_j^v(f(R)\boldsymbol{A}^h + p_{CR}^h\boldsymbol{I})\cdot\boldsymbol{e}_k d\Omega = 0, \qquad k = 1,\ 2,
\end{aligned}$$

$$\int_\Omega (De\boldsymbol{A}_{(1)}^h + \boldsymbol{A}^h - \boldsymbol{I}){:}\boldsymbol{e}_m\boldsymbol{e}_n\Psi_j^{\Sigma}d\Omega = 0, \qquad m,\ n = 1,\ 2. \tag{4.60}$$

The expanded form of the constitutive equation is simply

$$\left(\boldsymbol{\Psi}_j^A, \left[De\left(\frac{\partial \boldsymbol{A}^h}{\partial t} + \boldsymbol{v}^h\cdot\nabla\boldsymbol{A}^h - (\boldsymbol{G}^h)^T\cdot\boldsymbol{A}^h - \boldsymbol{A}^h\cdot\boldsymbol{G}^h\right)\right]\right) \tag{4.61}$$
$$+ \left(\boldsymbol{\Psi}_j^A, [\boldsymbol{A}^h - \boldsymbol{I}^h]\right) = 0, \qquad \forall\ \boldsymbol{\Psi}_j^A \in E^h(\Omega).$$

Again, this indicates the ease with which the DEVSS-G equations can be set up for different constitutive equations; only the momentum equation had to be slightly modified.

4.7 Time Integration

In the computation of transient partial differential equations, it is necessary to discretize the equations both spatially and temporally. There are several ways to do this: (i) discretize both simultaneously with the same method, (ii) discretize temporally then spatially or (iii) discretize spatially then temporally. An example of the first method is to discretize spatially using the finite element method as already discussed in this chapter and to discretize temporally using the finite element method as well. Usually, discontinuous basis functions in time are chosen, i.e., the discontinuous Galerkin method (Johnson, 1987). An example of the second method is the Taylor-Galerkin method in which the time discretization is performed first using a Taylor series expansion of the temporal derivatives and is followed by a spatial Galerkin finite element discretization. An example of the third method is a spatial finite element discretization followed by a temporal finite difference discretization; this is often referred to as the method of lines (LeVeque, 1990). This latter methodology is chosen here. Both fully implicit and semi-implicit time integration methods will be tested for the solution of the large set of ordinary differential equations that result from the spatial discretization. A detailed discussion of fully and semi-implicit methods will be examined in Chapter 8. This section will focus on the finite difference methods utilized in this thesis for both the nonlinear time dependent viscoelastic flow equations and the temporal linear stability equations for viscoelastic flow.

4.7.1 Nonlinear Time Dependent Problem

After spatial discretization by the finite element method as in Section 4.6, viscoelastic flow equations can be viewed as a system of coupled, nonlinear differential-algebraic equations for the nodal values of velocity, pressure, constitutive variable and interpolated variable:

$$\boldsymbol{M}_2\frac{d^2\boldsymbol{a}}{dt^2} + \boldsymbol{M}_1(\boldsymbol{a})\frac{d\boldsymbol{a}}{dt} + \boldsymbol{R}(\boldsymbol{a}) = \boldsymbol{0}, \tag{4.62}$$

where $\boldsymbol{a} = (\boldsymbol{a}^v, \boldsymbol{a}^p, \boldsymbol{a}^T, \boldsymbol{a}^G)$ and $\boldsymbol{a} \in R^N$, where $N = N_v + N_p + N_T + N_G$. Each N_i is the number of components for that vector unknown. The matrices $\boldsymbol{M}_1(\boldsymbol{a})$ and $\boldsymbol{M}_2$

are mass matrices while $\boldsymbol{R}(\boldsymbol{a})$ is a vector of nonlinear algebraic expressions resulting from the spatial discretization via the finite element method (steady-state residual vector). The matrix $\boldsymbol{M}_2$, which is constant, is non-zero only for the EEME/FEM with inertia ($Re \neq 0$); thus, it will be neglected, for the following discussion. The matrix $\boldsymbol{M}_1$ will not depend on $\boldsymbol{a}$ and is simply a constant for all equations examined in this thesis.

If $\boldsymbol{M}_1$ is singular, then eq. (4.62) is a set of differential-algebraic equations (DAEs) where some variables do not have time derivatives. For viscoelastic flows this is true of the continuity equation, the interpolation equations and the momentum equations, if inertia is neglected as is the case. DAEs necessitate an implicit treatment for the temporal discretization (Brenan *et al.*, 1989 and Northey *et al.*, 1990); thus, the treatment of eq. (4.62) by strictly explicit methods is not feasible as discussed by Ungar *et al.* (1988). Due to this, only fully and semi-implicit algorithms should be investigated for the integration of eq. (4.62). As mentioned before, the semi-implicit methods and their relation to fully implicit methods will be examined in Chapter 8.

The fully implicit time integration method is a robust, but costly, method to integrate the system of equations given by eq. (4.62). Two methods were implemented, the first and second order accurate Adams-Moulton methods (the backwards Euler and the Crank-Nicholson or trapezoid methods). Using the first order Adams-Moulton method to discretize eq. (4.62) yields, at the $(n+1)$th time step, the following system of nonlinear algebraic equations:

$$\boldsymbol{M}_1(\boldsymbol{a}_{n+1}) \left[\frac{\boldsymbol{a}_{n+1} - \boldsymbol{a}_n}{\Delta t} \right] + \boldsymbol{R}(\boldsymbol{a}_{n+1}) = \boldsymbol{0}, \tag{4.63}$$

where Δt is the step size and $\boldsymbol{a}_{n+1} = \boldsymbol{a}(t_{n+1})$ is the solution vector evaluated at the $(n+1)$th time step. The Newton-Raphson method is then used to solve the set of nonlinear algebraic equations. Let a modified residual vector $\hat{\boldsymbol{R}}(\boldsymbol{a}_{n+1})$ be set equal to the left hand side of eq. (4.63). Newton's method is then

$$\hat{\boldsymbol{J}}(\boldsymbol{a}_{n+1}^{m-1})(\boldsymbol{a}_{n+1}^{m} - \boldsymbol{a}_{n+1}^{m-1}) \;=\; -\hat{\boldsymbol{R}}(\boldsymbol{a}_{n+1}^{m-1})$$

$$= \boldsymbol{M}_1(\boldsymbol{a}_{n+1}^{m-1}) \left[\frac{\boldsymbol{a}_{n+1}^{m-1} - \boldsymbol{a}_n}{\Delta t} \right] - \boldsymbol{R}(\boldsymbol{a}_{n+1}^{m-1}), \quad (4.64)$$

where m is the iteration count of the Newton iteration and $\hat{\boldsymbol{J}}$ is the Jacobian of $\hat{\boldsymbol{R}}$ which is

$$\hat{\boldsymbol{J}} = \frac{\boldsymbol{M}}{\Delta t} + \left(\frac{\partial \boldsymbol{M}}{\partial \boldsymbol{a}} \right) \frac{\boldsymbol{a}}{\Delta t} + \boldsymbol{J}(\boldsymbol{a}) \Big|_{\boldsymbol{a}=\boldsymbol{a}_{n+1}}, \quad (4.65)$$

where $\boldsymbol{J}$ is the Jacobian for the steady-state equations. The second term on the right hand side, $(\partial \boldsymbol{M}/\partial \boldsymbol{a})\boldsymbol{a} = \boldsymbol{A}$ with $\{A_{ij}\} = \sum_k (\partial M_{ik}/\partial y_j) y_k$ for $k = 1, N$, is the derivative of the components of the mass matrix with respect to all unknowns multiplied by the unknown vector. Since the mass matrix $\boldsymbol{M}_1$ is constant, this term will always be zero.

The second-order Adams-Moulton method yields the following formula when used to discretize eq. (4.62)

$$\boldsymbol{M}_1(\boldsymbol{a}_{n+1}) \left(\boldsymbol{a}_{n+1} - \boldsymbol{a}_n - \frac{\Delta t_n}{2} \left(\frac{\partial \boldsymbol{a}}{\partial t} \right)_n \right) + \frac{\Delta t_n}{2} \boldsymbol{R}(\boldsymbol{a}_{n+1}) = \boldsymbol{0}, \quad (4.66)$$

where the time derivative term is calculated by

$$\left(\frac{\partial \boldsymbol{a}}{\partial t} \right)_n = \frac{2}{\Delta t_n} (\boldsymbol{a}_n - \boldsymbol{a}_{n-1}) - \left(\frac{\partial \boldsymbol{a}}{\partial t} \right)_{n-1}, \quad (4.67)$$

which is a recursion formula. Both eqs. (4.66) and (4.67) need to be initialized; the initialization steps are performed by using the first order Adams-Moulton method for the first two time steps. The nonlinear algebraic equations resulting from eq. (4.66) are solved via Newton's method as implemented for the first order Adams-Moulton method. At each Newton iteration, a linear system of equations is solved:

$$\begin{aligned} \hat{\boldsymbol{J}}(\boldsymbol{a}_{n+1}^{m-1})(\boldsymbol{a}_{n+1}^{m} - \boldsymbol{a}_{n+1}^{m-1}) &= -\hat{\boldsymbol{R}}(\boldsymbol{a}_{n+1}^{m-1}) \\ &= \boldsymbol{M}_1(\boldsymbol{a}_{n+1}^{m-1}) \left[\boldsymbol{a}_{n+1}^{m-1} - \boldsymbol{a}_n - \frac{\Delta t_n}{2} \left(\frac{\partial \boldsymbol{a}}{\partial t} \right)_n \right] \\ &\quad - \frac{\Delta t_n}{2} \boldsymbol{R}(\boldsymbol{a}_{n+1}^{m-1}), \end{aligned} \quad (4.68)$$

where the Jacobian is given by

$$\hat{\boldsymbol{J}} = \boldsymbol{M} + \left(\frac{\partial \boldsymbol{M}}{\partial \boldsymbol{a}}\right)\boldsymbol{a} + \frac{\Delta t_n}{2}\boldsymbol{J}(\boldsymbol{a})\Big|_{\boldsymbol{a}=\boldsymbol{a}_{n+1}}. \tag{4.69}$$

Again, the second term in $\hat{\boldsymbol{J}}$ is zero. The second-order Adams-Moulton method is usually implemented in a predictor-corrector scheme where the predictor is a second-order Adams-Bashforth (i.e., explicit) method and the corrector is the implicit second-order Adams-Moulton method. The explicit second-order Adams-Bashforth integration method is given by

$$\boldsymbol{a}^P_{n+1} = \boldsymbol{a}_n + \frac{\Delta t_n}{2}\left[\left(2 + \frac{\Delta t_n}{\Delta t_{n-1}}\right)\left(\frac{\partial \boldsymbol{a}}{\partial t}\right)_n - \frac{\Delta t_{n-1}}{\Delta t_{n-2}}\left(\frac{\partial \boldsymbol{a}}{\partial t}\right)_{n-1}\right], \tag{4.70}$$

where the time derivatives are calculated using the recursion formula eq. (4.67). Note that only the differential equations in the DAE set use the predictor equation, as the explicit update of an algebraic equation is the previous value ($\boldsymbol{y}^P_{n+1} = \boldsymbol{y}_n$ if $\boldsymbol{y}$ is the vector consisting of the algebraic variables). The predictor solution is then used as the initial guess for the $(n+1)$th time level in the corrector equation. Hopefully, this will result in an initial guess closer to the exact solution than the last time step would be and reduce the number of iterations required to obtain a converged solution at the new time step.

The predictor-corrector method also is often coupled with a scheme to vary the time step of the method in order to speed up the calculation (Derby, 1986, Gresho *et al.*, 1980 and Mehrabi & Brown, 1995). The strategies for time step variation schemes are based on local error estimation (Gear, 1971). The local truncation error for the second-order method is proportional to the lowest order neglected which is the third order term in the expansion of the time derivative, $\partial^3 \boldsymbol{a}/\partial t^3$ for the second-order Adams-Bashforth Adams-Moulton predictor-corrector method. In order to calculate this term, the second-order forward and backward time series expansions are set equal to one another and solved for the third-order. The local truncation error vector is

found to be

$$\Delta \boldsymbol{a} = \frac{\Delta t_n^3}{12} \frac{\partial^3 \boldsymbol{a}}{\partial t^3} = \frac{\boldsymbol{a}_{n+1} - \boldsymbol{a}_{n+1}^P}{3\left(1 + \frac{\Delta t_{n-1}}{\Delta t_n}\right)}, \tag{4.71}$$

where the predictor value is from eq. (4.70). The L_2-norm of the vector error term $\Delta \boldsymbol{a}$ normalized by the absolute value of the maximum component of $\boldsymbol{a}_i$ and by the total number of unknowns gives the local truncation error

$$\|e_{n+1}\| = \frac{1}{N} \frac{\left(\sum_{i=1}^{N} \Delta a_i^2\right)^{1/2}}{\max_i |a_i|}, \tag{4.72}$$

where N is the total number of unknowns and Δa_i is calculated from eq. (4.71). The next time step is chosen from the proportionality of the achieved error tolerance at step size Δt to the error tolerance set by the user ϵ,

$$\Delta t_{n+1} = \Delta t_n \left(\frac{\epsilon}{\|e_{n+1}\|}\right)^{1/3}. \tag{4.73}$$

This is the same procedure as first introduced by Gear (1971) and implemented by Derby (1986), Gresho *et al.* (1980) and Mehrabi & Brown (1995). The user selected error ϵ tolerance is set differently for each application, but usually is set to 0.001. An increase in ϵ increases the error allowed by the time integration and increases the allowable gap between the predictor and the corrector results; of course, decreasing ϵ results in a decrease in the error, but also increases the computational time. It is important to note that the unknowns considered in this error estimate are only those which are differential equations; the algebraic variables are not controlled. This makes sense in that the algebraic constraints are simply consistency conditions to the differential equations, but it could allow large errors if the variables in the differential and algebraic equations are tightly coupled. In the applications examined in this thesis, the stress variables would control the time step size and the local error in such a scheme.

The algorithm is A-stable for all time steps for a system of linear equations because it is fully implicit in all unknowns (Brenan *et al.*, 1989 and Gear, 1971). The main

drawback to this method is its computational expense due to the evaluation of the large system of algebraic equations at every Newton iteration for each time step (Northey *et al.*, 1990). The use of semi-implicit time integration methods such as the three introduced by Northey *et al.* (1990) and another based on operator splitting (Glowinski & Pironeau, 1992 and Saramito, 1994) will be discussed in Chapter 8 to reduce the computational effort required.

4.7.2 Linear Stability Problem

The linear stability of a set of equations is examined by considering the initial response of a disturbed solution of the steady-state problem (for more information regarding stability see Iooss & Joseph, 1980). The steady-state solution is perturbed by a small disturbance

$$\boldsymbol{a} = \boldsymbol{a}_s + \epsilon \hat{\boldsymbol{a}}(t), \tag{4.74}$$

where $\boldsymbol{a}_s$ is the steady-state solution vector, $\|\hat{\boldsymbol{a}}(0)\| \sim O(1)$ is the perturbation vector and $\epsilon \ll 1$. The set of differential-algebraic equations which describe the nonlinear time dependent viscoelastic flow equations in matrix form are

$$\boldsymbol{M}(\boldsymbol{a})\frac{d\boldsymbol{a}}{dt} + \boldsymbol{R}(\boldsymbol{a}) = \boldsymbol{0}. \tag{4.75}$$

Substitute eq. (4.74) into eq. (4.75) to get

$$\boldsymbol{M}\left(\boldsymbol{a}_s + \epsilon\hat{\boldsymbol{a}}(t)\right)\left[\frac{\partial \boldsymbol{a}_s}{\partial t} + \epsilon\frac{\partial \hat{\boldsymbol{a}}}{\partial t}\right] + \boldsymbol{R}\left(\boldsymbol{a}_s + \epsilon\hat{\boldsymbol{a}}(t)\right) = \boldsymbol{0}. \tag{4.76}$$

Each term is expanded in a Taylor series about the steady-state solution $\boldsymbol{a}_s$,

$$\begin{aligned}\left[\boldsymbol{M}(\boldsymbol{a}_s) + \epsilon\frac{\partial \boldsymbol{M}}{\partial \boldsymbol{a}}\hat{\boldsymbol{a}}(t) + O(\epsilon^2)\right]\left[\frac{\partial \boldsymbol{a}_s}{\partial t} + \epsilon\frac{\partial \hat{\boldsymbol{a}}}{\partial t}\right] \\ + \boldsymbol{R}(\boldsymbol{a}_s) + \epsilon\frac{\partial \boldsymbol{R}}{\partial \boldsymbol{a}}\hat{\boldsymbol{a}}(t) + O(\epsilon^2) = \boldsymbol{0}.\end{aligned} \tag{4.77}$$

Since $\boldsymbol{a}_s$ is the steady-state solution, $\partial \boldsymbol{a}_s/\partial t$ and $\boldsymbol{R}(\boldsymbol{a}_s)$ are zero. The linear stability equations are found by considering the $O(\epsilon)$ problem (all higher order terms are

neglected) which gives the linearized equations

$$\boldsymbol{M}(\boldsymbol{a}_s)\frac{\partial \hat{\boldsymbol{a}}}{\partial t} + \boldsymbol{J}(\boldsymbol{a}_s)\hat{\boldsymbol{a}} = \boldsymbol{0}, \tag{4.78}$$

where the mass matrix $\boldsymbol{M}$ and the steady-state Jacobian matrix $\boldsymbol{J} = \partial \boldsymbol{R}/\partial \boldsymbol{a}$ are evaluated at the steady-state solution $\boldsymbol{a}_s$. This equation determines the perturbation vector growth rate in time and spatial structure and is a constant coefficient, linear differential equation in time for $\hat{\boldsymbol{a}}$. The linear stability (or the $O(\epsilon)$) problem satisfies homogeneous boundary conditions because the steady-state (or $O(1)$) problem satisfies all of the boundary conditions to the problem.

The general solution to the linear stability problem, eq. (4.78), is of the form (Finlayson, 1980)

$$\hat{\boldsymbol{a}}(t) = \sum_{i=1}^{N} \alpha_i \mathrm{e}^{\sigma_i t}\boldsymbol{x}_i, \tag{4.79}$$

where α_i are constant coefficients, $\sigma_i \in \mathcal{C}$ is the ith eigenvalue and $\boldsymbol{x}_i$ is the ith eigenvector of the generalized eigenvalue problem

$$\sigma \boldsymbol{M}(\boldsymbol{a}_s)\boldsymbol{x} = \boldsymbol{J}(\boldsymbol{a}_s)\boldsymbol{x}. \tag{4.80}$$

This generalized eigenvalue problem arises from eq. (4.78). The real part of eigenvalues σ_i determine the stability of the steady-state solution $\boldsymbol{a}_s$ to local disturbances. If all of the eigenvalues have real parts less than zero, then the solution is locally stable. However, if one or more eigenvalues has a real part greater than zero, then the solution is unstable to small amplitude disturbances.

The computation of the eigenvalues of the linear stability problem is not feasible due to the large size of $\boldsymbol{a}$ which generally has $\sim 10^{4-5}$ components. The work required to solve the generalized eigenvalue problem with asymmetric and singular $\boldsymbol{M}$ uses several matrix transformations. Application of the **QZ** algorithm to reduce simultaneously the Jacobian matrix $\boldsymbol{J}$ to upper Hessenberg form and the mass matrix $\boldsymbol{M}$ to triangular form requires $\sim 6N^3$ operations. To calculate the eigenvalues, the number of operations necessary for the **QR** shifts is $\sim 13N^2$. The total operation count (OC)

for a finite element mesh with $N = 10^4$ degrees of freedom would be approximately 10^{13} operations which is clearly ridiculous. Furthermore, this discussion has not included the memory requirements for the storage of the large matrices involved which can make the calculation prohibitive in and of itself (Derby, 1986).

One alternative is to use Arnoldi based methods to determine a fixed number of eigenvalues ($m \ll N$) of eq. (4.80) containing the largest real part. These methods have been developed by Christodoulou & Scriven (1988) and Goldhirsch *et al.* (1987); recently, Sureshkumar & Beris (1995) have implemented the Arnoldi method for the linear stability analysis of viscoelastic Poiseuille flow with both inertia and viscoelasticity present ($Re, De \neq 0$).

Another alternative approach was proposed by Ghaddar *et al.* (1986) in which the linearized Navier-Stokes equations were integrated numerically for the disturbance to determine the stability of the flow of a Newtonian fluid through grooved channels. Examination of eq. (4.79) shows that at long times the most unstable eigenvector dominates the solution of the perturbation, as the other eigenvectors have decayed/grown exponentially faster/slower. Thus, the growth rate and the oscillation frequency of the perturbation at long times is the real and imaginary parts, respectively, of the eigenvalue with the largest real part. This growth rate and oscillation can be determined from the monitoring of the norm of the disturbance vector $\|\hat{\boldsymbol{a}}\|$ with time. This method was implemented by Northey *et al.* (1991) to compute the onset of an oscillatory instability in the Taylor-Couette flow of a UCM fluid and will be used here.

In order for the time dependent results to be definitive a stable time integration scheme must be used. Furthermore, since the linear stability problem being studied is a set of DAEs, the method must be A-stable (Brenan *et al.*, 1989) which is true for both of the finite difference methods introduced in the previous section. The first-order Adams-Moulton discretization of eq. (4.78) yields

$$\boldsymbol{M}(\boldsymbol{a}_s)\left[\frac{\hat{\boldsymbol{a}}_{n+1} - \hat{\boldsymbol{a}}_n}{\Delta t}\right] + \boldsymbol{J}(\boldsymbol{a}_s)\hat{\boldsymbol{a}}_{n+1} = \boldsymbol{0}. \tag{4.81}$$

The second-order Adams-Moulton discretization gives

$$\boldsymbol{M}(\boldsymbol{a}_s)\left(\hat{\boldsymbol{a}}_{n+1}-\hat{\boldsymbol{a}}_n-\frac{\Delta t}{2}\left(\frac{\partial \hat{\boldsymbol{a}}}{\partial t}\right)_n\right)+\frac{\Delta t}{2}\boldsymbol{J}(\boldsymbol{a}_s)\hat{\boldsymbol{a}}_{n+1}=\boldsymbol{0}, \tag{4.82}$$

where neither a predictor nor step-size control will be used since this is a linear problem. The time derivative term is calculated as before using eq. (4.67). Both of these methods can be reduced to solving

$$\left[\boldsymbol{M}(\boldsymbol{a}_s)+\frac{\Delta t}{c}\boldsymbol{J}(\boldsymbol{a}_s)\right]\hat{\boldsymbol{a}}_{n+1}=\boldsymbol{M}(\boldsymbol{a}_s)\left(\hat{\boldsymbol{a}}_n+b\frac{\Delta t}{2}\left(\frac{\partial \hat{\boldsymbol{a}}}{\partial t}\right)_n\right), \tag{4.83}$$

where $b=0$ and $c=1$ if the method is first order and $b=1$ and $c=2$ if the method is second order. This can be solved by performing one initial LU decomposition, storing it and using forward-backward substitution to march in time. The operation count (OC) for the LU decomposition of a sparse, banded matrix with bandwidth BW is $O\left(N(BW)^2\right)$. This is compared to the operation count for forward-backward substitution which is $O\left(N(BW)\right)$. There is a significant reduction in the amount of work performed at each time step in the linear stability analysis compared to the integration of the full nonlinear time dependent problem.

4.8 Local Mesh Refinement

If the solution field contains regions where the gradients in the unknowns are large, e.g., for stresses near solid boundaries, it is necessary to use very small element sizes to capture the nature of the solution, but if other regions in the domain are smooth, then fewer elements of larger size are needed there to obtain the same accuracy as in the sharp gradient region. One advantage of the finite element method is the ability to use elements of varying sizes; however, it can be a very difficult task to construct a mesh with a wide variety of element sizes while keeping it regular (i.e., the number of rows and columns of elements are kept constant throughout the domain). Moreover, keeping the mesh regular can also lead to regions where the discretization is overrefined and is wasting computational resources (see Figure 4-1). For this reason it

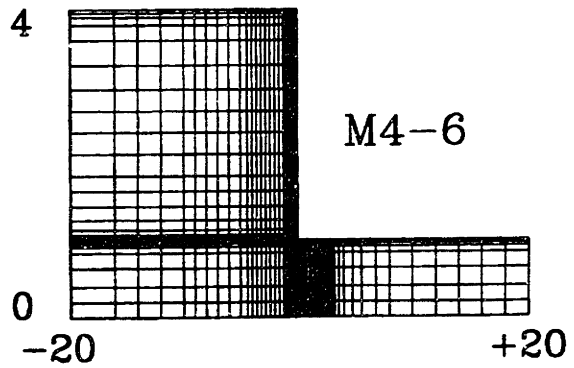

Figure 4-1: An example of a regular mesh with mesh refinement near the corner of the abrupt contraction. The refinement upstream of the corner into the bulk flow and the refinement near the centerline at the entrance of the contraction are examples of overrefined regions.

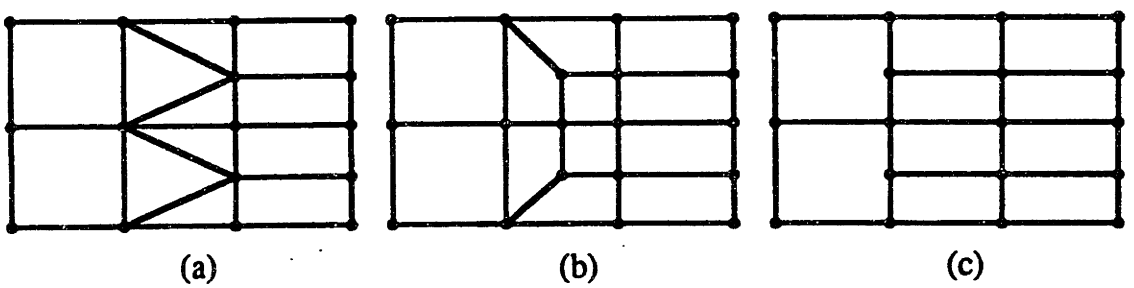

Figure 4-2: Transition from coarse to refined grids of quadrilaterals (Tsiveriotis & Brown, 1993); (a) transition layer using triangles, (b) transition layer using quadrilaterals only, (c) direct transition.

is important to devise methods of local mesh refinement which increases the number of elements only where needed and gives a transition from a small number of elements where the solution field is smooth to a large number of elements where there is a sharp gradient in the solution.

For quadrilateral elements in the finite element method, several local adaptive grid refinement methods have been proposed which take into account the continuity and accuracy required; three examples of such one-two element refinement are shown in Figure 4-2 (Chinnaswamy *et al.*, 1991, Gupta, 1978, Young *et al.*, 1991, Perry *et al.*, 1990 and Tsiveriotis & Brown, 1993). Continuity for conforming finite elements require elements to share a side with only one other element (Becker *et al.*, 1981); thus, only the transitions in Figure 4-2(a) and 4-2(b) (Chinnaswamy *et al.*, 1991)

are allowed for standard conforming finite elements. These two refinement schemes require special transition layers to be located between coarse and fine refinement. In Figure 4-2(a), the intermediate zone is made up of triangular elements which necessitates the use of basis functions defined for triangular elements to be added to the original quadrilateral basis function elements. The transition layer in Figure 4-2(b) avoids the introduction of new element types, but it still requires care in the construction of the intermediate zone for arbitrarily oriented elements.

The transition in Figure 4-2(c) eliminates the usage of a special intermediate zone altogether; however, it clearly violates the requirement of conforming elements to have only one neighbor per side. The easiest solution is simply to use non-conforming elements in the discretization; wherein, approximations are allowed with simple discontinuities of derivatives of order $(m-1)$ or lower for PDEs of order $2m$ (Carey & Oden, 1983). The cost of using non-conforming finite elements is that the method will be convergent only under special conditions such as when the *patch test* is satisfied (Carey & Oden, 1983); this has not been attempted on the direct transition elements of Figure 4-2(c) (Tsiveriotis & Brown, 1993). It also is possible to account for the lack of continuity in the basis functions through the application of the hybrid finite element method, but the additional programming necessary was deemed too costly to introduce into normal Lagrangian finite element codes (Tsiveriotis & Brown, 1993).

Another approach used to eliminate the problem without the loss of conforming elements was initially treated independently in solid mechanics by Gupta (1978) and in computational fluid dynamics by Young *et al.* (1991) and was extended to free surfaces by Tsiveriotis & Brown (1993). Georgiou and Crochet (1993) have developed a similar local mesh refinement method for patching the 2x2 and 4x4 bilinear stress elements used in the MIX1 and MIX4 formulations for viscoelastic calculations. The local mesh refinement introduces pseudo-nodes that are associated with finite element approximations in one element, but not in the adjacent, larger element; for example, the node G in Figure 4-3 is a vertex node in elements 2 and 3, but not 1. The values of the unknowns at pseudo-nodes are determined by interpolation between the solution values at the adjacent nodes on the boundary in the larger element; for

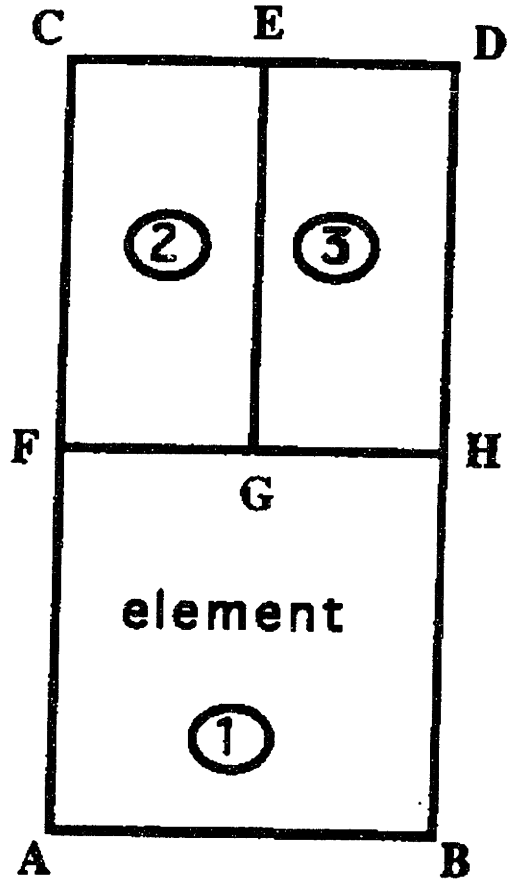

Figure 4-3: Schematic of one-to-two element splitting used in the local mesh refinement scheme of Tsiveriotis & Brown (1993).

example in Figure 4-3, the value at node G is determined by interpolation between the values at nodes F and H. The order of the interpolation depends on the degree of the Lagrangian basis functions and must be equivalent to ensure continuity across the transition. As a result, the finite element approximation to the variable is continuous across the element boundary, and the requirement for conforming finite elements, that the basis function is continuous along the edges, is satisfied without resorting to the specialized finite element methods such as non-conforming or hybrid finite elements mentioned previously.

Let $\{n_1^i, n_2^i, n_3^i\}$, $i = 1, \ldots, m$ be the nodes of the elements e_1, e_2 and e_3 along the boundaries FH, FG and GH, respectively, in Figure 4-3. Then $\{n_1^i\}$ are the regular nodes and $\{n_2^i, n_3^i\}$ are the pseudo-nodes on the transition boundary FH. Finally, let $\{\psi_j^n\}$ be the elemental basis function corresponding to node n and defined over element e_j. Since each basis function has local support, i.e., ψ_j^n is nonzero at node n and is zero at all other nodes of the elements e_j.

The elemental basis functions $\{\psi_1^{n_1^i}\}$ defined for the coarse element, e_1, cannot be extended from the regular nodes to the pseudo-nodes and their respective elemental basis functions $\{\psi_2^{n_2^i}\}$ and $\{\psi_3^{n_3^i}\}$. The discontinuity arising from this failure results in two problems: (i) the continuity of the solution is not guaranteed for an arbitrary set of nodal values of the unknowns and (ii) global basis functions Ψ cannot be formed at the transition boundaries by patching elemental basis functions together that have the continuity necessary for second-order elliptic problems, i.e.,

$$\Psi(\boldsymbol{x}) \in \mathcal{H}^1(\Omega) = \left\{ \Psi, \int_\Omega \left[\Psi^2 + |\nabla \Psi|^2 \right] d\Omega < \infty \right\}. \tag{4.84}$$

Continuity of the solution across the transition can be enforced at the boundary through the use of essential conditions for the values of the unknowns at the pseudo-nodes,

$$u_{n_2^i} = \sum_{j=1}^{m} w_{n_1^j}^{n_2^i} u_{n_1^j}, \qquad i = 1, \ldots, m, \tag{4.85}$$

$$u_{n_3^i} = \sum_{j=1}^{m} w_{n_1^j}^{n_3^i} u_{n_1^j}, \qquad i = 1, \ldots, m, \tag{4.86}$$

where u_n is the value of the unknown u at the node n and the weightings w_n^l are given by the shape function values at pseudo-nodes l corresponding to the regular nodes n or

$$w_{n_1^j}^{n_2^i} = \psi_1^{n_1^j}(n_2^i), \qquad i = 1, \ldots, m, \qquad j = 1, \ldots, m, \tag{4.87}$$

$$w_{n_1^j}^{n_3^i} = \psi_1^{n_1^j}(n_3^i), \qquad i = 1, \ldots, m, \qquad j = 1, \ldots, m. \tag{4.88}$$

The essential conditions, eqs. (4.85) and (4.86), remove the pseudo-nodes from the transition boundary FH so that only the regular nodes remain. This is similar to removal of nodes from the finite element formulation corresponding to essential boundary conditions. However, in this case the regular nodes still need to be introduced to the formulation through the definition of new global basis functions $\{\Psi_{n_1^i}\} \subset H^1(\Omega)$ on the regular nodes $\{n_1^i\}$. This contribution is found by patching the elemental basis functions for the regular nodes on the transition boundary to a weighted combination of the elemental basis functions for the pseudo-nodes where the weighting coefficients are the same as in eqs. (4.87) and (4.88). An example of this is shown in Tsiveriotis & Brown (1993).

This formulation can be implemented inside existing Lagrangian finite element codes with only a minimal amount of changes. In fact, the formation of *elemental* stiffness matrices and residuals is not affected at all! There are only two changes in a code, both of which are applied at the loading of the elemental data into the *global* stiffness matrix and residuals. At each pseudo-node n: (i) the residuals and stiffness entries corresponding to the pseudo-node n are replaced by the constraints eqs. (4.85) and (4.86) and (ii) the elemental data for the pseudo-node is weighted and loaded into the global entries for the regular nodes along the transition boundary. This approach is general and has been implemented for both bilinear and biquadratic Lagrangian finite element basis functions.

This mesh refinement strategy can be implemented successively to refine the mesh

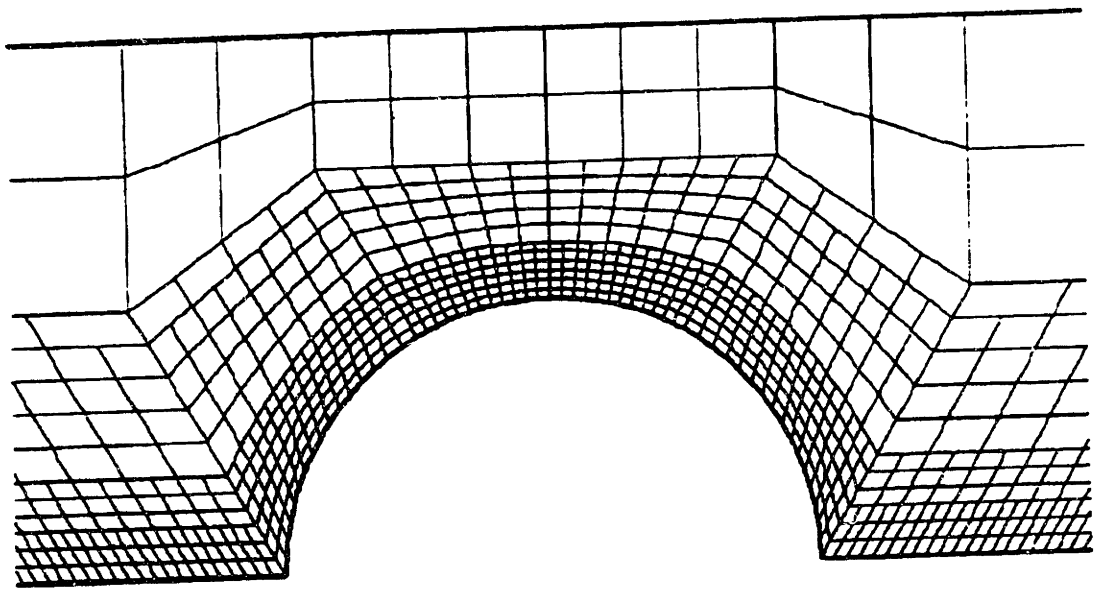

Figure 4-4: Example of local mesh refinement along a solid boundary.

to an arbitrary degree; two, three and four levels of refinement are shown in various regions of the mesh in Figure 4-4. In the implemented code, arbitrary splitting of elements is not allowed, as this could lead to more than one pseudo-node per element; an automatic test has been implemented that simply requires that all nodes are regular along the two sides of the element involved in the splitting[1].

4.9 Bandwidth Minimization

The finite element method requires the solution of a matrix problem that contains sparse and banded matrices. As noted above at the end of section 4.7, the operation count for the LU decomposition and forward-backward substitution for such matrices are $O\left(N(BW)^2\right)$ and $O\left(N(BW)\right)$, respectively, where N is the number of degrees of freedom and BW is the bandwidth of the matrix. In order to reduce the amount of CPU time to solve systems of equations for very large N, the BW needs to be reduced which led to the study of what governs the size of the bandwidth for a specific problem.

[1]There is no reason why these additional splittings are not allowed in theory; it was decided that the complex data structures required to implement such refinement was not worth the possible gain in accuracy.

It was found that the ordering of the nodes in the finite element mesh could increase or decrease the size of the bandwidth dramatically. For the frontal solution method, it is the element numbering not the node numbering that is important, but the same principles are involved. Efficient numbering of the equations and unknowns is crucial to cost-effective, efficient solution of the algebraic equations at each Newton iteration; this becomes even more important when time dependent equations are used, since LU decompositions are performed at each time step.

In order to examine several different schemes available in the literature, some definitions of the basic concepts need to be discussed, since this area is probably unfamiliar to the reader. Let $\boldsymbol{A}$ be a symmetric square matrix of order N. The row bandwidth b_i is defined as the the number of columns from the first non-zero entry in the row to the diagonal which is the difference between the row i and the column index of the first non-zero entry in row i plus one. The matrix bandwidth is then

$$BW = \max_{i \leq N} b_i. \tag{4.89}$$

The matrix profile is the sum of the row bandwidths

$$P = \sum_{i=1}^{N} b_i. \tag{4.90}$$

Let c_i be the number of active columns in row i where a column j is active for the row i if $j \geq i$ and a non-zero entry exists in that column in any row with index $k \leq i$. This leads to the concepts of the maximum, average and root-mean-square matrix wavefronts W

$$W_{max} = \max_{i \leq N} c_i, \tag{4.91}$$

$$W_{ave} = \frac{1}{N} \sum_{i=1}^{N} c_i = \frac{P}{N}, \tag{4.92}$$

$$W_{rms} = \left(\frac{1}{N} \sum_{i=1}^{N} c_i^2 \right)^{1/2}, \tag{4.93}$$

$$\begin{bmatrix} X & & X & & & X \\ & X & & X & X & \\ X & & X & & X & X \\ & X & & X & & \\ & X & X & & X & \\ X & & X & & & X \end{bmatrix}$$

Figure 4-5: An example 6x6 matrix to illustrate the definitions of matrix bandwidth, profile and wavefront (Everstine, 1976). An X indicates a non-zero entry.

i	b_i	c_i	c_i^2
1	1	3	9
2	1	5	25
3	3	4	16
4	3	3	9
5	4	2	4
6	6	1	1
$\sum_i$	18	18	64

Table 4.1: The matrix bandwidths, profiles and wavefronts for the 6x6 example matrix

where for a symmetric metric $P = \sum_{i=1}^{N} b_i = \sum_{i=1}^{N} c_i$.

To clarify the definitions, a simple example is given for a 6x6 matrix as shown in Figure 4.9 (Everstine, 1979). From this matrix, the row bandwidths, profiles and wavefronts are given in Table 4.1. The matrix bandwidth, profile and wavefronts for this matrix are $B = 6$, $P = 18$, $W_{max} = 5$, $W_{ave} = 3.0$, and $W_{rms} = 3.3$.

There have been many different algorithms proposed to reduce the bandwidths, profiles and wavefronts of matrices (see Everstine, 1979, Gibbs *et al.*, 1976a, 1976b, Lewis, 1982 and Scott & Han, 1994 and references therein). The earliest algorithms simply used symmetric row and column interchanges to reduce the bandwidth; needless to say, this is far from an optimal process. The next set of algorithms use graph theory to create level sets for use in the renumbering process. The first fairly successful applications included the Cuthill-McKee, reverse Cuthill-McKee and King algorithms. The second and third initially seemed to work the best with the second being faster (Gibbs *et al.*, 1976b). The Gibbs-Poole-Stockmeyer (Crane *et al.*, 1976

and Gibbs *et al.*, 1976a, 1976b) and Gibbs-King (Gibbs, 1976) were introduced at roughly the same time; they both performed better on sample problems than the reverse Cuthill-McKee and King algorithms (Gibbs *et al.*, 1976b and Everstine, 1979). The GPS algorithm was shown to outperform the GK algorithm in terms of computational time in a series of test problems by Everstine (1979); this set of problems has become the standard on which all new algorithms are benchmarked. Lewis (1982a, 1982b) introduced new, quicker versions of both the GPS and GK algorithms; the increased efficiency of the GK method makes it very competitive with the GPS method. These latter two methods were used in this thesis to reduce the bandwidth. Generally, only the GPS algorithm is used; however, it is possible to use the GPS results to initialize the GK algorithm if the results are not satisfactory. Little difference has been found between the two algorithms in our experiences. The actual code was obtained through the Association for Computing Machinery (ACM) distribution services as algorithm 582 (Lewis, 1982b).

Since the implementation of this algorithm in our code, several other bandwidth, profile and/or wavefront minimizers have been found in the literature and may be worthwhile comparing to the current algorithm especially for time dependent computations where a small decrease in the operation count for the LU decomposition can significantly reduce the total CPU time. The first is an optimization of the graph theory methods by Sloan (1986). It is indicated that on average the reduction in computational time is 40% when compared to Lewis' implementation of the GPS/GK algorithm while still obtaining equivalent or better results on the standard test problems of Everstine (1979). A second method by Scott & Han (1994) is a hybrid algorithm between the graph theory-based algorithms and the direct reduction algorithms (movement of columns and rows). The graph theory part of the algorithm was modified through a different starting procedure and compares favorably with the GPS algorithm and uses less computational time, but the timings were not compared to either Lewis' or Sloan's algorithm. The hybridization with the direct reduction included performs even better on the Everstine problems. The penalty paid for the decrease in the BW is an increase in computational time. The final new method also

starts with the graph theory methodology, but uses a divide-and-conquer approach that defines a series of graph partitioning subproblems that are solved by heuristic algorithms (Souza *et al.*, 1994). The different heuristic methods attempt to 'jiggle' the result from graph theory out of local minima so that it has a better opportunity to find the global minimum. The three heuristics studied were the Kernighan-Li deterministic technique, the non-deterministic Simulated Annealing and Stochastic Evolution algorithms. The previous graph theory methods are so-called 'greedy' strategies which are based on the picking of the next element in the ordering to produce the smallest increase in the current frontwidth. In order to come up with the best ordering several different starting nodes are input to the algorithm with the smallest result being picked. The divide-and-conquer methodology (Souza *et al.*, 1994) overcomes this shortfall by solving equipartition sub-problems which are based on a more global view of the graph than the 'greedy' algorithms. These subproblems are then solved by neighborhood search techniques (the heuristics). The Stochastic Evolution heuristic is the best method found by Souza *et al.* (1994). However, the benchmark Everstine test problems were not examined so that the performance against a wide variety of problems was not discussed; the only comparison made was to the reverse Cuthill-McKee algorithm not the Lewis implementation of GPS which is known to be both faster and lead to a smaller bandwidth. A comparison of the three new methods to the implemented Lewis algorithm may help further optimize the time dependent code.

Chapter 5

Temporal Linear Stability of Numerical Algorithms

"If you are sure you understand everything that is going on, you are hopelessly confused."

– Walter Mondale

The stability of inertialess planar Couette flow of an UCM fluid was chosen as a model problem to examine the temporal stability of the numerical method. The numerical stability to two-dimensional disturbances is tested by the calculation of the stability of inertialess, planar Couette flow of an UCM fluid generated by parallel moving and stationary solid surfaces. This problem is particularly well suited as a test problem for transient calculations because the eigenstructure of the linear stability problem is known in closed form (Gorodtsov and Leonov, 1967; Renardy and Renardy, 1986) and because the homogeneous base flow is represented exactly in the finite element approximations used in the mixed methods described in Chapter 4; hence all difficulties with spatial resolution can be attributed to the approximation of the linearized disturbances as long as the time integration method is known to be numerically stable. Moreover, in the absence of inertia, this flow is stable to two-dimensional disturbances for any De, although the most dangerous disturbance does

approach neutral stability with increasing De; the exponential decay rate for the most dangerous eigenvalues is $-1/(2De)$. This feature and the spatial complexity of the eigenfunctions make this linear stability calculation a difficult test for transient simulations.

Recently, Keiller (1992) has used the same linear stability problem as a test of the numerical stability of finite difference methods for the UCM, Oldroyd-B, and a FENE constitutive equation. He came to the conclusion that the critical value of De for the onset of numerical instability for the calculations was a function of the product of the spatial discretization in the streamwise and cross-stream directions. Keiller (1992) also implied that the calculations were stabilized by adding either a Newtonian solvent (the Oldroyd-B model) or by adding artificial diffusion to the discretization of the constitutive equation. Our calculations using the streamline upwind method seem to confirm this latter point. The mesh dependence described by Keiller (1992) is seen in calculations using the EVSS/FEM; however, it is not present in calculations with either the EVSS-G/FEM and DEVSS-G/FEM formulations described here.

Both the EEME/FEM and EVSS/FEM methods predict fictitious numerical instabilities for the Couette linear stability problem with the UCM model for high values of De. The instability is relatively independent of the numerical method used for solving the hyperbolic constitutive equation. This is consistent with the mechanism for the instability being driven by the singular structure of the constitutive equation near solid boundaries, because all the methods used for solving the constitutive equation essentially reduce to the Galerkin method in this limit. The eigenfunctions for the most dangerous disturbances are localized near the stationary surface, either a solid surface or at a plane in the flow, depending on the relative motion of the two planes. A modification to the EEME/FEM, EEME-P/FEM, was introduced in Brown *et al.* (1993) that moves the numerical instability to higher values of De. The EEME-P/FEM differs from the EEME formulation only in an ad-hoc change in the treatment of the pressure field in the momentum equation. The improved temporal stability of this formulation suggests that the numerical instability seen in the calculations with the EEME/FEM and EVSS/FEM is a result of an incompatibility in the

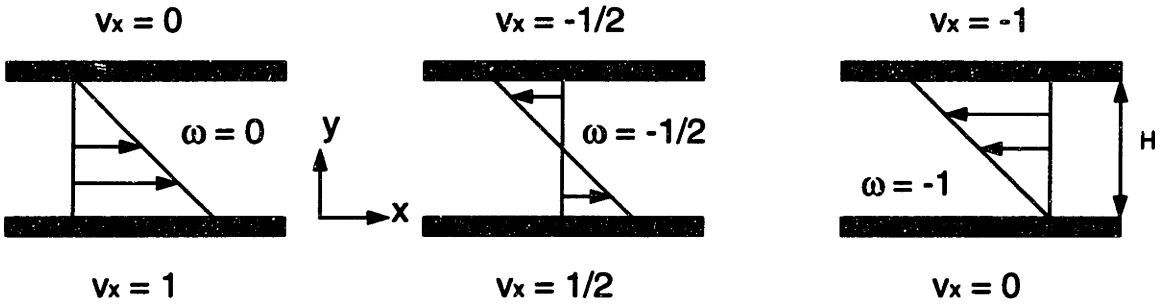

Figure 5-1: Schematic of planar Couette flow geometry showing the parameter ω for varying the motions of the surfaces.

finite element approximations. We argue that the compatibility of the stress and velocity gradient approximations is an issue, especially near stationary streamlines, such as exist along nonmoving solid boundaries, where the constitutive equation reduces to an algebraic relationship between these two variables.

Two new sets of mixed finite element approximations for the velocity, velocity gradient, deviatoric stress and pressure which appear to be compatible in this limit are introduced; the EVSS formulation that uses these approximations is denoted the EVSS-G method. The second method is denoted the DEVSS-G method; reasons for its formulation are discussed in both Chapter 4 and Chapter 8. This mixed set of finite element approximations is tested with the Galerkin method for the momentum/continuity equation pair and several discretizations for the hyperbolic constitutive equation; these are the streamline upwind (SU), the streamline upwind Petrov-Galerkin (SUPG), and the Galerkin least squares (GLS) techniques. The EVSS-G/FEM and DEVSS-G/FEM with the SUPG and SU discretizations are found to be numerically stable for planar Couette flow up to very high values of *De*.

5.1 Model Problem - Planar Couette Flow

The numerical stability characteristics of the finite element methods described above were tested by calculation of the linear stability of planar Couette flow, as shown in Figure 5-1. Here the steady-state flow is rectilinear with a constant velocity gradient and constant stresses. Using the velocity of the solid surface V as the velocity scale

and the gap between the planes H as the length scale gives the viscometric base flow for the UCM model as

$$v_x = 1 - y + \omega, \tag{5.1}$$

$$v_y = 0, \tag{5.2}$$

$$\tau_{xx} = -2De, \tag{5.3}$$

$$\tau_{yy} = 0, \tag{5.4}$$

$$\tau_{yx} = 1, \tag{5.5}$$

$$p = 0, \tag{5.6}$$

where ω is a parameter that fixes the relative velocities of the two solid surfaces (see Figure 5-1). The Deborah number is defined as $De \equiv \lambda V/H$. For $\omega = 0$, the lower plate is in motion at unit speed and the upper plate is stationary; the calculations of Keiller (1992) used $\omega = -1/2$.

The linear stability analysis of the inertialess flow was presented by Gorodtsov and Leonov (1967), who showed the presence of both discrete and continuous contributions to the eigenspectrum using a standard, normal-mode analysis. For infinitesimal amplitude, two-dimensional disturbances with spatial structure given as $g(y)exp(ikx+\sigma t)$, where $\sigma \in \mathcal{C}$, they showed that the continuous spectrum is composed of eigenvalues (σ_{cont})

$$Re(\sigma_{cont}) = -1/De, \tag{5.7}$$

$$|Im(\sigma_{cont})| \leq k, \tag{5.8}$$

where k is the spatial wavenumber in the flow direction. Since eq. (5.7) is always less than zero, the eigenfunction associated with the continuous contribution of the spectrum will decay in time. However, as $De \rightarrow \infty$ the real part does asymptote to zero or neutral stability; this could lead to fictitious instabilities due to numerical approximation errors for $De \gg 1$. The oscillatory component of the continuous spectrum, given by eq. (5.8), contains higher frequency components as the wavenumber

increases.

In addition to the continuous spectrum, a discrete spectrum that has eigenvalues occurring in pairs for each wavenumber k was found by Gorodtsov and Leonov (1967) and have been labelled Gorodtsov-Leonov pairs. The discrete eigenvalues, σ_{disc}, are found according to the formula:

$$\sigma_{disc} = -ik\left[\frac{1}{2} + iA \pm \sqrt{\frac{1}{4} - A^2 + B}\right], \tag{5.9}$$

where

$$A = \frac{kDe\sinh(k)\sinh(kCDe) - k^2CDe\sin(kDe)}{2k^2CDe[\cosh(k)\cosh(kCDe) - \cos(kDe) - CDe\sinh(k)\sinh(kCDe)]}, \tag{5.10}$$

$$B = \frac{kCDe\sinh(k)\cosh(kCDe) + k^2CDe\cos(kDe) - [k\cosh(k) + \sinh(k)]\sinh(kCDe)}{2k^2CDe[\cosh(k)\cosh(kCDe) - \cos(kDe) - CDe\sinh(k)\sinh(kCDe)]}, \tag{5.11}$$

$$C = \sqrt{1 + \frac{1}{De^2}}. \tag{5.12}$$

Most importantly, for $De \gg 1$, the real parts of the discrete eigenvalues approach $-1/(2De)$ and the imaginary parts approach 0 and k. Thus, as De is increased, members of both the discrete and continuous spectrum move closer to neutral stability, i.e., $Re(\sigma)$ approaches zero; hence, calculations with high De are expected to be more susceptible to numerical instability if the spatial structure of the associated eigenfunctions is not adequately resolved. This difficulty with numerical approximations has plagued attempts at the numerical solution of the eigenvalue problem with inertia (Lee and Finlayson, 1986; Renardy and Renardy, 1986).

The eigenfunctions corresponding to the discrete spectrum are most dangerous because $Re(\sigma_{disc}) > Re(\sigma_{cont})$. The difficulty with adequate spatial resolution of these functions is most clear from the form of the cross-stream component of the velocity (v_y) associated with each member of the discrete spectrum (Gorodtsov and Leonov, 1967):

$$v_y(x, y, t) = V_k(y)e^{ik(x-\sigma t)} \tag{5.13}$$

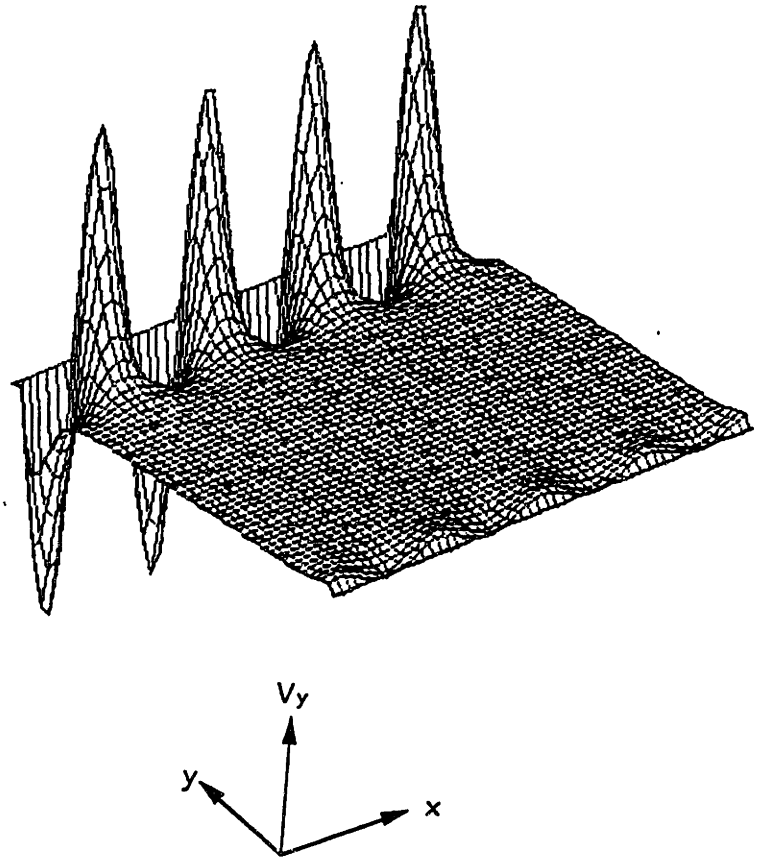

Figure 5-2: Contour plot of the eigenfunction for $k = 4$, $t = 0.1$, $De = 1.0$ and $\omega = 0$ calculated from the results of Gorodtsov and Leonov (1967). The cellular structure of the disturbance is concentrated near the stationary boundary at $y = 1$.

where

$$V_k(y) = c_{1k}(y-\sigma)e^{ky} + c_{2k}(y-\sigma)e^{-ky} + c_{3k}e^{-kDey(i-c_0)} + c_{4k}e^{-kDey(c_0+i)} \qquad (5.14)$$

for $\omega = 0$, and $\{c_0, c_{jk}\}$, $j = 1, \ldots, 4$ are constants computed from the boundary conditions and $c_0 \equiv \sqrt{1+De^{-2}}$. For $k \gg 1$ or $De \gg 1$, the disturbance contains roll cells both in the cross-stream and the streamwise flow directions. Fine scale structure is expected in the velocity field across the gap because of the terms proportional to e^{-ikDey} for $k \gg 1$. Moreover, the terms proportional to e^{-ky} and e^{ky} result in boundary layers near both the moving ($y = 0$) and the stationary ($y = 1$) boundaries for $k \gg 1$. The structure of $V_4(y)$ is shown as a three-dimensional surface in Figure 5-2 for $De = 1.0$, $t = 0.1$ and $\omega = 0$. The disturbance is concentrated near the

stationary boundary and the cellular structure along this boundary is obvious. It is interesting that this eigenfunction is trivial to compute only for low values of De, because round-off error becomes a factor for increasing values of De and k.

The form of eq. (5.13) and the asymptotic behavior of the eigenvalue suggests that numerical approximations of the linear dynamics for the UCM flow will be extremely difficult for high De and k. The value of the wavenumber inherent to the finite element analysis of the calculations is set by the number of elements used in the streamwise direction ($k \sim 2\pi/h_x$); the larger the number of elements in this direction, the better the resolution of the spatial structure of the eigenfunction and the more complex the spatial structure of the eigenfunction that can be resolved. Moreover, the temporal response also becomes more complex, because the frequency of the slowly decaying oscillation approaches k.

Computations of the linear stability of the planar Couette flow are carried out by solving the finite element equations numerically linearized about the base flow, eqs. (5.1) - (5.6). The disturbances are assumed to vanish on the solid surfaces and to be periodic in the streamwise- or x-direction; the dimensionless streamwise dimension of the computational domain is set to 1, i.e., the same as the gap width, so that the smallest value k that appears in the domain is $\pi/2$. Results are shown both as contours of the solution components as a function of time and as the evolution of the magnitude of the solution $\boldsymbol{x}(t)$ of the linearized equations, defined as

$$L_2(t) \equiv \|\boldsymbol{x}(t)\|_0 = \left(\sum_{i=1}^{N} x_i^2(t) \right)^{1/2}, \tag{5.15}$$

where $\{x_i(t)\}$ are the components of the solution vector. Transient simulations are started from random initial conditions for the stress and zero initial values for velocity and pressure. The most dangerous eigenfunction, i.e., the one with eigenvalue with largest real part, will dominate the numerical solution as the solution evolves in time. The real and imaginary parts of the corresponding eigenvalue are estimated from the long time behavior of eq. (5.15); this procedure was used by Northey et al. (1991) to compute the onset of oscillatory instability in Taylor-Couette flow of an UCM fluid.

The linear stability of planar Couette flow is a good problem to analyze the linear temporal stability properties of the numerical method being used to solve the problem. The solution is known in closed-form and is stable for all De so that if the numerical linear stability analysis gives an unstable solution, then the method is unstable. To ensure that it is the spatial discretization scheme, not the time discretization scheme causing the instability, the time integration methods used are fully implicit, either the backward Euler method, eq. (4.63), or the Crank-Nicholson method, eq. (4.66). The problem is not trivial to solve in that as $De \rightarrow \infty$ the most dangerous eigenvalue approaches neutral stability; errors in the numerical solution could lead to an exponentially growing disturbance. Finally, the eigenfunction contains large oscillations near the non-moving wall (Brown *et al.*, 1993); again, allowing for numerical errors to affect the solution.

5.2 Numerical Linear Instability of the EEME/GAL and EEME/SUPG Methods

Calculations for the UCM model were carried out using the EEME/FEM with the SUPG method used to discretize the constitutive equations. This is referred to as EEME/SUPG/FEM and was described in Section 4.6.1. Different finite element meshes and values of De were used also. Unless stated otherwise, the meshes were all square with N_{el}xN_{el} elements in each direction. The evolution of the amplitude of the disturbance is shown in Figure 5-3 as a function of Deborah number for $1 \leq De \leq 5$, $N_{el} = 14$, $\omega = 0$ and $\Delta t = 0.1$. The results for $De = 1.0$ and $De = 3.0$ show the exponential decay expected for the linear stable flow; moreover, the slopes of the curves agree approximately with the result of Gorodtsov and Leonov (1967) for the real part of the slowest decaying eigenvalue, $-1/(2De)$. The initial growth of the perturbation before the eventual decay (see Figure 5-3 for $De = 3$) is due to the non-normality of the linear operator which allows the growth of initial perturbations when all eigenmodes eventually decay exponentially (Reddy & Henningson, 1993, Reddy

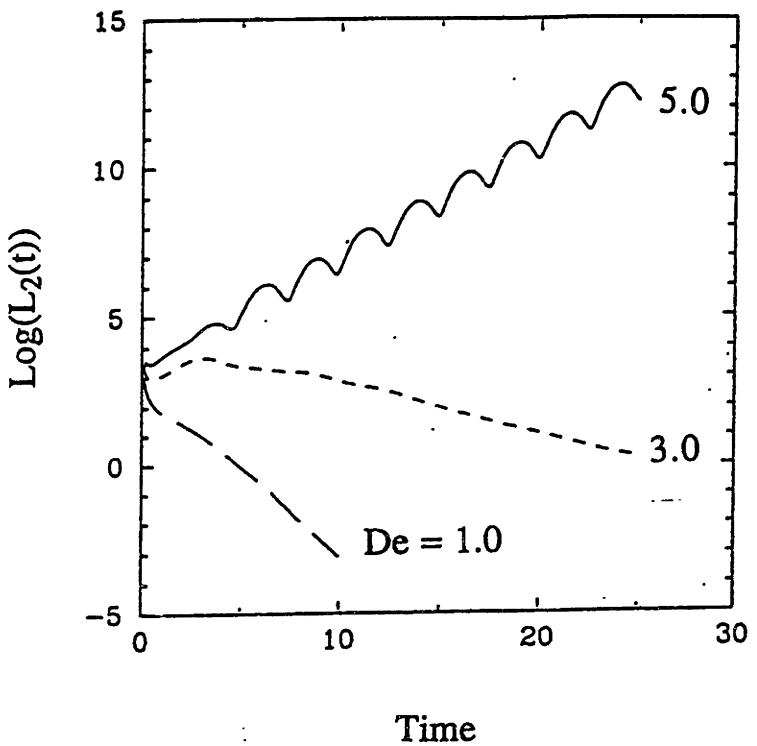

Figure 5-3: Transient response computed with the EEME/SUPG/FEM of the amplitude $L_2(t)$ defined by eq. (5.15) as a function of De for the mesh $N_{el} = 14$ and $\Delta t = 0.1$. Calculations are for the UCM model.

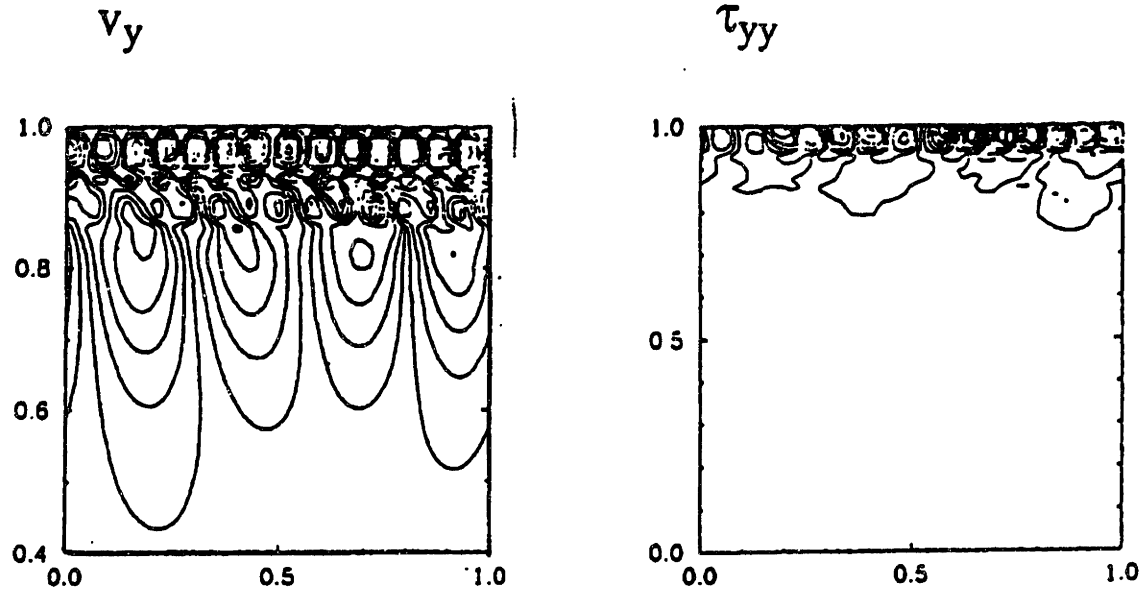

Figure 5-4: Contours of $v_y(x,y,t)$ and $\tau_{yy}(x,y,t)$ at $t = 10.0$ for $De = 1.0$ computed with EEME/SUPG/FEM with $N_{el} = 14$ and $\Delta t = 0.1$. This eigenfunction is stable in time, as indicated in Figure 5-3.

et al., 1992, Reddy & Trefethen, 1994 and Trefethen *et al.,* 1993). The predictions of an eigenvalue analysis can predict only the long-term behavior; it cannot be used to examine the initial transient. It was shown by Reddy and coworkers that there is no transient growth if and only if the numerical range of the linear operator lies in the lower half-plane which is equivalent to the conditions given by energy methods (Reddy *et al.,* 1992). The contours of components of the eigenfunction for $v_y(x,y,t)$ and $\tau_{yy}(x,y,t)$ corresponding to this mode are shown in Figure 5-4. The "energy" in the disturbance, defined by the L_2-norm, eq. (5.15), is concentrated near the stationary boundary and appears to have the longitudinal wavenumber $k = 28\pi$, which is the maximum value that can be resolved by the mesh with $N_{el} = 14$, assuming that two finite elements are required to approximate one flow cell in the disturbance. Thus, as expected from the analysis of Gorodtsov and Leonov (1967) , the most dangerous disturbance corresponds to the highest wavenumber k that can be approximated by the spatial discretization.

At $De = 5.0$, the behavior of the linear stability problem is qualitatively different; a discrete eigenmode becomes temporally unstable, as seen by the exponential growth

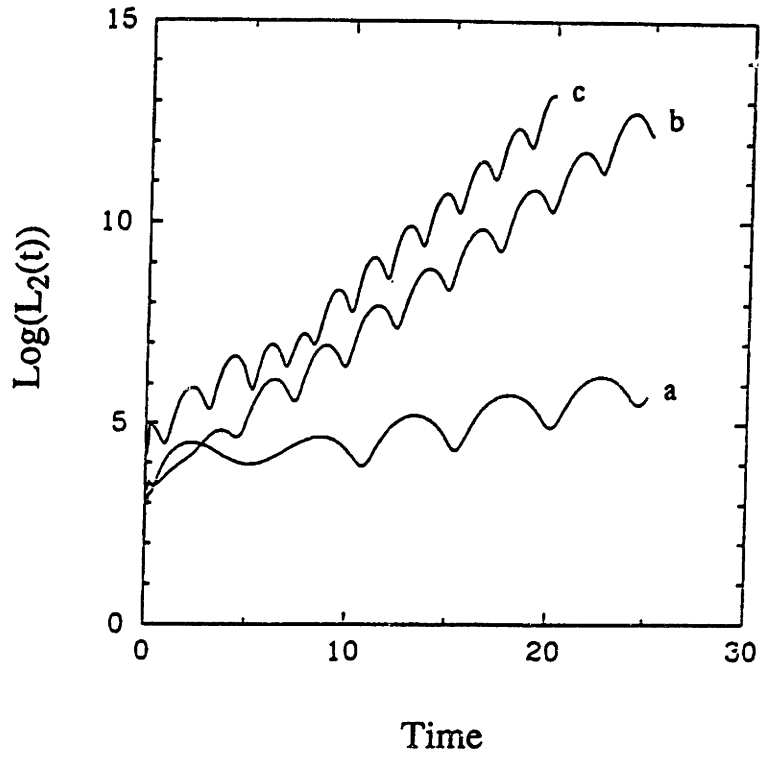

Figure 5-5: Transient response computed with the EEME/SUPG/FEM of the amplitude $L_2(t)$ defined by eq. (5.15) as a function of mesh size for $De = 5.0$ and $\Delta t = 0.1$. Calculations are for the meshes with N_{el} equal to (a) 10, (b) 14, and (c) 28.

shown in Figure 5-3. This mode is fictitious because the continuous problem admits no instability. Increasing the spatial discretization did not improve the numerical stability of the linear stability problem. Indeed, using finer meshes produce spurious eigenmodes that grew faster than those for a coarser mesh, as indicated in Figure 5-5 by the history of the L_2-norm as a function of time for three meshes with $\Delta t = 0.1$ and $De = 5.0$. The components of the most unstable eigenfunction, as determined for the mesh with $N_{el} = 28$, are shown in Figure 5-6; again the disturbance has the form of the highest wavenumber (56π) that is resolvable by the mesh and has energy concentrated near the stationary surface. Also, the frequency of the oscillations in the disturbance, as shown in Figure 5-5, increases with the mesh refinement; however, the frequency is well below the value $Im(\sigma_{disc}) = 56\pi$ expected for the most dangerous eigenfunction on this mesh. This is not unexpected because the time step $\Delta t = 0.1$ does not allow resolution of this frequency.

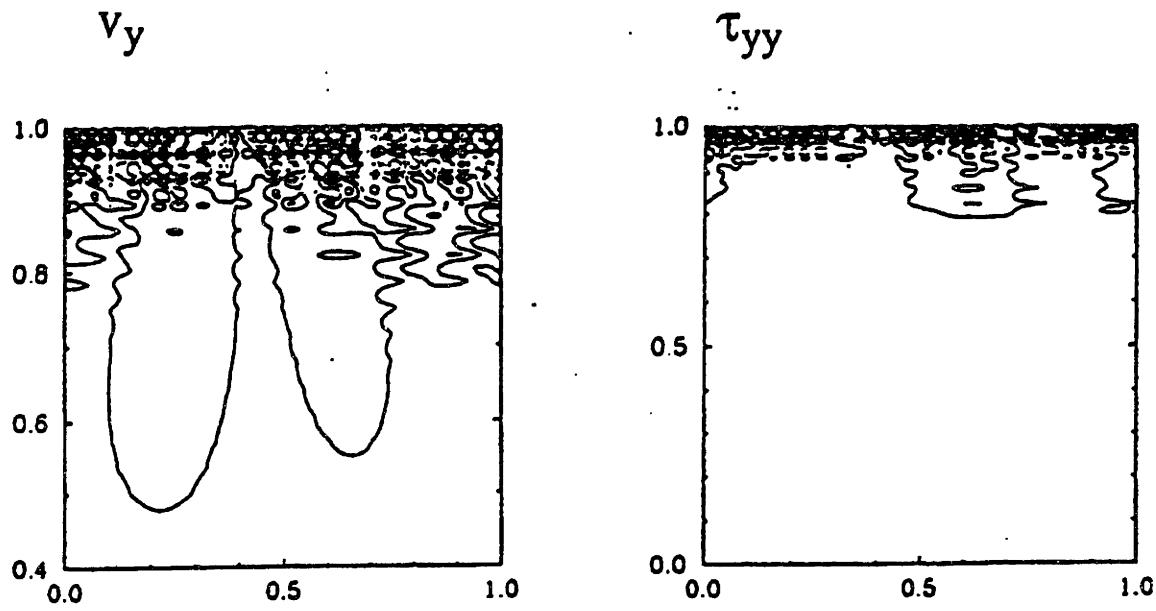

Figure 5-6: Contours of $v_y(x, y, t)$ and $\tau_{yy}(x, y, t)$ at $t = 20.0$ for $De = 5.0$ computed with EEME/SUPG/FEM with $N_{el} = 28$ and $\Delta t = 0.1$. This eigenfunction is unstable in time, as indicated in Figure 5-5.

The numerical instability displayed in Figures 5-3 – 5-6 results from the coupling between the constitutive equation and the elliptic saddle point problem. This is demonstrated by integrating the linear UCM constitutive equation for the planar Couette flow with the kinematics fixed as the rectilinear base flow. The results for $L_2(t)$ are shown in Figure 5-7 for $De = 20.0$ computed by integration using both the SUPG and Galerkin methods with the mesh $N_{el} = 10$ and $\Delta t = 0.1$. As expected from the form of the constitutive equations, the response is a decaying exponential with slope of approximately $-1/(2De)$. Although both methods give very similar values of $Re(\sigma)$, the eigenfunctions are distinctly different and are an excellent demonstration of the qualitative differences in the solution of hyperbolic equations by the SUPG and Galerkin methods. The τ_{xx} component of the eigenfunction is computed by the two techniques at $t = 150$ is shown in Figure 5-8. The SUPG method produces a solution that is streamwise (x-direction) smooth everywhere except near the stationary boundary, where the velocity vanishes; here small oscillations appear along the boundary. The solution computed by the Galerkin method (Figure 5-8(b)) has un-

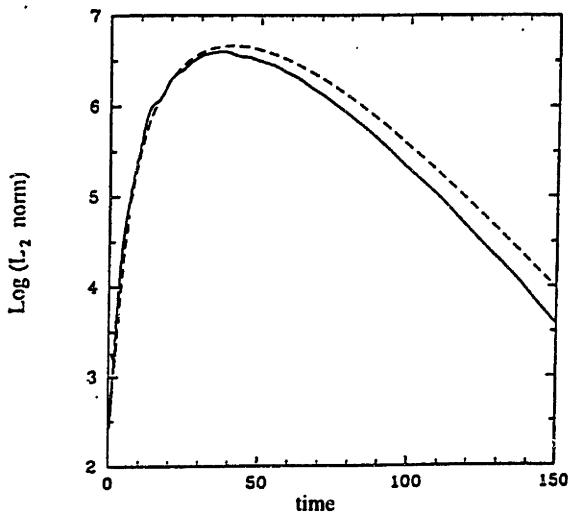

Figure 5-7: Transient response computed with the EEME/SUPG/FEM (- - -) and EEME/GAL/FEM (—) of the amplitude $L_2(t)$ defined by eq. (5.15) for $De = 20.0$ and $\Delta t = 0.1$. Calculations are for the UCM model with the kinematics held fixed so that only components of the stress tensor evolve in time; $N_{el} = 10$.

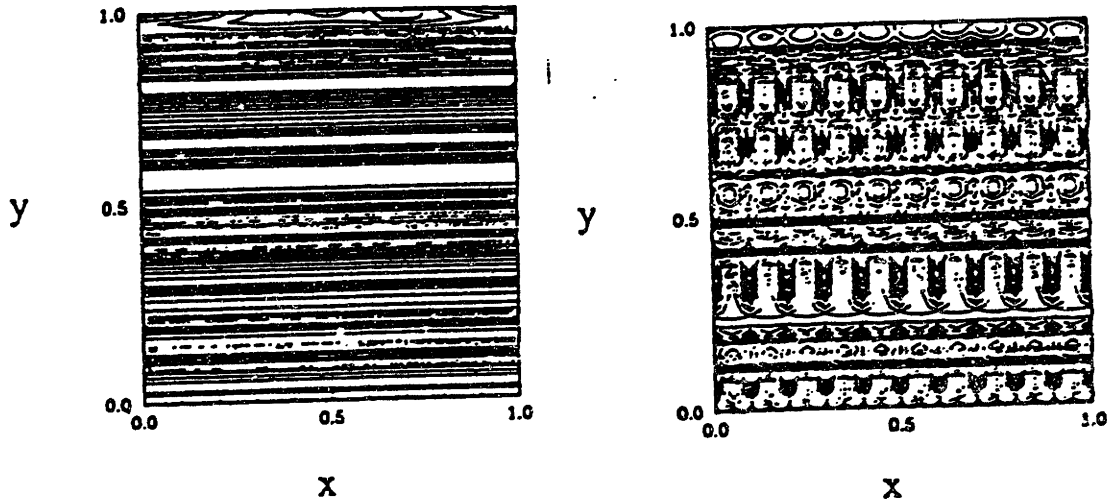

Figure 5-8: Contours of τ_{xx} at $t = 150.0$ for $De = 20.0$ corresponding to the solutions for the calculations with the fixed kinematics shown in Figure 5-7; calculations with the (a) SUPG and (b) Galerkin methods are shown. Note that the SUPG method gives results that are streamwise smooth, whereas the Galerkin method does not.

dulations throughout the solution, a clear indication of the spatial instability that is inherent to this method; see the discussion in section 3.3 and Johnson *et al.* (1984).

The concentration of the energy of the most dangerous disturbance near the zero streamline in the base flow was emphasized by linear stability calculations with the EEME/SUPG method in which the stationary surface was varied by changing the parameter ω to move the line of vanishing base velocity from the top boundary ($\omega = 0$; $y = 1$) to the bottom boundary ($\omega = -1$; $y = 0$) and to the midplane ($\omega = -1/2$; $y = 1/2$). For $De = 5.0$ and $N_{el} = 14$, the response of $L_2(t)$ was identical for all three calculations; however, the concentration of the energy in the eigenfunction was different. As shown by the plots of the contours of $v_x(x, y, t)$ in Figure 5-9, the energy was concentrated near the stationary streamline in the base flow, whether it corresponded to a solid boundary or to the midplane of the flow. For intermediate values of ω the disturbance also follows the zero streamline throughout the domain.

Finally, the boundary conditions on the base flow were changed to be

$$v_x(x, 0, t) = 2, \tag{5.16}$$

$$v_x(x, 1, t) = 1, \tag{5.17}$$

which corresponds to $\omega = 1$, to study the linear stability of a flow without a stationary streamline. The response of $L_2(t)$ is shown in Figure 5-10 for $De = 5.0$, $N_{el} = 14$ and $\Delta t = 0.1$ for the EEME/GAL/FEM and EEME/SUPG/FEM methods. Components of the eigenfunction are shown in Figure 5-11 for discretization of the constitutive equation using the EEME/SUPG/FEM; both the GAL and SUPG techniques give the correct decaying exponential; however, the most dangerous eigenfunction for the EEME/SUPG/FEM is not concentrated near any boundary and has no streamwise structure at all and, thus, is not characteristic of any of the eigenfunctions described by Gorodtsov and Leonov (1967). The form of the most dangerous eigenfunction has been changed by making a change in the frame of reference of the numerical method.

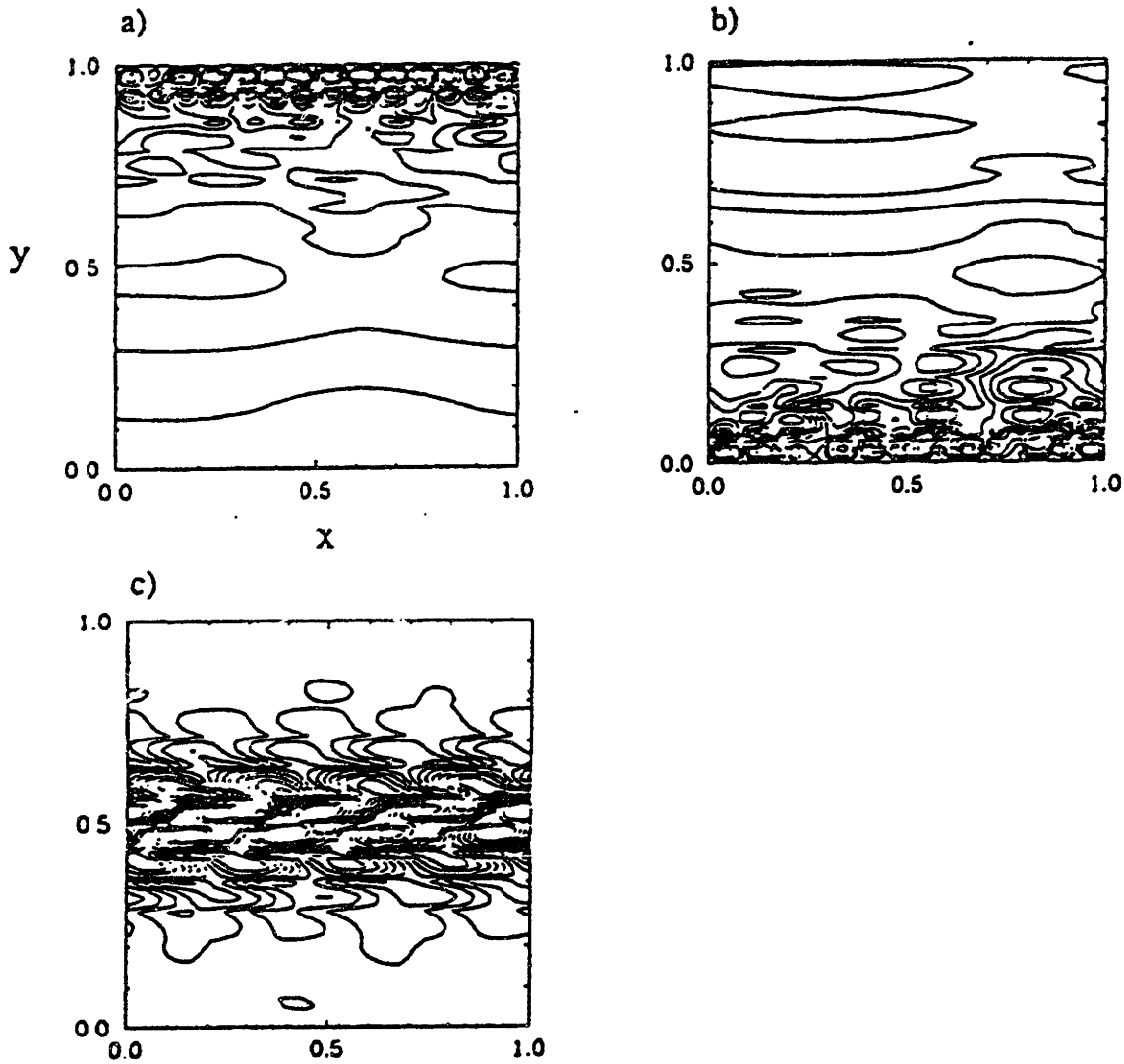

Figure 5-9: Contours of $v_x(x, y, t)$ at $t = 10.0$ for $De = 5.0$ computed with the EEME/SUPG/FEM with $N_{el} = 14$ and $\Delta t = 0.1$; (a) $\omega = 0$, (b) $\omega = -1$, and (c) $\omega = -1/2$.

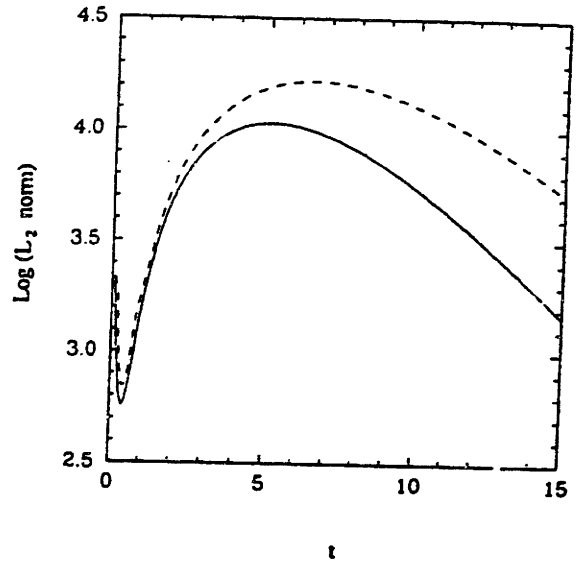

Figure 5-10: Transient response computed with the EEME/SUPG/FEM (- - -) and the EEME/GAL/FEM (—) of the amplitude $L_2(t)$ defined by eq. (5.15) with the boundary conditions given by eqs. (5.16) and (5.17); $N_{el} = 14$, $De = 5.0$, and $\Delta t = 0.1$.

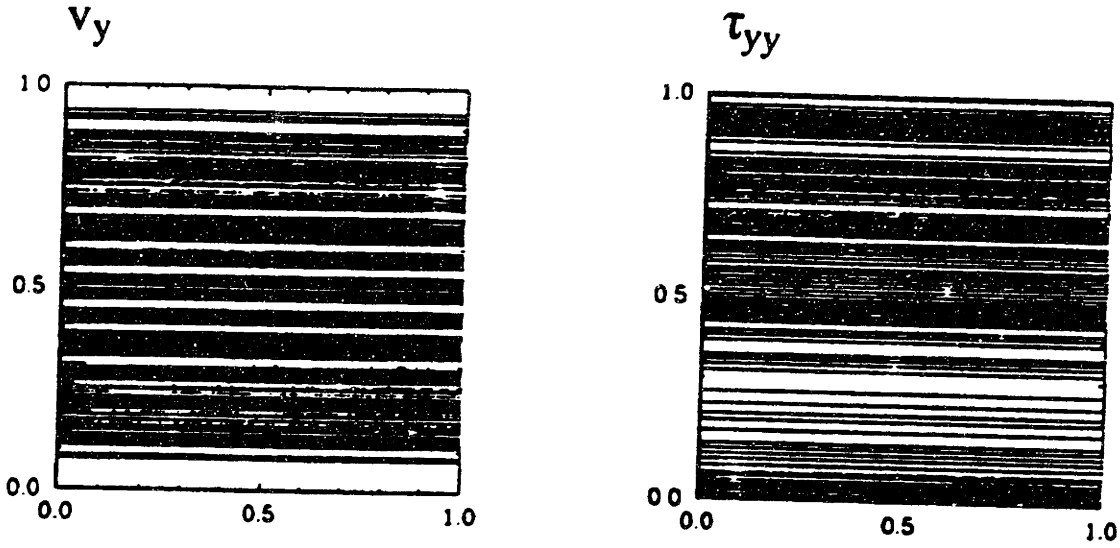

Figure 5-11: Contours of $v_y(x, y, t)$ and $\tau_{yy}(x, y, t)$ at $t = 20.0$ for $De = 5.0$ computed with the EEME/SUPG/FEM and the boundary condition given by eqs. (5.16) and (5.17); $N_{el} = 28$ and $\Delta t = 0.1$. This eigenfunction is stable in time as indicated in Figure 5-10.

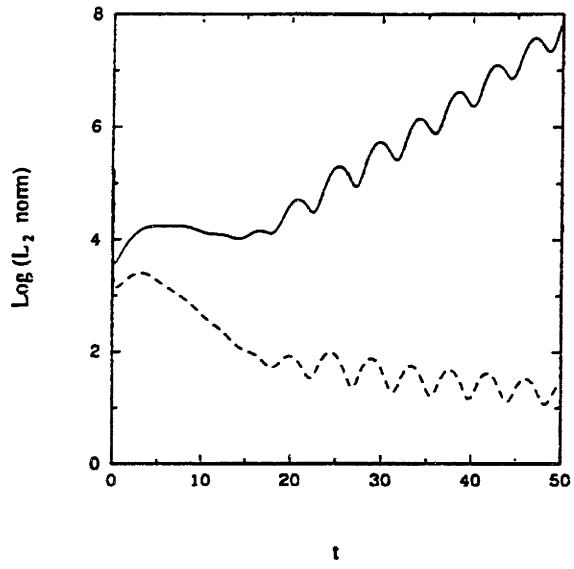

Figure 5-12: Transient response computed with the EVSS/SUPG/FEM of the amplitude $L_2(t)$ defined by eq. (5.15) for $De = 3.0$ (- - -) and $De = 5.0$ (—) for the mesh $N_{el} = 14$ and $\Delta t = 0.1$.

5.3 The Numerical Linear Instability of the EVSS/SUPG/FEM

The numerical stability of the EVSS/SUPG method was tested using the planar Couette flow of a UCM fluid in a manner similar to the calculations described above for the EEME/FEM. The response of $L_2(t)$ for $De = 3.0$ and $De = 5.0$ is shown in Figure 5-12 for $\omega = 0$, $N_{el} = 14$ and $\Delta t = 0.1$. Just as for the EEME/FEM, the method is numerically stable for $De = 3.0$ and unstable for $De = 5.0$. The frequency of oscillation and the critical value of De for the instability are approximately the same as those predicted by the EEME/SUPG/FEM; moreover, the energy of the eigenfunction also is concentrated near the stationary boundary ($y = 1$), as shown in Figure 5-13.

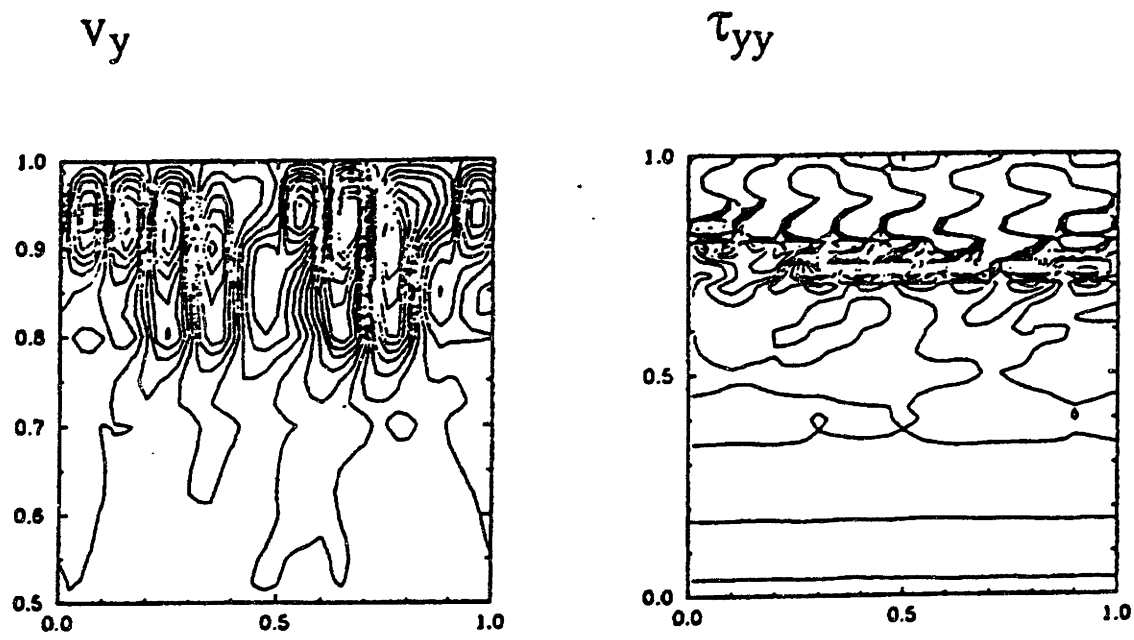

Figure 5-13: Contours of $v_y(x, y, t)$ and $\tau_{yy}(x, y, t)$ at $t = 15.0$ for $De = 5.0$ computed with the EVSS/SUPG/FEM with $N_{el} = 28$ and $\Delta t = 0.1$. This eigenfunction is unstable in time, as indicated in Figure 5-12.

5.4 Why are Zero Streamlines Special?

Because fully implicit integration methods are used for solving the constant coefficient, linear equation sets that result for the linear stability formulation, the issue of numerical stability of the time integration is directly related to the spatial discretization. The instability, therefore, seems to be inherent to the EEME and EVSS formulations. Two f acts stand out from the calculations in the previous two sections. First, when the coupling between the constitutive equation and the momentum/continuity equation pair is broken, there is no instability (see Figure 5-7). Second, the calculations in which the parameter ω were varied focuses the study of the instability around the zero streamline; especially, the result that the instability is not observed if the zero streamline is removed (see Figure 5-10). This, in turn, raises two possibilities for the problem with the numerical formulation. Either the coupling between the conservation and constitutive equations is not being accounted for properly or there is an incompatibility in the finite element approximation at the zero streamline in the

constitutive equation. Each option will be examined in turn.

5.4.1 Coupling of the Momentum/Continuity Equation and the Constitutive Equation

The coupling of the equations as the cause of the instability was examined by Brown *et al.*, (1993) and Northey (1991). In the latter numerical experiments were run which calculated the linear stability of the equations while "freezing" individual terms in the governing viscoelastic flow equations, i.e., certain variables in the residual equations were replaced by their base flow values. This was performed to determine the terms in the equations that are essential to the numerical instability. From these results, Northey (1991) found that the coupling between the velocity gradients in the constitutive equation and the lower order stress terms $\nabla \boldsymbol{v} \cdot (\nabla \cdot \boldsymbol{\chi})$ appear to be necessary for the instability to occur. Since the lower-order stress term is introduced via the substitution of q for p, a new method was developed, the EEME-P/FEM, which differs from the EEME formulation only in an ad-hoc change in the treatment of the pressure field ($q(\boldsymbol{x})$) in the momentum equation. In the EEME-P formulation, the modified pressure is removed, i.e., $q \Rightarrow p$ through eq. (4.5) which reintroduces the terms $\nabla \cdot (\boldsymbol{v} \nabla p)$ and $\partial p / \partial t$ into the momentum equation, eq. (4.6). The term, $\nabla \cdot (\boldsymbol{v} \nabla p)$, is integrated-by-parts in the weak form and the resulting line integral vanishes on all boundaries with either specified velocity or periodicity. This is the only difference between the EEME and EEME-P formulations.

The EEME-P/SUPG/FEM and EEME-P/GAL/FEM were tested for the computation of the stability of planar Couette flow for the UCM model in an identical way to that described above for the EEME/SUPG/FEM (Northey, 1991). The plot of $L_2(t)$ for $De = 5.0$, $\omega = 0$ and $\Delta t = 0.1$ is shown in Figure 5-14 for meshes with N_{el} values of 14 and 28. The numerical instability seen in the EEME methods has been removed and all the calculations appear to decay with a rate very similar to $-1/(2De)$. Components of the eigenfunction for the calculation with $N_{el} = 28$ and the EEME-P/SUPG/FEM are shown in Figure 5-15 for $t = 50.0$. Again the energy

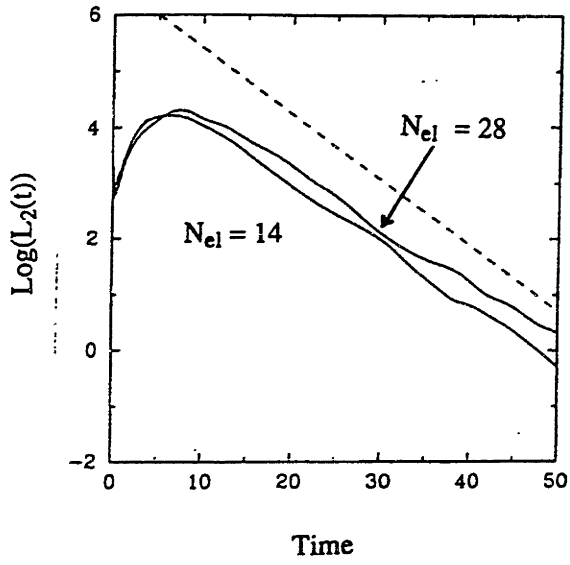

Figure 5-14: Transient response computed with the EEME-P/SUPG/FEM of the amplitude $L_2(t)$ defined by eq. (5.15) for $De = 5.0$ for meshes with $N_{el} = 14$ and $N_{el} = 28$; $\Delta t = 0.1$ (Brown *et al.*, 1993).

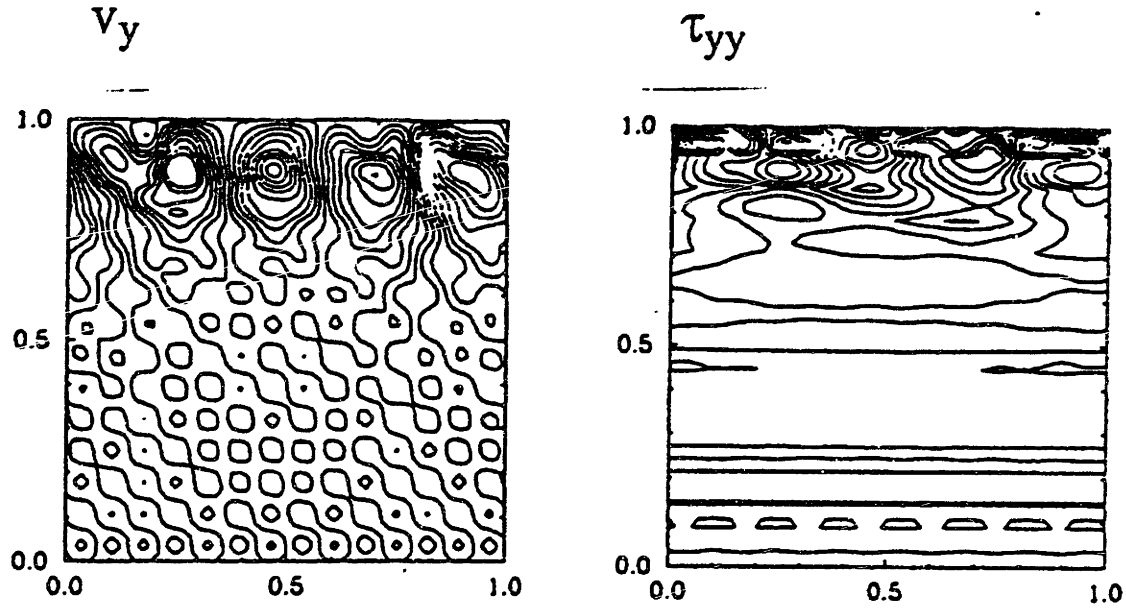

Figure 5-15: Contours of the disturbance $v_y(x, y, t)$ and $\tau_{yy}(x, y, t)$ at $t = 50.0$ for $De = 5.0$ computed with the EEME-P/SUPG/FEM with $N_{el} = 14$ and $\Delta t = 0.1$. This eigenfunction is stable in time, as indicated in Figure 5-14 (Brown *et al.*, 1993).

in the disturbance is concentrated near the stationary boundary ($y = 1$), although a large-scale structure in the velocity field is discernible. Linear stability calculations were stable with the EEME-P method up to $De = 10$ with the time evolution of $L_2(t)$ and the eigenfunction behaving similarly to that depicted in Figures 5-14 and 5-15, respectively.

The EEME-P formulation delays the onset of the instability, but it does not appear to have corrected the formulational problem in the EEME method. An equivalent decoupling of the pressure does not appear in the EVSS/FEM so the *cause* of the instability still has not been properly addressed. In steady-state calculations (Northey, 1991), the EEME-P results were less accurate than the original EEME method due to the greater significance being placed on the bilinearly approximated variable $p(\boldsymbol{x})$.

5.4.2 Incompatibility of the Approximating Spaces

The instability may result from an incompatibility in the approximating spaces for the unknowns due to a condition similar to the LBB or inf-sup condition, eq. (3.22) from the Stokes problem, which is violated in the limit of vanishing velocity. This compatibility condition could relate either the velocity or velocity gradient to the stress approximation. Northey (1991) examined the use of LBB circumventing techniques introduced by Hughes *et al.* (1986) and Hughes *et al.* (1989) which allow the use of approximations for the velocity and pressure in the Stokes problem that usually lead to spurious results (e.g., bilinear velocities and pressures). These methods were applied to the EEME/continuity pair, but both methods failed to remedy the numerical instabilities in the UCM equations and produced fictitious bifurcations in the steady-state equations as well (Northey, 1991).

A second attempt at overcoming the incompatibility, was the use of a modification in the stress weighting function designed so that the stress gradients will not vanish from the weak form of the continuity equations. The gradient-Galerkin least squares (GGLS) method introduced by Franca & Dutra Do Carmo (1989) was examined. The GGLS method has not been shown to be convergent for purely hyperbolic equations; when the method was tested for a simple hyperbolic example with known solution

the results were not qualitatively correct, much less quantitatively. Therefore, the use of a higher order weighting function method cannot remove the instabilities either (Northey, 1991).

In the limit of zero velocity, the constitutive equation reduces from a partial differential equation in time and space to an ordinary differential equation in time. If the steady-state case only is considered, this becomes an algebraic equation, e.g., for the EVSS formulation

$$\boldsymbol{\Sigma} - De\left[(\boldsymbol{\nabla v})^T \cdot \boldsymbol{\Sigma} + \boldsymbol{\Sigma} \cdot (\boldsymbol{\nabla v})\right] = De(1-\beta)\left[(\boldsymbol{\nabla v})^T \cdot \dot{\boldsymbol{\gamma}} + \dot{\boldsymbol{\gamma}} \cdot (\boldsymbol{\nabla v})\right]. \qquad (5.18)$$

This degeneracy of the constitutive equations affects the mathematical type of the UCM equations as discussed in Section 2.4. The characteristic slope of the two real characteristics of the UCM equations are indeterminate for $v_x = v_y = 0$. This means the characteristics switch from hyperbolic to elliptic (all directions are characteristic) when the velocity is zero.

In examining the approximations used for the constitutive equation, the stresses are *continuous* and biquadratic, the rate-of-strain tensor is *continuous* and bilinear and the velocity gradients are *discontinuous* and bilinear. It is obvious that the space of allowable stresses, $H^1(\Omega)$, does not contain the velocity gradient forcing data which is in $H^0(\Omega)$. This incompatibility can be rectified by interpolating the velocity gradient onto a *continuous* set of basis functions via a least-squares variational method instead of the rate-of-strain tensor. Substituting this new velocity gradient into the constitutive equation for every occurrence of the velocity gradient (not just in the rate-of-strain tensor) fixes the incompatibility of approximating spaces. However, the stress uses biquadratic basis function while the velocity gradient uses bilinear basis functions. Dropping the interpolation of the stress from biquadratic to bilinear makes eq. (5.18) compatible. The derivation of the equations and the finite element formulation of this new method, the EVSS-G/FEM, is given in Sections 4.4 and 4.6.4, respectively.

This is a heuristic argument that is similar to that of Taylor & Hood (1973) in

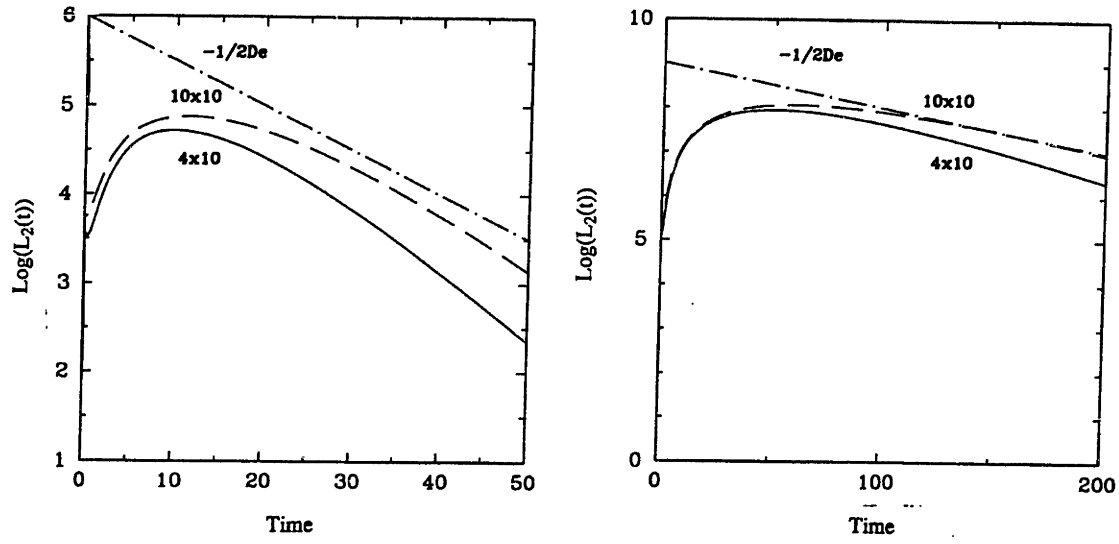

Figure 5-16: Effect of varying resolution of the mesh in the x- and y- directions on the temporal stability as computed with the EVSS-G/SUPG/FEM. Results are shown for $(N_x, N_y) = (4, 10)$ and $(10, 10)$ with $\Delta t = 0.1$; (a) $De = 10.0$ and (b) $De = 50.0$.

the introduction of the finite element used to solve the Navier-Stokes equations.

5.5 Numerical Linear Stability of EVSS-G/FEM

5.5.1 EVSS-G/SUPG/FEM

The EVSS-G/SUPG/FEM uses the bilinear Lagrangian interpolation for the velocity gradient field in all terms in the constitutive equation and bilinear interpolation for the components of the elastic stress tensor Σ. The temporal stability of this method was tested by calculation of the linear stability of planar Couette flow exactly as described above. The most significant result is that the EVSS-G/SUPG/FEM appears to be numerically stable to very high values of De for fixed finite element discretization. The response of the energy of the disturbance, $L_2(t)$, with time is shown in Figure 5-16 for calculations with $\omega = 0$ and $\Delta t = 0.1$; calculations are shown for (a) $De = 10.0$ and (b) $De = 50.0$ for a mesh with $N_x = 4$ (streamwise elements) and $N_y = 10$ (cross-stream elements) and for a mesh with $N_{el} = 10$ in both directions. The calculations with both meshes are numerically stable; however, results with the finer mesh give a better approximation to the correct decay rate of $-1/(2De)$.

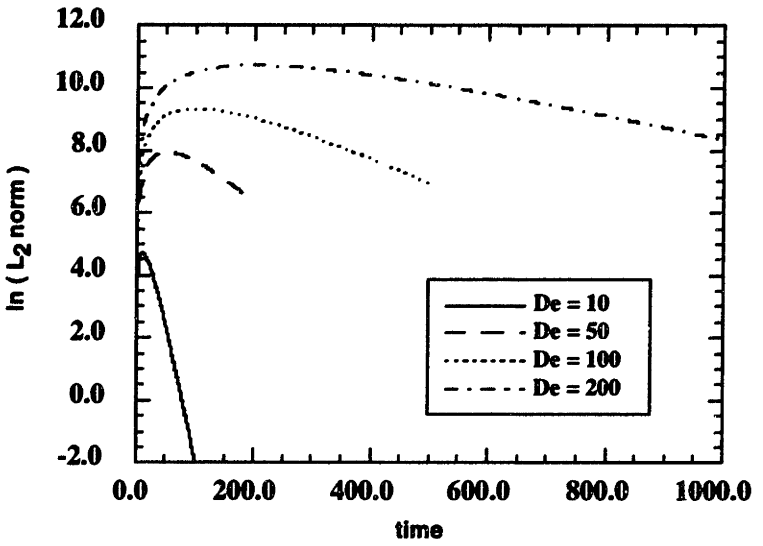

Figure 5-17: Transient responses computed with the EVSS-G/SUPG/FEM of the amplitude $L_2(t)$ defined by eq. (5.15) are shown for $(N_x, N_y) = (4, 10)$ and $5.0 \leq De \leq 200.0$ with $\Delta t = 0.1$.

The evolution of the energy of the disturbance for a sequence of calculations with $5.0 \leq De \leq 200.0$ is shown in Figure 5-17 for the 4x10 mesh with $\Delta t = 0.1$. The behavior reproduces the analytical eigenvalue for long time. Although the calculations were stable and accurate for $De = 200.0$, they were not continued to higher values of De because of the long simulation times associated with the slow decay rate for the disturbances. The contours of the eigenfunction for $v_y(x, y, t)$ and $\Sigma_{yy}(x, y, t)$ at $t = 25.0$ are shown in Figure 5-18, as computed with $N_{el} = 10$ and $De = 10.0$. The structure of the eigenfunction matches what is expected from the theory.

The behavior of the energy of the disturbance with decreasing time step is shown in Figure 5-19(a) and clearly demonstrates the temporal stability of the EVSS-G/SUPG/FEM; decreasing Δt by a factor of 200.0 leads to simulations with almost the identical decay rate for the disturbance. However, the oscillation frequency of the disturbance does depend slightly on Δt . This is not unexpected because this temporal frequency approaches k, the streamwise wavenumber, for large De; k is approximately 8π for the 4x10 mesh. The finest two time steps $\Delta t = 0.05$ and $\Delta t = 0.005$ resolve this frequency, but the largest time step ($\Delta t = 0.1$) does not. The results for the finest two time steps are very similar. The behavior of the energy

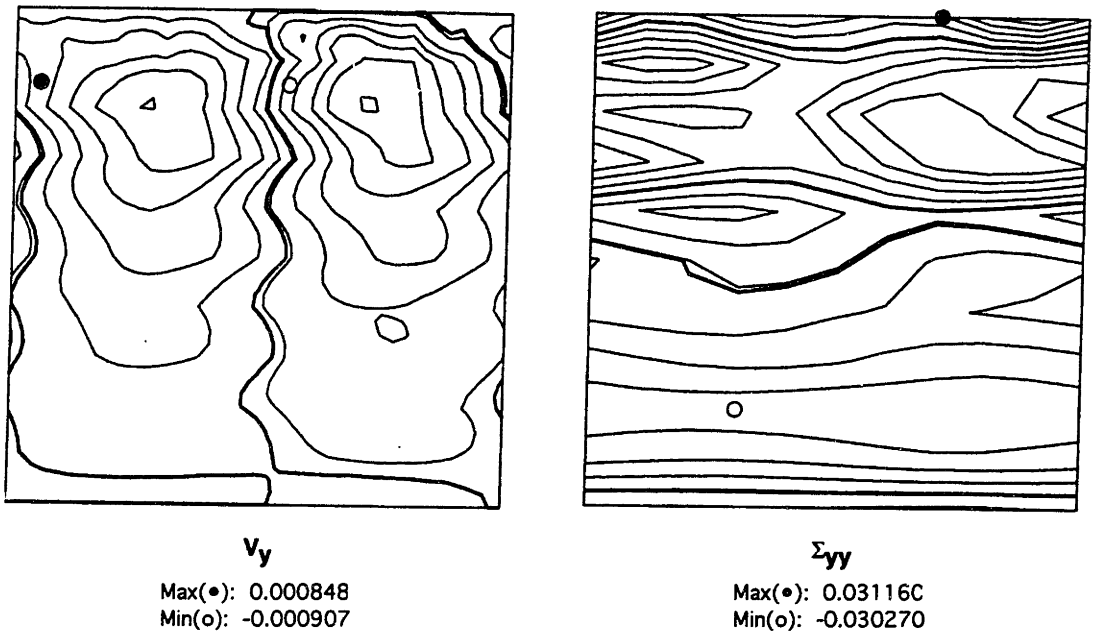

Figure 5-18: Contours of the disturbance to the velocity field $v_y(x, y, t)$ and stress field $\Sigma_{yy}(x, y, t)$ at $t = 25.0$ for $De = 10.0$ computed with the EVSS-G/SUPG/FEM with $N_{el} = 10$ and $\Delta t = 0.1$. This eigenfunction is temporally stable, as indicated in Figure 5-17. Maximum and minimum values of the function are shown.

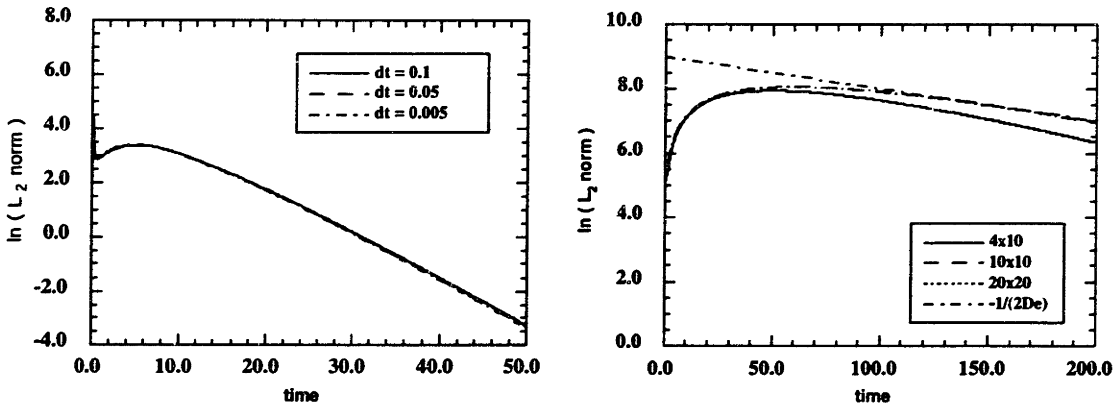

Figure 5-19: Effect of time step on the evolution of the energy of the disturbance $L_2(t)$ for the EVSS-G/SUPG/FEM. (a) Results are shown for $0.005 \leq \Delta t \leq 0.1$ with $(N_x, N_y) = (4, 10)$ and $De = 1.0$. (b) Results are shown for $(N_x, N_y) = (4, 10)$, $(10, 10)$ and $(20, 20)$ with $De = 1.0$ and $\Delta t = 0.1$.

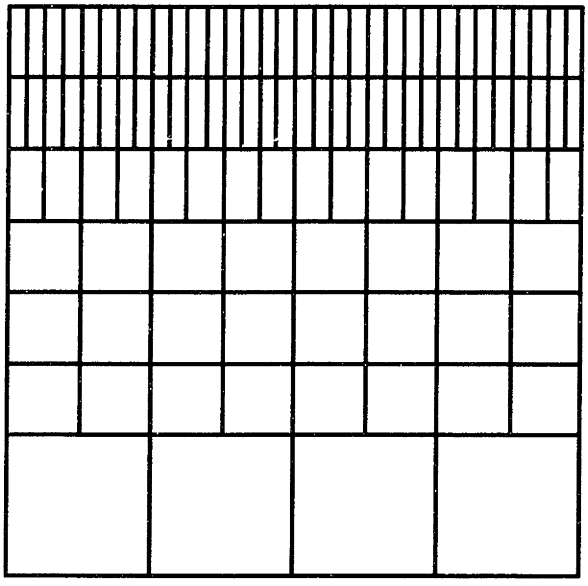

Figure 5-20: The most refined finite element mesh used in the local mesh refinement study. This is a $3x - 1y$ refinement.

of the disturbance with increasing mesh refinement is shown in Figure 5-19. Again, the method becomes more accurate upon mesh refinement with the final two meshes becoming indistinguishable.

Because locally refined meshes will be used for more difficult problems, its effect on the numerical stability of the algorithm is examined. The finite element meshes used in these calculations are based on a uniform mesh of 4 elements in both the x- (streamwise) and y- (cross-stream) directions with levels of local refinement. This uniform mesh is the crudest possible for resolving the periodic structure of the flow and stress fields expected in the unit-length periodic flow domain. Finer streamwise meshes on the same computational domain might be expected to resolve disturbances with higher spatial wavenumbers, but with the same decay rate. The local refinement is focussed near the stationary boundary ($y = 1$) to improve the resolution of the larger gradients of velocity and stress that are present in the disturbance near this boundary. The meshes are denoted by the number of levels of refinement in the x- and y-directions; for example, $3x - 1y$ denotes a mesh with three levels of element splitting in the x-direction and one level in the y-direction closest to the boundary $y = 1$; this mesh is shown in Figure 5-20.

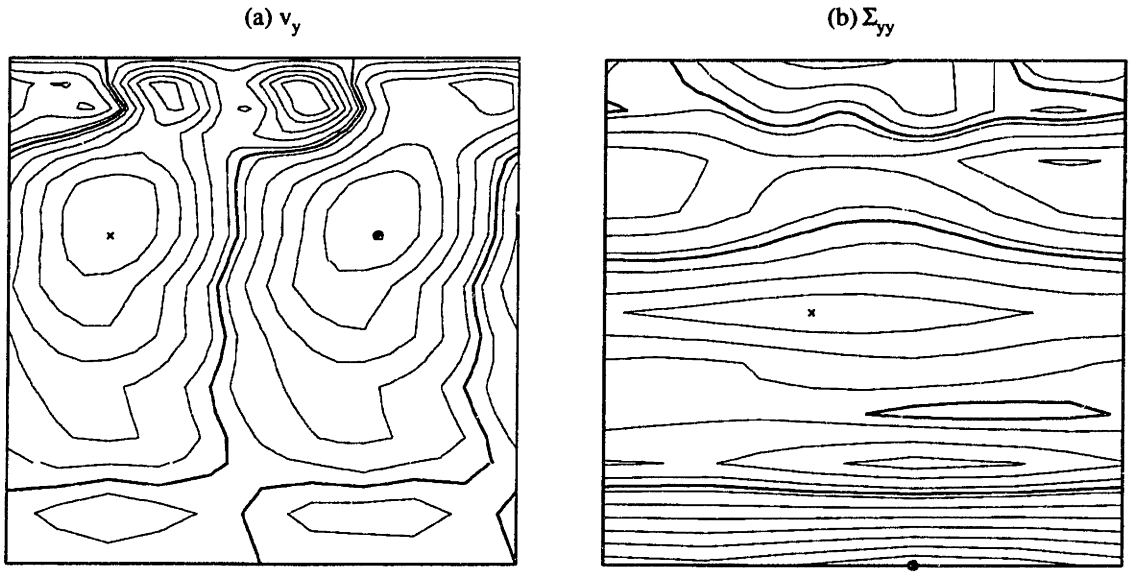

Figure 5-21: Contours of $v_y(x, y, t)$ and $\Sigma_{yy}(x, y, t)$ at $t = 25.0$ for $De = 10.0$ computed with the EVSS-G/SUPG/FEM with the locally refined mesh shown in Figure 5-20 and $\Delta t = 0.1$. These eigenfunctions are stable in time.

Contours of the variables $v_x(x, y, t)$ and $\Sigma_{yy}(x, y, t)$ for the disturbance are shown in Figure 5-21, as computed with the mesh shown in Figure 5-20. These contours are plotted for $t = 25.0$ for $De = 10.0$. The velocity component $v_y(x, y, t)$ shows considerable cross-stream and streamwise structure near the stationary boundary, whereas the disturbance in the elastic stress component $\Sigma_{yy}(x, y, t)$ does not show the same lateral structure. Interestingly, the streamwise structure of the disturbance seen at long times appears to select the spatial wavelength resolved by the crudest portion of the mesh (near $y = 0$), except near the stationary wall where a structure with twice the streamwise wavenumber is seen. Since both disturbances have the same decay rate, at least for $De \gg 1$, only the local mesh refinement seems to distinguish between which one is found in the calculations.

The decay of the energy in the disturbance as a function of De is shown in Figure 5-22(a), as computed with the mesh in Figure 5-20 for a range of Deborah numbers. Each result shows the characteristic decay rate of $-1/(2De)$ after an initial increase in the energy in the system. As before, calculations with very large values of De are extremely costly because of the length of the time integration required. The effect

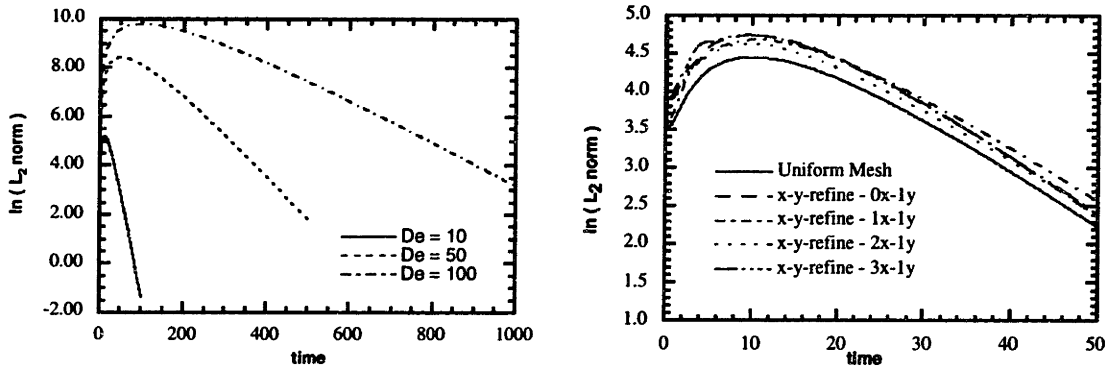

Figure 5-22: (a) Computed energy in the finite element disturbance as a function of time for varying De using EVSS-G/SUPG/FEM. Calculations are for the mesh shown in Figure 5-20. The stability of the calculations is apparent as is the decay rate at long times of $-1/(2De)$. (b) Computed energy in the finite element disturbance as a function of time for increasing local mesh refinement and $De = 10.0$.

of local mesh refinement on the predicted decay rates is shown in Figure 5-22(b) for four meshes with local mesh refinement and $De = 10$. All four meshes give the same decay rate for the disturbance. The calculations were performed with slightly different random initial guesses constructed for each mesh. This slight difference is one reason why the results of the finest two meshes are close at long times, but not at short times. It is important to understand that precise mesh convergence is difficult to achieve with this problem because adding refinement in the x-direction allows resolution of eigenfunctions with higher wavenumbers all of which decay at the same rate. Hence, the energy in the linear stability solution may be different for different meshes, but will decay at the same rate, $-1/(2De)$.

5.5.2 EVSS-G/SU/FEM

The calculations with the EVSS-G/SUPG/FEM clearly demonstrate the improved stability of this formulation over the equivalent method, but without the approximation for the velocity gradient. We demonstrate that this stability is a characteristic of the finite element approximations to the variables and can be reproduced using any of the methods described in Section 3.3.2 for solving the hyperbolic constitutive equation. The streamline upwind method was used to discretize the constitutive equation

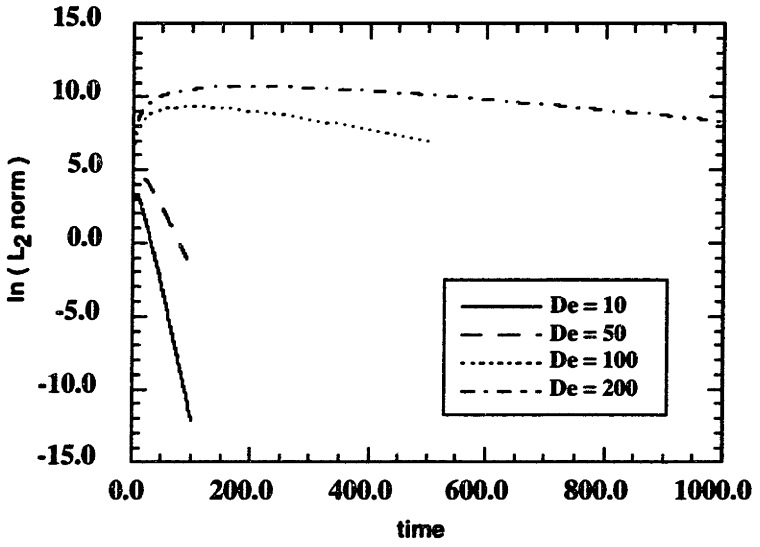

Figure 5-23: Transient response computed with the EVSS-G/SU/FEM of the amplitude $L_2(t)$ defined by eq. (5.15) as a function of De for the mesh $N_{el} = 10$ and $\Delta t = 0.1$.

with the EVSS-G formulation of the equation set. The resulting method, referred to as the EVSS-G/SU/FEM technique has enhanced linear stability for planar Couette flow, as demonstrated by the evolution of $L_2(t)$ in Figure 5-23 for $\omega = 0$, $N_{el} = 10$ and $\Delta t = 0.1$. The EVSS-G/SU/FEM has similar numerical stability characteristics to the EVSS-G/SUPG/FEM; the time dependent calculations for the linear stability problem reproduce the response expected from the analytical solution up to high values of De. The most dangerous disturbance computed for $De = 50.0$ and $t = 200.0$ is shown in Figure 5-24. The concentration of the energy toward the stationary boundary is still apparent; however, the energy seems to be spread more uniformly in the cross-stream direction, possibly because of the effect of the cross-stream diffusivity in the method.

5.5.3 EVSS-G/GLS/FEM

Stability calculations for the EVSS-G/GLS/FEM were carried out in a manner like those described above. Interestingly, changing from the SUPG or SU to the GLS method for the solution of the hyperbolic constitutive equation led to instabilities, as seen in the EEME and EVSS formulations for $De > 10$. The evolution of the

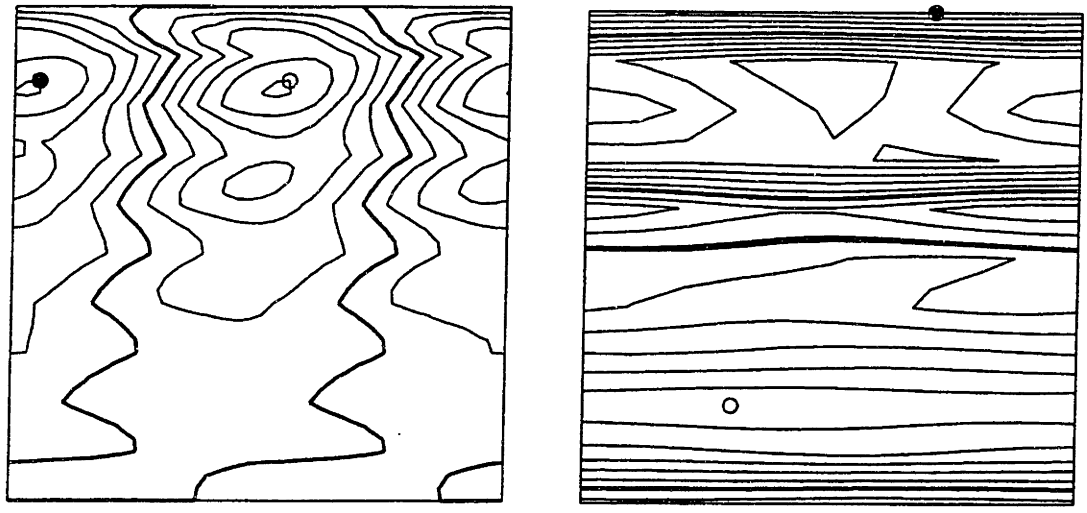

Figure 5-24: Contours of the disturbance to the velocity ($v_y(x,y,t)$) and stress ($\Sigma_{yy}(x,y,t)$) field at $t = 25.0$ for $De = 5.0$ computed with the EVSS-G/SU/FEM with $N_{el} = 10$ and $\Delta t = 0.1$. This eigenfunction is stable in time, as indicated by Figure 5-23. Maximum and minimum values of the functions are shown.

disturbance, $L_2(t)$, and the form of the most dangerous eigenfunction are shown in Figures 5-25 and 5-26, respectively. The reason for the loss of stability is not understood, but must be connected to the use of the GLS method for discretization of the hyperbolic constitutive equation.

5.5.4 DEVSS-G/SUPG/FEM

The DEVSS-G/FEM method was introduced as a simplification in the derivation of the EVSS-G/FEM and to eliminate the upper convective derivative of the rate-of-strain tensor in the constitutive equation that was a result of the transformation to the EVSS-type equations (see Chapter 4 and 8 for further information regarding the derivation this method). The DEVSS-G/FEM is stable to very high De as is the EVSS-G/FEM. The decay of the energy in the disturbance for $De = 10.0$, 50.0 and 100.0 is shown in Figure 5-27(a). The characteristic decay rate of $-1/(2De)$ appears for each case at sufficiently long times following an initial increase in the energy of

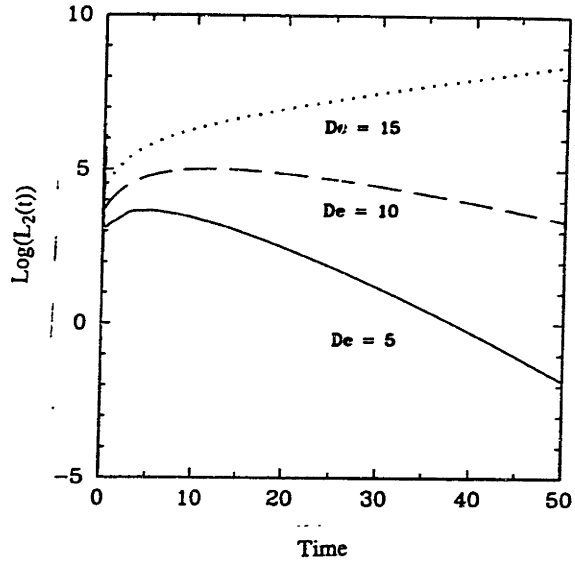

Figure 5-25: Transient response computed with the EVSS-G/GLS/FEM of the amplitude $L_2(t)$ defined by eq. (5.15) as a function of De for the mesh $N_{el} = 10$ and $\Delta t = 0.1$.

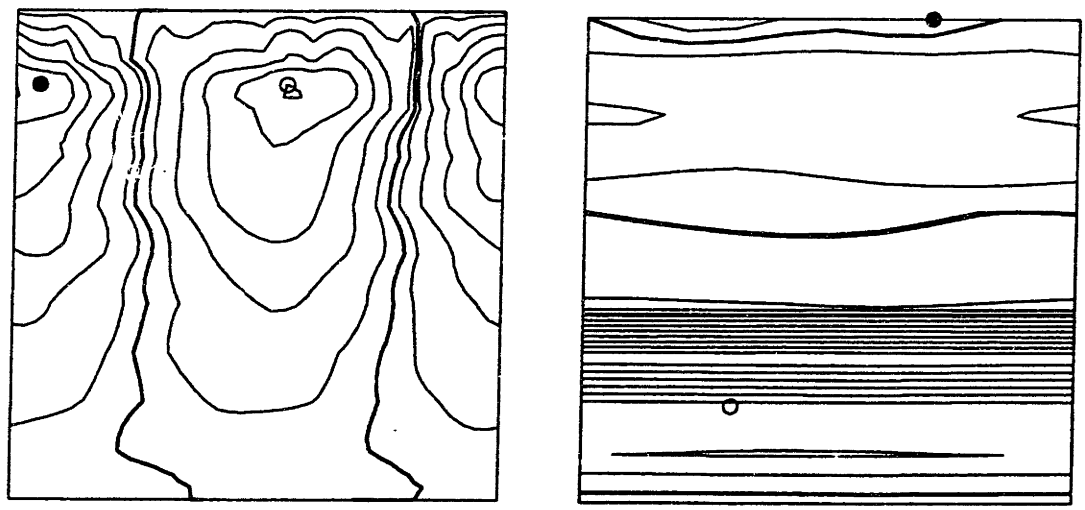

Figure 5-26: Contours of the disturbance to the velocity ($v_y(x, y, t)$) and stress ($\Sigma_{yy}(x, y, t)$) field at $t = 25.0$ for $De = 15.0$ computed with the EVSS-G/GLS/FEM with $N_{el} = 10$ and $\Delta t = 0.1$. This eigenfunction is stable in time, as indicated by Figure 5-25. Maximum and minimum values of the functions are shown.

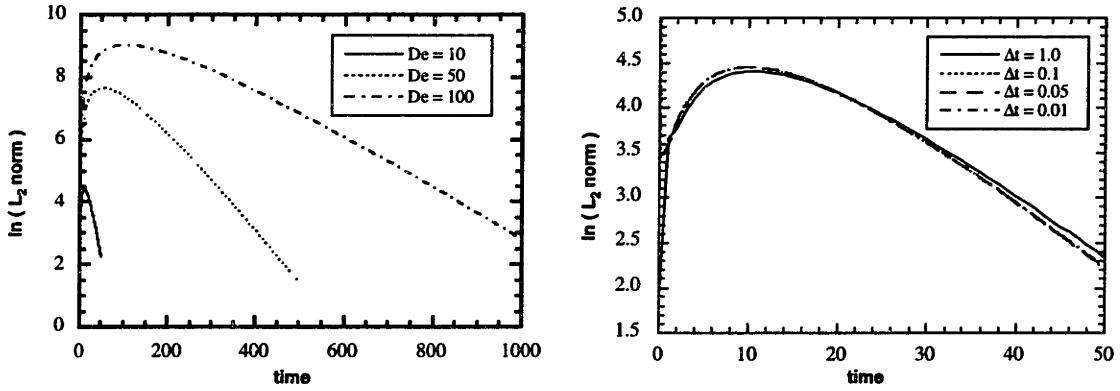

Figure 5-27: (a) Computed energy in the finite element disturbance as a function of time for varying De.The stability of the calculations for the DEVSS-G/FEM using the SUPG method is apparent, as is the the decay rate at long times of $-1/(2De)$. (b) Computed energy in the finite element disturbance as a function of time for decreasing step size for the DEVSS-G/FEM using the SUPG method. The convergent results are apparent.

the system. In Figure 5-27(b) the convergence of the results with decreasing time step is shown for $De = 10.0$. The decay rate is better matched as Δt decreases and the final three are indistinguishable. Finally, in Figure 5-28, the EVSS-G and the DEVSS-G methods are compared for $De = 10.0$ and $\Delta t = 0.1$. Except for a tiny difference at small times, the two solutions are practically identical; this is also true for the contours of the disturbance.

5.6 Summary

Above all, the calculations described here establish the difficulty with the temporal stability of finite element methods for the solution of viscoelastic flows. The numerical calculation of the linear stability of planar Couette flow is an excellent problem for establishing temporal stability because the behavior of the most dangerous eigenvalue and the structure of the eigenfunction are known analytically from Gorodtsov and Leonov (1967). The results demonstrated here show that algorithms like the EEME/SUPG and EVSS/SUPG, which give accurate and numerically stable results for smooth steady-state flows, are limited by numerical instabilities for time-dependent calculations. The instabilities are linked to the very difficult problem

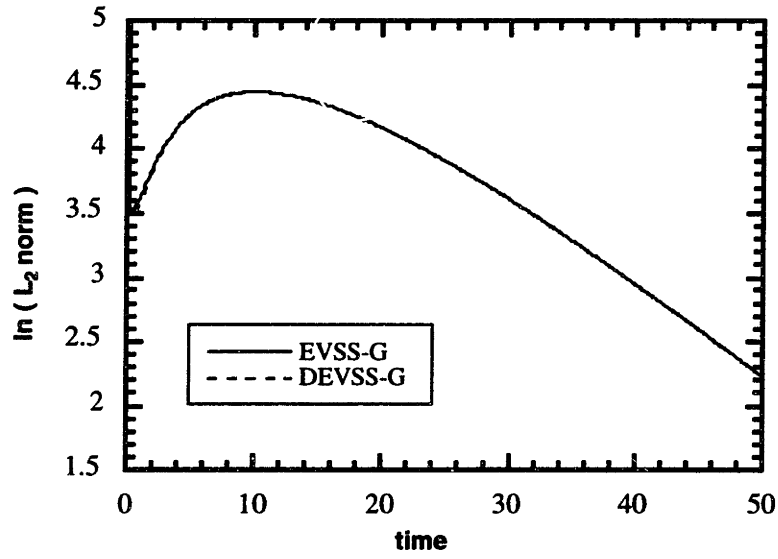

Figure 5-28: Transient response computed with the EVSS-G/SUPG/FEM and DEVSS-G/SUPG/FEM of the amplitude $L_2(t)$ defined by eq. (5.15) for $De = 10$, $N_{el} = 5$ and $\Delta t = 0.1$. The EVSS-G/FEM and DEVSS-G/FEM are shown to be virtually identical at long times.

associated with accurate calculation of the eigenvalue spectrum for simple shear flow. The most dangerous eigenvalue has a real part that approaches $-1/(2De)$ and an imaginary part that scales as k, where k is the streamwise wavenumber, for $De \gg 1$; moreover, the eigenfunction develops boundary layer structure in the cross-stream direction. It is hard to imagine a more difficult problem to resolve.

Because fully implicit time integration methods are used for solving the constant coefficient, linear equation sets that result for the linear stability formulation, the issue of numerical stability of the time integration is directly related to the spatial discretization. The instability seen in the EEME/SUPG and EVSS/SUPG methods is related to numerical instabilities that are inherent to these formulations. The calculations reported in Sections 5.2 and 5.3 show that the energy in the most dangerous disturbance is concentrated near a stationary streamline. This fact led us to conclude, using a heuristic argument, that the numerical instability was related to the compatibility of the finite element spaces for velocity gradient and stress in the limit where the constitutive equation reduces to an algebraic equation between these variables.

The EVSS-G and DEVSS-G formulations use an independent interpolation of the components of the velocity gradient tensor constructed so as to give compatible approximates for the velocity gradient and deviatoric stress. The two new numerical methods constructed are the EVSS-G and the DEVSS-G mixed methods. The EVSS-G/FEM was tested using the SUPG, SU and GLS hyperbolic equation solvers. Each appears to have much greater numerical stability than the original mixed finite element methods. In the two cases, EVSS-G/SUPG/FEM and EVSS-G/SU/FEM, no upper bound was found for the loss of stability in the plane Couette flow analysis up to $De = 200.0$. The DEVSS-G/FEM with the SUPG method also had no loss of stability up to $De = 100.0$; no doubt the methods are actually stable to higher values of De. The improved numerical stability of the EVSS-G/FEM results from the systematic balancing of the approximations to the velocity gradient terms and the stress in the constitutive equation, which gives a qualitative compatibility, at least in polynomial order, in the constitutive equation, when the velocity vanishes and the equation reduces to an algebraic equation.

Because no numerical stability limit was identified with these methods, the idea of Keiller (1992) that the onset of numerical instability, as seen in his finite difference discretizations, was connected with poor cross-stream resolution relative to the streamwise direction could not be tested in the context of our calculations with the EVSS-G methods, because no instability could be found. Possibly, the instability exists at higher values of De. Alternatively, the numerical results of Keiller (1992) may also be caused by the application of incompatible finite difference approximations for velocity gradients and stresses and would disappear with proper discretization.

One final caveat to developers of numerical methods needs to be mentioned. In our case a numerical method that was shown to be convergent with mesh refinement, accurate and robust for steady-state flow calculations still has a positive eigenvalue in the discretization of the spatial equations which was not detected in the normal tests for steady-state calculations. Both the EEME/FEM and EVSS/FEM are quite successful in the approximation of steady two-dimensional flows described by the UCM model. However, solution of the linear stability equations for planar Couette flow

with these two methods shows that the eigenspectrum of the continuous problem is not approximated accurately. Inaccuracy in the steady-state problem is generally found by the existence of "wiggles" or fictitious bifurcations that produce a singular Jacobian matrix. The inaccuracy found here is the result of a complex conjugate pair of eigenvalues that cross the imaginary axis, i.e., an oscillatory instability or a Hopf bifurcation. The presence of this instability cannot be determined by "wiggles" or a singular Jacobian matrix in the linearized system of steady-state equations. This shows the importance of testing an algorithm which is being extended to time dependent calculations for both the temporal stability, which checks the spatial discretization, as well as stability of the time integrator.

Chapter 6

Steady-State Computations with the EVSS-G/FEM and DEVSS-G/FEM

"And new Philosophy calls all in doubt,
The Element of fire is quite put out,
The Sun is lost, and th' earth, and no mans wit
Can well direct him; where to look for it."

– John Donne

The important observation in the previous chapter for the EVSS-G/FEM and DEVSS-G/FEM was that no numerical temporal instability was observed for the calculation of the linear stability of planar Couette flow using either SUPG or SU for the solution of the viscoelastic flow equations. This enhanced stability of the two mixed finite element methods has motivated the steady-state calculations presented here. The purpose of this chapter is to present calculations for steady-state flows to establish the accuracy and convergence with mesh refinement of the methods. Results for the calculation of two steady-state flows are given in detail. In addition, two other

geometries are mentioned where calculations have been performed by members of our group. The calculations are performed using finite element discretizations using embedded, irregular quadrilateral elements which allows local mesh refinement of the solution in regions of steep velocity and stress gradients. This mesh refinement is discussed in detail in Section 4.8.

Two steady-state test problems are included to demonstrate the accuracy of the EVSS-G/FEM and the DEVSS-G/FEM for steady-state flows. The first test problem is the flow of an Upper-Convected Maxwell fluid between eccentric rotating cylinders, which is well established as a test problem for the accuracy of numerical methods for viscoelastic flows (Beris *et al.,* 1983 and 1987, King *et al.,* 1988, and Rajagopalan *et al.,* 1990b). In the high eccentricity limit, this flow geometry is also known as the journal bearing. The calculations are presented for the UCM model because these calculations offer the greatest difficulty for numerical simulations (Rajagopalan *et al.,* 1990b). The EVSS-G/FEM is shown to be accurate and convergent with mesh for this flow. The second test problem is the flow of a CR-FENE fluid through an infinite periodic linear array of cylinders in a channel. First, the EVSS-G/FEM is examined and then the DEVSS-G/FEM is shown to give practically identical results. Finally a brief summary is given of calculations through two other geometries by members of our research group at MIT. These include the flow of an Oldroyd-B fluid through a wavy-walled tube, another very common test problem (Burdette *et al.,* 1989, Crochet & Legat, 1990 and Pilitsis & Beris, 1989), and the flow of a UCM fluid through an infinite two-dimensional, periodic square array of cylinders, as introduced by Khomami *et al.* (1994). These calculations serve to demonstrate the robustness of the combination of the EVSS-G/FEM and DEVSS-G/FEM with the locally adaptive mesh refinement for computing complex viscoelastic flows.

For confined flows, the partial differential equations defining the viscoelastic flow are solved with specified boundary conditions on the components of velocity along solid boundaries, appropriate inlet and outlet boundary conditions on the velocity field and stress conditions specified only on inflow boundaries. On solid surfaces the fluid is assumed to satisfy no-slip and no-penetration conditions so that the veloc-

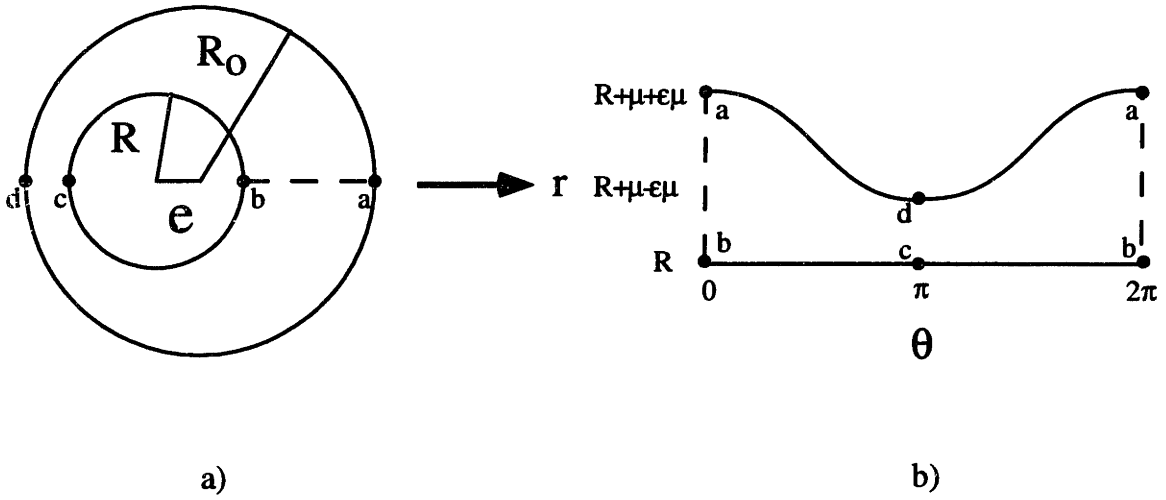

a) b)

Figure 6-1: Schematic diagram of the eccentric cylinder geometry: (a) original geometry and (b) mapped geometry used in contour plots.

ity field vanishes there. All the flows considered here are spatially periodic in one-dimension so that periodic constraints replace the need for inlet and outlet boundary conditions. In the two-dimesional periodic square array of cylinders, symmetry boundaries are included.

6.1 Eccentric Cylinder for EVSS-G/FEM

6.1.1 Flow Geometry

The geometry for viscoelastic flow between eccentric rotating cylinders is shown schematically in Figure 6-1(a). Fluid flows in the gap between two nested cylinders whose axes are parallel, but offset by a distance e. The inner cylinder has radius R and is rotating at an angular velocity of Ω. The outer cylinder has radius R_o and is stationary. The length and velocity scales are the radius of the inner cylinder R and the linear velocity ΩR, respectively. The geometry is defined by two dimensionless parameters: the mean gap thickness

$$\mu \equiv \frac{R_o - R}{R_o}, \tag{6.1}$$

and the eccentricity

$$\epsilon \equiv \frac{e}{R_o - R}, \tag{6.2}$$

both of which vary between zero and one. For the calculations presented here, only the mean gap thickness, $\mu = 0.1$, is used as in the previous studies found in the literature. The flow is almost one-dimensional in the limit of small eccentricity. The equations are written in polar coordinates to take advantage of this feature with the center of the inner cylinder taken as the polar origin so that the inner rotating cylinder is a coordinate surface. Flow separation exists for larger eccentricity for both the Newtonian and UCM fluids in creeping flow, as has been established by asymptotic analysis (Beris *et al.*, 1983) and by spectral/finite element calculations (Beris *et al.*, 1987). High eccentricity flow is difficult to compute numerically because it is a combination of different types of kinematics: a lubrication-like flow in the narrow gap region and a complex two-dimensional flow in the wide gap region. Results are presented here as contour maps of variables plotted in the modified domain formed by straightening the outer surface and stretching the gap between the cylinders as shown in Figure 6-1(b). This representation has been used in other publications of calculations for this flow.

This is a convenient problem to analyze because the flow geometry is smooth and no sharp corners exist that may introduce singularities or discontinuities into the viscoelastic flow equations. This simplification along with periodicity allows for the focus to be on the performance of the numerical formulation and not on other external factors. The boundary conditions to be imposed are no slip and no penetration along the boundary walls. Along the inner cylinder this can be expressed as

$$v_\theta(R,\theta) = \Omega R, \qquad 0 \le \theta \le 2\pi, \tag{6.3}$$

$$v_r(R,\theta) = 0, \qquad 0 \le \theta \le 2\pi, \tag{6.4}$$

and along the outer cylinder,

$$v_\theta(r,\theta) = v_r(r,\theta) = 0, \qquad 0 \le \theta \le 2\pi. \tag{6.5}$$

The pressure boundary condition is specified on the outer cylinder at $\theta = 0 = 2\pi$

$$p(R + \mu + \epsilon\mu, 0) = p(R + \mu + \epsilon\mu, 2\pi) = 0. \tag{6.6}$$

This flow geometry was chosen as a benchmark problem for comparisons between various numerical algorithms at the 5th International Workshop on Numerical Methods in Non-Newtonian Flow. Thus, there is adequate data available in the literature for direct comparison; we will compare our results with the EVSS-G/FEM to the EVSS/FEM calculations which in turn has been shown to be accurate and convergent with mesh in this geometry (Rajagopalan *et al.*, 1990b and Rajagopalan, 1991).

6.1.2 Concentric Cylinders (Eccentricity = 0.0)

For a UCM fluid there is an analytical solution to the concentric ($\epsilon = 0.0$) cylinder problem for all De and μ in the inertialess limit

$$v_r = 0, \tag{6.7}$$

$$v_\theta = c_1 r + c_2/r, \tag{6.8}$$

$$\tau_{rr} = 0, \tag{6.9}$$

$$\tau_{\theta\theta} = De\left(\frac{-8c_2^2}{r^4}\right), \tag{6.10}$$

$$\tau_{r\theta} = 2c_2/r^2, \tag{6.11}$$

$$p = p_0 + De\left[2c_2^2\left(\frac{1}{r^4} - \frac{1}{(1+\mu)^4}\right)\right], \tag{6.12}$$

$$G_{rr} = \frac{\partial v_r}{\partial r} = 0, \tag{6.13}$$

$$G_{r\theta} = \frac{\partial v_\theta}{\partial r} = c_1 - c_2/r^2, \tag{6.14}$$

$$G_{\theta r} = \frac{1}{r}\frac{\partial v_r}{\partial \theta} - \frac{v_\theta}{r} = -c_1 - c_2/r^2, \tag{6.15}$$

where

$$c_1 = 1 - c_2, \tag{6.16}$$

$$c_2 = \frac{(1+\mu)^2}{(1+\mu)^2 - 1}, \tag{6.17}$$

$$p_0 = 0. \tag{6.18}$$

For the EVSS, EVSS-G, and DEVSS-G formulations the extra stress $\boldsymbol{\tau}$ is converted into the elastic stress, $\boldsymbol{\Sigma}$, via eq. (4.20). Using this equation to substitute the analytic solution results in the following form of the elastic stress components

$$\Sigma_{rr} = 0, \tag{6.19}$$

$$\Sigma_{\theta\theta} = De\left(\frac{-8c_2^2}{r^4}\right), \tag{6.20}$$

$$\Sigma_{r\theta} = 0. \tag{6.21}$$

Now if we let $\mu = 0.1$, then $c_1 = -4.76$ and $c_2 = 5.76$ which gives the following ranges for the nonzero variables for $r = [1, 1.1]$: $v_\theta = [1, 0]$, $G_{r\theta} = [-10.52, -9.52]$, $G_{\theta r} = [-1, 0]$, $\Sigma_{\theta\theta} = De[-265, -181]$ and $p = De[21, 0]$. These values will be used for comparison with the numerical method to determine the error in the approximation.

Both upwinding methods, SU and SUPG, were examined; it was found that for concentric cylinders, the results were identical. Thus, only SUPG results will be shown. Also, only the contours of the two variables which vary with De, $\Sigma_{\theta\theta}$ and p, will be examined on a uniform 10x10 mesh. The development of the flow field for the concentric cylinder calculation with $\mu = 0.1$ for the UCM fluid is shown in Figure 6-2 for $De = 1.0$ and 7.0. The maximum and minimum values of the variables are listed in Table 6.1 and compared to the exact solution; the percent error is always less than 0.5%. No upper limit in De was found for this flow. This shows the excellent accuracy attained for the EVSS-G/FEM for a one-dimensional shear flow.

6.1.3 Eccentricity = 0.1

The finite element meshes used for the eccentricity greater than zero cases are uniform in both the θ- and r-directions with 20x5, 40x10 and 80x20 elements in each direction, respectively; these meshes result in 2 858, 11 430 and 45 720 degrees of freedom in

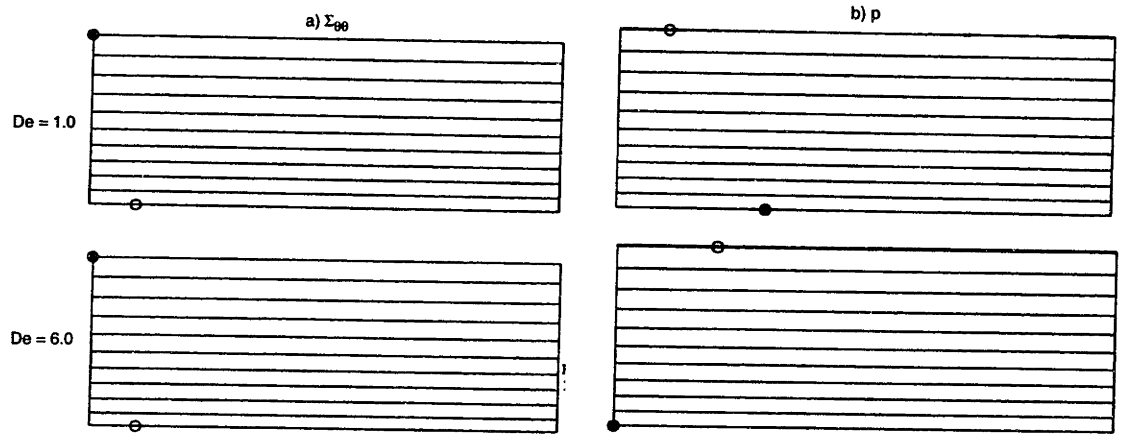

Figure 6-2: Contours of solution fields of (a) $\Sigma_{\theta\theta}$ and (b) p for flow between concentric rotating cylinders for the UCM model with $\mu = 0.1$ and Deborah numbers of 1.0 and 7.0. Contours are shown as computed with the SUPG or SU discretization of the constitutive equations.

Variable	De	Value	Exact
$\Sigma_{\theta\theta}$	1.0	-181.4	-181.4
		-265.6	-265.6
	7.0	-1267	-1270
		-1864	-1859
p	1.0	21.04	21.05
		0.0	0.0
	7.0	147.3	147.3
		0.0	0.0

Table 6.1: Comparison of the numerical and exact solution for concentric cylinder flow of a UCM model with $\mu = 0.1$. SUPG and SU give the same results with the EVSS-G/FEM. Calculations were performed on a 10x10 mesh and $De = 1.0$ and 7.0.

the finite element calculations, respectively. The development of the flow field for $\epsilon = \mu = 0.1$ for the UCM fluid on an 80x20 mesh is shown in Figures 6-3 – 6-8 for Deborah numbers of 0.0, 1.0 and 5.0 as computed using the Galerkin method to discretize the constitutive equations. The results for $De = 5.0$ show the spurious oscillations and wiggles that are indicative of the Galerkin method, especially in the contours for v_θ. The $De = 1.0$ results are well-behaved and fairly accurate (see Table 6.3 below). The highest achievable De with an 80x20 mesh was 5.2.

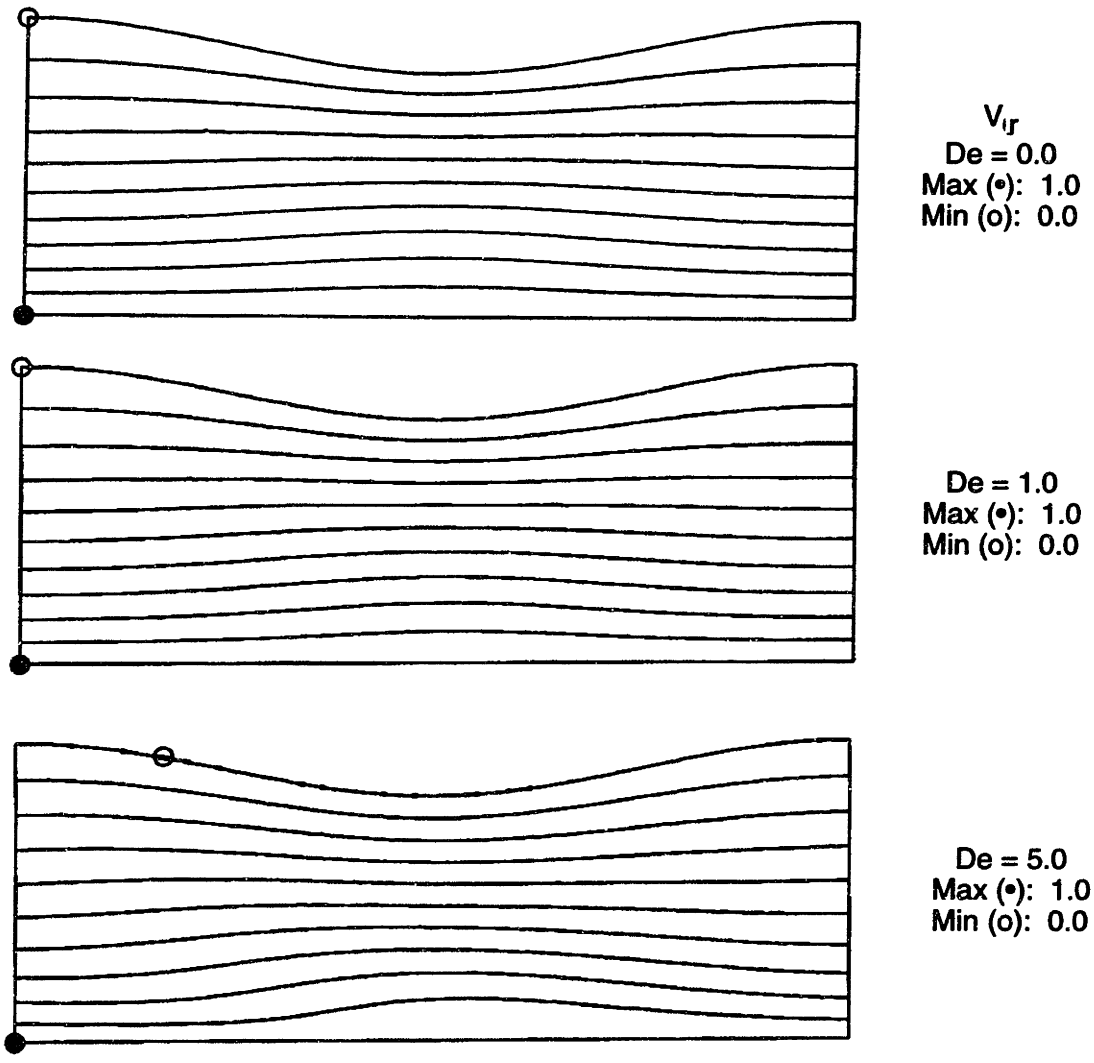

Figure 6-3: Contours of the solution field for v_r for the flow between eccentric rotating cylinders for the UCM model with $\epsilon = \mu = 0.1$ and Deborah numbers of 0.0, 1.0, and 5.0 as computed with the Galerkin discretization of the constitutive equations. Maximum and minimum values of the variable are shown.

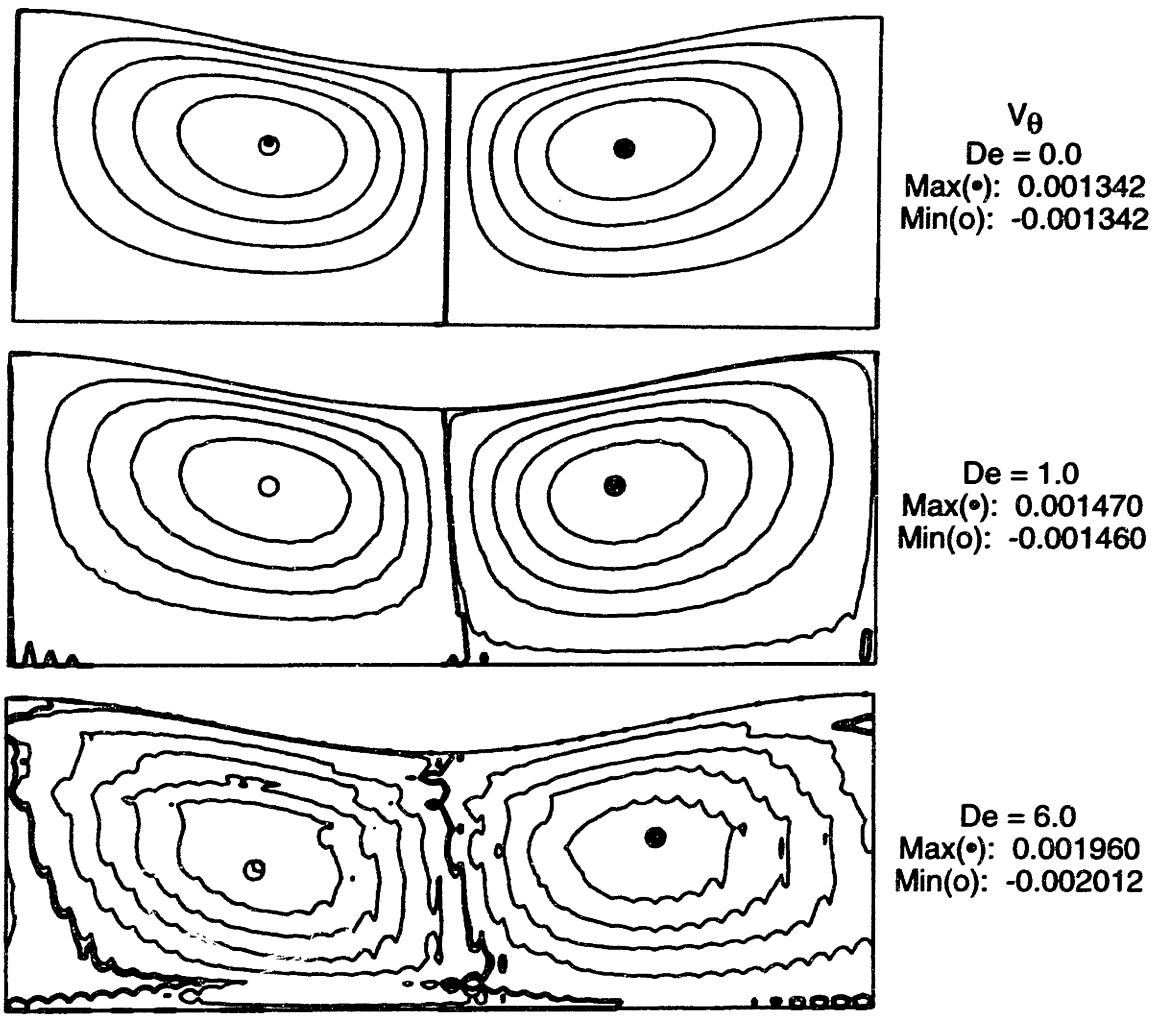

Figure 6-4: Contours of the solution field for v_θ for the flow between eccentric rotating cylinders for the UCM model with $\epsilon = \mu = 0.1$ and Deborah numbers of 0.0, 1.0, and 5.0 as computed with the Galerkin discretization of the constitutive equations. Maximum and minimum values of the variable are shown.

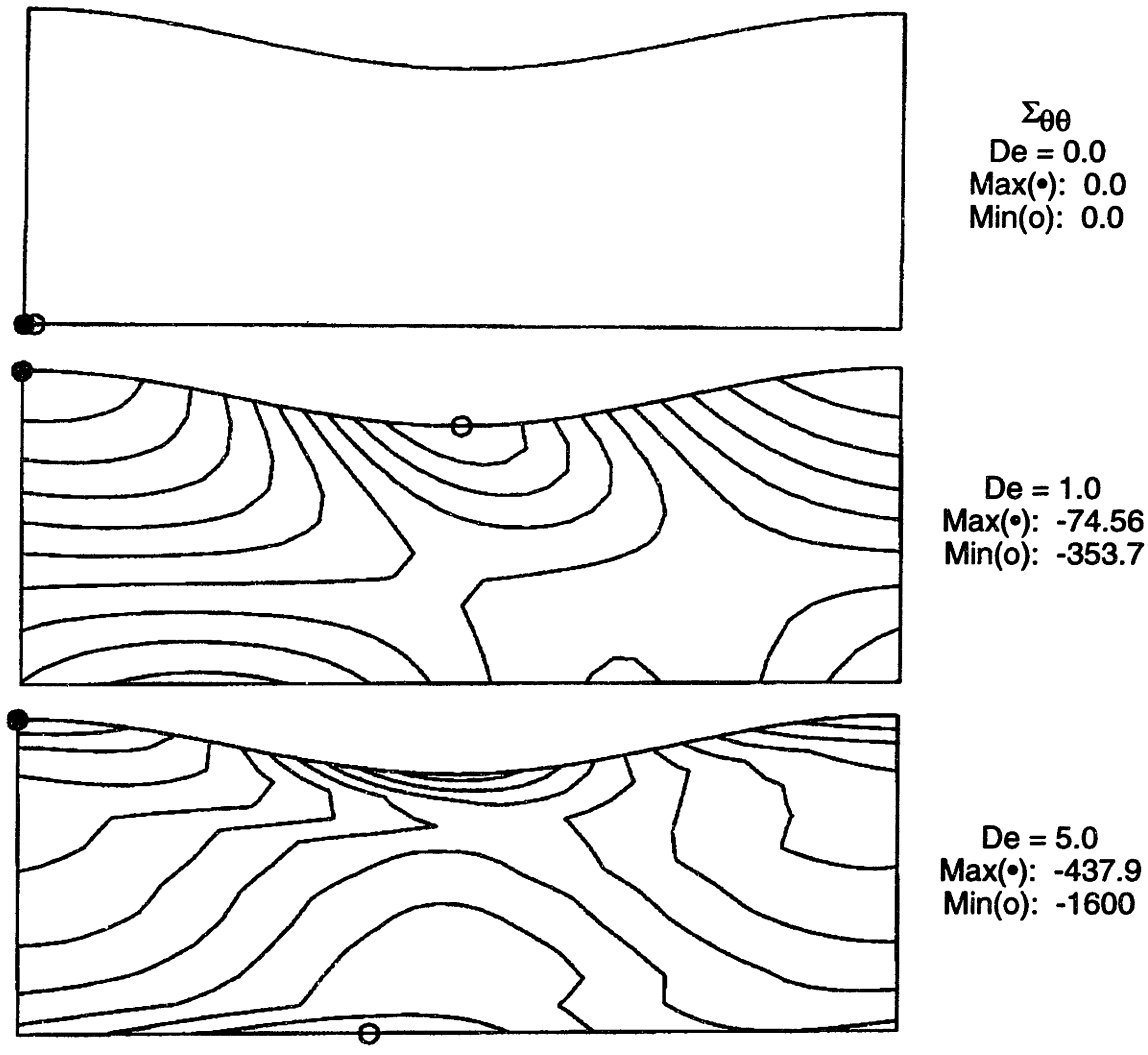

Figure 6-5: Contours of the solution field for $\Sigma_{\theta\theta}$ for the flow between eccentric rotating cylinders for the UCM model with $\epsilon = \mu = 0.1$ and Deborah numbers of 0.0, 1.0, and 5.0 as computed with the Galerkin discretization of the constitutive equations. Maximum and minimum values of the variable are shown.

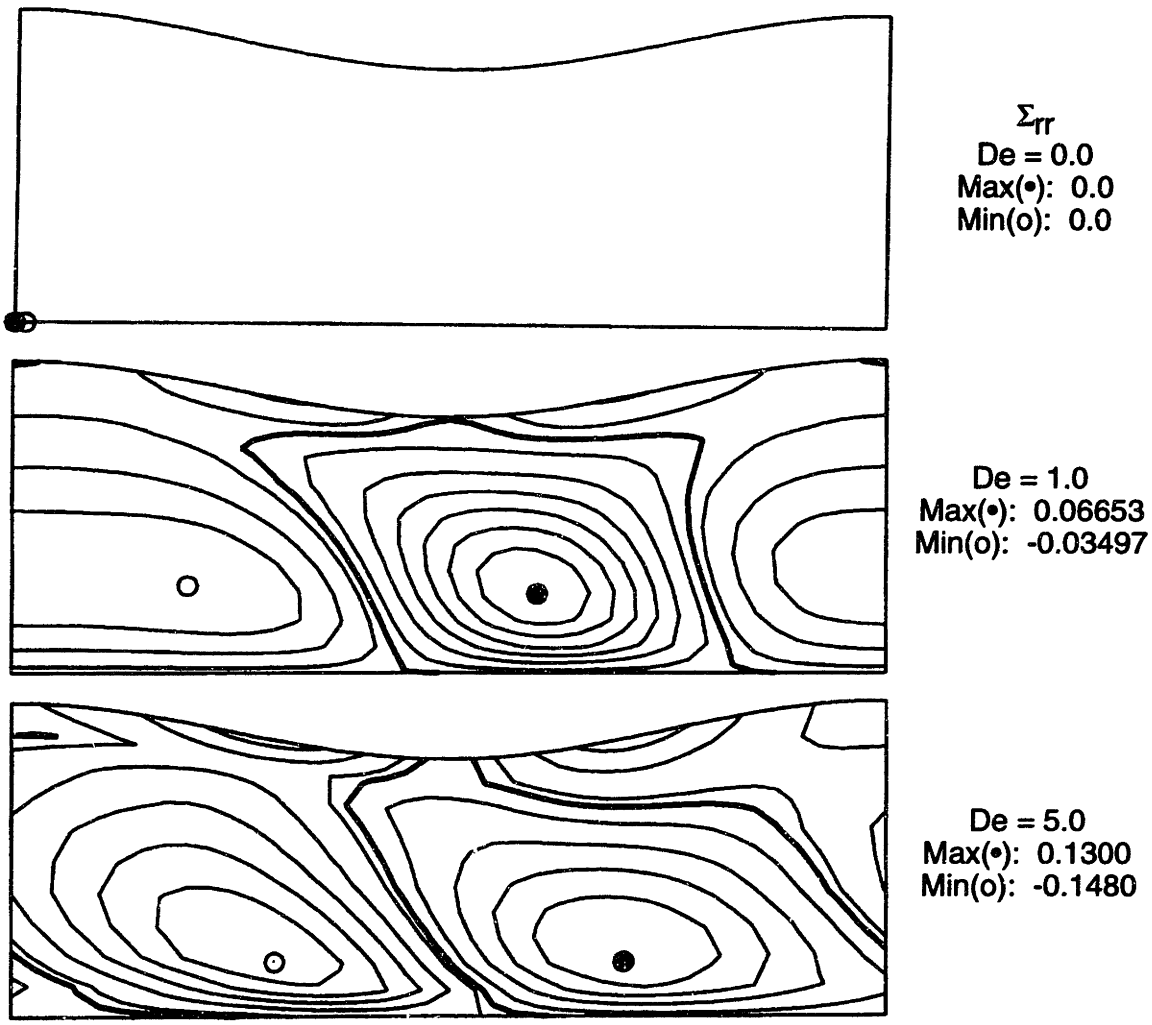

Figure 6-6: Contours of the solution field for Σ_{rr} for the flow between eccentric rotating cylinders for the UCM model with $\epsilon = \mu = 0.1$ and Deborah numbers of 0.0, 1.0, and 5.0 as computed with the Galerkin discretization of the constitutive equations. Maximum and minimum values of the variable are shown.

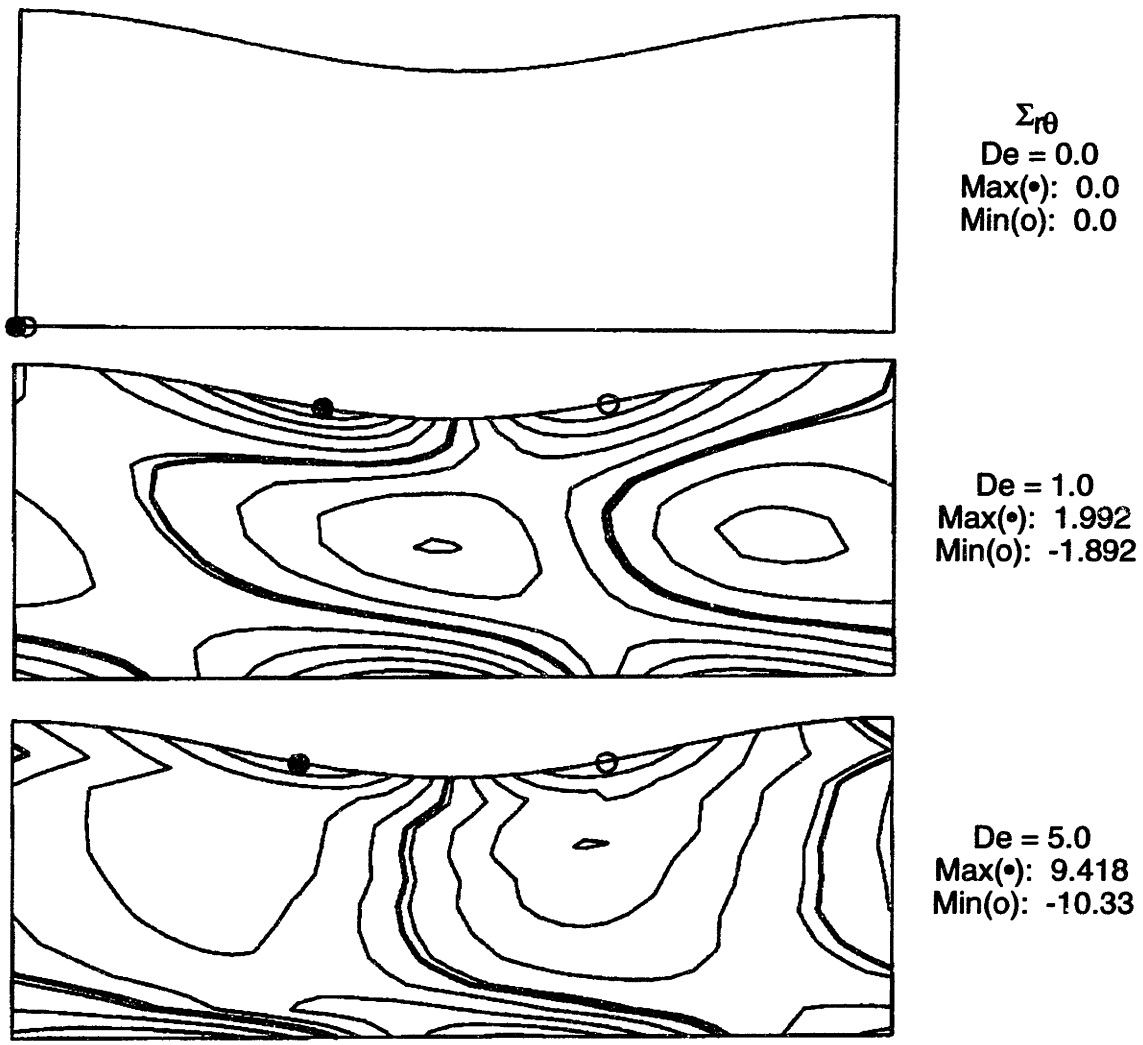

Figure 6-7: Contours of the solution field for $\Sigma_{r\theta}$ for the flow between eccentric rotating cylinders for the UCM model with $\epsilon = \mu = 0.1$ and Deborah numbers of 0.0, 1.0, and 5.0 as computed with the Galerkin discretization of the constitutive equations. Maximum and minimum values of the variable are shown.

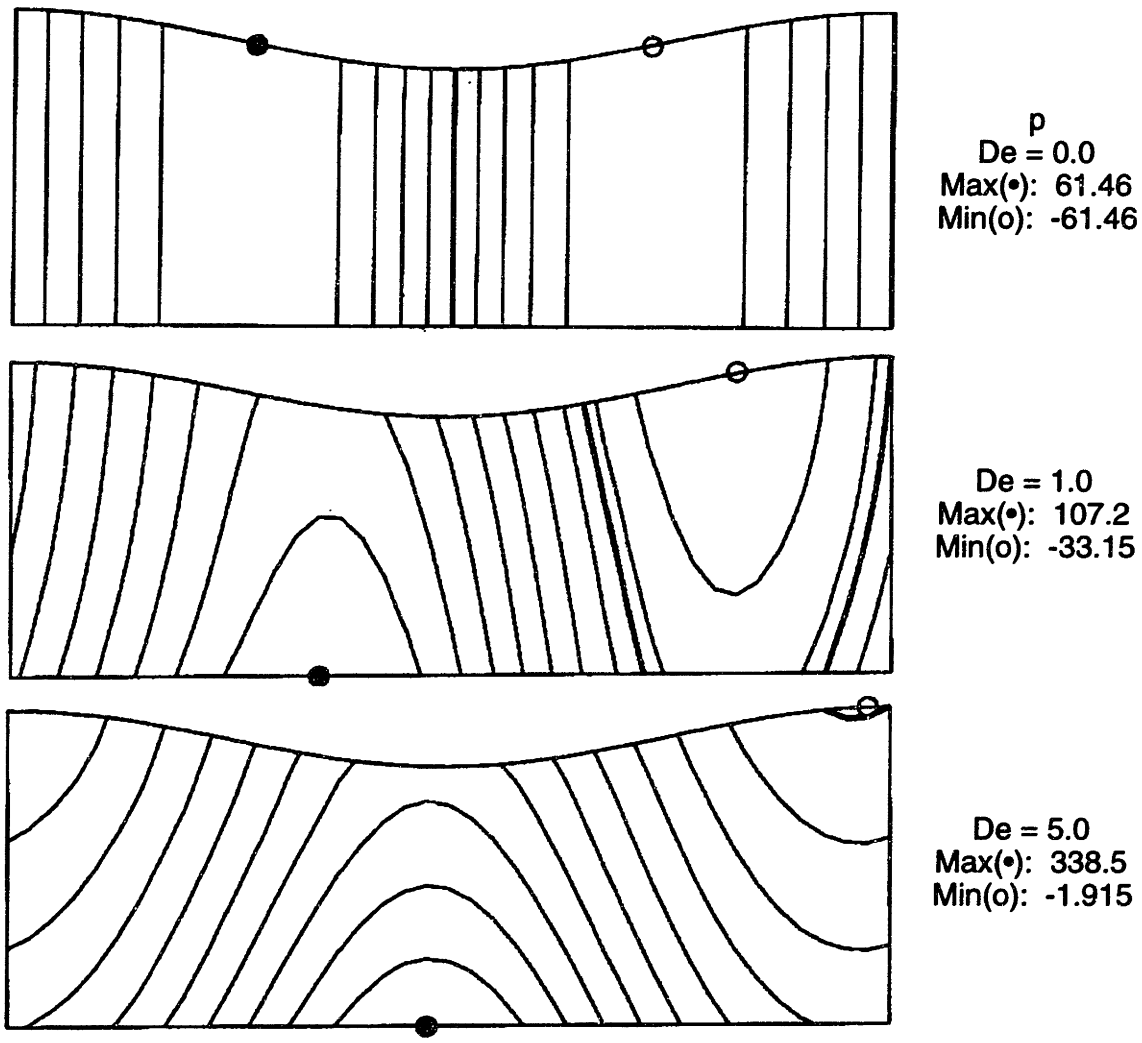

Figure 6-8: Contours of the solution field for p for the flow between eccentric rotating cylinders for the UCM model with $\epsilon = \mu = 0.1$ and Deborah numbers of 0.0, 1.0, and 5.0 as computed with the Galerkin discretization of the constitutive equations. Maximum and minimum values of the variable are shown.

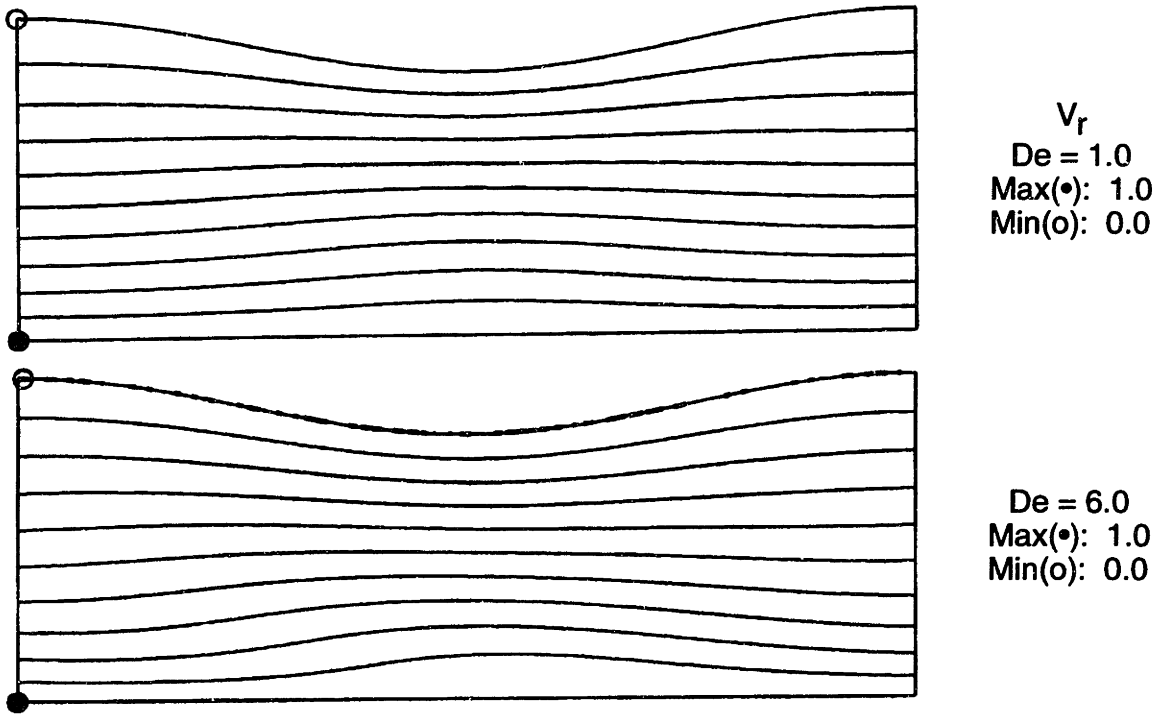

Figure 6-9: Contours of the solution field for v_r for the flow between eccentric rotating cylinders for the UCM model with $\epsilon = \mu = 0.1$ and Deborah numbers of 1.0 and 6.0 as computed with the SUPG discretization of the constitutive equations. Maximum and minimum values of the variable are shown.

The development of the flow field for $\epsilon = \mu = 0.1$ for the UCM fluid on an 80x20 mesh is shown in Figures 6-9 – 6-14 for Deborah numbers of 1.0 and 6.0 as computed using the SUPG method to discretize the constitutive equations. The maximum and minimum values for the two variables, v_θ and $\Sigma_{\theta\theta}$, shown in Figures 6-10 and 6-11, respectively, are listed in Table 6.2 for the three finite element meshes with $De = 1.0$. The values computed by Rajagopalan *et al.* (1990b) with the EVSS method and the 80x20 mesh also are listed; the EVSS and EVSS-G results are in excellent agreement, with the largest difference being less than 1.5%. The contour plots for these two solution fields, v_θ and $\Sigma_{\theta\theta}$, are plotted as a function of mesh refinement in Figures 6-15 and 6-16, respectively. This shows the convergence of the EVSS-G/FEM with uniform mesh refinement.

Calculations implementing the SU method for the small eccentricity case are shown in Figures 6-17 – 6-22 for $De = 1.0$ and 6.0. Table 6.3 is organized similar to

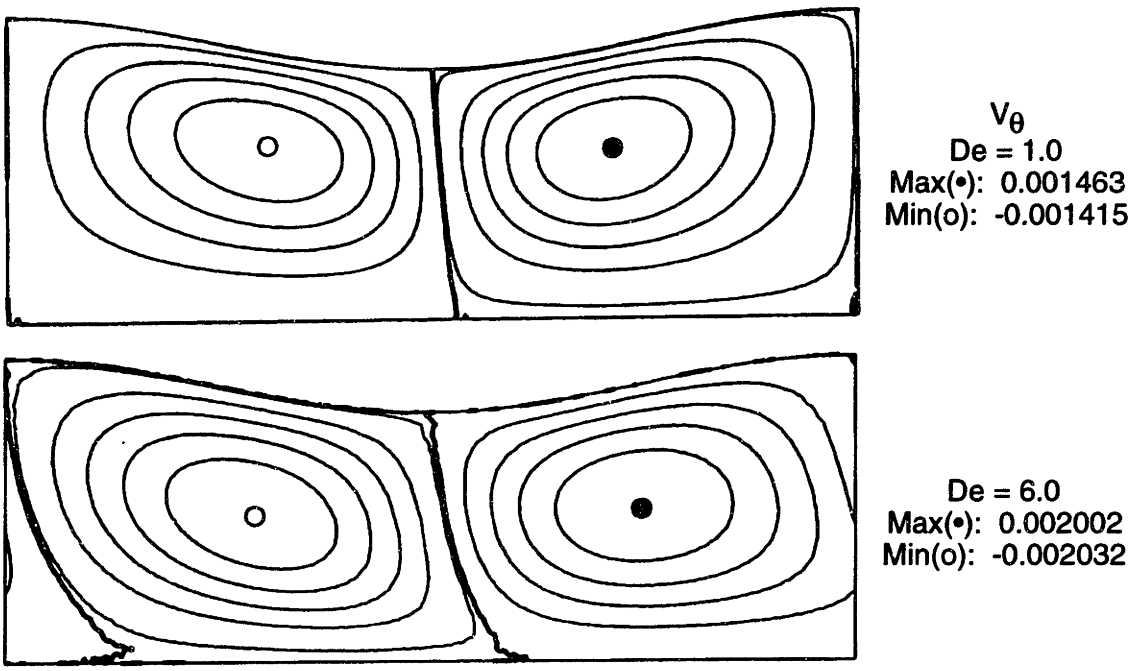

Figure 6-10: Contours of the solution field for v_θ for the flow between eccentric rotating cylinders for the UCM model with $\epsilon = \mu = 0.1$ and Deborah numbers of 1.0 and 6.0 as computed with the SUPG discretization of the constitutive equations. Maximum and minimum values of the variable are shown.

Variable	Method/Mesh	Maximum Value	Minimum Value	d.o.f.
v_θ	EVSS-G/20x5	0.001544	−0.001437	2858
	EVSS-G/40x10	0.001472	−0.001417	11430
	EVSS-G/80x20	0.001463	−0.001415	45720
	EVSS/80x20	0.001481	−0.001426	40640
$\Sigma_{\theta\theta}$	EVSS-G/20x5	−73.18	−359.6	2858
	EVSS-G/40x10	−74.56	−353.7	11430
	EVSS-G/80x20	−74.88	−352.6	45720
	EVSS/80x20	−75.16	−352.5	40640

Table 6.2: Convergence of calculations for eccentric rotating cylinder flow for the UCM model with $De = 1.0$ and $\epsilon = \mu = 0.1$. Calculations are listed for the EVSS-G/FEM with three meshes and the results of Rajagopalan *et al.* (1990b) for an 80x20 mesh.

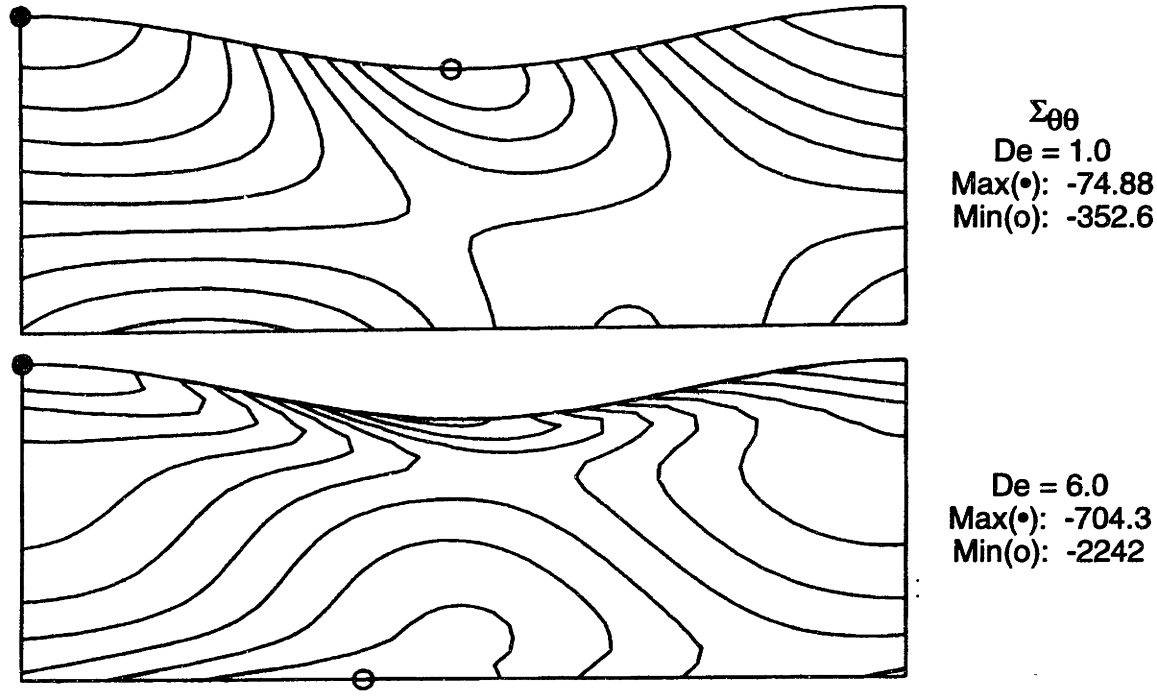

Figure 6-11: Contours of the solution field for $\Sigma_{\theta\theta}$ for the flow between eccentric rotating cylinders for the UCM model with $\epsilon = \mu = 0.1$ and Deborah numbers of 1.0 and 6.0 as computed with the SUPG discretization of the constitutive equations. Maximum and minimum values of the variable are shown.

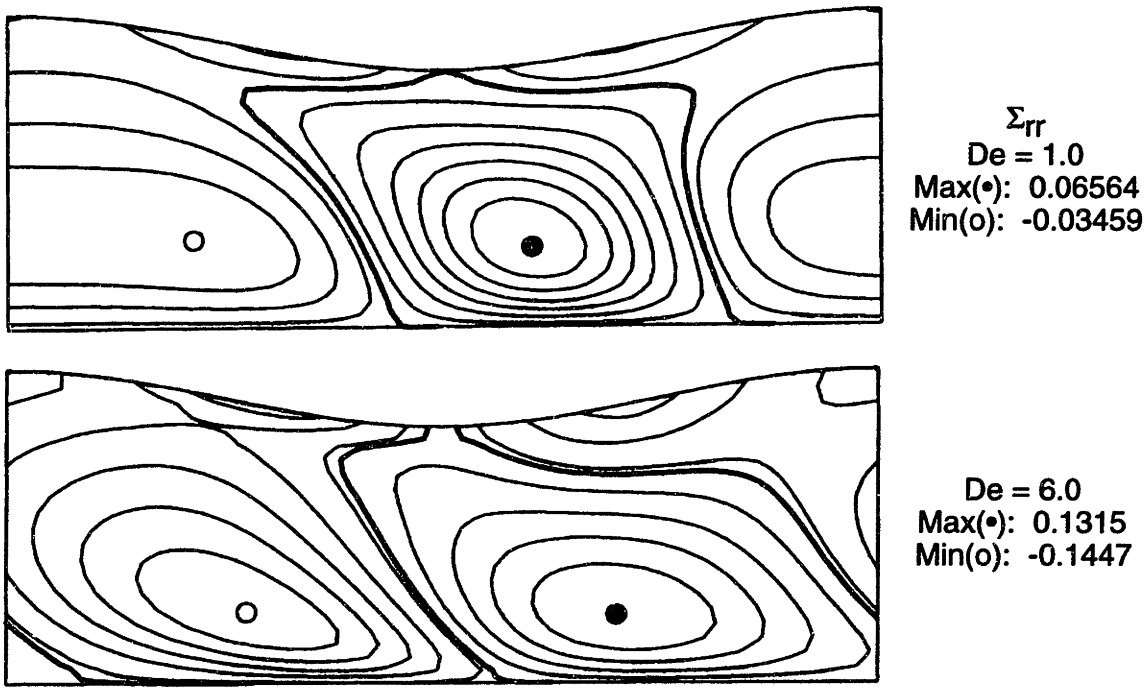

Figure 6-12: Contours of the solution field for Σ_{rr} for the flow between eccentric rotating cylinders for the UCM model with $\epsilon = \mu = 0.1$ and Deborah numbers of 1.0 and 6.0 as computed with the SUPG discretization of the constitutive equations. Maximum and minimum values of the variable are shown.

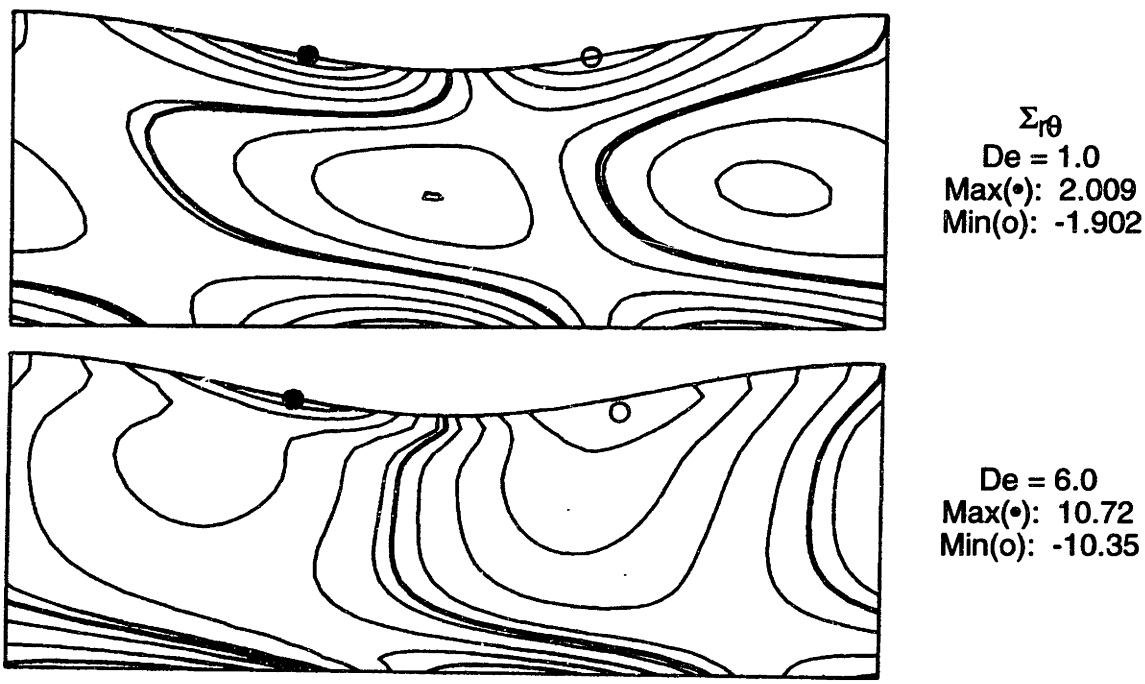

Figure 6-13: Contours of the solution field for $\Sigma_{r\theta}$ for the flow between eccentric rotating cylinders for the UCM model with $\epsilon = \mu = 0.1$ and Deborah numbers of 1.0 and 6.0 as computed with the SUPG discretization of the constitutive equations. Maximum and minimum values of the variable are shown.

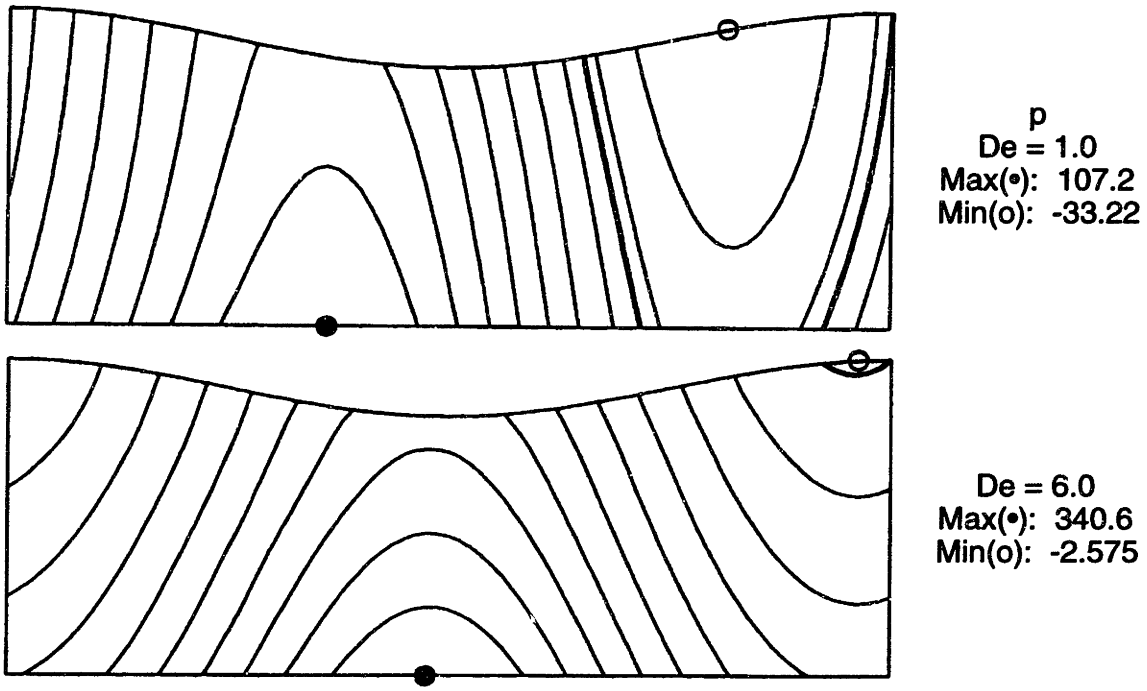

Figure 6-14: Contours of the solution field for p for the flow between eccentric rotating cylinders for the UCM model with $\epsilon = \mu = 0.1$ and Deborah numbers of 1.0 and 6.0 as computed with the SUPG discretization of the constitutive equations. Maximum and minimum values of the variable are shown.

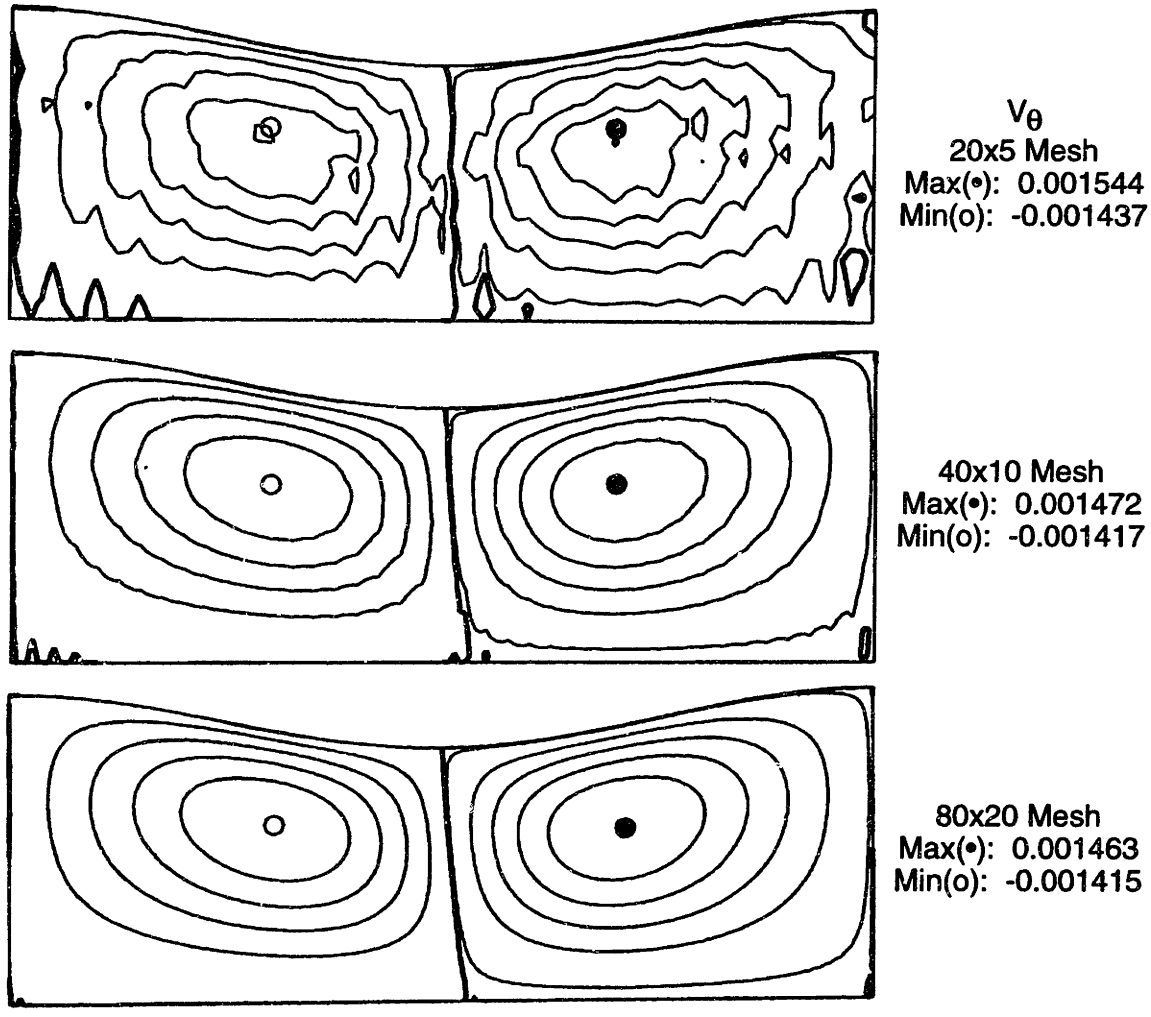

Figure 6-15: Contours of the solution field for v_θ for the flow between eccentric rotating cylinders for the UCM model with $\epsilon = \mu = 0.1$ and $De = 1.0$ for the three meshes 20x5, 40x10, and 80x20 as computed with the SUPG discretization of the constitutive equations. Maximum and minimum values of the variable are shown.

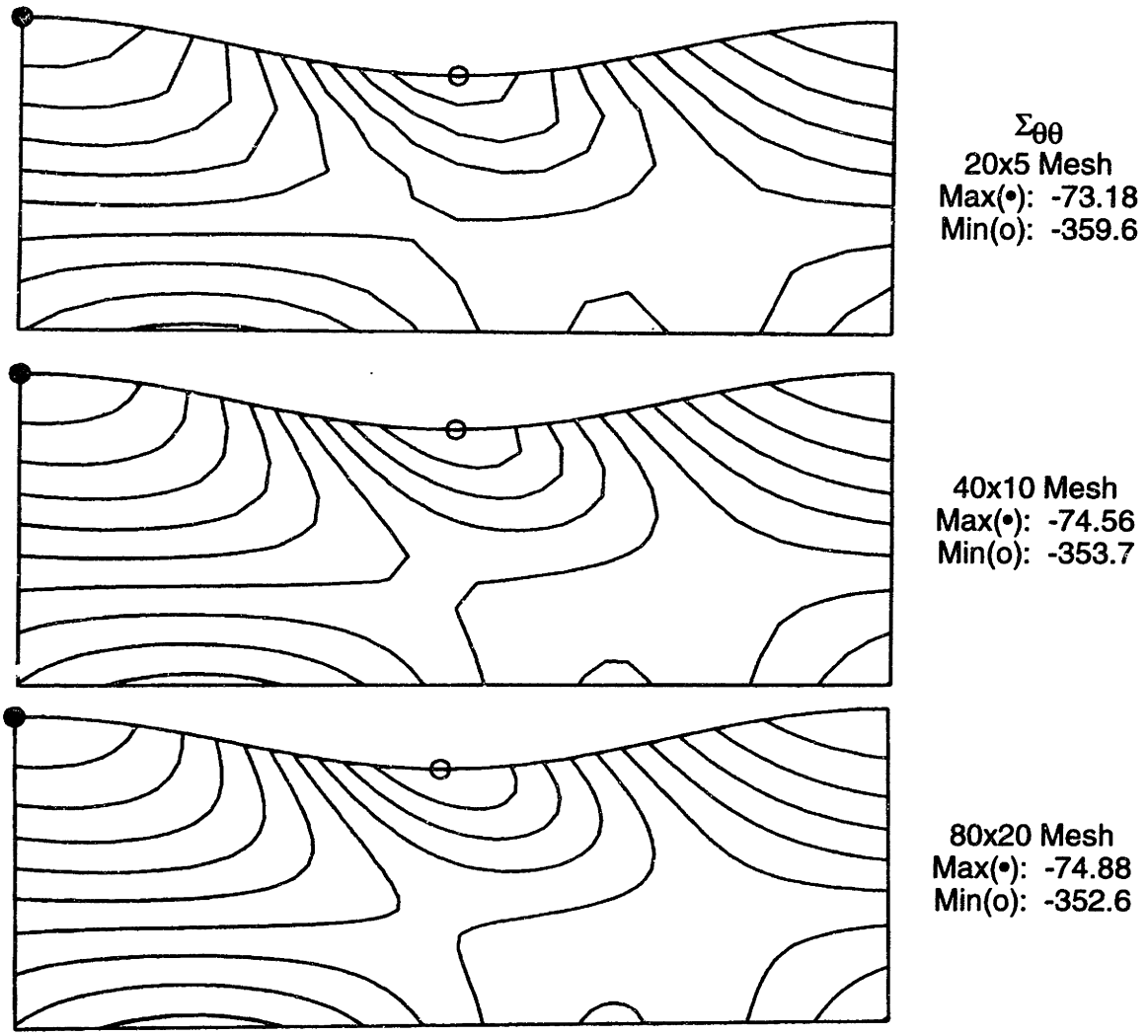

Figure 6-16: Contours of the solution field for $\Sigma_{\theta\theta}$ for the flow between eccentric rotating cylinders for the UCM model with $\epsilon = \mu = 0.1$ and $De = 1.0$ for the three meshes 20x5, 40x10, and 80x20 as computed with the SUPG discretization of the constitutive equations. Maximum and minimum values of the variable are shown.

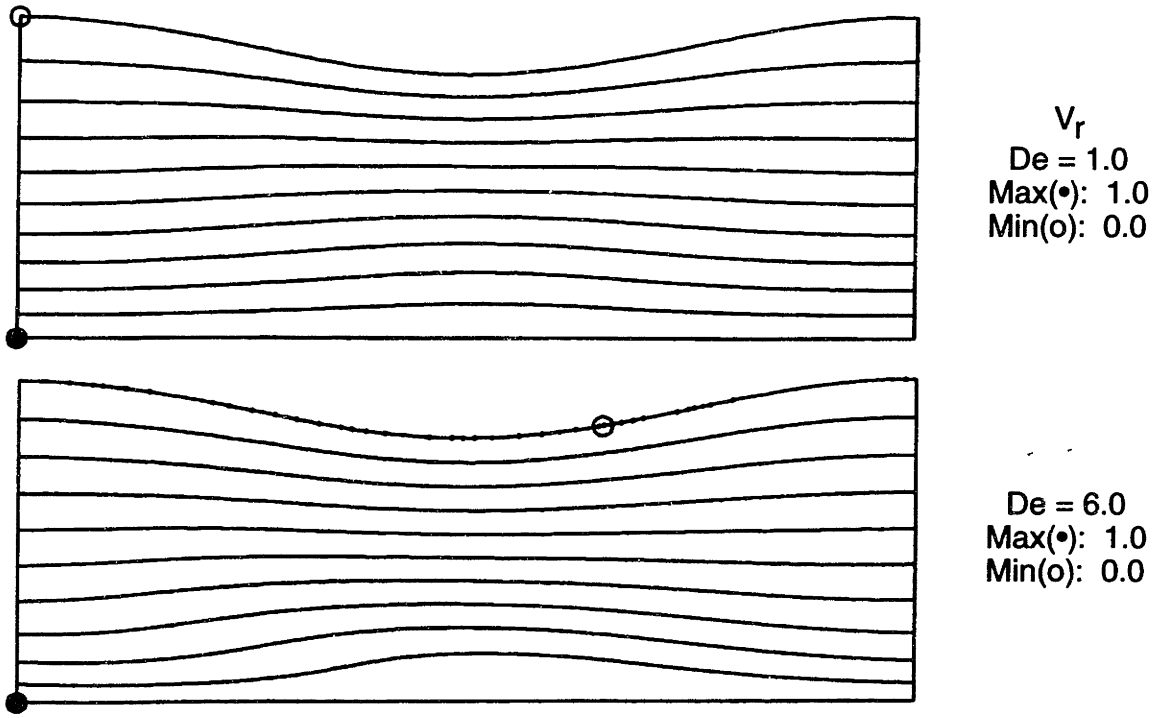

Figure 6-17: Contours of the solution field for v_r for the flow between eccentric rotating cylinders for the UCM model with $\epsilon = \mu = 0.1$ and Deborah numbers of 1.0 and 6.0 as computed with the SU discretization of the constitutive equations. Maximum and minimum values of the variable are shown.

Table 6.2 to compare the calculations using the EVSS-G finite element discretization with the GAL, SUPG and SU methods at Deborah numbers of 1.0 and 6.0. The results are in close agreement for $De = 1.0$, but are less so for $De = 6.0$ with the largest difference being less than 15%.

This divergence of the results between the SU and SUPG methods will be examined further in Section 6.3. The maximum attainable Deborah number with the uniform 80x20 mesh for three values of the eccentricity are shown in Table 6.4. The values are comparable except for $\epsilon = 0.8$, where there is significant flow recirculation. The trend shown in Table 6.3 for $\epsilon = 0.1$ continues for the two other eccentricities calculated ($\epsilon = 0.4$ and 0.8) in that the SUPG and SU methods produce slightly different results as De is increased.

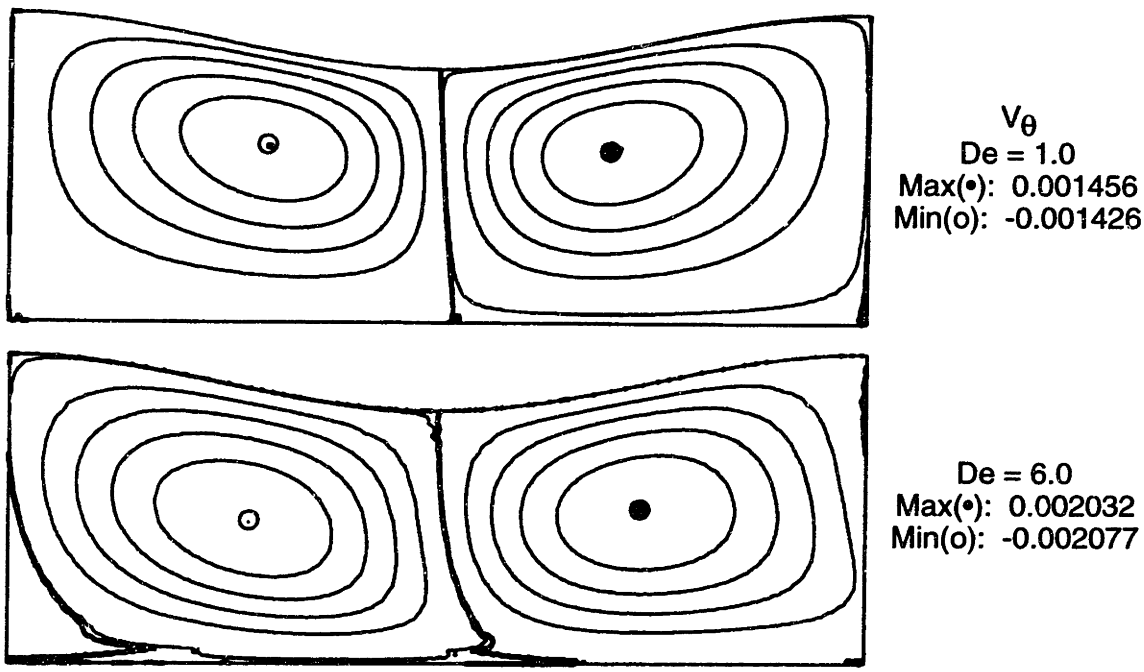

Figure 6-18: Contours of the solution field for v_θ for the flow between eccentric rotating cylinders for the UCM model with $\epsilon = \mu = 0.1$ and Deborah numbers of 1.0 and 6.0 as computed with the SU discretization of the constitutive equations. Maximum and minimum values of the variable are shown.

Variable	De	Upwind Method	Maximum Value	Minimum Value
v_θ	1.0	SUPG	0.001463	−0.001415
		SU	0.001456	−0.001426
		GAL	0.001470	−0.001407
	6.0	SUPG	0.002002	−0.002099
		SU	0.002032	−0.002077
$\Sigma_{\theta\theta}$	1.0	SUPG	−74.88	−359.6
		SU	−74.91	−352.5
		GAL	−74.56	−353.7
	6.0	SUPG	−704.3	−2242
		SU	−617.1	−1919

Table 6.3: Comparison of calculations for eccentric rotating cylinder flow for the UCM model with $\epsilon = \mu = 0.1$ for the SUPG and SU discretizations with the EVSS-G/FEM. The Galerkin discretization results are included for $De = 1.0$. Calculations are listed with an 80x20 mesh and $De = 1.0$ and 6.0.

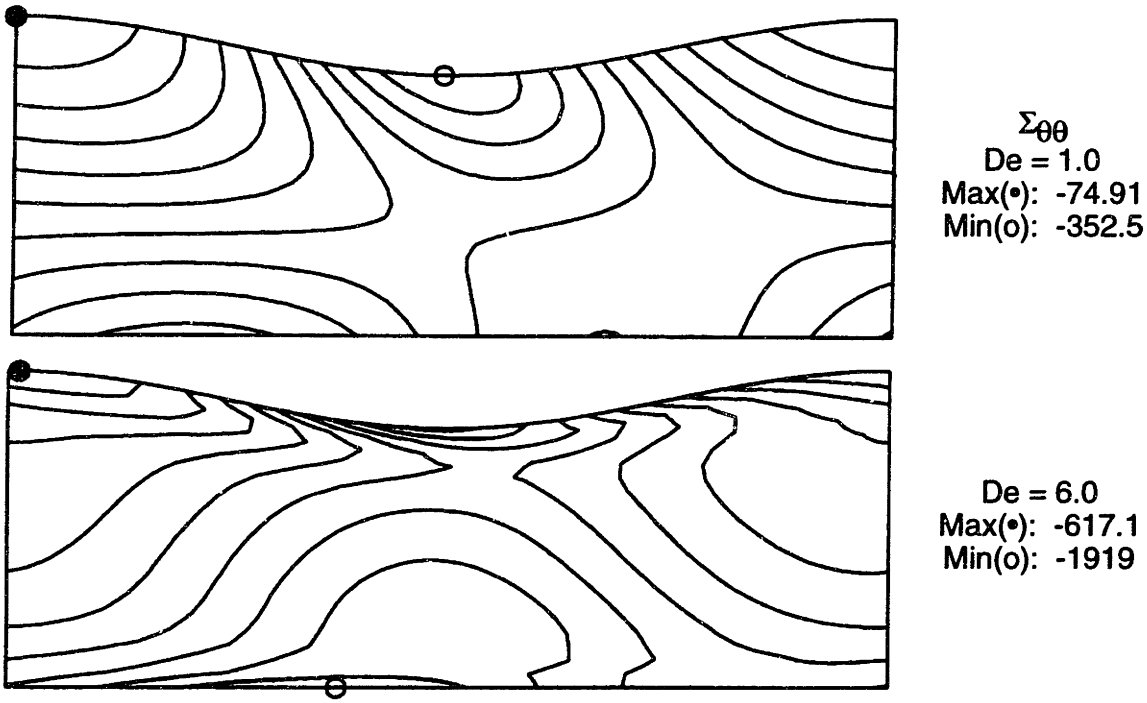

Figure 6-19: Contours of the solution field for $\Sigma_{\theta\theta}$ for the flow between eccentric rotating cylinders for the UCM model with $\epsilon = \mu = 0.1$ and Deborah numbers of 1.0 and 6.0 as computed with the SU discretization of the constitutive equations. Maximum and minimum values of the variable are shown.

Eccentricity, ϵ	Upwind Method	Maximum Attainable De
0.1	SUPG	6.9
	SU	6.7
	GAL	5.2
0.4	SUPG	2.0
	SU	2.4
0.8	SUPG	0.85
	SU	0.5

Table 6.4: Comparison of maximum attainable De for a uniformly spaced 80x20 mesh and $\mu = 0.1$ at three eccentricities using SUPG and SU for the EVSS-G/FEM. The Galerkin method is included for $\epsilon = 0.1$.

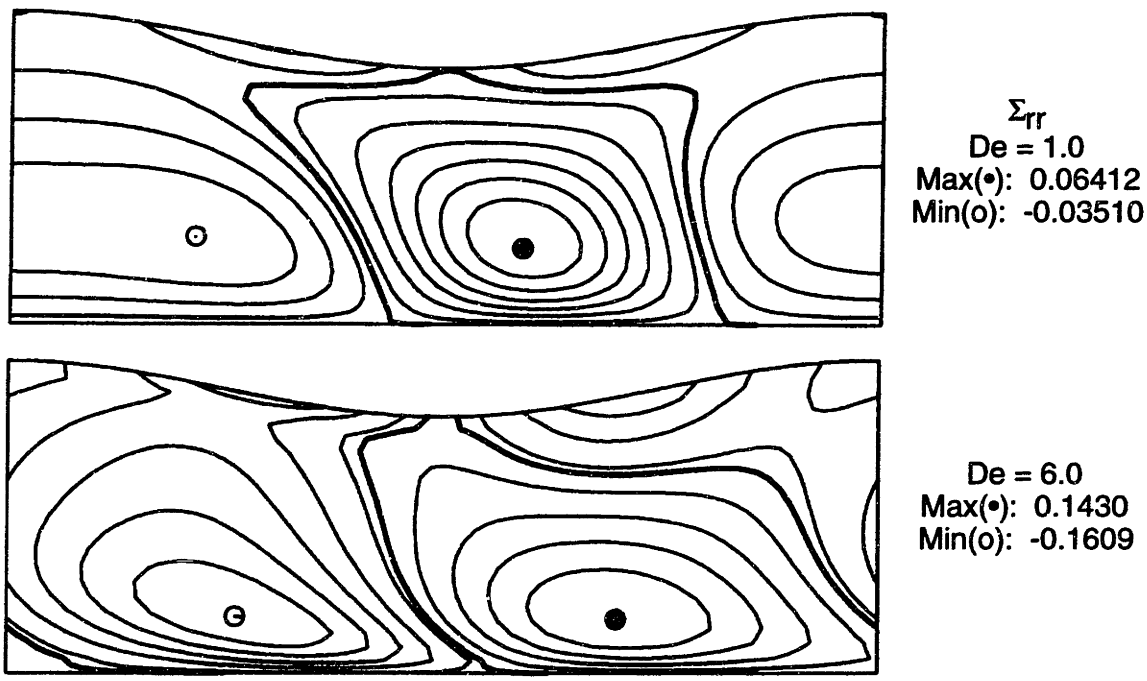

Figure 6-20: Contours of the solution field for Σ_{rr} for the flow between eccentric rotating cylinders for the UCM model with $\epsilon = \mu = 0.1$ and Deborah numbers of 1.0 and 6.0 as computed with the SU discretization of the constitutive equations. Maximum and minimum values of the variable are shown.

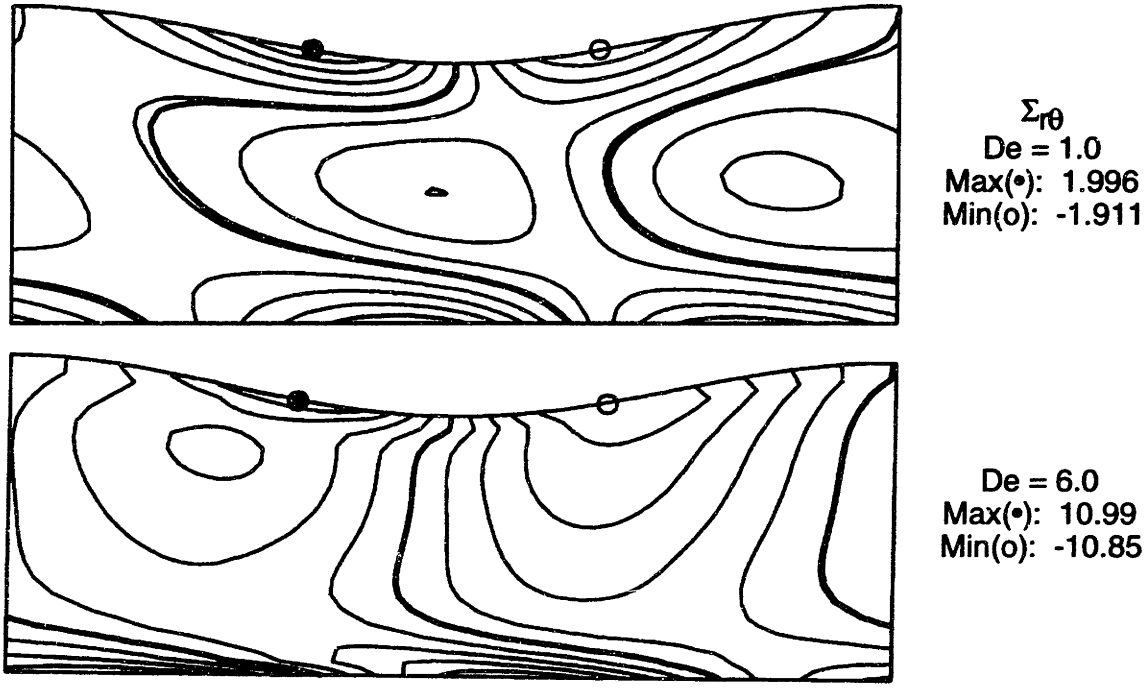

Figure 6-21: Contours of the solution field for $\Sigma_{r\theta}$ for the flow between eccentric rotating cylinders for the UCM model with $\epsilon = \mu = 0.1$ and Deborah numbers of 1.0 and 6.0 as computed with the SU discretization of the constitutive equations. Maximum and minimum values of the variable are shown.

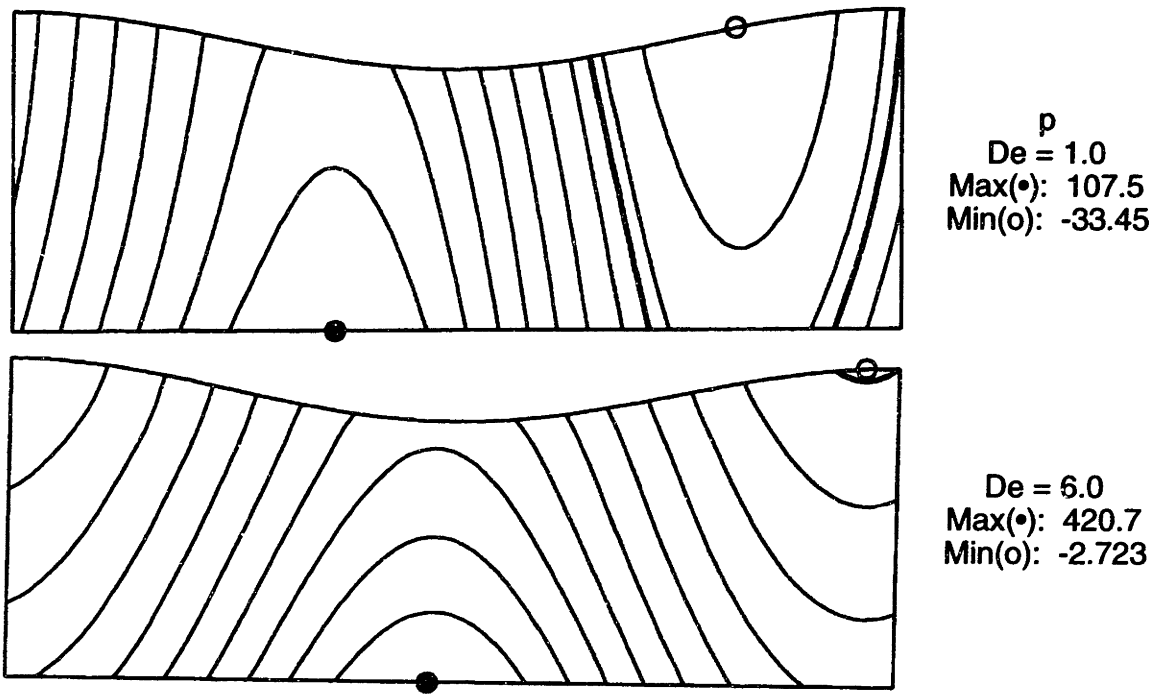

Figure 6-22: Contours of the solution field for p for the flow between eccentric rotating cylinders for the UCM model with $\epsilon = u = 0.1$ and Deborah numbers of 1.0 and 6.0 as computed with the SU discretization of the constitutive equations. Maximum and minimum values of the variable are shown.

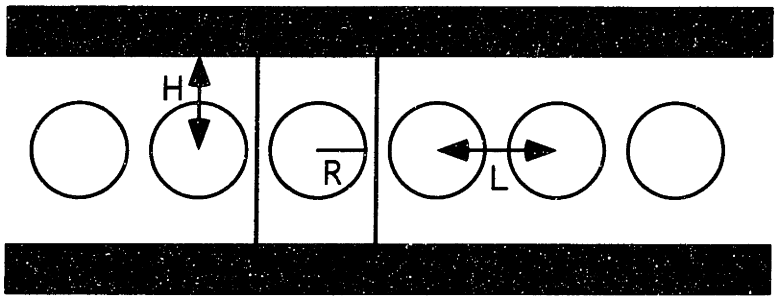

Figure 6-23: Computational geometry for transverse flow past an infinite linear periodic array of cylinders in a channel; $R/H = 0.5$ and $L/R = 2.5$. The computational domain is shown as a shaded area. The boundaries of the computational domain are periodic flow boundaries or no slip and no penetration surfaces.

6.2 Flow Through a Linear Array of Cylinders

The computational domain for the calculation of flow through an infinite linear array of cylinders in a channel is shown in Figure 6-23. The cylinders are spaced with cylinder centers L apart in the flow direction and are a distance H away from the channel walls. The channel half-width H is used as the length scale and the velocity scale V is defined in terms of the volumetric flow rate per unit cross-section, Q, as $V \equiv Q/H$. The Weissenberg number is then defined as $We \equiv \lambda_0 Q/d^2$. The calculations reported here are for the cylinder geometry constructed by setting $R/H = 0.5$ and $L/R = 2.5$. The finite element mesh is shown in Figure 6-24 and incorporates local mesh refinement adjacent to the cylinder where steep stress gradients are encountered. The local mesh refinement was performed as described in Section 4.8. The mesh does not utilize a symmetry boundary condition around the line of centers because the examination of the whole flow domain allows the disturbance to the linearized equations in the numerical linear stability analysis to be either symmetric or asymmetric (see Chapter 7). Also, the nonlinear time dependent simulations will be allowed to have asymmetric solutions (see Chapter 8). The mesh has 2,592 elements and 41,652 degrees-of-freedom for the calculations reported below. The flow is generated by a constant pressure drop across one cylinder similar to that resulting from a constant displacement pump.

Contours of the solution field for We = 0.25 are shown in Figures 6-25 and 6-26

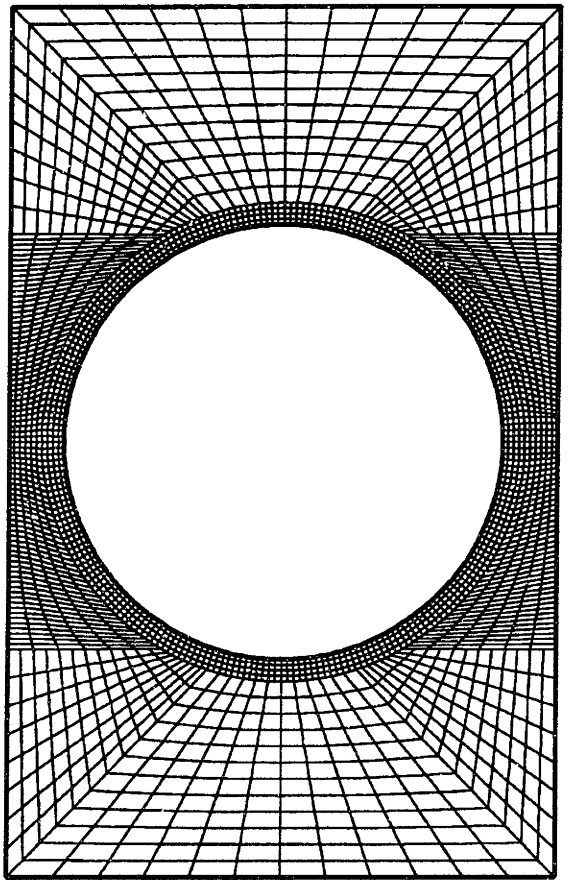

Figure 6-24: Finite element mesh used in the computations for the flow of a CR-FENE fluid through a linear array of cylinders. The mesh includes the whole flow domain to allow symmetric and asymmetric solutions for the linear stability analysis and the nonlinear time dependent solutions. The mesh has 2,592 elements and 41,652 degrees-of-freedom.

Variable	Method	Maximum Value	Minimum Value
Ψ	DEVSS-G	2.0370	-2.0370
	EVSS-G	2.0370	-2.0370
Δp	DEVSS-G	24.8737	–
	EVSS-G	24.8144	–
τ_{pxx}	DEVSS-G	0.5450	-43.0826
	EVSS-G	0.5460	-42.9580
τ_{pyy}	DEVSS-G	0.8515	-10.2106
	EVSS-G	0.8537	-10.1786
τ_{pxy}	DEVSS-G	15.6554	-15.6513
	EVSS-G	15.6033	-15.5991
$tr\langle QQ\rangle$	DEVSS-G	27.7178	2.9946
	EVSS-G	27.5841	2.9946

Table 6.5: Convergence of calculations for flow past a linear array of cylinders of a CR-FENE model at $We = 0.25$ and $R/H = 0.5$ and $L/R = 2.5$. Calculations are listed for the EVSS-G/FEM and DEVSS-G/FEM from the results of Figures 6-25, 6-26, 6-27, and 6-28, respectively.

for the EVSS-G/FEM and in Figures 6-27 and 6-28 for the DEVSS-G/FEM. For this geometry there is a region of flow separation between the cylinders resulting in a flow recirculation around the line of centers of the cylinders. Since both the velocity and velocity gradients are small here, the stresses are also small; thus, unlike a single cylinder flow, the strong extensional flow along the centerline does not exist for this array of cylinders. In Table 6.5 the accuracy of the DEVSS-G/FEM is demonstrated by a direct comparison of the maximum and minimum values for the variables in Figures 6-27 and 6-28 with the EVSS-G/FEM values in Figures 6-25 and 6-26. The EVSS-G/FEM and DEVSS-G/FEM are in excellent agreement, with the largest difference being less than 0.5%.

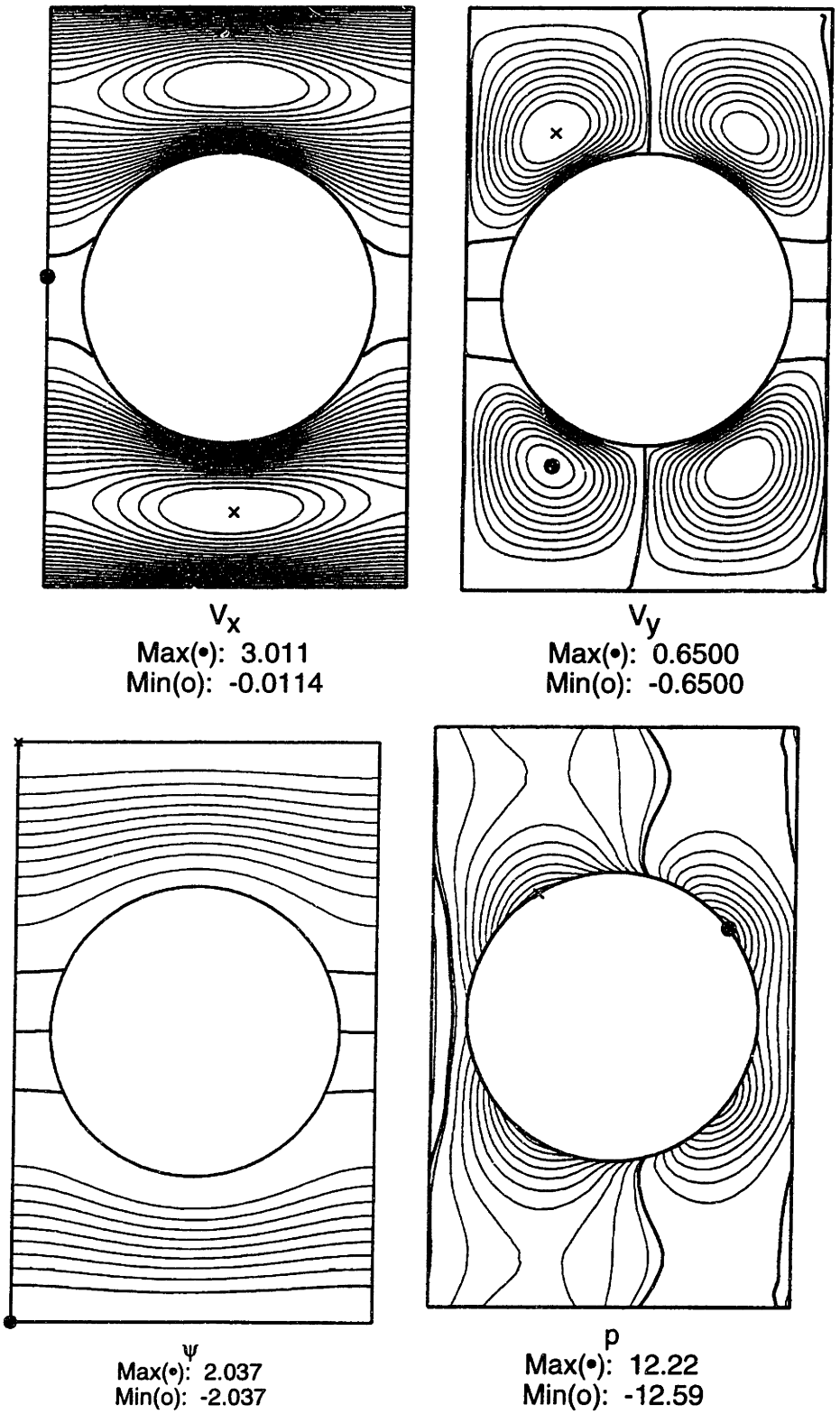

Figure 6-25: (a-b) Components of the velocity, (c) stream function, and (d) pressure for the flow of a CR-FENE fluid at $We = 0.25$ using the EVSS-G/FEM; $\beta = 0.59$ and $L = 20.0$. Maximum and Minimum values of the variables are shown.

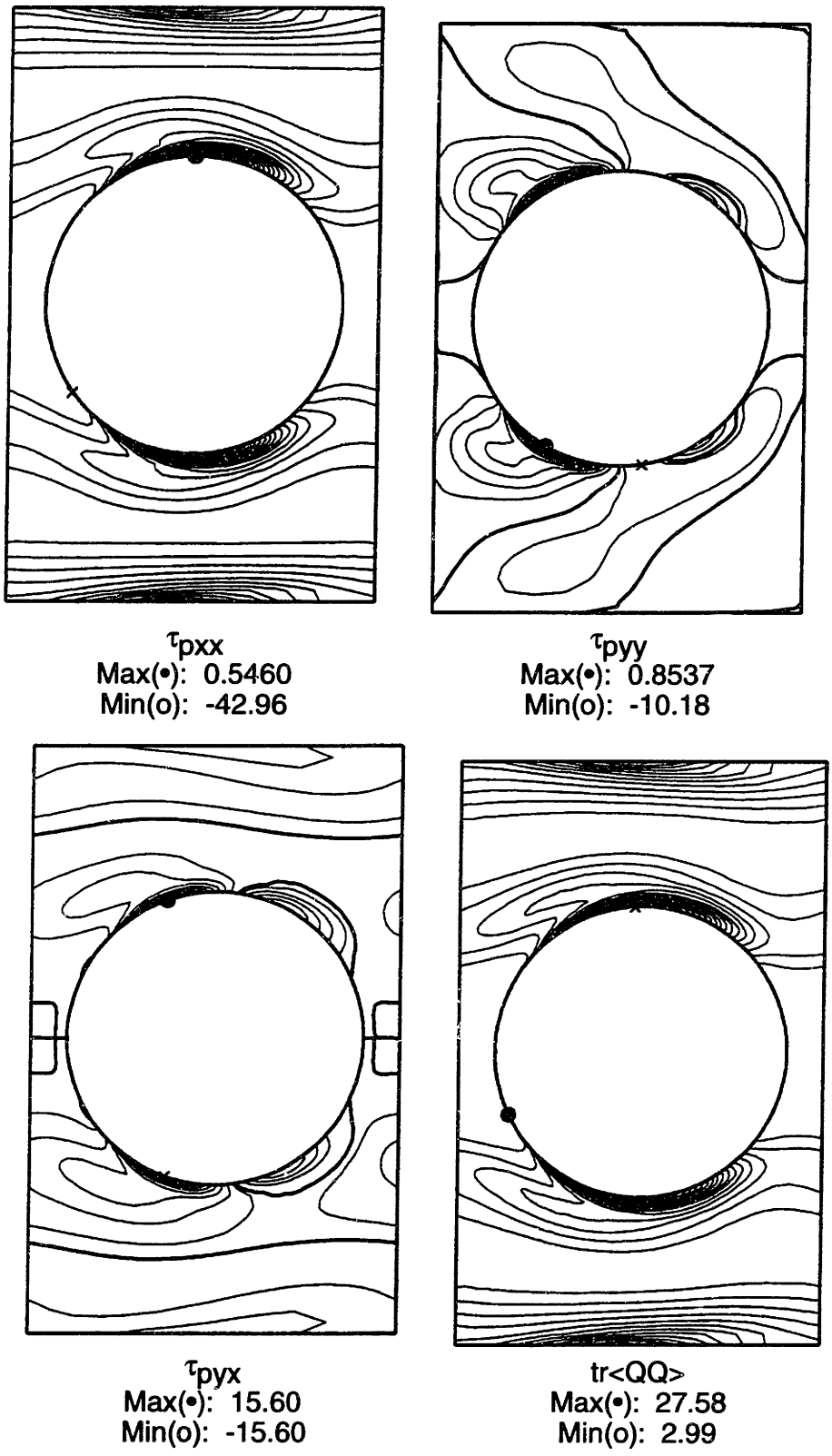

Figure 6-26: (a-c) Components of the polymeric stress, and (d) the molecular extension for the flow of a CR-FENE fluid at $We = 0.25$ using the EVSS-G/FEM; $\beta = 0.59$ and $L = 20.0$. Maximum and Minimum values of the variables are shown.

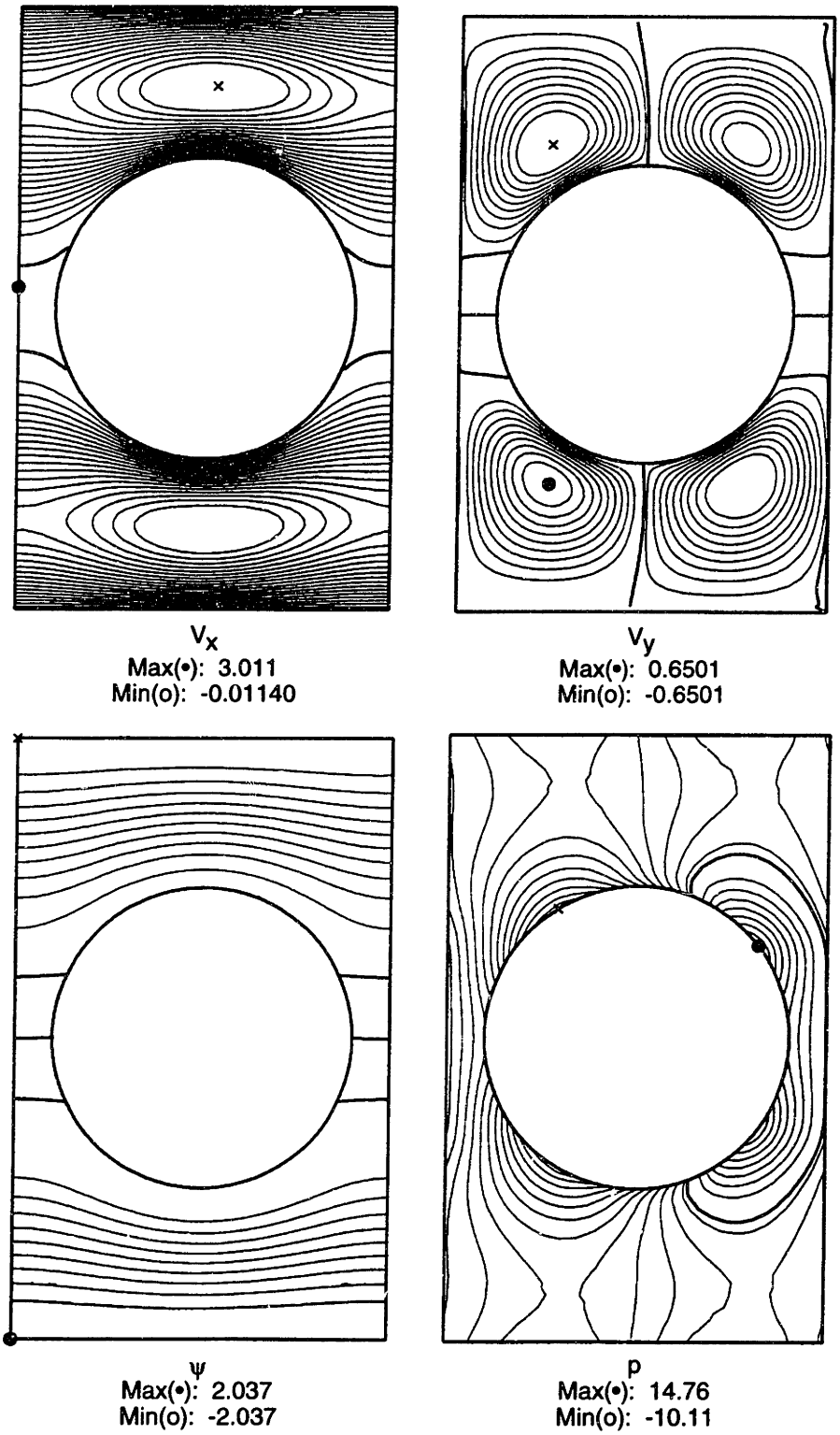

Figure 6-27: (a-b) Components of the velocity, (c) stream function, and (d) pressure for the flow of a CR-FENE fluid at $We = 0.25$ using the DEVSS-G/FEM; $\beta = 0.59$ and $L = 20.0$. Maximum and Minimum values of the variables are shown.

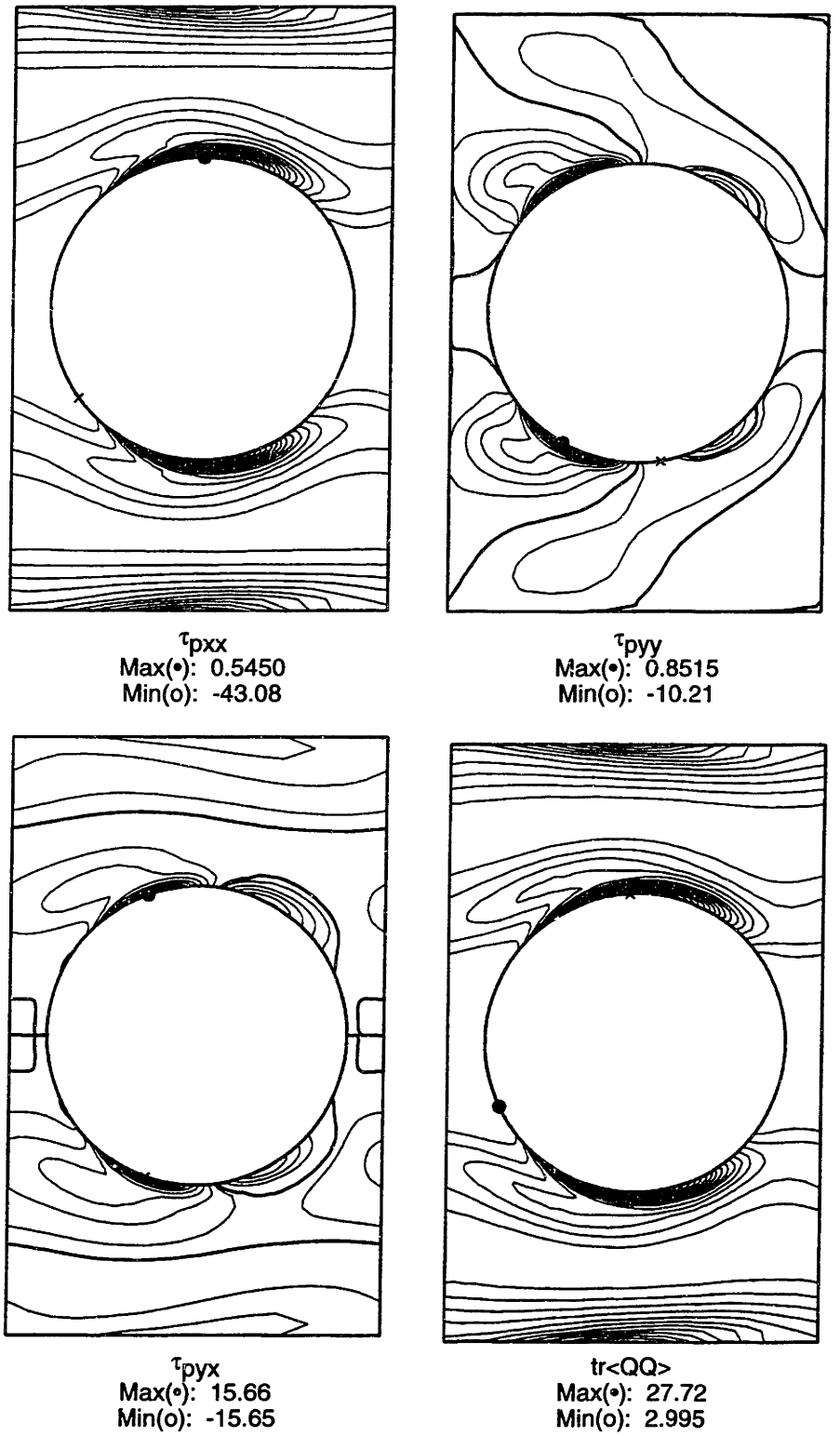

Figure 6-28: (a-c) Components of the polymeric stress and (d) molecular extension for the flow of a CR-FENE fluid at $We = 0.25$ using the DEVSS-G/FEM; $\beta = 0.59$ and $L = 20.0$. Maximum and Minimum values of the variables are shown.

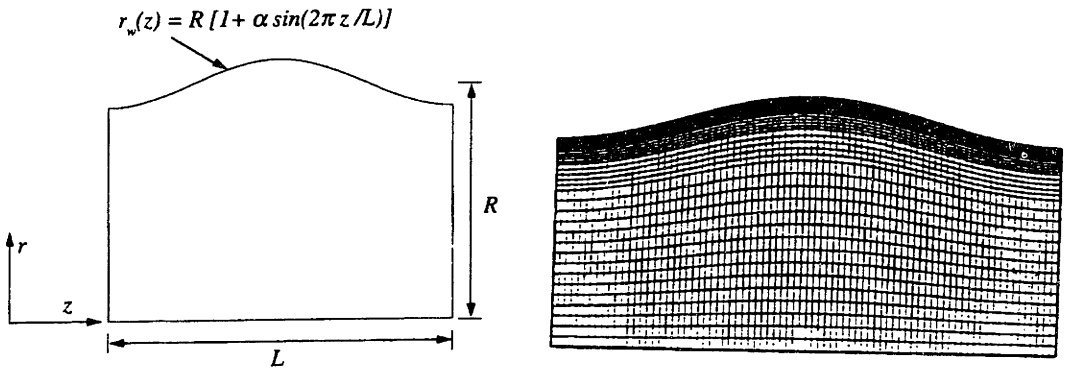

Figure 6-29: (a) Flow geometry for flow through a wavy-walled tube. In dimensional form, the tube wall is given by $R_{wall}(z) = R[1 - \alpha \sin(2\pi z/L)]$. (b) Finite element mesh used in the computations. It is highly refined along the wall of the channel, where steep stress gradients are located.

6.3 Other Applications

6.3.1 Flow Through a Wavy-Walled Tube

The geometry for the axisymmetric flow through a wavy-walled tube is shown in Figure 6-29(a) and was calculated by T.R. Salamon in Szady *et al.* (1995). The field equations are written by using the mean radius R of the tube as the length scale and defining the velocity scale as $V = Q/R^2$, where Q is the volumetric flow rate through the tube. Using these scales, the geometry is determined by the dimensionless corrugation amplitude α and the wavelength $N \equiv R/L$ of the corrugation. The calculations reported here use the parameter values ($N = 0.5$, $\alpha = 0.1$) first used by Pilitsis & Beris (1989) in pseudospectral calculations for an Oldroyd-B fluid.

Following their terminology, redefine De as a Weissenberg number, $We \equiv \lambda_0 Q/R^3$. The finite element mesh used in these calculations is shown in Figure 6-29(b) and is formed from a uniform mesh of 80 elements in the z-direction and 20 elements in the r-direction, with three layers of local refinement added within $0.2R$ of the tube wall where steep gradients of the stress are expected from previous calculations. This mesh gives 48,601 degrees-of-freedom in the finite element calculations. A uniform mesh with similar refinement near the wall would have 435,840 degrees-of-freedom. Calculations were performed with the EVSS-G/FEM using SUPG for discretization

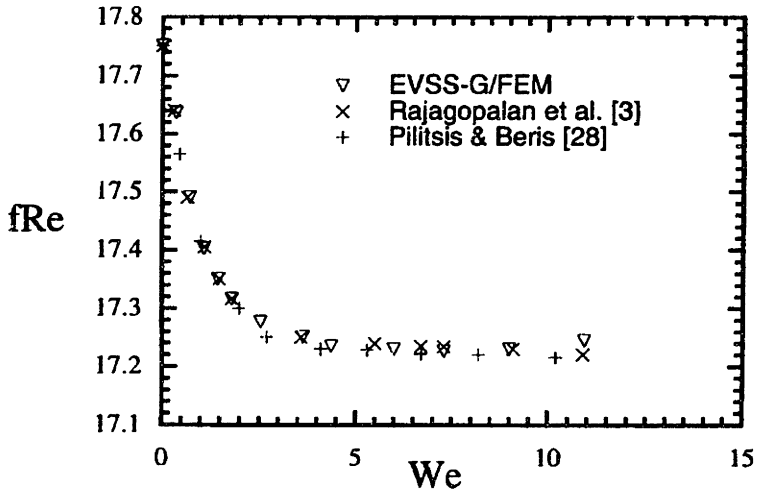

Figure 6-30: Flow resistance (fRe) in a wavy-walled tube as a function of We computed with the EVSS-G/FEM for the mesh shown in Figure 6-29(b). Results also are shown for the EVSS/FEM taken from Rajagopalan *et al.* (1990b) and for the pseudospectral calculations of Pilitsis & Beris (1989). These calculations were performed by T.R. Salamon (Szady *et al.*, 1995).

of the constitutive equation.

The stress fields found for the calculations were indeed smooth up to high We. The convergence of the solution with increasing mesh refinement was demonstrated in Szady *et al.* (1995) by comparisons of the solution field for $\Sigma_{zz}(r,z)$ for $We = 7.29$ computed with three meshes; the first two are uniform and third is the locally refined mesh. Convergence of the field was indicated by the smooth approximations to the rapidly varying stress field near the tube wall. The quality of the solutions computed with the EVSS-G/FEM is best illustrated by comparing the flow resistance, defined as $fRe \equiv 2\pi\Delta pR^4/L\eta_0 Q$, as a function of We to results of previous calculations with other methods. This comparison is shown in Figure 6-30 for the parameters $N = 0.5$ and $\alpha = 0.1$. The results of the EVSS-G/FEM calculations are in good agreement with previous calculations up to $We \approx 9$; moreover, the calculations without the local mesh refinement (for a mesh with 80 axial and 20 radial elements) are accurate only to a value of $We \approx 5$. The EVSS/FEM calculations, taken from Rajagopalan *et al.* (1990b), are for the uniform 80x20 mesh. The EVSS and EVSS-G algorithms give essentially the same results except at very high values of We, where the extra

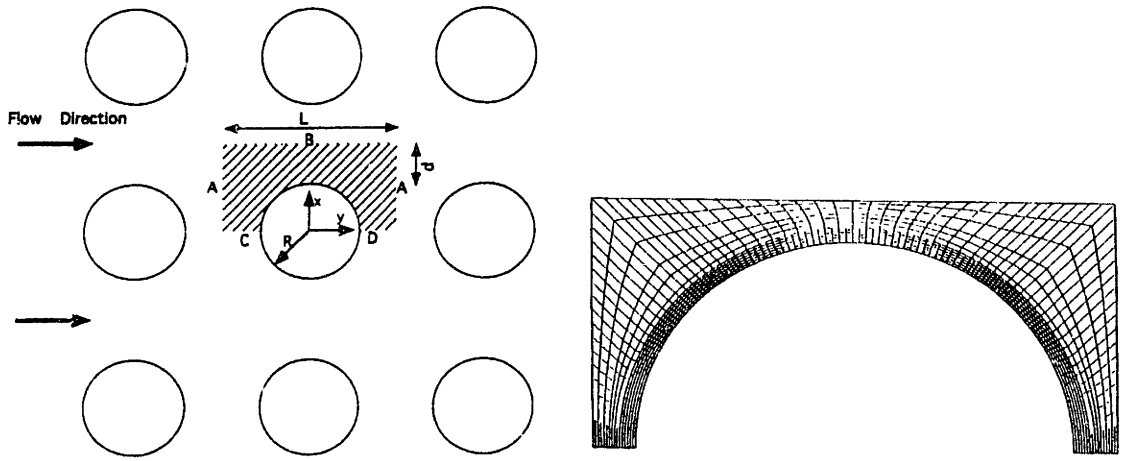

Figure 6-31: (a) Flow geometry for transverse flow past an infinite two-dimensional, periodic square array of cylinders, each of radius R. $L/R = 2.4$ and $d/R = 0.2$. The computational domain is shown as a shaded area. The boundaries of this area are either periodic flow boundaries (A) or planes of reflective symmetry(B-D). (b) Finite element mesh used in the computations.

resolution of the stress layers near the wall supplied by the local mesh refinement used with the EVSS-G/FEM is expected to improve the calculations. The local mesh refinement improves the resolution of the boundary layers and facilitates accurate calculations to higher values of We.

6.3.2 Flow Through a 2-D Array of Cylinders

The computational domain for the calculation of the flow through an infinite two-dimensional, periodic square array of cylinders is shown in Figure 6-31(a), using the same nomenclature used by Talwar & Khomami (1992). The calculations were performed by A.W. Liu in Szady *et al.* (1995). The cylinders are spaced with centers L apart in the flow direction and d in the direction orthogonal to the flow. The cylinder spacing d is used as the length scale and the velocity scale V is defined in terms of the flow rate per unit cross-section Q as $V \equiv Q/d$. With these definitions the Weissenberg number is defined as $We \equiv \lambda_0 Q/d^2$. The calculations reported here are for the cylinder geometry constructed by setting $d/R = 0.2$ and $L/R = 2.4$, as used by Talwar & Khomami (1992) in their benchmark calculations. The finite element mesh is shown in Figure 6-31(b) and incorporates local mesh refinement adjacent to

the cylinder where steep stress gradients are encountered. The flow is generated by a constant pressure gradient across a cylinder as in the linear array of Section 6.2.

For the close cylinder spacing used here, the flow is separated between the cylinders creating a recirculation cell along the line of centers of the cylinders. Both the recirculation rate and the velocity gradients are low, leading to low stresses in this region. Strong extensional flows are not seen along the line of centers because of the weakness of the flow there; this behavior is unlike the flow around a single cylinder, where strong extensional flows create high extensional stresses along the line of symmetry (McKinley *et al.*, 1993). The most notable feature of the solution field is the development of sharp stress gradients in the gap between cylinders situated orthogonal to the flow direction. The size of the flow recirculation region also decreases slightly as We increases (Szady *et al.*, 1995).

The calculations with the EVSS-G/FEM are compared directly with the spectral element calculations reported by Khomami *et al.* (1993) by comparing the value of the flow resistance through the periodic array, as defined by

$$fRe \equiv \frac{fRe_{\mathrm{UCM}}}{fRe_{\mathrm{Newt}}} = \frac{Q_{\mathrm{UCM}}}{Q_{\mathrm{Newt}}}, \tag{6.22}$$

as a function of We. In eq. (6.22) the subscripts UCM and Newt refer to values computed for the UCM and Newtonian fluid models and Q is the volumetric flow rate. These results are shown in Figure 6-32 for $We \leq 10$, as computed using both SU and SUPG methods for discretizing the constitutive equation. The calculations with the EVSS-G/FEM and the SUPG method have accuracy similar to the spectral element results reported in Khomami *et al.* (1994) using 24 elements and 10th degree polynomials to compute the stress and velocity fields. The flow resistance computed with the EVSS-G formulation using the SU method begins to differ for $We > 2$ and diverges rapidly from the predictions of the SUPG method for $We > 4$. Very similar behavior of the SU method was reported by Lunsmann *et al.* (1993) for the flow around a sphere falling in a tube for the EVSS method using these two techniques for discretizing the constitutive equation. Debae *et al.* (1994) made similar predictions.

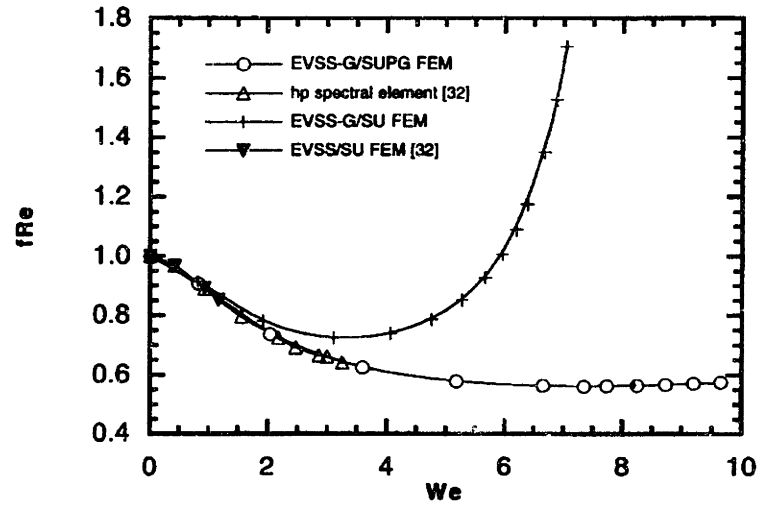

Figure 6-32: Evolution of the flow resistance (fRe) with increasing We for $L/R = 2.4$ and $d/R = 0.2$. Calculations are shown for the EVSS-G/SUPG/FEM described here (o), for the hp-spectral/finite element calculations of Khomami *et al.* (1994) ($\triangle$), for the EVSS-G/SU/FEM (+) and the EVSS/SU/FEM as implemented by Khomami *et al.* (1994) (∇). These calculations were performed by A.W. Liu (Szady *et al.*, 1995).

The EVSS/SU calculations reported in Khomami *et al.* (1994) and plotted in Figure 6-32 also begin to deviate from the EVSS-G/FEM and spectral element results for $We \approx 1$.

6.4 Summary

The calculations described here demonstrate that the EVSS-G/FEM formulation is numerically accurate, convergent with mesh refinement and robust for the solution of viscoelastic flow problems governed by the upper-convected Maxwell, Oldroyd-B and CR-FENE constitutive equations. The DEVSS-G/FEM was shown to give equivalent results to the EVSS-G/FEM. Experience suggests that these properties will carry over to other complex, nonlinear viscoelastic models that incorporate shear thinning of the viscosity and normal stresses and so describe less elastic fluids.

The use of bilinear stress interpolations makes it convenient to compare the accuracy of calculations using the SU and SUPG methods for the discretization of the constitutive equations. Once again, as found in the literature, the accuracy of cal-

culations using streamwise upwinding (SU) diverge beyond a critical value of De for a given mesh. Although the calculations converge to a high value of De, in some instances higher values than are achievable with the SUPG method and the same discretization, the results become meaningless. For example, in the calculations for the flow through a square array of cylinders, the flow resistance computed using SU is wrong by a factor of 2 for $We > 6$! Streamline upwinding must be used with caution.

Calculations for the steady-state problems demonstrate the accuracy of the EVSS-G/FEM and DEVSS-G/FEM for the solution of high De flows. The calculations demonstrate that the EVSS-G/FEM and DEVSS-G/FEM combined with local mesh refinement using the concept of embedded elements gives accurate results in a range of De that is comparable to other discretization methods, including the EVSS/FEM developed by Rajagopalan *et al.* (1990b), the pseudospectral methods of Beris and coworkers and the spectral element methods of Khomami and coworkers. The power of the local mesh refinement results from the ability to locally place finite element refinement in regions of steep gradients of the solution, usually the stress field, to improve the resolution of the solutions there. Because the meshes are highly irregular, no attempt has been made for these steady-state flows to demonstrate convergence with mesh, which would require uniformly increasing the discretization to uniformly change the characteristic mesh size. An alternative approach that has more potential is to use local error indicators, such as elemental momentum and continuity balances, to systematically assess the need for local mesh refinement for solutions with given levels of error on an elemental level.

The EVSS-G/FEM and DEVSS-G/FEM with SUPG gives increased stability and comparable accuracy to the EVSS/FEM introduced by Rajagopalan *et al.* (1990b) at a considerable savings that results from using bilinear interpolation of the stress components instead of the much more costly biquadratic interpolation; this savings will become even more evident when multi-mode constitutive models are used (Rajagopalan *et al.*, 1990a and Rajagopalan *et al.*, 1992). The EVSS-G/FEM and DEVSS-G/FEM also extend easily to three-dimensional flows, where the application of the now trilinear stress approximations will considerably simplify the calculations.

A major component of the cost of time dependent calculations remains the need for fully implicit time integration methods, such as the Euler integration algorithm used here or the Crank-Nicholson method to be used in Chapter 7, to guarantee numerical stability. Some attempts have been made to apply operator splitting methods to viscoelastic flows [Bristeau *et al.,* 1985, Saramito, 1994, and Singh & Leal, 1993). Theoretically, these methods substitute the solution of two or three decoupled systems of equations each requiring much less computational effort than the solution of the nonlinear equation set at each time step that results from a fully implicit integrator. This saving has been realized by algorithms for Newtonian flows (Bristeau *et al.,* 1985) and by some algorithms for viscoelastic fluids (Saramito, 1994), but not by others (Singh & Leal, 1993). The computationally efficient application of these methods to the EVSS-G and DEVSS-G formulations will be discussed in Chapter 8 where another major advantage of the DEVSS-G formulation over the EVSS-G formulation appears. This advantage and the simplicity in obtaining the formulation will make the DEVSS-G/FEM the preferred method for future calculations.

Chapter 7

Numerical Linear Stability of Viscoelastic Flows

"Mathematics is the gate and key of the sciences ... Neglect of mathematics works injury to all knowledge, since he who is ignorant of it cannot know the other sciences or the things of this world. And what is worse, men who are thus ignorant are unable to perceive their own ignorance and so do not seek a remedy."

– Roger Bacon

In Chapter 5, both the EVSS-G/FEM and the DEVSS-G/FEM was shown to be temporally stable for the planar Couette flow of a UCM fluid. In the last Chapter, these methods were shown to be convergent with mesh, numerically accurate and robust. Thus, all of the tests for a good numerical method have been met and it is now possible to move towards solving problems with no known solution with confidence that the results will be correct. It is still possible that the numerical methods may fail; however, the likelihood of this is less than for a method which has not been as rigorously tested. Using the previous calculations in this thesis as an indication that neither numerical method will give fictitious instabilities, the linear stability of planar Couette flow using the CR-FENE model, where the exact solution is not known, will be computed numerically. These calculations will be performed using the DEVSS-

G/FEM and the SUPG method with the model parameters chosen as $\beta = 0.59$ and $L^2 = 400$ and are given in Section 7.1. These values have been used previously as an estimate for a Boger fluid (McKinley *et al.*, 1995). The time integration methods used are the first and second order fully implicit Adams-Moulton methods.

As a second problem, the numerical linear stability of the flow through an infinite periodic linear array of cylinders in a channel for a fluid described by the CR-FENE constitutive equation. The steady-state solution for low We was examined in Section 6.2. This is a more complicated flow than the previously studied planar Couette flow and should provide a good test of the DEVSS-G/FEM.

7.1 Planar Couette Flow of a CR-FENE Fluid

The calculation of the numerical linear stability of the planar Couette flow of a CR-FENE fluid does not have a closed-form solution as was the case for the UCM fluid studied in Chapter 5. Because this is still simple shear flow, it is still expected that the flow will remain stable for reasonable De. The biggest question regarding this flow is the asymptotic decay rate of the most unstable eigenvalue and how the change in the fluid model effects this. It might be expected that the asymptotic rate will remain much the same as the UCM fluid, but there is no guarantee that the additional nonlinear terms introduced to limit the extensibility of the polymer molecule will not change the large De limit.

The evolution of the energy of the disturbance as a function of time $L_2(t)$ defined in eq. (5.15) is shown in Figure 7-1 for $De = 1.0$, 5.0, 10.0 and 50.0 for the backward Euler time integration scheme. The slope of the decay for $De = 1.0$ is close to that predicted for the UCM fluid, i.e., $-1/(2De)$, but as the De increases the slope is much larger than this would predict. The cause of this lies in the shear thinning behavior of the CR-FENE fluid. In Figure 7-2, the zero shear rate Deborah number (De_0) is plotted against the shear-rate dependent Deborah number ($De(\dot{\gamma})$). The Oldroyd-B and UCM models do not shear thin; thus the two De are identical. On the other hand, the CR-FENE model incorporates shear thinning behavior; thus, the

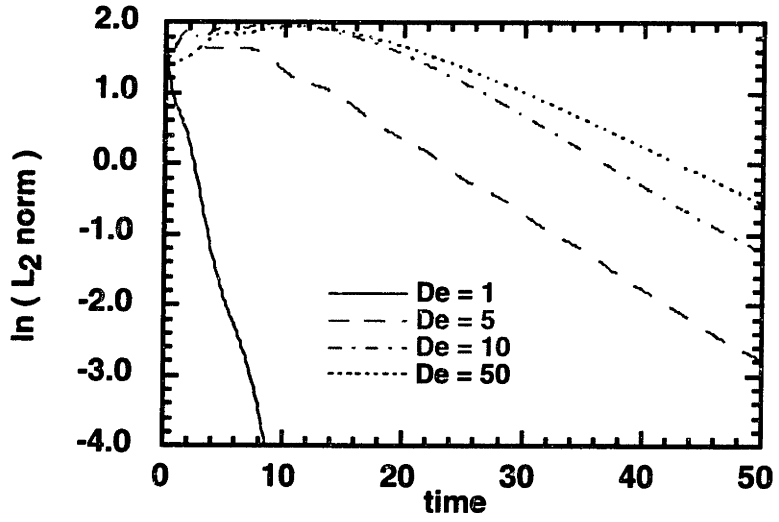

Figure 7-1: Transient response computed with the DEVSS-G/FEM and the first order Adams-Moulton time integration method of the amplitude $L_2(t)$ defined by eq. (5.15) as a function of time for a CR-FENE fluid for varying De.

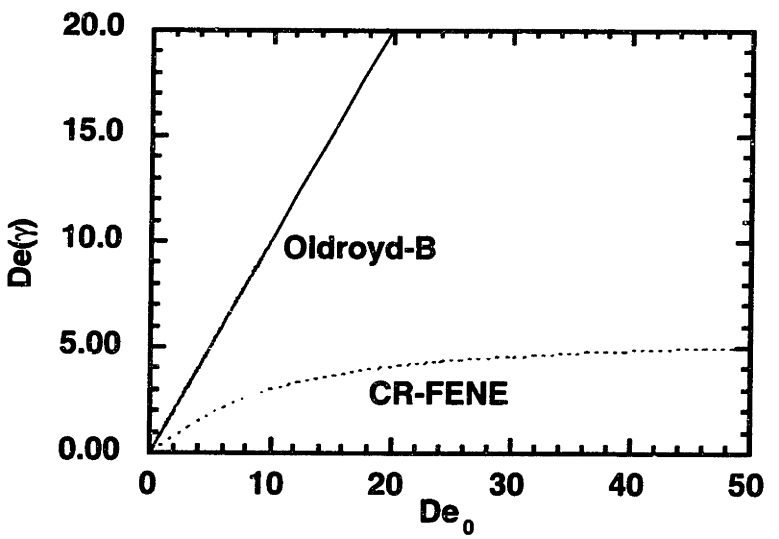

Figure 7-2: The shear-rate dependent De as a function of the zero-shear-rate dependent De. The Oldroyd-B and UCM models do not shear thin; thus the two De are identical. On the other hand, the CR-FENE model incorporates shear-thinning behavior; thus, the actual De experienced by the fluid is given by $De(\dot{\gamma})$ not De_0.

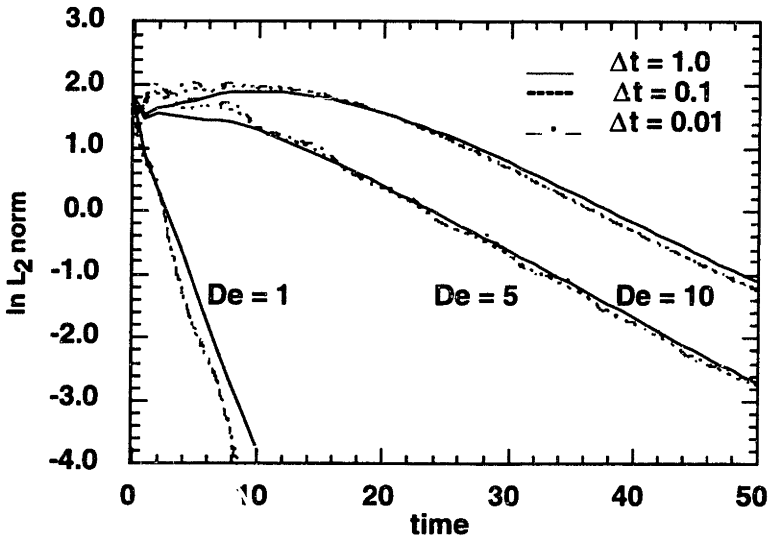

Figure 7-3: Transient response computed with the DEVSS-G/FEM and the Crank-Nicholson time integration method of the amplitude $L_2(t)$ defined by eq. (5.15) as a function of time for a CR-FENE fluid for varying De. Three time steps are shown ($\Delta t = 0.01$, 0.1 and 1.0); the convergence is obvious.

actual De experienced by the fluid is given by $De(\dot{\gamma})$ not De_0. This gives the correct decay rate for the computed energy in the finite element disturbance in Figure 7-2 as $-1/(2De(\dot{\gamma}))$. This may be an indication that the most dangerous eigenvalue as $De \rightarrow \infty$ is of this general form for any viscoelastic fluid in planar Couette flow.

Only a first order in time integrator (backward Euler) has been used so far. Since the higher accuracy of a second order method will become necessary in the next section, the Crank-Nicholson method is introduced and compared to the backward Euler method for planar Couette flow results first. In Figure 7-3, three different time steps are shown ($\Delta t = 1.0$, 0.1 and 0.01) for $De = 1.0$, 5.0 and 10.0; the convergence is obvious. The first and second order Adams-Moulton methods are compared in Figure 7-4 for $\Delta t = 0.1$. The advantage of using a second order method is the expectation of the use of larger time steps while obtaining the same accuracy; this will be demonstrated next in the numerical linear stability of flow through a linear array of cylinders in a channel.

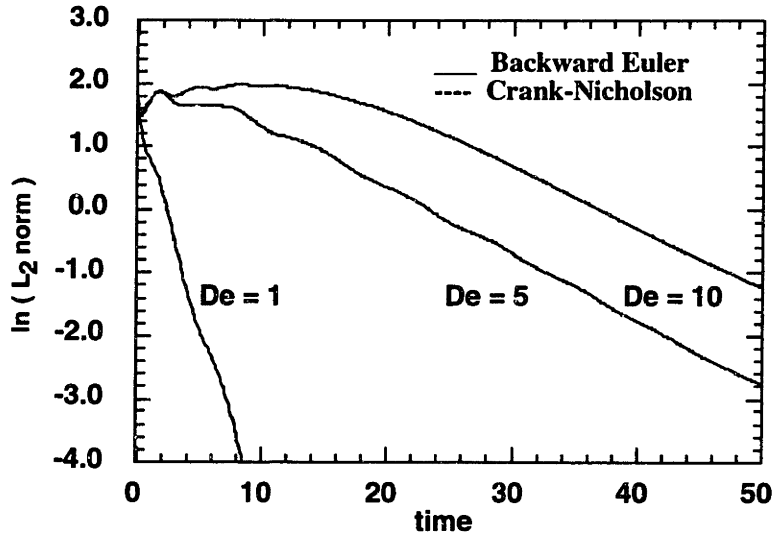

Figure 7-4: Transient response computed with the DEVSS-G/FEM of the amplitude $L_2(t)$ defined by eq. (5.15) as a function of time for a CR-FENE fluid for varying De. Both the backward Eulers and Crank-Nicholson methods are shown and are indistinguishable.

7.2 Flow Through a Periodic Linear Array of Cylinders in a Channel for a CR-FENE Fluid

The motivation for the studying the linear stability of the flow through an infinite periodic linear array of cylinders in a channel is based on two recent experimental observations. McKinley *et al.* (1993) and Oztekin *et al.* (1995) have performed experiments examining the flow of Boger fluids about a single cylinder in a channel. A viscoelastic instability was observed in which the flow goes from symmetric and two-dimensional to asymmetric and three-dimensional. Chmielewski & Jayaraman (1993) studied the flow through a two-dimensional square array of cylinders placed so that recirculation occurred behind the cylinders (much like the steady-state flow studied in Section 6.3.2). A time dependent instability was found wherein, above a critical We, the recirculation region between the centers of the cylinders along the flow direction exhibited periodic oscillations (see Figure 7-5).

It was decided to examine the flow through a periodic, linear array of cylinders in a channel. The inlet/outlet boundary conditions are accounted for by periodic

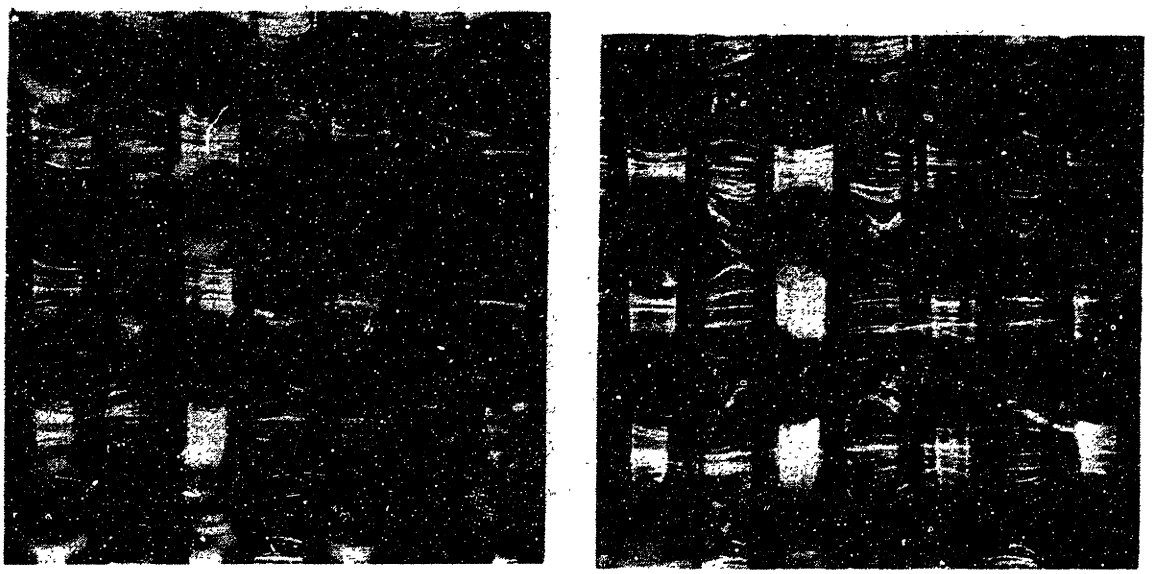

(a) (b)

Figure 7-5: Flow visualization photographs of the flow of a Boger fluid through a 2-D square array of cylinder geometry (form Chmielewski & Jayaraman, 1993). (a) Below the critical We, the flow is basically the same as for the Newtonian case. The flow recirculation behind the cylinders can be seen. (b) Above the critical We the flow is asymmetric and time periodic. The recirculation regions oscillate up and down as can be seen by examining the recirculation region behind several cylinders.

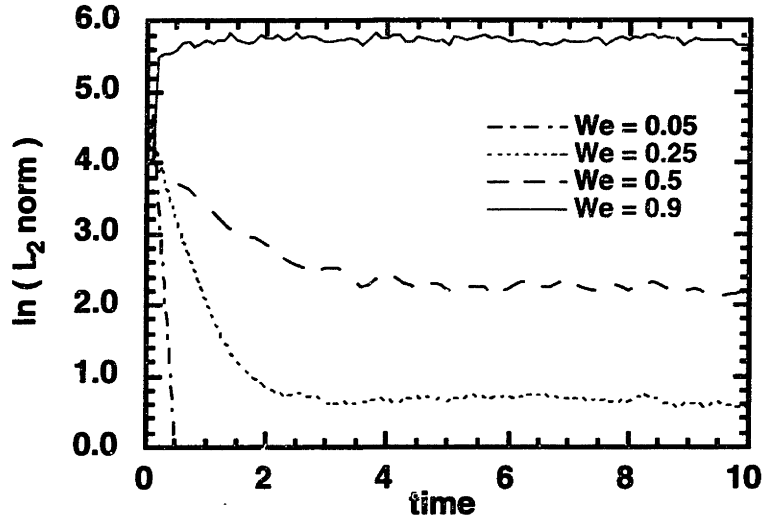

Figure 7-6: Transient response computed with the DEVSS-G/FEM and the backward Eulers time integration method of the amplitude $L_2(t)$ defined by eq. (5.15) as a function of time for a CR-FENE fluid for varying We. An increase in the integration error appears to be causing the plateau after $t \sim 2-3$.

boundary conditions. Also, A.W. Liu in the MIT research group will be performing experiments in this geometry in the near future to examine flow instabilities in this geometry (Liu *et al.*, 1995).

The flow geometry and finite element mesh are shown in Figure 6-23 and 6-24, respectively. The use of the full geometry allows for asymmetric disturbances to be examined and the mesh refinement in the recirculation region is there to capture the dynamics of the recirculation zone's dynamic oscillations (if they occur). The steady-state solutions calculated in Section 6.2 were used as the base state for a numerical linear stability analysis for the flow of an infinite periodic linear array of cylinders in a channel.

Initially, the calculations were performed using the first-order Adams-Moulton time integration method; however, the truncation error is so large that as the We increased, the solution to the equations decayed until, it was simply overcome by this error. This led to a solution that was simply a reflection of the truncation error at $We = 0.9$ and did not indicate the true nature of the linear stability of the continuous equations. An example is shown in Figure 7-6 for several We with $\Delta t = 0.1$. The result for $We = 0.05$ displays the expected rapid decay indicating linear stability.

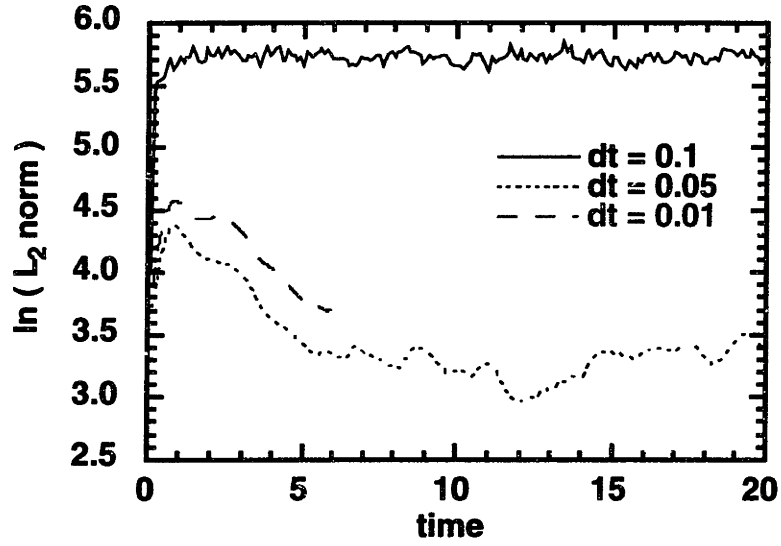

Figure 7-7: Transient response computed with the DEVSS-G/FEM and the backward Eulers time integration method of the amplitude $L_2(t)$ defined by eq. (5.15) as a function of time for a CR-FENE fluid for varying Δt at $We = 0.9$. Decreasing the time step appears to delay the onset of the plateau region indicating that the truncation error is the cause. $\Delta t = 0.01$ was stopped due to the extremely long computational time.

However, the $We = 0.25$ and 0.5 results plateau at $t \sim 2 - 3$ while the $We = 0.9$ result is a constant from the very start. This initial decay leading to a constant value is not a solution expected of a normal-mode analysis solution which is simply a sum of exponentials. The possibility that these results are due to the truncation error is shown by an examination of Figure 7-7 where various time steps are shown for $We = 0.9$. Using $\Delta t = 0.05$ delays the onset of the plateau region for the computed energy of the finite element disturbance, but only to $t = 5.0$. Reducing the time step further to $\Delta t = 0.01$ produced results along the same lines, but due to the extremely long CPU time required, the calculation was terminated at $t = 6$, but the same general trend is expected to be observed if the calculations were continued. At this point the calculations indicated that all of the examined We were stable. The second-order Adams-Moulton time integration method was implemented to reduce the errors and still obtain the solution in a reasonable amount of CPU time to check this conclusion. The implementation of this method was discussed in Section 4.7 and a comparison of results with the first order method was performed in the previous

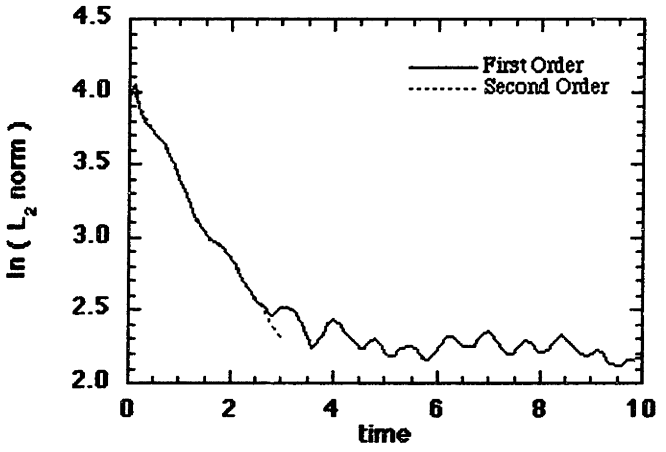

Figure 7-8: Transient response computed with the DEVSS-G/FEM and the (a) first order and (b) second order Adams-Moulton time integration methods of the amplitude $L_2(t)$ defined by eq. (5.15) as a function of time for a CR-FENE fluid for $We = 0.5$ and $\Delta t = 0.1$.

section.

The $O(\Delta t^2)$ time integration method has given results that appear to avoid the problem of truncation errors swamping the solution for moderate time steps. The computed energy in the finite element disturbance is shown as a function of time in Figure 7-8 and 7-9 for $We = 0.5$ and $We = 0.9$, respectively. Both are clearly linearly stable. Figure 7-8 shows that both the first and second order Adams-Moulton time integration methods yield virtually identical results. Two different time steps are shown in Figure 7-9 for $We = 0.9$; both exhibit similar behavior. This result confirms that the flow is linearly stable for all We examined. The decay rates appear to follow the simple form of $-1/(2De(\dot{\gamma}))$ as in the planar Couette numerical linear stability calculations. Linear stability calculations were not attempted for higher values of We because the steady-state solution calculation at higher We loses the positive definiteness of the $\langle QQ \rangle$ tensor above $We = 0.9$. The calculations can be continued with further mesh refinement of the regions where the positive definiteness is lost, but the expense of the additional calculations precluded attempting this at the present time.

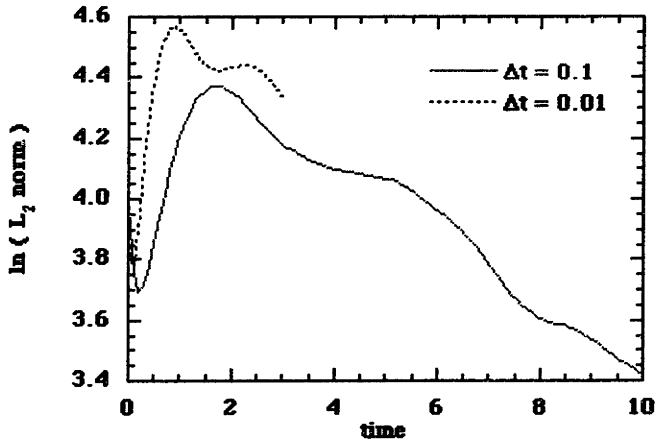

Figure 7-9: Transient response computed with the DEVSS-G/FEM and the second order Adams-Moulton time integration method of the amplitude $L_2(t)$ defined by eq. (5.15) as a function of time for a CR-FENE fluid for $We = 0.9$ (a) $\Delta t = 0.2$ and (b) $\Delta t = 0.1$.

The eigenfunctions at $t = 10$ for the velocity components, v_x and v_y are plotted in Figure 7-10 and the configuration tensor components, A_{xx}, A_{yy} and A_{yx}, and pressure, p, are plotted in Figure 7-11 for $We = 0.9$ which is linearly stable as shown in Figure ??. The eigenfunctions are markedly asymmetric and do not appear to approach a symmetric form during their time dependent development. There is a marked absence of structure in the recirculation region of the flow between the two cylinders; for the configuration tensor components of the eigenstructure, the contours found in the recirculation region are remnants of the initial random perturbation which has not completely died out at this time. The pressure eigenfunction has structure which is mainly localized along the surface of the cylinder.

The eigenfunctions for the configuration tensor appear to have structure oriented around their steady-state solution structure. The steady-state components of the configuration tensor are shown in Figure 7-12. This is especially true of the yy-component which only appears to have structure in the eigenfunction at the same four lobes as the steady state solution. The xx- and yx-components appear to decay to streamwise structures located away from the cylinder near the channel walls and

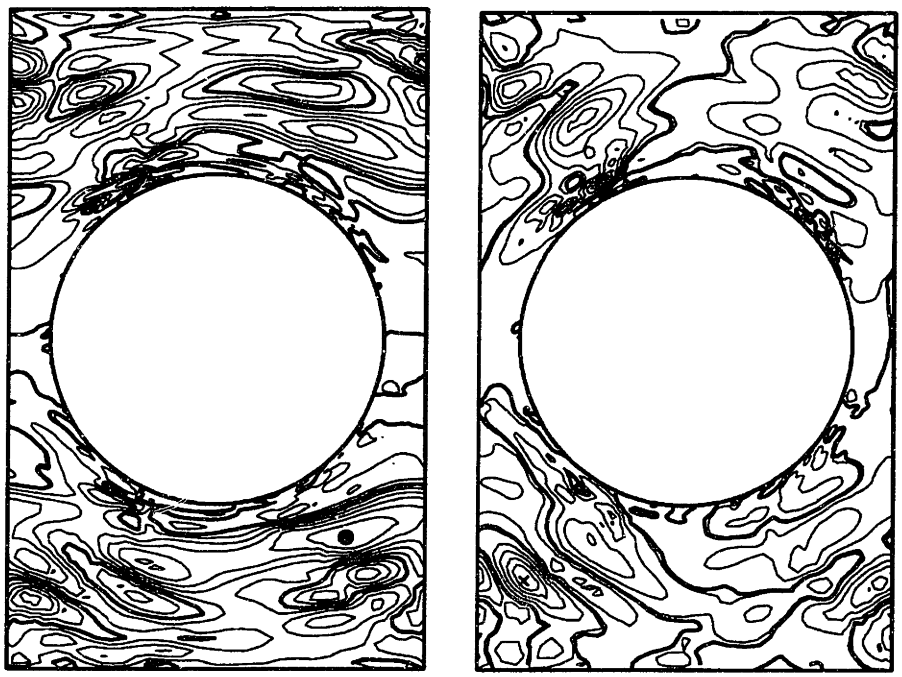

Figure 7-10: The eigenfunction computed with the DEVSS-G/FEM and the second order Adams-Moulton time integration method at $We = 0.9$ and $t = 10.0$ for a CR-FENE fluid in a periodic linear array of cylinders in a channel. (a) x-component of velocity and (b) y-component of velocity.

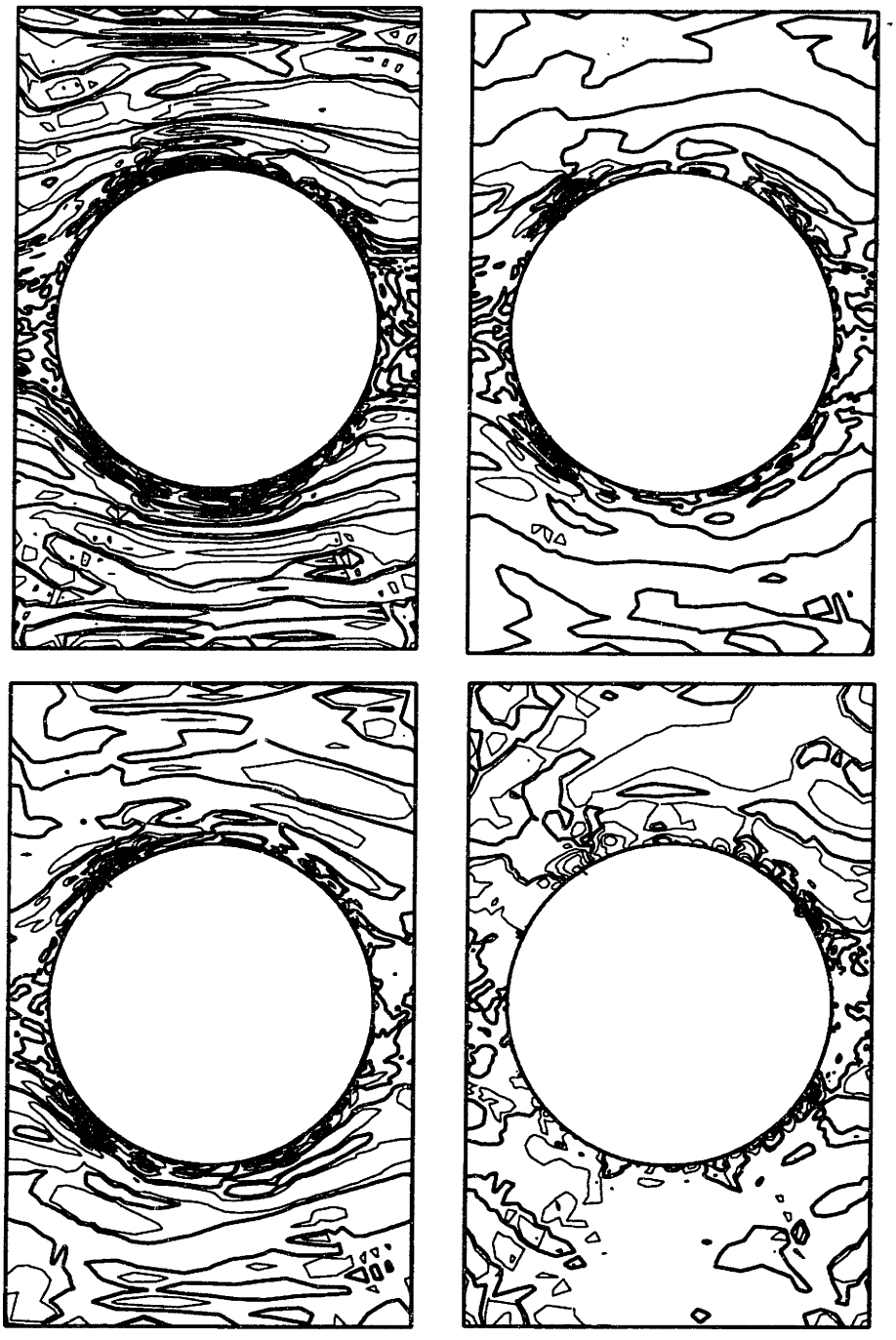

Figure 7-11: The eigenfunction computed with the DEVSS-G/FEM and the second order Adams-Moulton time integration method at $We = 0.9$ and $t = 10.0$ for a CR-FENE fluid in a periodic linear array of cylinders in a channel. (a) xx-component of the configuration tensor, (b) yy-component of the configuration tensor, (c) yx-component of the configuration tensor, and (d) pressure.

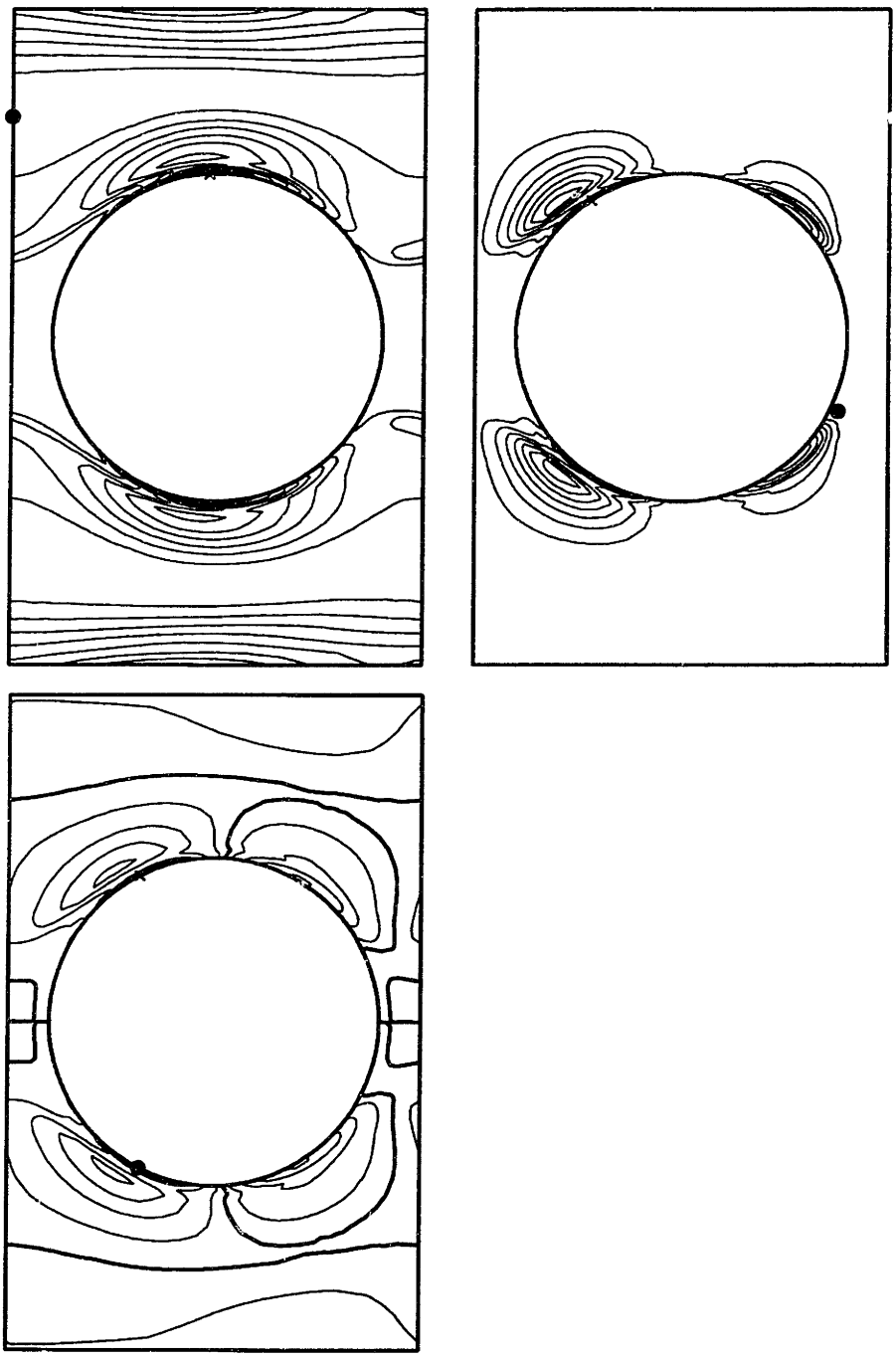

Figure 7-12: The steady-state components of the configuration tensor computed with the DEVSS-G/FEM at $We = 0.9$ for a CR-FENE fluid in a periodic linear array of cylinders in a channel. (a) xx-component, (b) yy-component, (c) yx-component, and (d) pressure.

have a much richer structure around the cylinder itself.

The fine scale structure near the channel walls and the cylinder surface is similar to what was found for the eigenfunctions in the planar Couette flow. Near the solid boundaries in both flows, shear flow governs the structure of the eigenfunctions. The structure of the eigenfunctions away from the zero velocity streamlines decays almost completely away. As in the planar Couette flow where both walls were moving in opposite directions, significant flow structure exists along the zero streamline separating the recirculation region from the rest of the flow. Thus, similar behavior for different regions of the flow exists between the planar Couette geometry and the linear array of periodic cylinders.

7.3 Summary

The DEVSS-G/FEM with SUPG method is used to perform linear stability calculations of flows for which no closed-form solution exists. The linear stability of planar Couette flow of a CR-FENE fluid was shown to be stable for values of De up to at least 50.0. Both a first and second order Adams-Moulton time integrators are shown to yield converged results. The decay rate was found to have the same general form as the UCM fluid, but the De needed to be redefined in terms of the shear rate experienced by the fluid. The real part of the most dangerous eigenvalue is given by $-1/\left(2De(\dot{\gamma})\right)$ as De_0 becomes large. It is possible that this is the general form of the most dangerous eigenvalue for viscoelastic fluids in planar Couette flow.

The linear stability of the flow through an infinite periodic linear array of cylinders in a channel was also calculated for an initially asymmetric, random perturbation which allows for both symmetric and asymmetric disturbances. For all We examined, the flow was *stable*. The first order Adams-Moulton time integration method results were affected by the truncation error as We increased until for $We = 0.9$ the solution was simply an indication of this error, not a true representation of the solution. This situation was rectified by using a second order Adams-Moulton integrator. The eigenfunction structure appears asymmetric throughout its time development; however, the

structure of eigenfunction itself is based on the symmetric steady-state configuration. The same basic fine scale structure was observed near the zero streamlines and the lack thereof away from the stationary streamlines as for the planar Couette geometry. In the next chapter we will examine fully nonlinear time dependent calculations to confirm these linear stability results.

In Brown *et al.* (1992) and Northey (1991), the linear stability of a falling sphere using the UCM model was examined using the EEME-p/SUPG/FEM. The results indicated that the solution was approaching neutral stability as the maximum attainable De for the steady-state calculations was reached. The eigenfunctions also exhibited an oscillatory nature at $De = 1.6$ indicating the possibility of a Hopf bifurcation to a time dependent flow. A comparison between the results presented here to Northey's calculations are made difficult due to the different nature of the two flow geometries. The sphere geometry has an inlet and an outlet for the flow which are independent of each other leading to vortices that can move along with the flow over time. Due to its periodic nature, the cylinder geometry lends itself more to standing waves. Another difference in the two geometries is the lack of a steady-state solution above $De \sim 1.6$ for the sphere problem; whereas, the periodic array of cylinders exhibits a steady-state solution above $We = 3.0$. It is surprising that there is a distinct lack of structure in the velocity eigenfunctions along the walls of the cylinder in which the sphere is falling. The results obtained here indicate that some fine scale structure should be observed near the wall. The stability of the results by Northey appear reasonable overall; however, the conclusion that neutral stability is being approached near $De = 1.6$ cannot be confirmed until fully nonlinear time dependent calculations are performed as in Chapter 8 for the periodic array of cylinders.

Chapter 8

Nonlinear Time Dependent Viscoelastic Flow Calculations

"For every complex question, there is a simple answer and it is wrong."

– H.L. Mencken

The goal of this thesis is to implement a numerical method capable of solving nonlinear time dependent viscoelastic flow calculations. In order to gain confidence in the numerical method, linear stability calculations were performed to ensure the temporal stability of the algorithm. Then linear stability calculations for two flows with no known solution were examined. In this chapter, the EVSS-G/FEM and DEVSS-G/FEM will be examined for the solution of startup up calculations for both planar Couette flow and the flow through an infinite periodic array of cylinders in a channel. Finally, nonlinear stability calculations will be performed to validate the results of the linear stability problems without closed-form solutions.

8.1 Fully Implicit Methods

To this point, all time dependent calculations have been linear; thus, the time solver is basically the implementation of forward-backward substitution once a pre-processing

LU decomposition has been performed. The implementation of the time integrator was briefly discussed in Chapter 4 where it was stated that due to the nature of the equations being solved (differential-algebraic equations), strictly explicit methods are not feasible (Ungar *et al.*, 1988). This leaves the possibility of using fully implicit and semi-implicit methods. Only fully implicit methods (i.e., first and second order Adams-Moulton methods) were implemented for the linear stability calculations presented in Chapter 5. The application of these two methods in eqs. (4.63) and (4.66) is fully implicit in all unknowns; so the algorithm is numerically stable if applied to a system of linear equations. This fact was utilized in the linear stability problem to show that the instability found was caused by the EEME and EVSS spatial discretizations. The major drawback of fully implicit time integration methods is the computational time required to solve the large system of nonlinear equations that must be solved at every Newton iteration for each time step.

In order to gain a perspective on the large computational time that may be required, an order of magnitude estimate can be found through a simple examination of the computational time required for the steady- state simulations. A steady-state simulation of the flow of a CR-FENE fluid through a periodic linear array of cylinders in a channel as described in Section 6.2 with 41,652 degrees-of-freedom takes approximately two hours per Newton iteration on an HP9000 Series 735 workstation. If three iterations are required for convergence in the nonlinear time dependent simulation, then this results in approximately 6 hours of computational time per time step. If, say, six hundred time steps are necessary to determine the time dependent nature of the solution, then this would require approximately 3,600 hours (150 days) of CPU time, which is clearly not feasible. Upgrading the machine platform to the CRAY-C90 does not help too much. Based on experience from steady-state simulations, only an order-of-magnitude decrease in CPU time will result from this change (at most a factor 15-20).

The algorithm can be optimized somewhat by using a quasi-Newton algorithm in which the *LU* decomposition from one time step is retained as the operator for the Newton iteration for several iterations or (hopefully) several timesteps. This is

usually implemented using a predictor-corrector type scheme as outlined in Chapter 4. In several test calculations for planar Couette flow, this method did not appear to be fruitful due to the poor prediction properties of the predictor. It appeared as if the predictor equation was so unstable that the error between the predicted and corrected solution were large enough to initially require extremely small time steps. For this reason semi-implicit time integration methods (SITIMs) were examined.

8.2 Semi-Implicit Time Integration Methods

The idea of a semi-implicit time integration method is very simple; some variables are handled implicitly while others are handled explicitly. Most semi-implicit methods are of the decoupled type where equations that are dependent on one another are split apart and solved sequentially. If an iteration scheme is incorporated, in the limit of infinite iterations, the fully implicit result is guaranteed to result. Two types of methods are examined; the first is a simple sequential solution of blocks of the unknowns as was examined previously by Northey (1991) and the second is based on operator splitting methods which were reviewed in Glowinski & Periaux (1992).

8.2.1 Decoupled, Semi-Implicit Method

In decoupled, semi-implicit methods, the equations to be solved are divided into blocks and each block is then solved separately using an implicit method with the variables passed explicitly between the blocks. For the discretized viscoelastic flow equations, the first order Adams-Moulton method for the time discretization is expressed as

$$\boldsymbol{M}^{\tau}(\boldsymbol{a}_{n+1})\left[\frac{\boldsymbol{a}_{n+1}-\boldsymbol{a}_{n}}{\Delta t}\right]+\boldsymbol{R}^{\tau}(\boldsymbol{a}_{n+1})=\boldsymbol{0}, \tag{8.1}$$

$$\boldsymbol{R}^{v}(\boldsymbol{a}_{n+1})=\boldsymbol{0}, \tag{8.2}$$

where $\boldsymbol{M}^{\tau}$ is the mass matrix for the stress variables, $\boldsymbol{R}^{\tau}$ is the steady-state residual vector for the constitutive equations and $\boldsymbol{R}^{v}$ is the steady-state residual for the momentum, continuity and velocity gradient interpolation equations. In a decoupled,

semi-implicit time integration method, the equations would be split up by unknowns and solved in blocks. For example, one method introduced in Northey (1991) for the EEME discretization (no interpolation unknowns, see Chapter 4) consists of first solving the velocity and shear stress ($\boldsymbol{a}^v$) and the pressure ($\boldsymbol{a}^q$) at the $(n+1)$th time step

$$\boldsymbol{M}^v(\boldsymbol{a}^v_{n+1})\left[\frac{\boldsymbol{a}^v_{n+1}-\boldsymbol{a}^v_n}{\Delta t}\right] + \boldsymbol{R}^v(\boldsymbol{a}^v_{n+1}, \boldsymbol{a}^q_{n+1}, \boldsymbol{a}^\tau_n) = \boldsymbol{0} \tag{8.3}$$

$$\boldsymbol{R}^q(\boldsymbol{a}^v_{n+1}, \boldsymbol{a}^\tau_n) = \boldsymbol{0} \tag{8.4}$$

where the normal stresses ($\boldsymbol{a}^\tau$) are evaluated at the previous time step. After the solution of these equations, the normal stresses are updated to the new time step by solving

$$\boldsymbol{M}^\tau(\boldsymbol{a}^v_n)\left[\frac{\boldsymbol{a}^\tau_{n+1}-\boldsymbol{a}^\tau_n}{\Delta t}\right] + \boldsymbol{R}^\tau(\boldsymbol{a}^v_n, \boldsymbol{a}^\tau_{n+1}) = \boldsymbol{0}, \tag{8.5}$$

where the velocity and shear stress unknowns are evaluated from the solution of eqs. (8.3) and (8.4). A Picard iteration scheme can be implemented for the two sets of equations or the next time step can be proceeded to directly. Obviously, the more iterations performed the less the error introduced by the semi-implicit solution scheme.

Fortin & Esselaoui (1987) and Serdokowski & Caswell (1988) have used such a method, but with limited success. Neither were able to obtain convergence for large values of De. In their methods, the solution of the momentum and continuity equation is decoupled from the calculation of the constitutive equations; the equations were left in their original form. The type of the variables was not taken into account by these methods; thus, the equation type was mixed across the blocks. Northey (1991) suggested that the mathematical type of the equations is an important factor in the splitting of the original equations into subsets to be solved. He examined three semi-implicit methods, the first of which was introduced above. Utilizing the EEME formulation, the velocity, shear stress $\tau_{r\theta}$ and the pressure q make up one block while the normal stresses ($\tau_{rr}, \tau_{\theta\theta}$) make up the other. This effectively decouples the EEME equations into an elliptic and a hyperbolic block which is consistent with the

mathematical type of the unknowns. Two decouplings with mixed type across the equation blocks were also examined by Northey (1991): the momentum/continuity equation pair in one block and the stresses in another as done previously by Fortin & Esselaoui (1987) and Serdokowski & Caswell (1988) and the velocity, pressure and the azimuthal stress $\tau_{\theta\theta}$ in one block and the shear and radial normal stresses ($\tau_{rr}, \tau_{r\theta}$) in the other. In numerical results using the startup of concentric cylinder flow, the latter two methods were found to be unstable in time whereas the elliptic/hyperbolic decoupling produced numerically stable results. Using a second iteration through the latter equations, the accuracy was increased as expected. The semi-implicit method was found to take approximately one-third of the computational time of the fully implicit method.

Examination of the decoupled semi-implicit method for the EVSS-G formulation, while keeping the type of the equations in mind, results in a splitting into three blocks. The first consists of the elliptic saddle point problem defined by the momentum and continuity equations where the stress acts as a non-homogeneous forcing term, the second is the interpolation of the velocity gradients and, finally, the stresses are calculated using the velocities and velocity gradients previously found. A big advantage to this type of decoupling scheme is in the use of multi-mode constitutive models; additional modes could be added as additional blocks of equations to be solved after the first three previously mentioned blocks, as each mode is linearly independent of the others. The increase in computational time would be approximately linear with the number of unknowns N rather than the fully implicit result with an $N(BW)^2$ increase.

This method was evaluated for the linear stability of planar Couette flow for a UCM fluid as studied in Chapter 5 for the EVSS-G formulation. An advantage of this is that the constitutive equation block is also linear because the nonlinearity arises from the bilinear terms of the velocity, velocity gradient and the stresses and is decoupled in this approach. The viscoelastic flow problem is solved using the following process:

1. Initial conditions are introduced for the stress field (the only variable that sat-

isfies a differential equation for the inertialess flow). Self consistent values of the velocity, pressure and velocity gradient fields are used which is calculated by solving the momentum, continuity and velocity gradient interpolation equations using the initial condition of the stress as inhomogeneous data as in step 3 below. For the linear stability problem, the velocity, pressure and velocity gradient are all set to zero for the initial disturbance.

2. Solve the constitutive equations using the previous time step for the velocity and velocity gradient variables. A first order Adams-Moulton method was used to integrate the equations in time with the SUPG finite element formulation for the spatial discretization.

3. Solve the momentum/continuity equation pair as a Stokes problem with inhomogeneous data.

4. Interpolate the velocities onto the bilinear continuous velocity gradient unknowns.

5. Solve the constitutive equations as in Step 2 using the values of the velocity from Step 3 and velocity gradient from Step 4.

6. Evaluate the error criteria to determine if the solution can proceed to the next time step. Repeat steps 3-5 until convergence of the error criteria.

Steps 3-6 are repeated for each time step. The error criterion is based on the stress variables as these are the variables of the most interest,

$$\frac{\boldsymbol{\tau}_{m+1}^{n+1} - \boldsymbol{\tau}_{m}^{n+1}}{\boldsymbol{\tau}_{m+1}^{n+1}} \leq \epsilon, \tag{8.6}$$

where m is the iteration number and ϵ is the user specified error tolerance.

In the comparison of the fully implicit method to the semi-implicit method (with iterations) it is instructive to obtain an initial estimate for the "break-even" point between using the two methods. For frontal algorithms, the operation count is proportional to the number of elements multiplied by the square of the bandwidth or front-

width. Since this is a comparison of two frontal algorithms for the same problem, the operation count should roughly depend on the bandwidth squared. The bandwidth will be roughly the number of quadratic unknowns times the nine quadratic nodes plus the number of linear unknowns times the four linear nodes, since the other factors should approximately factor out. For the EVSS-G/FEM, two quadratic unknowns and seven linear unknowns results in a bandwidth squared of 2116. Repeating the same for each block in the semi-implicit method yields $484 + 144 + 144 = 772$ for the bandwidth squared. Thus, approximately three iterations result in approximately identical times between the fully implicit method and the semi-implicit method. Northey (1991) found that the semi-implicit methods would give slightly better results than this; so it is estimated that approximately 5 iterations will be required for the fully implicit method to be preferred over the semi-implicit method. For multi-mode models, this will become even more favorable for the semi-implicit method where 10-12 iterations will be the cross-over point for a 4-mode model. The semi-implicit method will be favored unless a large number of the Picard iterations (step 6) are needed to satisfy the error criterion.

Unfortunately, this is exactly what was found; the semi-implicit method requires a large number of iterations per time step to remain linearly stable and reproduce the stability characteristics displayed by the continuous problem. The coupling between the velocity and the stress variables appears to be so strong that small changes in the velocity field ($O(10^{-2})$) can cause $O(1)$ changes in the stress field. Thus, as the velocity field slowly converges, the stress changes dramatically and the error criterion in eq. (8.6) cannot be met. Setting the error tolerance to 10^{-2} resulted in an unstable algorithm while 10^{-3} still took excessively long times to converge (> 15 iterations). Typically a 10^{-4} error criterion could not be met in the calculations even after 50 iterations. This method was abandoned due to these results and efforts were focused on finding other semi-implicit methods used in other fields which may be applicable to the viscoelastic flow equations. The only method found found successful for these calculations was the operator splitting technique, which is discussed in the next section.

8.2.2 Operator Splitting Methods

Operator splitting techniques were first introduced by Peaceman & Rachford (1955) as the alternating direction implicit method. In these methods the differential equation is taken to be of the form

$$\frac{d\boldsymbol{u}}{dt} + \boldsymbol{A}(\boldsymbol{u}) = \boldsymbol{f}, \tag{8.7}$$

$$\boldsymbol{u}(0) = \boldsymbol{u}^0, \tag{8.8}$$

where $\boldsymbol{u} \in H$ which is a real Hilbert space as discussed in Chapter 3, $\boldsymbol{A}$ is an operator from H to H, $\boldsymbol{f}$ is a source term and $\boldsymbol{u}_0$ is the initial condition. Let $\boldsymbol{A}_1$ and $\boldsymbol{A}_2$ be two operators such that

$$\boldsymbol{A} = \boldsymbol{A}_1 + \boldsymbol{A}_2. \tag{8.9}$$

The operator splitting methods utilize this decomposition of the operator to facilitate the integration of the initial value problem. The operator splitting techniques have been extended by numerous researchers since the initial work of Peaceman & Rachford (1955) and include Strang (1968), Yanenko (1971), Marchuk (1975), Beale & Majda (1981), Leveque & Oliger (1983), Fortin & Glowinski (1983), Glowinski & LeTallec (1989) and the references therein.

The basic concepts behind operator splitting can be shown by examining the Peaceman-Rachford alternating-direction implicit finite difference method. The initial value problem of eq. (8.7) is solved by taking the usual time step, $k = \Delta t$, and dividing it into two subintervals using the midpoint $(n + 1/2)k$. Over the first subinterval, the equation is discretized using the first order Adams-Moulton method with respect to the first operator $\boldsymbol{A}_1$ and the first order Adams-Bashforth method with respect to $\boldsymbol{A}_2$. On the second subinterval, this procedure is reversed so that the implicit method is applied to the second operator $\boldsymbol{A}_2$. To advance to the next time level, the following scheme is used:

$$\frac{\boldsymbol{u}^{n+1/2} - \boldsymbol{u}^n}{k/2} + \boldsymbol{A}_1(\boldsymbol{u}^{n+1/2}) + \boldsymbol{A}_2(\boldsymbol{u}^n) = \boldsymbol{f}_{n+1/2}, \tag{8.10}$$

$$\frac{\boldsymbol{u}^{n+1} - \boldsymbol{u}^{n+1/2}}{k/2} + \boldsymbol{A}_1(\boldsymbol{u}^{n+1/2}) + \boldsymbol{A}_2(\boldsymbol{u}^{n+1}) = \boldsymbol{f}_{n+1}. \tag{8.11}$$

To examine the convergence and stability of this scheme, assume, for simplicity, that $\boldsymbol{f} = \boldsymbol{0}$ and $\boldsymbol{A}$ is an NxN symmetric, positive definite matrix. Solve eqs. (8.10) and (8.11) for $\boldsymbol{u}^{n+1}$ as

$$\boldsymbol{u}^{n+1/2} = (\boldsymbol{I} + \tfrac{k}{2}\boldsymbol{A}_1)^{-1}(\boldsymbol{I} - \tfrac{k}{2}\boldsymbol{A}_2)\boldsymbol{u}^n, \tag{8.12}$$

$$\boldsymbol{u}^{n+1} = (\boldsymbol{I} + \tfrac{k}{2}\boldsymbol{A}_2)^{-1}(\boldsymbol{I} - \tfrac{k}{2}\boldsymbol{A}_1)\boldsymbol{u}^{n+1/2}. \tag{8.13}$$

Substituting eq. (8.12) into eq. (8.13) yields

$$\boldsymbol{u}^{n+1} = (\boldsymbol{I} + \frac{k}{2}\boldsymbol{A}_2)^{-1}(\boldsymbol{I} - \frac{k}{2}\boldsymbol{A}_1)(\boldsymbol{I} + \frac{k}{2}\boldsymbol{A}_1)^{-1}(\boldsymbol{I} - \frac{k}{2}\boldsymbol{A}_2)\boldsymbol{u}^n. \tag{8.14}$$

If we take a simple operator splitting to be

$$\boldsymbol{A}_1 = \alpha\boldsymbol{A}, \tag{8.15}$$

$$\boldsymbol{A}_2 = \beta\boldsymbol{A}, \tag{8.16}$$

where $\alpha + \beta = 1$ and $0 < \alpha$ and $\beta < 1$. This will result in the following equation at the $(n+1)$th time step:

$$\boldsymbol{u}^{n+1} = (\boldsymbol{I} + \beta\frac{k}{2}\boldsymbol{A})^{-1}(\boldsymbol{I} - \alpha\frac{k}{2}\boldsymbol{A})(\boldsymbol{I} + \alpha\frac{k}{2}\boldsymbol{A})^{-1}(\boldsymbol{I} - \beta\frac{k}{2}\boldsymbol{A})\boldsymbol{u}^n. \tag{8.17}$$

Using a vector basis consisting of the eigenvectors of $\boldsymbol{A}$ (allowable since it is positive definite) this last equation can be rewritten using the eigenvalues of $\boldsymbol{A}$ ordered from smallest to largest, $0 < \lambda_1 \leq \lambda_2 \leq \ldots \leq \lambda_N$,

$$\boldsymbol{u}_i^{n+1} = \frac{(1 - \alpha\frac{k}{2}\lambda_i)(1 - \beta\frac{k}{2}\lambda_i)}{(1 + \alpha\frac{k}{2}\lambda_i)(1 + \beta\frac{k}{2}\lambda_i)}\boldsymbol{u}_i^n. \tag{8.18}$$

The coefficient in eq. (8.18), $\boldsymbol{R}_1$, is always less than one in absolute value so this method is unconditionally stable for all time steps. The convergence of this scheme

has been proved for much more general conditions on the properties of $\boldsymbol{A}_1$ and $\boldsymbol{A}_2$ such as nonlinearities and even multi-valued operators are allowed (Glowinski & Pironneau 1992). For stiff problems ($\lambda_N/\lambda_1 \gg 1$), which will give for the coeficient in eq. (8.18)

$$\lim_{x\to\infty} \boldsymbol{R}_1(x) = \lim_{x\to\infty} \frac{(1-\alpha\frac{k}{2}x)(1-\beta\frac{k}{2}x)}{(1+\alpha\frac{k}{2}x)(1+\beta\frac{k}{2}x)} = 1. \tag{8.19}$$

Thus, the Peaceman-Rachford scheme does not damp the components of $\boldsymbol{u}^n$ corresponding to both large and small eigenvalues of $\boldsymbol{A}$ well; the result is a poor scheme for the computation of stiff problems. Since differential-algebraic equations are equivalent to infinitely stiff problems ($x = \infty$ in eq. (8.19)), the solution cannot be expected to exhibit good convergence properties (for steady-state solutions it could take an infinite amount of time to converge). The accuracy of this scheme will also be examined. The exact solution of eq. (8.7) is given by

$$\boldsymbol{u}(t) = u_0 e^{-t\boldsymbol{A}}. \tag{8.20}$$

This solution can be expanded in a Taylor series since

$$e^{-x} = 1 - x + \frac{1}{2}x^2 + x^2\boldsymbol{\epsilon}(x). \tag{8.21}$$

The coefficient from eq. (8.18), $\boldsymbol{R}_1(x)$, can also be expanded into a Taylor series as

$$\boldsymbol{R}_1(x) = 1 - x + \frac{1}{2}x^2 + x^2\boldsymbol{\eta}(x). \tag{8.22}$$

In the limit of vanishing x,

$$\lim_{x\to 0} \boldsymbol{\epsilon}(x) = \lim_{x\to 0} \boldsymbol{\eta}(x) = 0. \tag{8.23}$$

For this simple case for $\boldsymbol{A}$, the scheme is second order accurate.

Since incompressible flow problems are differential-algebraic equations, several different methods have been developed to overcome the difficulty of the Peaceman-Rachford scheme for stiff problems. Several methods are discussed in Marchuk (1975);

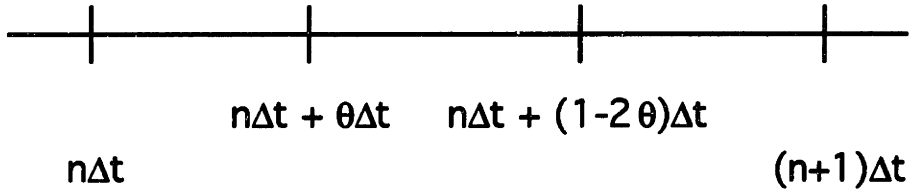

Figure 8-1: Schematic diagram of the division of the time interval $[n\Delta t, (n+1)\Delta t]$ into three subintervals in the θ-method.

another was given by Strang(1968) and studied by LeVeque & Oliger (1983) and Beale & Majda (1985). This latter method was generalized by Glowinski and coworkers (Bristeau *et al.*, 1985, 1987, Glowinski 1984, 1986, 1988, Glowinski & LeTallec 1989, and Glowinski & Pironneau, 1992) into the θ-method. In this scheme, the time interval $[n\Delta t, (n+1)\Delta t]$ is divided into the three subintervals $[n\Delta t, (n+\theta)\Delta t]$, $[(n+\theta)\Delta t, (n+1-\theta)\Delta t]$, and $[(n+1-\theta)\Delta t, (n+1)\Delta t]$ as indicated in Figure 8-1. As in the Peaceman-Rachford scheme, the two operators are discretized in time using either the first order Adams-Moulton or Adams-Bashforth method and is switched on alternating time steps. This gives the following method:

$$\frac{\boldsymbol{u}^{n+\theta} - \boldsymbol{u}^{n}}{\theta\Delta t} + \boldsymbol{A}_1(\boldsymbol{u}^{n+\theta}) + \boldsymbol{A}_2(\boldsymbol{u}^{n}) = \boldsymbol{f}^{n+\theta}, \tag{8.24}$$

$$\frac{\boldsymbol{u}^{n+1-\theta} - \boldsymbol{u}^{n+\theta}}{(1-2\theta)\Delta t} + \boldsymbol{A}_1(\boldsymbol{u}^{n+\theta}) + \boldsymbol{A}_2(\boldsymbol{u}^{n+1-\theta}) = \boldsymbol{f}^{n+1-\theta}, \tag{8.25}$$

$$\frac{\boldsymbol{u}^{n+1} - \boldsymbol{u}^{n+1-\theta}}{\theta\Delta t} + \boldsymbol{A}_1(\boldsymbol{u}^{n+1}) + \boldsymbol{A}_2(\boldsymbol{u}^{n+1-\theta}) = \boldsymbol{f}^{n+1}, \tag{8.26}$$

where $\theta \in (0,1)$.

In order to examine the basic stability and convergence properties of this scheme, let $\boldsymbol{A}$ be split as above, eqs. (8.15) and (8.16), $\boldsymbol{f} = \boldsymbol{0}$ and solve for $\boldsymbol{u}^{n+1}$ to give

$$\begin{aligned}\boldsymbol{u}^{n+1} = &(\boldsymbol{I} + \alpha\theta\Delta t\boldsymbol{A})^{-1}(\boldsymbol{I} - \beta\theta\Delta t\boldsymbol{A})(\boldsymbol{I} + \beta(1-\theta)\Delta t\boldsymbol{A})^{-1} \\ &(\boldsymbol{I} - \alpha(1-\theta)\Delta t\boldsymbol{A})(\boldsymbol{I} + \alpha\theta\Delta t\boldsymbol{A})^{-1}(\boldsymbol{I} - \beta\theta\Delta t\boldsymbol{A})\boldsymbol{u}^{n}.\end{aligned} \tag{8.27}$$

Using a vector basis of eigenvectors of $\boldsymbol{A}$ as used in the derivation of eq. (8.18) yields

$$\boldsymbol{u}_i^{n+1} = \frac{(1-\beta\theta\Delta t\lambda_i)^2(1-\alpha(1-\theta)\Delta t\lambda_i)}{(1+\alpha\theta\Delta t\lambda_i)^2(1+\beta(1-\theta)\Delta t\lambda_i)}\boldsymbol{u}_i^n. \tag{8.28}$$

From this, a rational function $\boldsymbol{R}_2(x)$ can be defined as the coefficient in eq. (8.29)

$$\boldsymbol{R}_2(x) = \frac{(1-\beta\theta\Delta tx)^2(1-\alpha(1-\theta)\Delta tx)}{(1+\alpha\theta\Delta tx)^2(1+\beta(1-\theta)\Delta tx)}. \tag{8.29}$$

The eigenvalues of $\boldsymbol{A}$ are always greater than zero; so in the limit $x \to 0$, $\boldsymbol{R} < 1$ and in the limit as $x \to \infty$

$$\lim_{x\to\infty} |\boldsymbol{R}_2(x)| = \beta/\alpha. \tag{8.30}$$

To ensure the unconditional stability of the algorithm $\alpha \geq \beta$. In order to avoid the problem with stiff problems that troubled the Peaceman-Rachford scheme, $\alpha > \beta$.

The accuracy of this method compared to the Peaceman-Rachford method. Expanding eq. (8.29) in a Taylor series yields

$$\boldsymbol{R}_2(x) = 1 - x + \frac{1}{2}x^2\left(1 + (\beta^2-\alpha^2)(2\theta^2-4\theta+1)\right) + x^2\boldsymbol{\eta}(x). \tag{8.31}$$

In the limit of vanishing x, eq. (8.23) again holds. In order for the scheme to be second order accurate either

$$\alpha = \beta, \tag{8.32}$$

or

$$\theta = 1 - \sqrt{2}/2. \tag{8.33}$$

But the first condition is ruled out to prevent the original problem with stiff ordinary differential equations that the Peaceman-Rachford method had. The optimal choice of θ is given by eq. (8.33).

With the simple splitting of the operator given in eqs. (8.15) and (8.16), it is possible to minimize the work done at each step by ensuring the implicit matrix to

be inverted is the same for each of the three steps in the method. This requires that

$$\alpha\theta = \beta(1 - 2\theta). \tag{8.34}$$

This implies that

$$\alpha = \frac{1 - 2\theta}{1 - \theta}, \tag{8.35}$$

$$\beta = \frac{\theta}{1 - \theta}. \tag{8.36}$$

Using this to substitute into eq. (8.29) yields

$$\lim_{x \to \infty} |\boldsymbol{R}(x)| = \beta/\alpha = \theta/(1 - 2\theta) < 1. \tag{8.37}$$

This gives an upper bound on θ of $1/3$ and it can be shown (Bristeau *et al.*, 1987) that the lower bound for θ is $\theta^* = 0.087385580\ldots$ for the unconditional stability of the θ-method for α, β given by eqs. (8.35) and (8.36), respectively. It is also true that the scheme has good asymptotic properties as $n \to \infty$ and is a good method for the solution of stiff problems. In this work, two values of θ were used and were found to be indistinguishable in terms of the results in planar Couette flow, $\theta = 1/4,\ 1 - \sqrt{2}/2$ which gives $\alpha = 2/3,\ 2 - \sqrt{2}$ and $\beta = 1/3,\ \sqrt{2} - 1$, respectively.

The application of the θ-method to the Navier-Stokes equations is discussed in the work of Glowinski and coworkers. In general, they found that the value of $\theta = 1 - \sqrt{2}$ is nearly optimal for a variety of problems. This method was proved to be convergent for the Navier-Stokes equations by Fernandez-Cara & Beltran (1989) for $\theta = 1/4$ and for general θ by Kloucek & Rys (1994).

The θ-method was first applied to the viscoelastic flow equations by Saramito(1994) and Saramito & Piau (1994) in which the equations were split into hyperbolic and parabolic parts to be solved alternately. The Oldroyd-B constitutive equations were used in conjunction with the viscous formulation, eqs. (4.14)–(4.16). The operator

splitting was done as follows:

$$\boldsymbol{A}_1 = \begin{pmatrix} \frac{\omega}{2\alpha}\boldsymbol{\tau} - \boldsymbol{D}(\boldsymbol{u}) \\ \boldsymbol{\nabla}\cdot\boldsymbol{\tau} + (1-\alpha)\triangle\boldsymbol{u} - \boldsymbol{\nabla}p \\ \boldsymbol{\nabla}\cdot\boldsymbol{u} \end{pmatrix}, \tag{8.38}$$

$$\boldsymbol{A}_2 = \begin{pmatrix} \frac{De}{2\alpha}\left[(\boldsymbol{u}\cdot\boldsymbol{\nabla})\boldsymbol{\tau} + \beta_a(\boldsymbol{\tau}, \boldsymbol{\nabla}\boldsymbol{u}) + \frac{1-\omega}{2\alpha}\boldsymbol{\tau}\right] \\ \boldsymbol{0} \\ \boldsymbol{0} \end{pmatrix}, \tag{8.39}$$

where $\omega \in [0.5, 1.0)$, $\boldsymbol{D}(\boldsymbol{u}) = 2\dot{\boldsymbol{\gamma}}$, and $\beta_a(\boldsymbol{\tau}, \boldsymbol{\nabla}\boldsymbol{u}) = -(\boldsymbol{\nabla}\boldsymbol{u})^T\cdot\boldsymbol{\tau} - \boldsymbol{\tau}\cdot\boldsymbol{\nabla}\boldsymbol{u}$. The mass matrix for the system of equations is

$$\boldsymbol{M} = \text{diag}\left(\frac{De}{2\alpha}, -Re, 0\right). \tag{8.40}$$

Note that Saramito (1994) elected to keep the velocity time derivative while at the same time neglecting the steady-state inertia term $\boldsymbol{u}\cdot\boldsymbol{\nabla}\boldsymbol{u}$. The θ-algorithm introduced by Saramito (1994) is

1. a) Calculate explicitly the expressions

$$\boldsymbol{\gamma}^n = (\boldsymbol{u}^n\cdot\boldsymbol{\nabla})\boldsymbol{\tau}^n + \beta_a^n(\boldsymbol{\tau}^n, \boldsymbol{\nabla}\boldsymbol{u}^u), \tag{8.41}$$

$$\boldsymbol{f}_1 = \lambda\boldsymbol{u}^n + c_1\boldsymbol{\nabla}\cdot\boldsymbol{\tau}^n + c_2\boldsymbol{\nabla}\cdot\boldsymbol{\gamma}^n. \tag{8.42}$$

b) Calculate implicitly $(\boldsymbol{u}^{n+\theta}, p^{n+\theta})$

$$\lambda\boldsymbol{u}^{n+\theta} - \eta\triangle\boldsymbol{u}^{n+\theta} + \boldsymbol{\nabla}p^{n+\theta} = \boldsymbol{f}_1, \tag{8.43}$$

$$\boldsymbol{\nabla}\cdot\boldsymbol{u}^{n+\theta} = \boldsymbol{0}. \tag{8.44}$$

c) Calculate explicitly the stresses $(\boldsymbol{\tau}^{n+\theta})$

$$\boldsymbol{\tau}^{n+\theta} = c_1\boldsymbol{\tau}^n + c_2\boldsymbol{\gamma}^n + c_3\boldsymbol{D}(\boldsymbol{u}^{n+\theta}). \tag{8.45}$$

2. a) Calculate explicitly the velocity $(\boldsymbol{u}^{n+1-\theta})$

$$\boldsymbol{g}^{n+1-\theta} = c_4\boldsymbol{\tau}^{n+\theta} + c_5\boldsymbol{D}(\boldsymbol{u}^{n+\theta}), \tag{8.46}$$

$$\boldsymbol{u}^{n+1-\theta} = \frac{1-\theta}{\theta}\boldsymbol{u}^{n+\theta} - \frac{1-2\theta}{\theta}\boldsymbol{u}^{n}. \tag{8.47}$$

b) Calculate implicitly the stresses $(\boldsymbol{\tau})$

$$(\boldsymbol{u}^{n+1-\theta}\cdot\nabla)\boldsymbol{\tau}^{n+1-\theta} + \beta_a^{n+1-\theta}(\boldsymbol{\tau}^{n+1-\theta}, \boldsymbol{u}^{n+1-\theta}) + \nu\boldsymbol{\tau}^{n+1-\theta} = \boldsymbol{g}^{n+1-\theta}. \tag{8.48}$$

3. Repeat 1 but with $n+1 \leftarrow n+\theta$ and $n+1-\theta \leftarrow n$.

In these steps the constants are defined as follows:

$$\theta = 1 - 1/\sqrt{2}, \tag{8.49}$$

$$\lambda = Re/\theta\Delta t, \tag{8.50}$$

$$\eta = 1 - \alpha\frac{De - (1-\omega)\theta\Delta t}{De + \omega\Delta t}, \tag{8.51}$$

$$\nu = \frac{1}{(1-2\theta)\Delta t} + \frac{1-\omega}{De}, \tag{8.52}$$

$$c_1 = \frac{De - (1-\omega)\theta\Delta t}{De + \omega\theta\Delta t}, \tag{8.53}$$

$$c_2 = -\frac{De\theta\Delta t}{De + \omega\theta\Delta t}, \tag{8.54}$$

$$c_3 = \frac{2\alpha\theta\Delta t}{De + \omega\theta\Delta t}, \tag{8.55}$$

$$c_4 = \frac{1}{(1-2\theta)\Delta t} - \frac{\omega}{De}, \tag{8.56}$$

$$c_5 = 2\alpha/De. \tag{8.57}$$

In the evaluation of this method, steps 1 and 3 consist simply of solving a nonhomogeneous Stokes problem for the velocity and pressure (a linear, symmetric problem) and the stress is found through an explicit update. This will be extremely fast. Step 2 consists of an explicit update of the velocity followed by the solution of a nonlinear hyperbolic transport equation in time. Actually for the Oldroyd-B constitutive equations, this is a linear hyperbolic equation set, but for a more complex constitutive

equation set such as the CR-FENE model it will be nonlinear. Because there are only three unknowns involved in the solution of the problem at this step, it will be significantly faster than the fully implicit method.

Singh & Leal (1993) also have introduced an operator splitting θ-method for the viscoelastic flow problem using the CR-FENE model. However, unlike Saramito, all three of their steps are nonlinear and remain coupled for all of the unknowns. Therefore, instead of reducing the total computational time needed for the fully implicit method, Singh and Leal actually compute essentially three fully implicit problems to advance one time step. Another splitting method was introduced by Baaijens (1993). The method essentially consists of solving an estimate for the stress using the Hessian matrix then solving the fully implicit problem applying the discontinuous Galerkin method to the stresses so as to eliminate them at the element level. These two steps are then iterated to convergence. This method probably will not save a lot of computational time, since the entire problem must still be calculated in step 2 although the stresses are eliminated at the elemental level which will reault in some savings. However, the solution of the Hessian to estimate the stresses and then iterating over the entire scheme will probably offset the gain in computational time through the elemental elimination of the stress. It appears that the Saramito-type operator splitting may be fruitful in the EVSS-G/FEM and DEVSS-G/FEM framework and is examined in the next sections.

8.2.3 θ-Method Applied to the EVSS-G/FEM

The EVSS-G formulation will be examined in light of the θ-method along the lines of Saramito (1994). The total equation operator $\boldsymbol{A}$ is split into an elliptic operator

$$\boldsymbol{A}_1 = \begin{pmatrix} \omega\boldsymbol{\Sigma} \\ -\triangle\boldsymbol{u} + \boldsymbol{\nabla}\cdot\boldsymbol{\Sigma} + \boldsymbol{\nabla}p \\ \boldsymbol{\nabla}\cdot\boldsymbol{u} \\ \boldsymbol{G} - \boldsymbol{\nabla}\boldsymbol{u} \end{pmatrix}, \tag{8.58}$$

and a hyperbolic operator

$$\boldsymbol{A}_2 = \begin{pmatrix} (1-\omega)\boldsymbol{\Sigma} + De[\boldsymbol{u}\cdot\nabla\boldsymbol{\Sigma} - \boldsymbol{G}^T\cdot\boldsymbol{\Sigma} - \boldsymbol{\Sigma}\cdot\boldsymbol{G}] \\ -(1-\beta)De\left[\boldsymbol{u}\cdot\nabla(\boldsymbol{G}+\boldsymbol{G}^T) - \boldsymbol{G}^T\cdot\boldsymbol{G}^T - 2\boldsymbol{G}^T\cdot\boldsymbol{G} - \boldsymbol{G}\cdot\boldsymbol{G}\right] \\ \boldsymbol{0} \\ \boldsymbol{0} \\ \boldsymbol{0} \end{pmatrix}. \tag{8.59}$$

The mass matrix for the EVSS-G method looks like

$$\boldsymbol{M} = \begin{pmatrix} De & 0 & 0 & -(1-\beta)De \\ 0 & 0 & 0 & 0 \\ 0 & 0 & 0 & 0 \\ 0 & 0 & 0 & 0 \end{pmatrix}. \tag{8.60}$$

Now, the θ-scheme can be formulated for the EVSS-G/FEM as

1. a) Calculate implicitly the velocity and pressure $(\boldsymbol{u}^{n+\theta}, p^{n+\theta})$

$$\begin{aligned} -c_6\Delta\boldsymbol{u}^{n+\theta} + \nabla p^{n+\theta} &= -c_2\boldsymbol{\Sigma}^n + c_4\nabla\cdot[\boldsymbol{G}^n + (\boldsymbol{G}^n)^T] \\ &+ c_3\nabla\cdot[\boldsymbol{u}^n\cdot\nabla\boldsymbol{\Sigma}^n - (\boldsymbol{G}^n)^T\cdot\boldsymbol{\Sigma}^n - \boldsymbol{\Sigma}^n\cdot\boldsymbol{G}^n] \\ &- c_5\nabla\cdot\left[\boldsymbol{u}^n\cdot\nabla(\boldsymbol{G}^n + (\boldsymbol{G}^n)^T) - (\boldsymbol{G}^n)^T\cdot(\boldsymbol{G}^n)^T\right. \\ &\left. - 2(\boldsymbol{G}^n)^T\cdot\boldsymbol{G}^n - \boldsymbol{G}^n\cdot\boldsymbol{G}^n\right], \end{aligned} \tag{8.61}$$

$$\nabla\cdot\boldsymbol{u}^{n+\theta} = \boldsymbol{0}. \tag{8.62}$$

b) Calculate the interpolation of the velocity gradient $(\boldsymbol{G}^{n+\theta})$

$$\boldsymbol{G}^{n+\theta} - \nabla\boldsymbol{u}^{n+\theta} = \boldsymbol{0}. \tag{8.63}$$

c) Calculate explicitly the stresses $(\boldsymbol{\Sigma}^{n+\theta})$

$$\boldsymbol{\Sigma}^{n+\theta} = c_2\boldsymbol{\Sigma}^n - c_3[\boldsymbol{u}^n\cdot\nabla\boldsymbol{\Sigma}^n - (\boldsymbol{G}^n)^T\cdot\boldsymbol{\Sigma}^n - \boldsymbol{\Sigma}^n\cdot\boldsymbol{G}^n]$$

$$
\begin{aligned}
&+ c_4[\boldsymbol{G}^{n+\theta} + (\boldsymbol{G}^{n+\theta})^T - \boldsymbol{G}^n - (\boldsymbol{G}^n)^T] \\
&+ c_5 \left[\boldsymbol{u}^n \cdot \boldsymbol{\nabla}(\boldsymbol{G}^n + (\boldsymbol{G}^n)^T) - (\boldsymbol{G}^n)^T \cdot (\boldsymbol{G}^n)^T \right. \\
&\left. - 2(\boldsymbol{G}^n)^T \cdot \boldsymbol{G}^n - \boldsymbol{G}^n \cdot \boldsymbol{G}^n \right],
\end{aligned} \tag{8.64}
$$

where the constants in this step are evaluated as

$$c_1 = De + \omega\theta\Delta t, \tag{8.65}$$

$$c_2 = \frac{De - (1-\omega)\theta\Delta t}{c_1}, \tag{8.66}$$

$$c_3 = \frac{De\theta\Delta t}{c_1}, \tag{8.67}$$

$$c_4 = \frac{(1-\beta)De}{c_1}, \tag{8.68}$$

$$c_5 = c_4\theta\Delta t, \tag{8.69}$$

$$c_6 = 1 - c_4. \tag{8.70}$$

2. Calculate implicitly the elastic stresses ($\boldsymbol{\Sigma}^{n+1-\theta}$)

$$
\begin{aligned}
&De\frac{\boldsymbol{\Sigma}^{n+1-\theta} - \boldsymbol{\Sigma}^{n+\theta}}{(1-2\theta)\Delta t} + (1-\omega)\boldsymbol{\Sigma}^{n+1-\theta} \\
&\quad + De[\boldsymbol{u}^{n+1-\theta} \cdot \boldsymbol{\nabla}\boldsymbol{\Sigma}^{n+1-\theta} - (\boldsymbol{G}^{n+1-\theta})^T \cdot \boldsymbol{\Sigma}^{n+1-\theta} - \boldsymbol{\Sigma}^{n+1-\theta} \cdot \boldsymbol{G}^{n+1-\theta}] \\
&\quad - (1-\beta)De\frac{\boldsymbol{G}^{n+1-\theta} + (\boldsymbol{G}^{n+1-\theta})^T - \boldsymbol{G}^{n+\theta} - (\boldsymbol{G}^{n+\theta})^T}{(1-2\theta)\Delta t} \\
&\quad - (1-\beta)De\left[\boldsymbol{u}^{n+1-\theta} \cdot \boldsymbol{\nabla}(\boldsymbol{G}^{n+1-\theta} + (\boldsymbol{G}^{n+1-\theta})^T)\right. \\
&\quad \left. - (\boldsymbol{G}^{n+1-\theta})^T \cdot (\boldsymbol{G}^{n+1-\theta})^T - 2(\boldsymbol{G}^{n+1-\theta})^T \cdot \boldsymbol{G}^{n+1-\theta} - \boldsymbol{G}^{n+1-\theta} \cdot \boldsymbol{G}^{n+1-\theta}\right].
\end{aligned} \tag{8.71}
$$

The explicit update of algebraic variables is simply the old value of the variables. Thus, in eq. (8.71), the values of the interpolated velocity gradient at time $n+1-\theta$ are equal to the values at $n+\theta$. However, this causes a problem in the method because the time derivative of the interpolated velocity gradient (term 4 in eq. (8.71)) will always be zero in this formulation; this will result in an inconsistency of the equations since one term will not be present in the numerical method. Because of this, the θ-method cannot be applied to the EVSS-G formulation. The DEVSS-G formulation

does not include the upper convected derivative of the interpolated velocity in the constitutive equation; therefore, this method should be successful when applied to the θ-method.

8.2.4 θ-Method Applied to the DEVSS-G/FEM

The second major advantage of the DEVSS-G formulation over the EVSS-G formulation is the elimination of the upper convected derivative of the rate-of-strain tensor. This will allow a successful application of the θ-scheme to this formulation of the viscoelastic flow equations. As in the EVSS-G/FEM the operator, for the Oldroyd-B model, $\boldsymbol{A}$ is split into an elliptic operator

$$\boldsymbol{A}_1 = \begin{pmatrix} \omega\boldsymbol{\tau}_p \\ -\triangle\boldsymbol{u} + (1-\beta)\boldsymbol{\nabla}\cdot(\boldsymbol{G}+\boldsymbol{G}^T) + \boldsymbol{\nabla}\cdot\boldsymbol{\tau}_p + \boldsymbol{\nabla}p \\ \boldsymbol{\nabla}\cdot\boldsymbol{u} \\ \boldsymbol{G} - \boldsymbol{\nabla}\boldsymbol{u} \end{pmatrix}, \tag{8.72}$$

and a hyperbolic operator

$$\boldsymbol{A}_2 = \begin{pmatrix} (1-\omega)\boldsymbol{\tau}_p + De[\boldsymbol{u}\cdot\boldsymbol{\nabla}\boldsymbol{\tau}_p - \boldsymbol{G}^T\cdot\boldsymbol{\tau}_p - \boldsymbol{\tau}_p\cdot\boldsymbol{G}] \\ \quad + (1-\beta)(\boldsymbol{G}+\boldsymbol{G}^T) \\ \boldsymbol{0} \\ \boldsymbol{0} \\ \boldsymbol{0} \end{pmatrix}. \tag{8.73}$$

The mass matrix for the DEVSS-G formulation is

$$\boldsymbol{M} = \mathrm{diag}(De, 0, 0, 0). \tag{8.74}$$

The θ-method applied to the DEVSS-G/FEM is

1. a) Calculate implicitly $(\boldsymbol{u}^{n+\theta}, p^{n+\theta}, \boldsymbol{G}^{n+\theta})$

$$
\begin{aligned}
&-\triangle \boldsymbol{u}^{n+\theta} + (1-\beta)\boldsymbol{\nabla}\cdot(\boldsymbol{G}^{n+\theta} + (\boldsymbol{G}^{n+\theta})^T) + \boldsymbol{\nabla} p^{n+\theta} \\
&\quad = -c_2 \boldsymbol{\nabla}\cdot{\boldsymbol{\tau}_p}^n + c_3 \boldsymbol{\nabla}\cdot(\boldsymbol{u}^n\cdot\boldsymbol{\nabla}\boldsymbol{\tau}_p - (\boldsymbol{G}^n)^T\cdot\boldsymbol{\tau}_p - \boldsymbol{\tau}_p\cdot\boldsymbol{G}) \\
&\quad + c_4 \boldsymbol{\nabla}\cdot(\boldsymbol{G}^n + (\boldsymbol{G}^n)^T),
\end{aligned}
\tag{8.75}
$$

$$
\boldsymbol{\nabla}\cdot\boldsymbol{u}^{n+\theta} = \boldsymbol{0}, \tag{8.76}
$$

$$
\boldsymbol{G}^{n+\theta} - \boldsymbol{\nabla}\boldsymbol{u}^{n+\theta} = \boldsymbol{0}. \tag{8.77}
$$

b) Calculate explicitly the polymeric stress $(\boldsymbol{\tau}_p)$

$$
\begin{aligned}
{\boldsymbol{\tau}_p}^{n+\theta} &= c_2 {\boldsymbol{\tau}_p}^n \\
&\quad - c_3(\boldsymbol{u}^n\cdot\boldsymbol{\nabla}{\boldsymbol{\tau}_p}^n - (\boldsymbol{G}^n)^T\cdot{\boldsymbol{\tau}_p}^n - {\boldsymbol{\tau}_p}^n\cdot\boldsymbol{G}^n) + c_4\boldsymbol{\nabla}\cdot(\boldsymbol{G}^n + (\boldsymbol{G}^n)^T),
\end{aligned}
\tag{8.78}
$$

where the constants are given by

$$
c_1 = De + \omega\theta\Delta t, \tag{8.79}
$$

$$
c_2 = \frac{De - (1-\omega)\theta\Delta t}{c_1}, \tag{8.80}
$$

$$
c_3 = \frac{De\theta\Delta t}{c_1}, \tag{8.81}
$$

$$
c_4 = \frac{(1-\beta)\theta\Delta t}{c_1}. \tag{8.82}
$$

2. a) For an explicit update of algebraic variables $(\boldsymbol{u}^{n+1-\theta}, p^{n+1-\theta}, \boldsymbol{G}^{n+1-\theta})$ the old value is the new value or

$$
\boldsymbol{u}^{n+1-\theta} = \boldsymbol{u}^{n+\theta}, \tag{8.83}
$$

$$
p^{n+1-\theta} = p^{n+\theta}, \tag{8.84}
$$

$$
\boldsymbol{G}^{n+1-\theta} = \boldsymbol{G}^{n+\theta}. \tag{8.85}
$$

b) Calculate implicitly the polymeric stress $(\boldsymbol{\tau}_p{}^{n+1-\theta})$

$$\begin{aligned}&\frac{(De+(1-\omega)(1-2\theta)\Delta t)}{(1-2\theta)\Delta t}\boldsymbol{\tau}_p{}^{n+1-\theta}\\&\quad+De(\boldsymbol{u}^{n+\theta}\cdot\nabla\boldsymbol{\tau}_p{}^{n+1-\theta}-(\boldsymbol{G}^{n+\theta})^T\cdot\boldsymbol{\tau}_p{}^{n+1-\theta}-\boldsymbol{\tau}_p{}^{n+1-\theta}\cdot\boldsymbol{G}^{n+\theta})\\&\quad=\frac{De-\omega(1-2\theta)\Delta t}{(1-2\theta)\Delta t}\boldsymbol{\tau}_p{}^{n+\theta}-(1-\beta)(\boldsymbol{G}^{n+\theta}+(\boldsymbol{G}^{n+\theta})^T).\end{aligned}\tag{8.86}$$

3. Repeat 1 but with $n+1\leftarrow n+\theta$ and $n+1-\theta\leftarrow n$.

The elimination of the convective derivative of the rate-of-strain tensor in the constitutive equation in the DEVSS-G formulation allows the θ-method to give a consistent set of equations which can be solved. The first and third steps are simply the solution of a nonhomogoeneous Stokes-G problem where the velocity gradient interpolation equations have been added to the normal Stokes equations. This is not a symmetric problem, but it is still a linear set of equations which can be solved relatively fast. The stress is explicitly updated in these steps also. Step 2 requires the solution of a hyperbolic set of differential equations, but as in Saramito's formulation it consists of only the stress variables. For the Oldroyd-B model, the hyperbolic equations are linear. This formulation reduces a nonlinear fully implicit scheme to a set of three linear equations, all of which are smaller than the original equation set, to be solved.

For the CR-FENE model, the operator $\boldsymbol{A}$ is split into an elliptic operator

$$\boldsymbol{A}_1=\begin{pmatrix}\omega\boldsymbol{A}\\-\Delta\boldsymbol{u}+(1-\beta)\nabla\cdot(\boldsymbol{G}+\boldsymbol{G}^T)-\frac{(1-\beta)}{De}\nabla\cdot(f(R)\boldsymbol{A})+\nabla p_{CR}\\\nabla\cdot\boldsymbol{u}\\\boldsymbol{G}-\nabla\boldsymbol{u}\end{pmatrix},\tag{8.87}$$

and a hyperbolic operator

$$\boldsymbol{A}_2 = \begin{pmatrix} (1-\omega)\boldsymbol{A} + \frac{De}{f(R)}[\boldsymbol{u}\cdot\nabla\boldsymbol{A} - \boldsymbol{G}^T\cdot\boldsymbol{A} - \boldsymbol{A}\cdot\boldsymbol{G}] - \boldsymbol{I} \\ \mathbf{0} \\ \mathbf{0} \\ \mathbf{0} \end{pmatrix}. \tag{8.88}$$

The mass matrix is given by eq. (8.74). The θ-method applied to a CR-FENE fluid in the DEVSS-G/FEM is

1. a) Calculate implicitly the Stokes-G $(\boldsymbol{u}^{n+\theta}, p^{n+\theta}, \boldsymbol{G}^{n+\theta})$

$$\begin{aligned} &-\Delta\boldsymbol{u}^{n+\theta} + (1-\beta)\nabla\cdot(\boldsymbol{G}^{n+\theta} + (\boldsymbol{G}^{n+\theta})^T) + \nabla p_{CR}^{n+\theta} \\ &\quad = \frac{(1-\beta)}{De}\nabla\cdot(F^n(R)(c_8\boldsymbol{A}^n - c_9[\boldsymbol{u}^n\cdot\nabla\boldsymbol{A}^n - (\boldsymbol{G}^n)^T\cdot\boldsymbol{A}^n \\ &\quad - \boldsymbol{A}^n\cdot\boldsymbol{G}^n] + c_{10}\boldsymbol{I})) \end{aligned} \tag{8.89}$$

$$\nabla\cdot\boldsymbol{u}^{n+\theta} = \mathbf{0}, \tag{8.90}$$

$$\boldsymbol{G}^{n+\theta} - \nabla\boldsymbol{u}^{n+\theta} = \mathbf{0}. \tag{8.91}$$

b) Calculate explicitly the configuration tensor $(\boldsymbol{A})$

$$\boldsymbol{A}^{n+\theta} = c_8\boldsymbol{A}^n - c_9(\boldsymbol{u}^n\cdot\nabla\boldsymbol{A}^n - (\boldsymbol{G}^n)^T\cdot\boldsymbol{A}^n - \boldsymbol{A}^n\cdot\boldsymbol{G}^n) + c_{10}\boldsymbol{I}. \tag{8.92}$$

2. a) For the explicit update of algebraic variables $(\boldsymbol{u}^{n+1-\theta}, p^{n+1-\theta}, \boldsymbol{G}^{n+1-\theta})$ the old value is the new value or

$$\boldsymbol{u}^{n+1-\theta} = \boldsymbol{u}^{n+\theta}, \tag{8.93}$$

$$p^{n+1-\theta} = p^{n+\theta}, \tag{8.94}$$

$$\boldsymbol{G}^{n+1-\theta} = \boldsymbol{G}^{n+\theta}. \tag{8.95}$$

b) Calculate implicitly the configuration tensor $(\boldsymbol{A}^{n+1-\theta})$

$$c_{11}\boldsymbol{A}^{n+1-\theta} \tag{8.96}$$

$$+ De(\boldsymbol{u}^{n+\theta}\cdot\nabla\boldsymbol{A}^{n+1-\theta} - (\boldsymbol{G}^{n+\theta})^T\cdot\boldsymbol{A}^{n+1-\theta} - \boldsymbol{A}^{n+1-\theta}\cdot\boldsymbol{G}^{n+\theta}) \quad (8.97)$$
$$- f^{n+1-\theta}(R)\boldsymbol{I} = c_{12}\boldsymbol{A}^{n+\theta}.$$

3. Repeat 1 but with $n+1 \leftarrow n+\theta$ and $n+1-\theta \leftarrow n$.

The constants are given by

$$c_7 = De + \omega f^n(R)\theta\Delta t, \quad (8.98)$$
$$c_8 = \frac{De - (1-\omega)f^n(R)\theta\Delta t}{c_7}, \quad (8.99)$$
$$c_9 = \frac{De\theta\Delta t}{c_7}, \quad (8.100)$$
$$c_{10} = \frac{f^n(R)\theta\Delta t}{c_7}, \quad (8.101)$$
$$c_{11} = \frac{De + f^{n+1-\theta}(R)(1-\omega)(1-2\theta)\Delta t}{(1-2\theta)\Delta t}, \quad (8.102)$$
$$c_{12} = \frac{De - \omega f^{n+1-\theta}(R)(1-2\theta)\Delta t}{(1-2\theta)\Delta t}. \quad (8.103)$$

For the CR-FENE model, Step 2 is nonlinear so it will be calculated here using Newton's method in the frontal solver. It may be possible in the future to use a semi-implicit or even an explicit method to calculate this step.

In summary the θ-method can be summarized as an algorithm in which the following steps are performed:

1. Initial conditions are introduced for the stress field (the only variable that satisfies a differential equation for the inertialess flow). Self- consistent values of the velocity, pressure and velocity gradient fields are used which are calculated by solving the momentum, continuity and velocity gradient interpolation equations using the initial condition of the stress as inhomogeneous data as in step 2 below. For the linear stability problem, the velocity, pressure and velocity gradient are all set to zero for the initial disturbance.

2. In the first time step ($[t, t+\theta\Delta t]$, where $0 < \theta < 0.3$), the momentum, continuity and velocity gradient interpolation equations (Stokes-G problem) are solved

implicitly (first order Adams-Moulton method) while the constitutive equation is solved explicitly (first order Adams-Bashforth method). The implicit equations are simply a modified inhomogeneous Stokes problem using the stress at the updated time step as data; this results in a linear algebraic set of equations in $(\boldsymbol{u}, p, \boldsymbol{G})$ and can be solved efficiently even though it is not a symmetric problem.

3. In the second time step ($[t + \theta\Delta t, t + \theta\Delta t + (1 - 2\theta)\Delta t]$), the constitutive equations are solved implicitly (first order Adams-Moulton method). Since, the momentum, continuity, aand velocity gradient equations are algebraic, an explicit update results in the same values in Step 2. This results in the solution of a set of hyperbolic equations in time which depending on the constitutive equation can be linear or nonlinear.

4. In the third time step ($[t + \theta\Delta t + (1 - 2\theta)\Delta t, t + \Delta t)$, the first step is repeated using the results from Step 3 as data. Again, this is a linear, asymmetric algebraic set of equations in $(\boldsymbol{u}, p, \boldsymbol{G})$ and can be solved efficiently and quickly.

The steps 2-4 are repeated for each time step. Steps 2 and 4 are amenable to iterative solution schemes as well as direct factorization. The advantage of the direct factorization results from the linear nature of the problem; the LU decomposition can be computed once as a pre-processing step resulting in only forward-backward substitution to obtain the solution. Step 3 is where the implementation of an iterative scheme may be faster than the direct factorization for large problems.

In an attempt to estimate the savings in computational time required to perform the calculation of the time dependent problem, an initial estimate of the operation counts for the two methods will be made. As mentioned in Section 8.2.1, the operation count for a frontal algorithm is proportional to the number of elements multiplied by the square of the bandwidth. For the fully implicit method the bandwisth squared was estimated to be 2116 while the semi-implicit step consisting of just the stress variables was 144. Assuming that the forward-backward substitution operations required in Steps 2 and 4 of the θ-method are negligible compared to the full nonlinear

computation of Step 3, the comparison between the fully implicit method and the *theta*-method reduces to the ratio of the bandwidth squared (both are frontal methods). This gives an operational count savings of approximately 15 in the use of the θ-method.

8.3 Startup of Planar Couette Flow

The startup of planar Couette flow is examined for a CR-FENE fluid with the θ-method. The expected form of the solution for an inertialess fluid will have the velocity, pressure and velocity gradient interpolation immediately going to the steady-state solution at the first time step. The stress will increase from zero to its steady-state value exponentially in time. Although this is a nonlinear problem, for low shear rates, the nonlinear term $f(R)$ is approximately a constant. From this assumption, the exponential forms of $\boldsymbol{\tau}_p$ can be found as

$$\tau_{pxx} = \tau_{pxx}(t_0)\left(1 - e^{-(\frac{f}{De}(\tau_{pxx}-1)+2\tau_{pyx})t}\right), \tag{8.104}$$

$$\tau_{pyy} = \tau_{pyy}(t_0)\left(1 - e^{-\frac{f}{De}(\tau_{pyy}-1)t}\right), \tag{8.105}$$

$$\tau_{pyx} = \tau_{pyx}(t_0)\left(1 - e^{-(\frac{f}{De}\tau_{pyx}+\tau_{pyy})t}\right). \tag{8.106}$$

The numerical results from the startup calculations for a CR-FENE fluid with $\beta = 0.59$ and $L = 20$ for $De = 1.0$ is shown in Figure 8-2. The components of the configuration tensor all follow an exponential of the forms found in eqs. (8.104)-(8.106), respectively. The convergence with stepsize is also shown.

In the θ-method several different parameter values were examined. Two values of θ were examined, $1 - \sqrt{2}/2$ and $1/4$ as well as two values of ω, 0.5 and $2 - \sqrt{2}$. No discernible difference was found in the quality of the solutions computed for any combination of these parameters. From the discussion of the θ-method in Section 8.2.2, it was decided that $\theta = 1 - \sqrt{2}/2$ and $\omega = 2 - \sqrt{2}$ would be used for all future calculations. No bound in time step size was found, as shown in Figure 8-2.

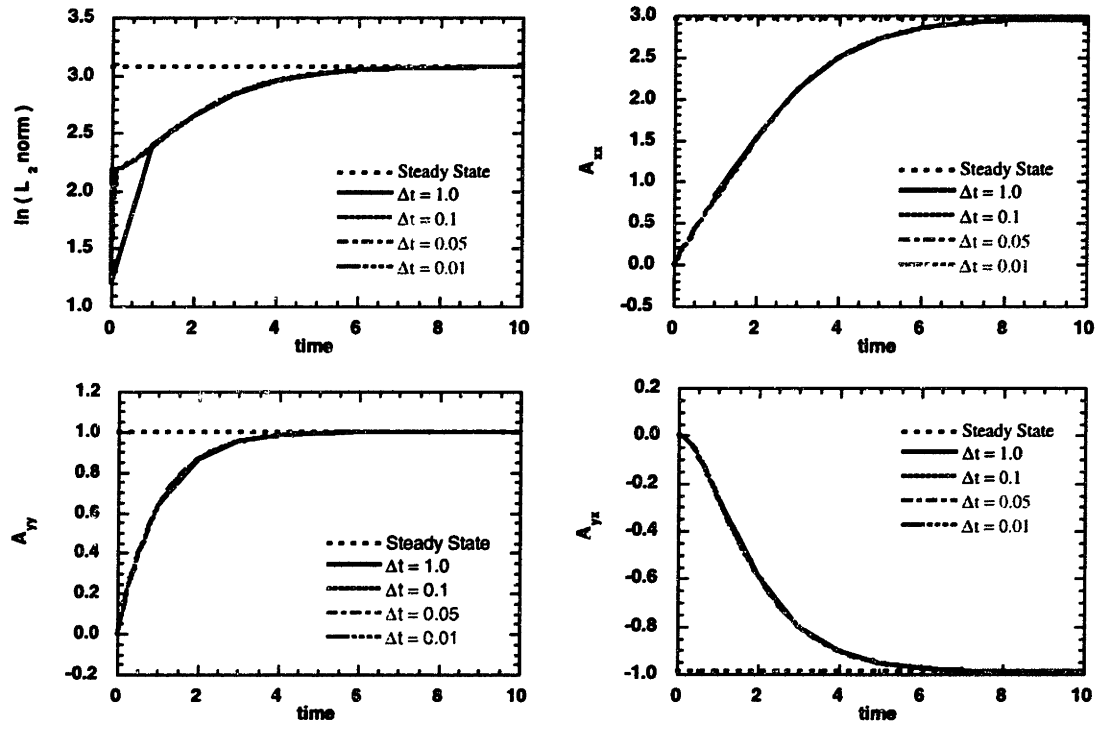

Figure 8-2: Startup calculations for planar Couette flow of CR-FENE fluid at $De = 1.0$. (a) The L_2-norm of the solution vector as defined in eq. (5.15). The configuration tensor as a function of time are shown for (b) the xx-component, (c) the yy-component, and (d) the yx-component.

8.4 Startup of Flow Through a Periodic Array of Cylinders in a Channel

Calculations to study the startup of flow through a periodic array of cylinders in a channel were performed. Due to the lack of inertia, the algebraic variables will jump to large values at the first time step and adjust as the stresses increase. For low values of We, the solution is expected to go to a steady-state solution; however, as We is increased it is hoped that a time dependent solution will be found. For the steady-state calculations examined in Chapter 6, as We increased beyond 0.9, the $\langle \boldsymbol{QQ} \rangle$ tensor is found to have negative values in the area of high shear between the cylinder and the wall. Since this tensor is related to the end-to-end distance of the dumbbell, a negative value is aphysical and indicative of error in the numerical approximation. Moreover, these negative values were found to disappear if the mesh refinement is increased in the regions of the negative $\langle \boldsymbol{QQ} \rangle$ tensor (Liu *et al.* 1995). It was found that the essential flow characteristics away from these aphysical values were unchanged with mesh refinement so the affects were localized and should not affect the global solution fields in either the steady-state calculations or the time dependent calculations performed here.

Startup calculations were performed were performed using the θ-method at $We =$ 0.5, 0.9, 1.5, and 3.0. The amplitude $L_2(t)$ as defined in eq. (5.15) is shown in Figure 8-3 as a function of We. This measure of the solution shows a large initial jump due to the instantaneous adjustment of the algebraic variables in the absence of inertia, as expected. This is followed by a relatively stationary period before the final exponential increase to the steady-state value.

The time dependent evolution of the velocity, configuration tensor and pressure is shown in Figures 8-4 – 8-12. The algebraic variables (Figures 8-4, 8-5 and 8-12) all respond in a like manner. They all begin symmetric about the midplane of the flow ($y = 0$). v_x is also symmetric about the vertical midplane ($x = 0$) while v_y is anti-symmetric about this plane. As time advances, the variables are slightly convected downstream until at $t = 5.0$ the steady-state result is achieved. The time evolution

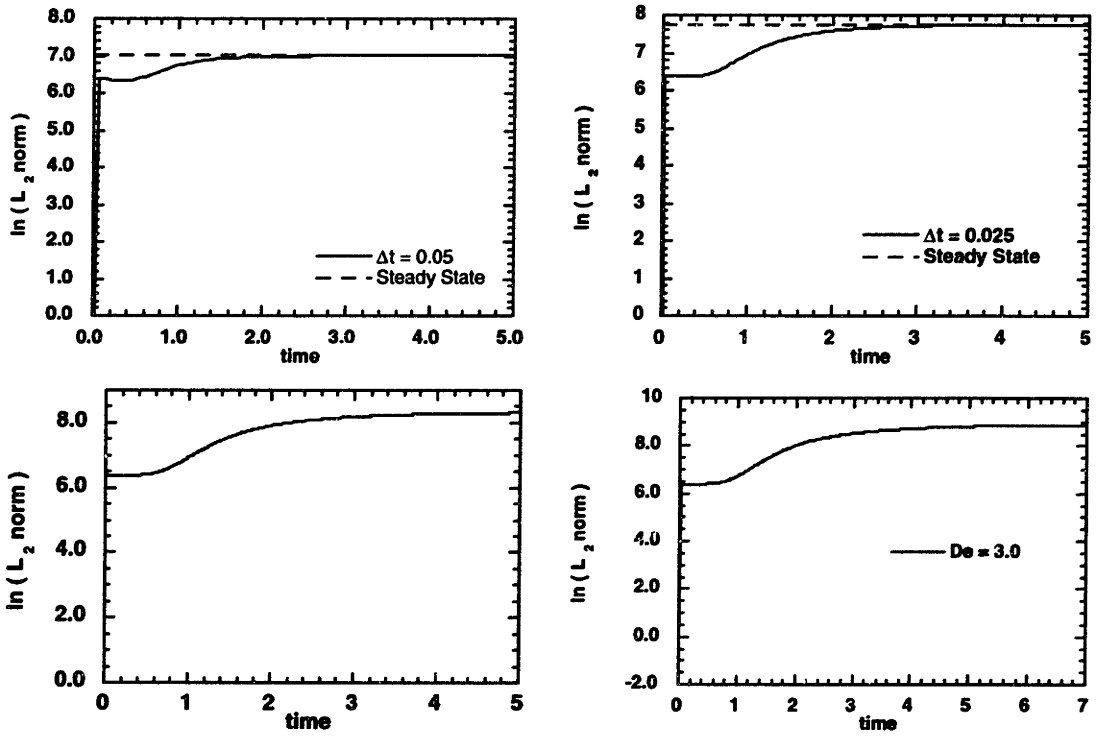

Figure 8-3: Startup calculations for the flow of CR-FENE fluid in a linear periodic array of cylinders in a channel computed with the DEVSS-G/FEM. The transient response is shown as the L_2-norm of the solution vector as defined in eq. (5.15). (a) $We = 0.5$ and $\Delta t = 0.05$, (b) $We = 0.9$ and $\Delta t = 0.025$, (c) $We = 1.5$ and $\Delta t = 0.01$, and (d) $We = 3.0$ and $\Delta t = 0.025$.

of various points in the flow for the algebraic variables monotonically increase or decrease from the initial value attained after the first time step; an example is shown for a point on the vertical midplane ($x = 0$) for the x-component of the velocity in Figure 8-13. The exponential decrease is seen for all We. As the We increases, the velocity decreases faster towards a larger steady-state value which shows the effect of an increasing convection on the velocity evolution. The development in time of the algebraic variables is not significantly different as We increased form the $We = 0.5$ case; therefore, only the final solution at $t = 5.0$ is shown in Figures 8-14 – 8-16 for $We = 0.9$ and 1.5. For $We = 3.0$, the solution at $t = 3.0$ is shown in Figure 8-17 for the algebraic variables.

The evolution of the configuration tensor is markedly different from the algebraic variables because it is the solution of a differential equation. In Figures 8-6 – 8-11 (and all other contour plots in this thesis), the (x) indicates the position of the maximum value while the (•) indicates the position of the minimum value.

Again, the effect of the flow convection on the variable time evolution is apparent. For A_{xx}, the area in which the polymer molecule is extended grows until it reaches from one cylinder to the next. This forms three distinct regions in the flow: the wall shear region, the stagnation regions between the cylinders and the region where the extension from the previous cylinder is still felt. The position of the minimum shifts from the cylinder to the shear region between the channel wall and the cylinder between $t = 1.0$ and 2.0. The position of the maximum moves from $x > 0$ to $x < 0$ as time increases. Away from significant gradients, the configuration tensor increases or decreases exponentially to the steady-state value. However, in regions of high gradients such as near the maximum value, overshoots and undershoots are observed as shown in Figure 8-18. As We increases, the absolute value of A_{xx} increases, but the overall behavior remains the same. This is demonstrated in Figures 8-19 – 8-21 for $We = 0.9$, 1.5 and 3.0. It is interesting to note that the configuration tensor (all components) is always symmetric with respect to the midplane of the flow ($y = 0$).

For A_{yy}, the structure is concentrated into four lobes located roughly at the NE, NW, SE and SW directions on the cylinder (see Figures 8-8 and 8-9). As the config-

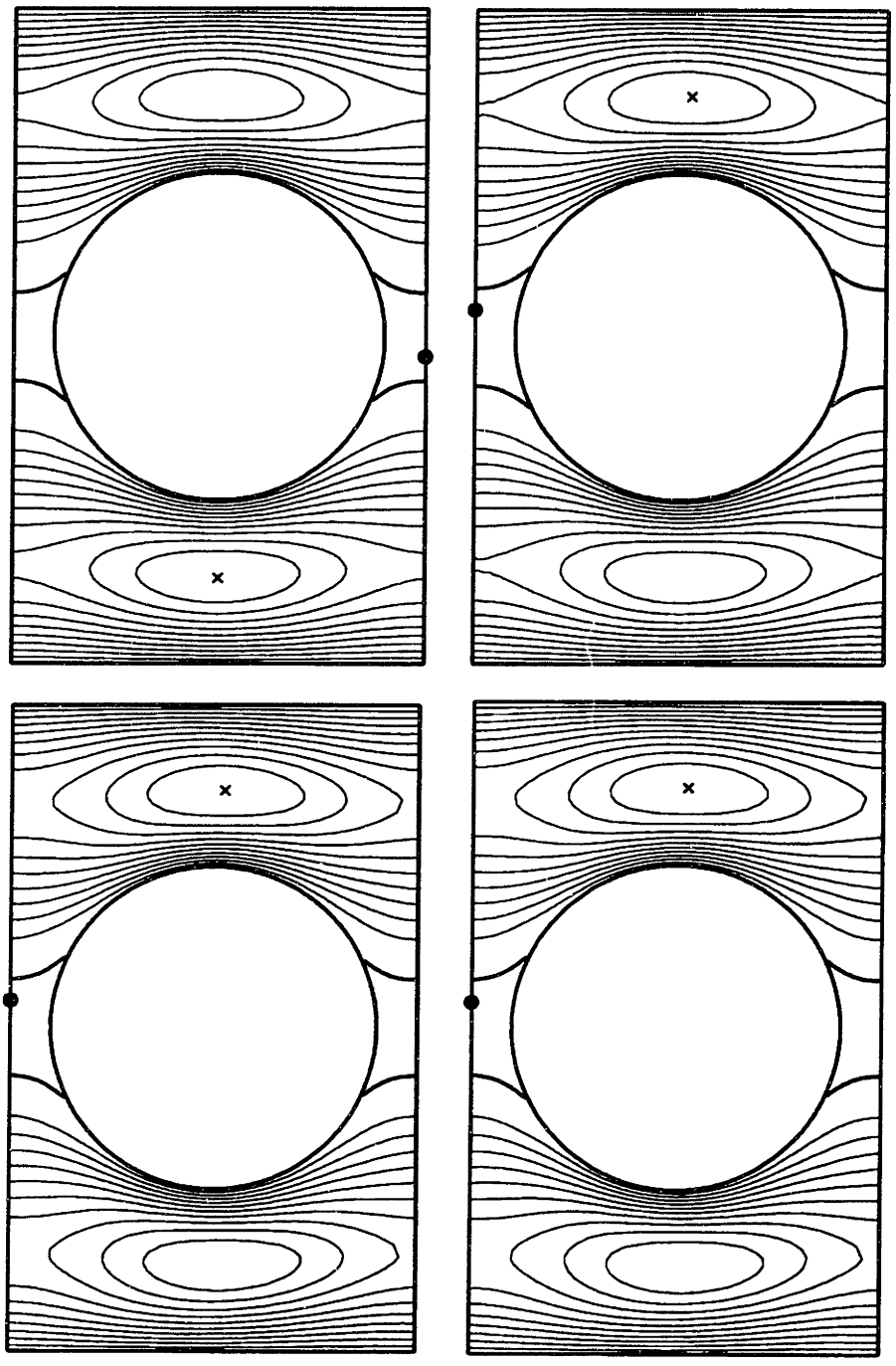

Figure 8-4: The contours of the x-component of velocity as a function of time computed with the DEVSS-G/FEM and the θ-method at $We = 0.5$ and $\Delta t = 0.05$ for a CR-FENE fluid in a periodic linear array of cylinders in a channel. (a) $t = 0.1$, (b) $t = 1.0$, (c) $t = 3.0$, and (d) $t = 5.0$.

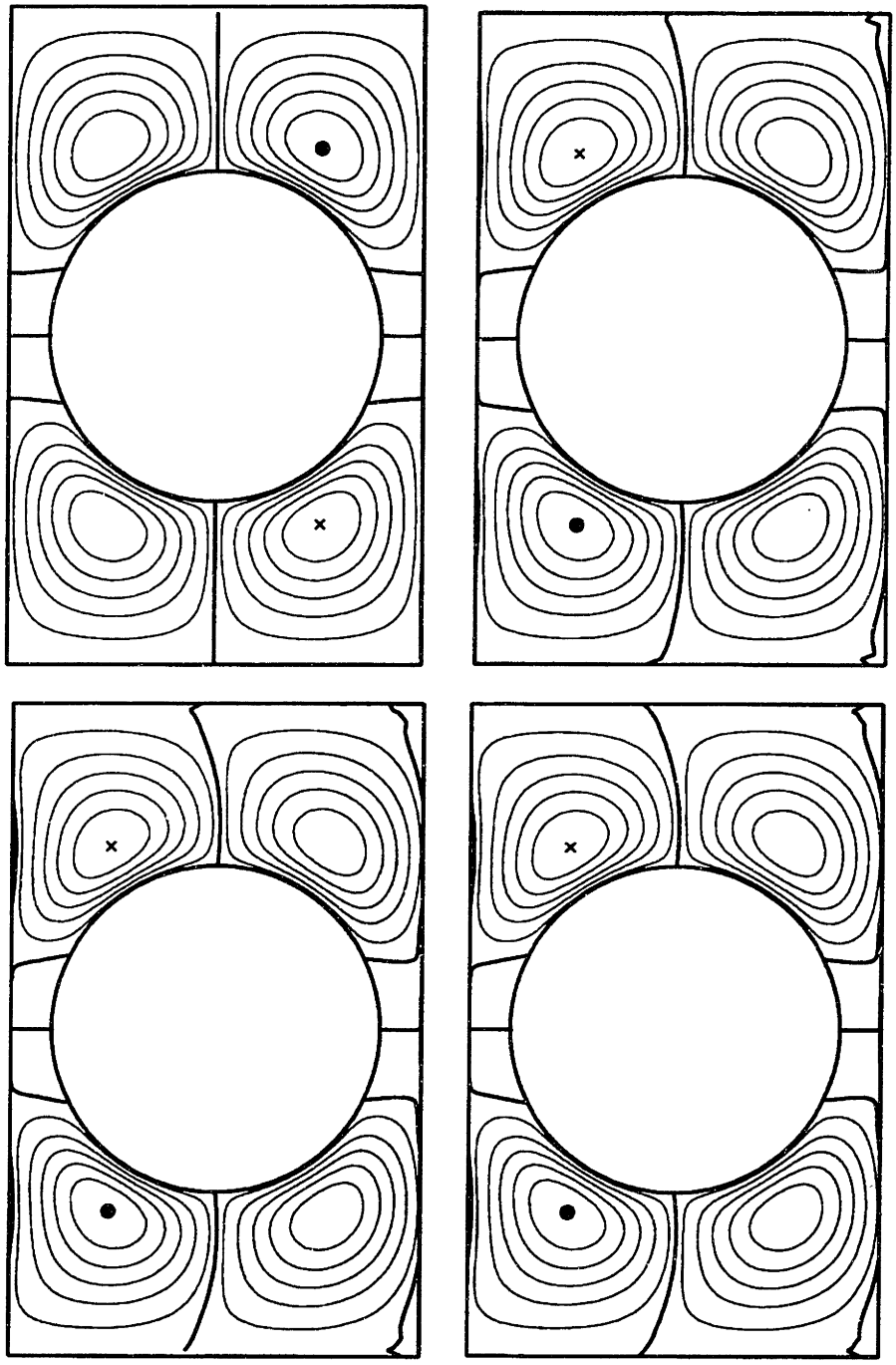

Figure 8-5: The contours of the y-component of velocity as a function of time computed with the DEVSS-G/FEM and the θ-method at $We = 0.5$ and $\Delta t = 0.05$ for a CR-FENE fluid in a periodic linear array of cylinders in a channel. (a) $t = 0.1$, (b) $t = 1.0$, (c) $t = 3.0$, and (d) $t = 5.0$.

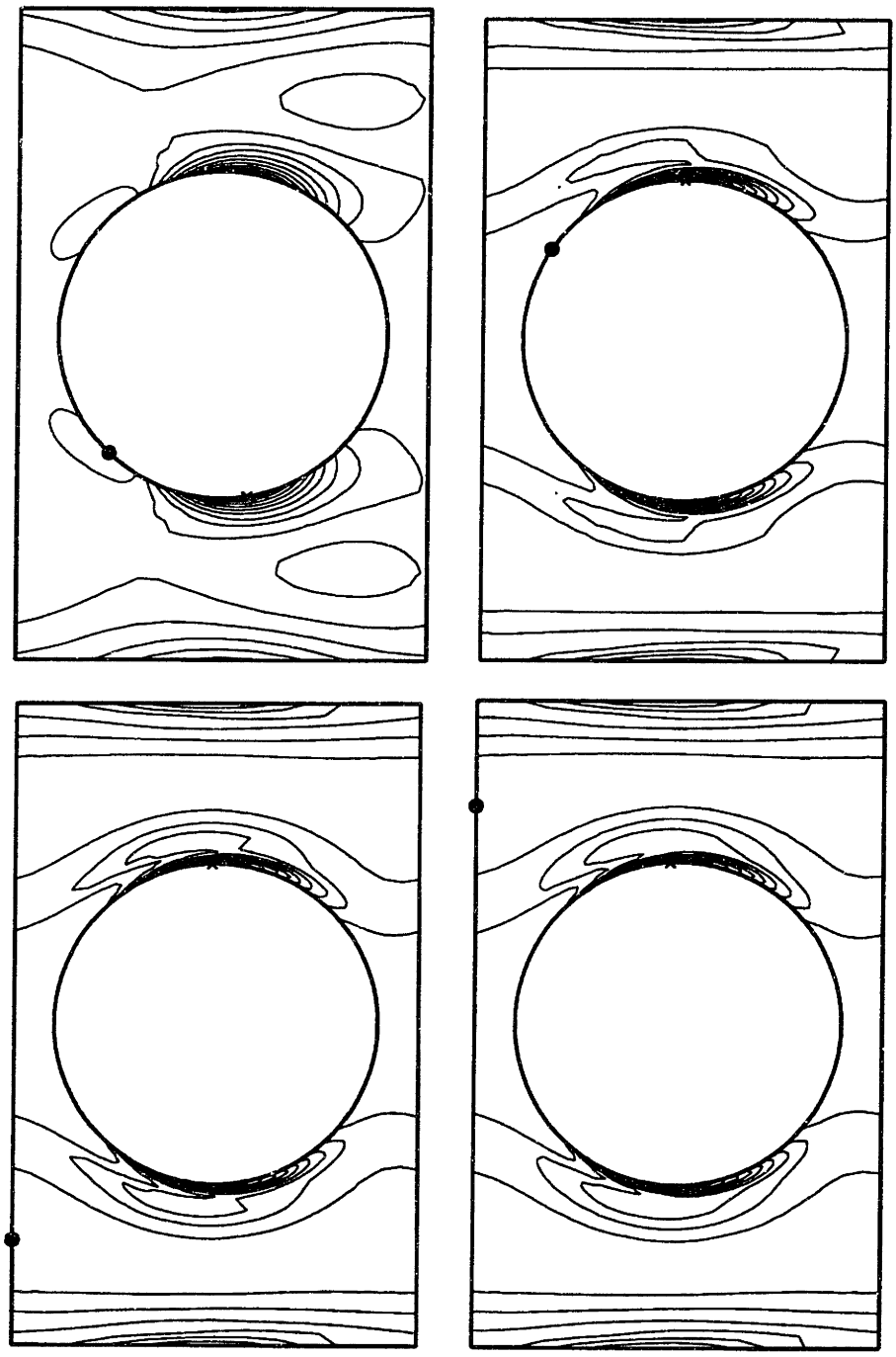

Figure 8-6: The contours of the xx-component of the configuration tensor as a function of time computed with the DEVSS-G/FEM and the θ-method at $We = 0.5$ and $\Delta t = 0.05$ for a CR-FENE fluid in a periodic linear array of cylinders in a channel. (a) $t = 0.1$, (b) $t = 1.0$, (c) $t = 2.0$, and (d) $t = 3.0$.

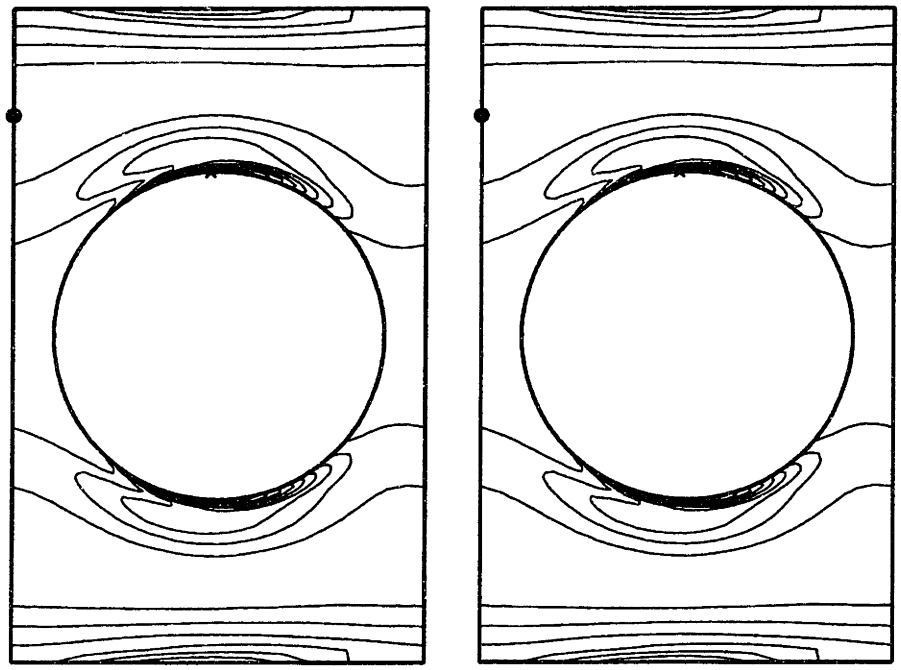

Figure 8-7: Continuation of Figure 8-6. (a) $t = 4.0$ and (b) $t = 5.0$.

uration tensor increases in strength, the gradients of the configuration tensor localize around the four lobes. The position of the minimum fairly quickly shifts off of the cylinder and moves towards the vertical midplane ($x = 0$) while the position of the maximum hardly changes. The rest of the behavior is similar to the xx-component and the time evolution for $We = 0.9$, 1.5 and 3.0 is shown in Figures 8-22 - 8-24.

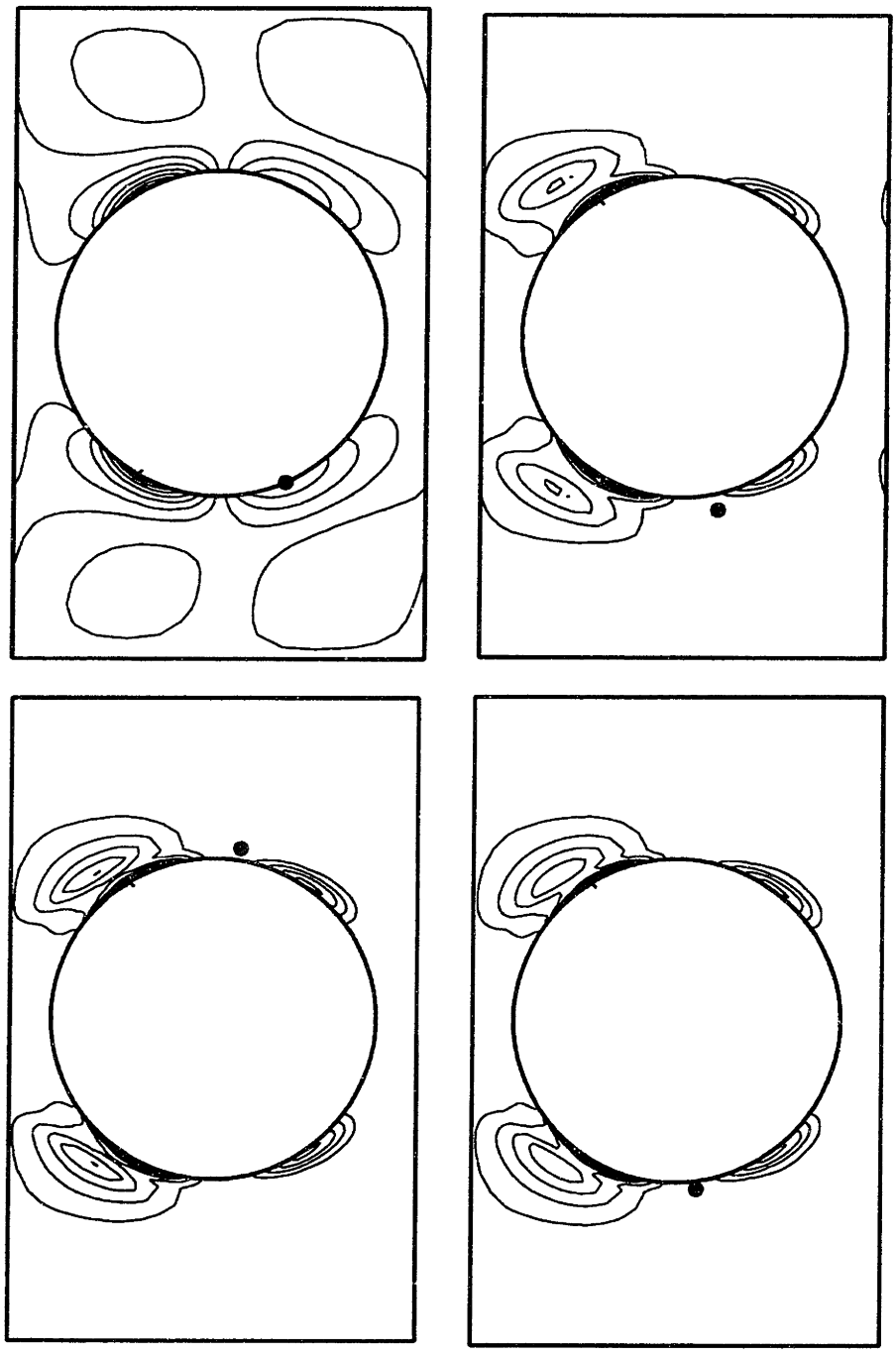

Figure 8-8: The contours of the yy-component of the configuration tensor as a function of time computed with the DEVSS-G/FEM and the θ-method at $We = 0.5$ and $\Delta t = 0.05$ for a CR-FENE fluid in a periodic linear array of cylinders in a channel. (a) $t = 0.1$, (b) $t = 1.0$, (c) $t = 2.0$, and (d) $t = 3.0$.

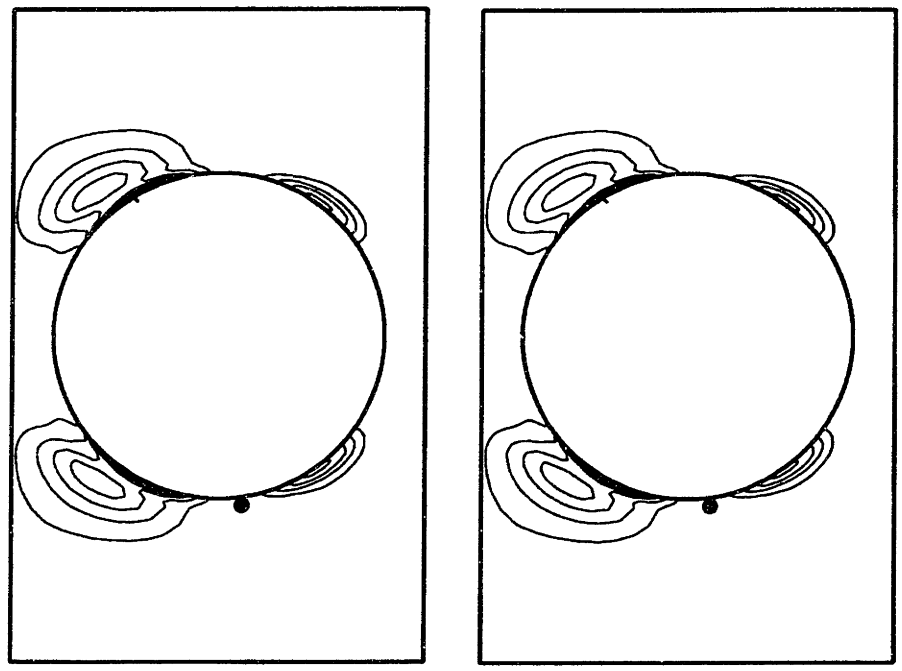

Figure 8-9: Continuation of Figure 8-8. (a) $t = 4.0$ and (b) $t = 5.0$.

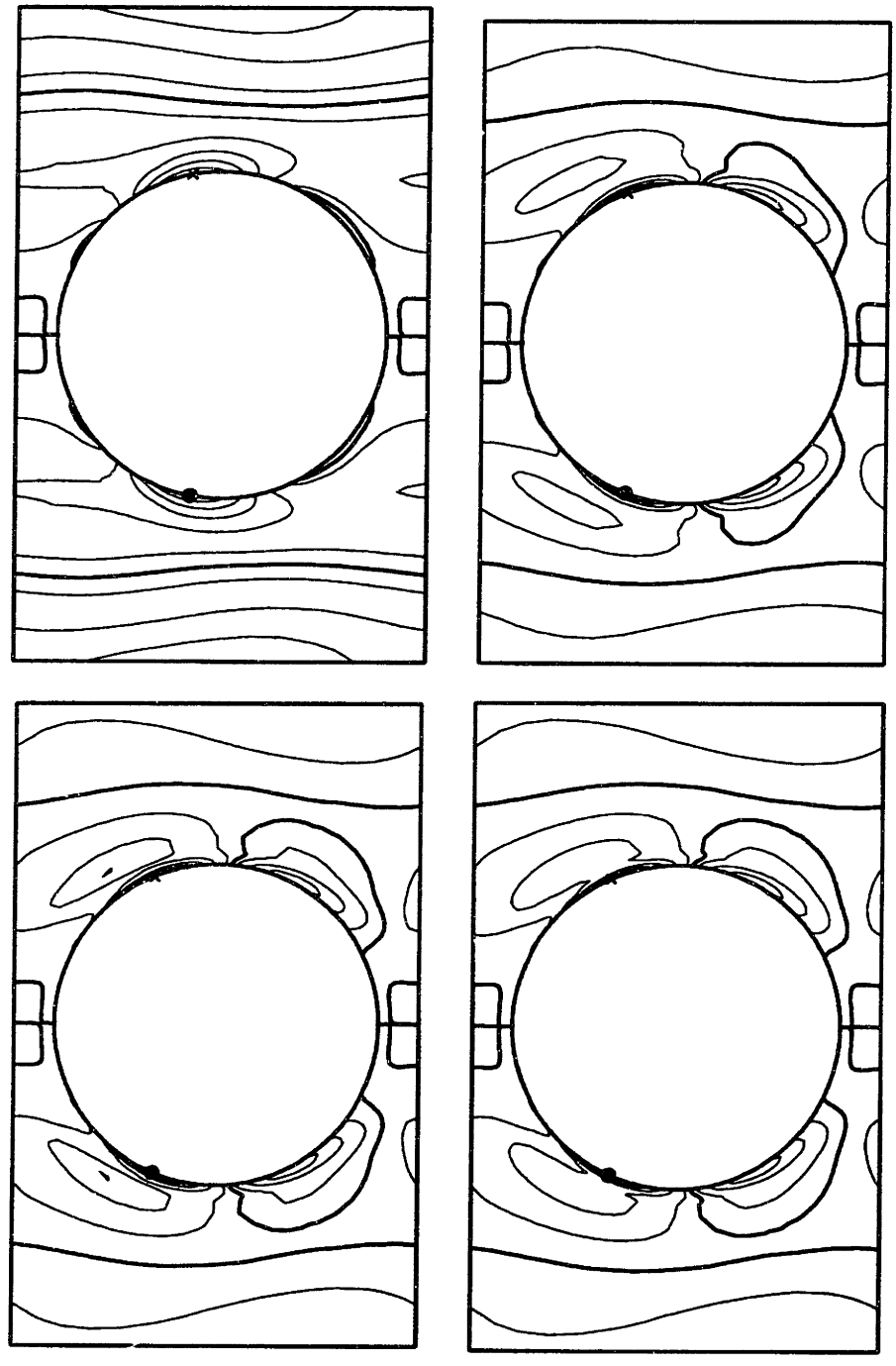

Figure 8-10: The contours of the yx-component of the configuration tensor as a function of time computed with the DEVSS-G/FEM and the θ-method at $We = 0.5$ and $\Delta t = 0.05$ for a CR-FENE fluid in a periodic linear array of cylinders in a channel. (a) $t = 0.1$, (b) $t = 1.0$, (c) $t = 2.0$, and (d) $t = 3.0$.

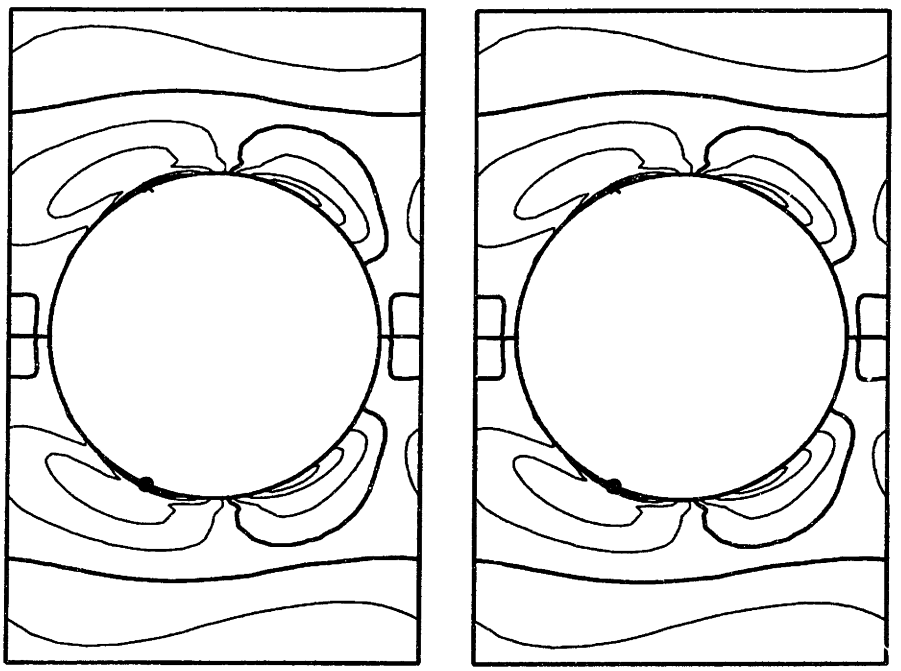

Figure 8-11: Continuation of Figure 8-10. (a) $t = 4.0$ and (b) $t = 5.0$.

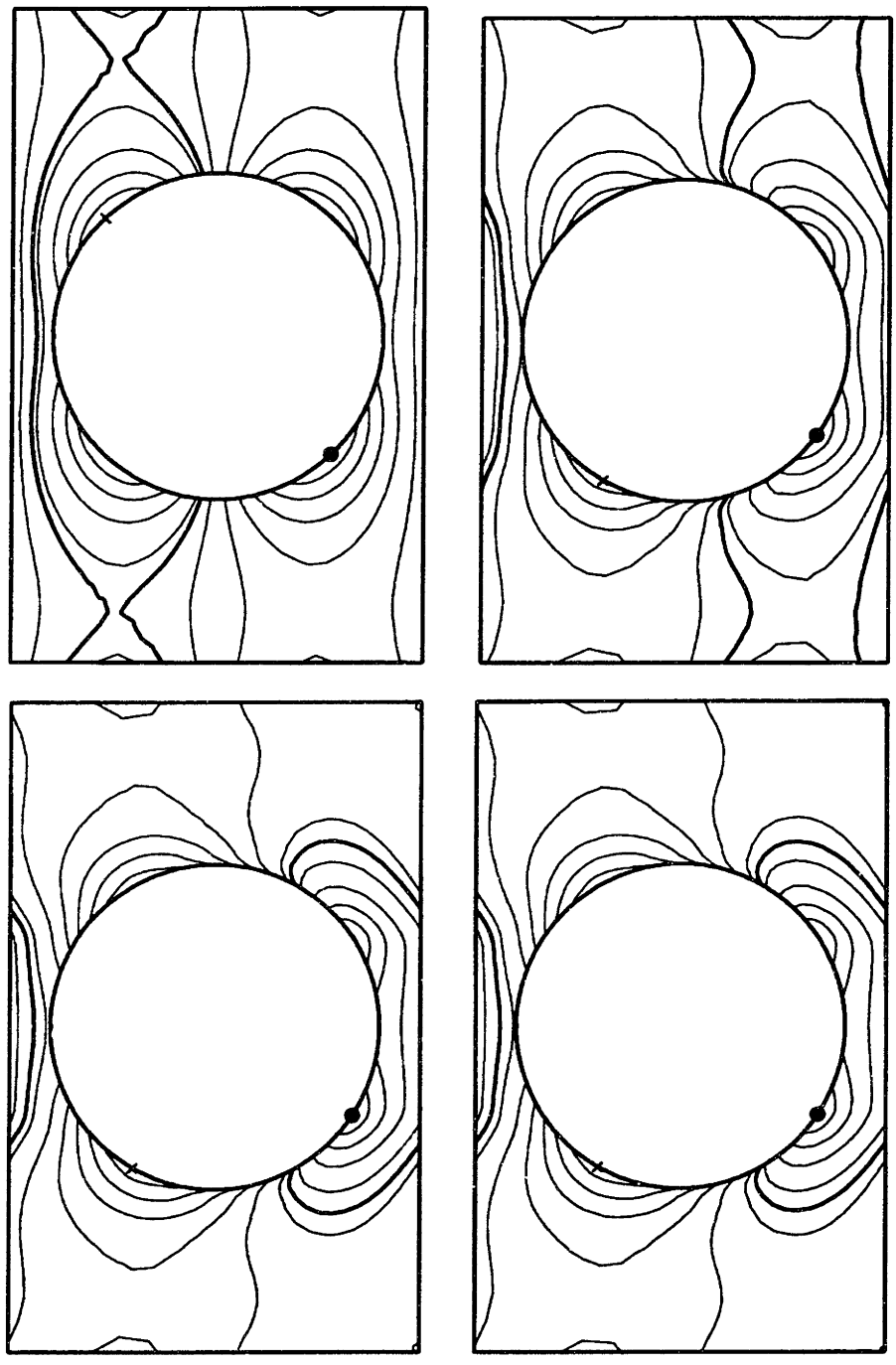

Figure 8-12: The contours of the pressure as a function of time computed with the DEVSS-G/FEM and the θ-method at $We = 0.5$ and $\Delta t = 0.05$ for a CR-FENE fluid in a periodic linear array of cylinders in a channel. (a) $t = 0.1$, (b) $t = 1.0$, (c) $t = 3.0$, and (d) $t = 5.0$.

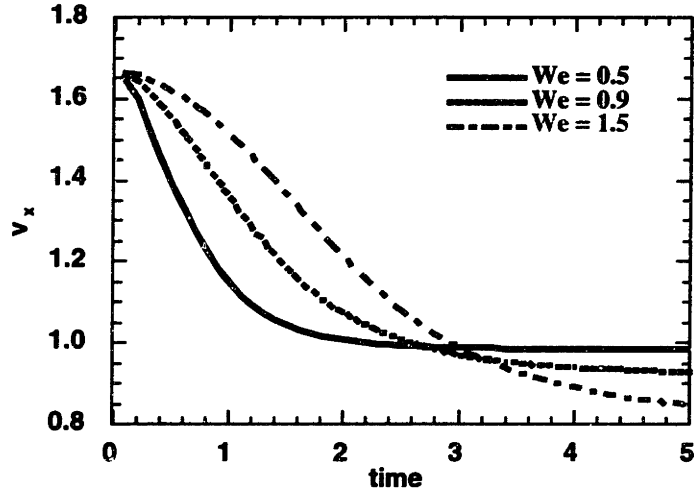

Figure 8-13: The time evolution of the x-component of velocity at the vertical mid-plane ($x = 0$) and about 1/6 of the distance between the cylinder and the top of the channel for $We = 0.5$, 0.9 and 1.5. The value decreases monotonically in an exponential fashion.

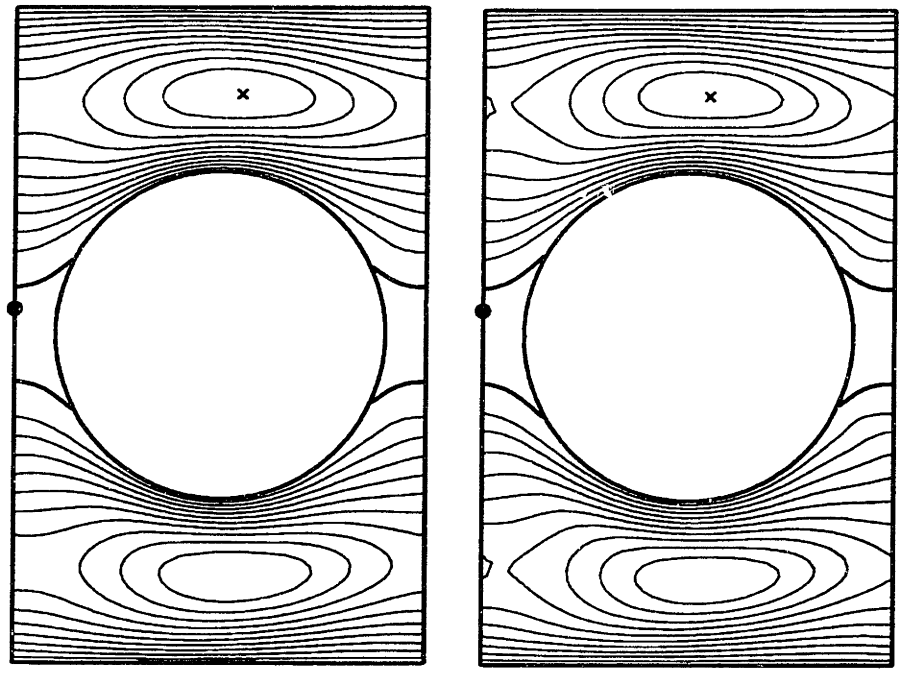

Figure 8-14: The contours of the x-component of the velocity computed with the DEVSS-G/FEM and the θ-method at $t = 5.0$ which is indistinguishable from the steady-state solution for a CR-FENE fluid in a periodic linear array of cylinders in a channel. (a) $We = 0.9$, (b) $We = 1.5$.

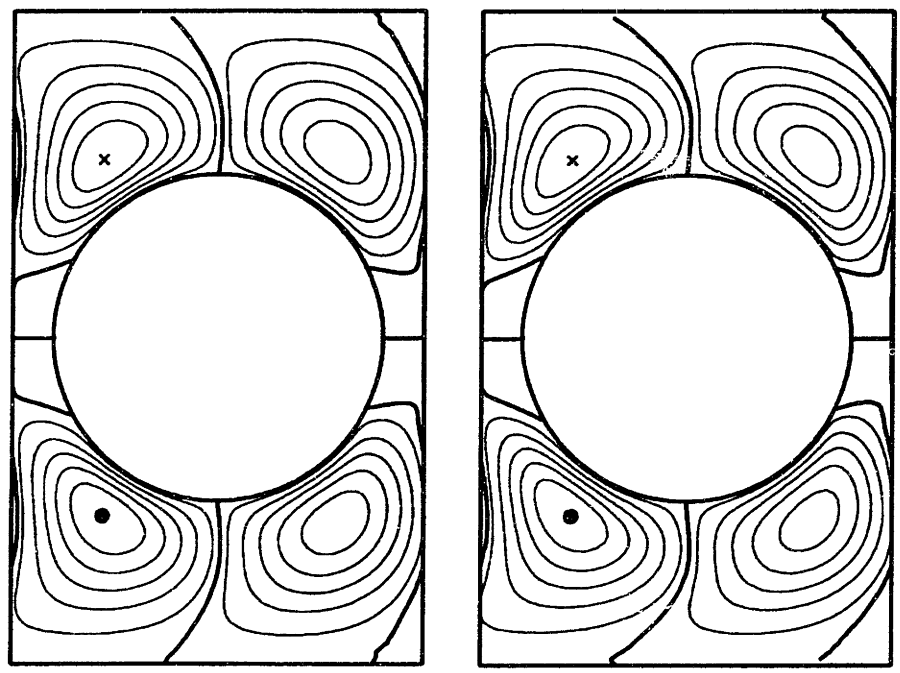

Figure 8-15: The contours of the y-component of the velocity computed with the DEVSS-G/FEM and the θ-method at $t = 5.0$ which is indistinguishable from the steady-state solution for a CR-FENE fluid in a periodic linear array of cylinders in a channel. (a) $We = 0.9$, (b) $We = 1.5$.

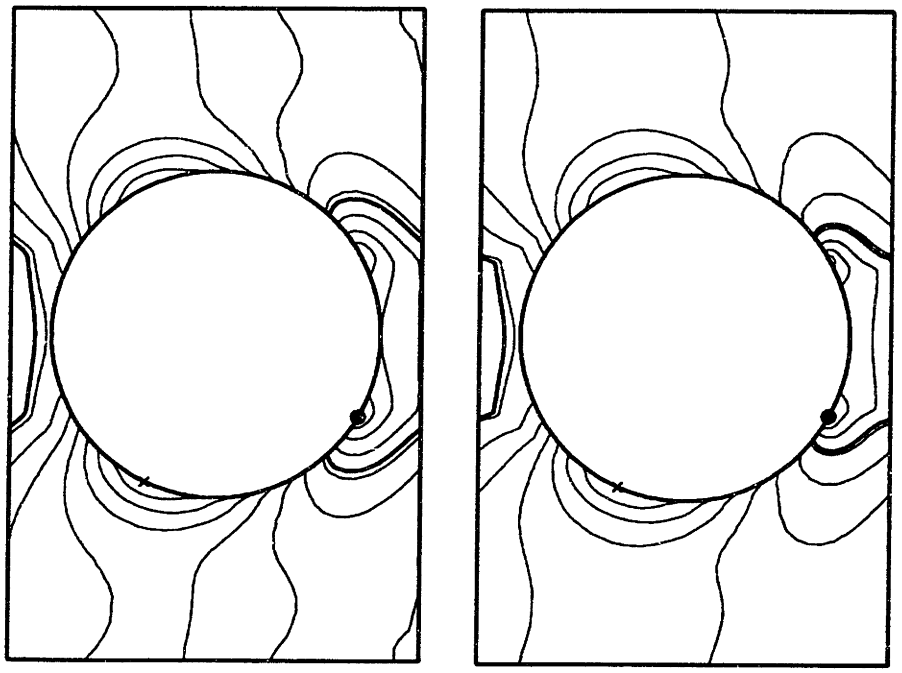

Figure 8-16: The contours of the pressure computed with the DEVSS-G/FEM and the θ-method at $t = 5.0$ which is indistinguishable from the steady-state solution for a CR-FENE fluid in a periodic linear array of cylinders in a channel. (a) $We = 0.9$, (b) $We = 1.5$.

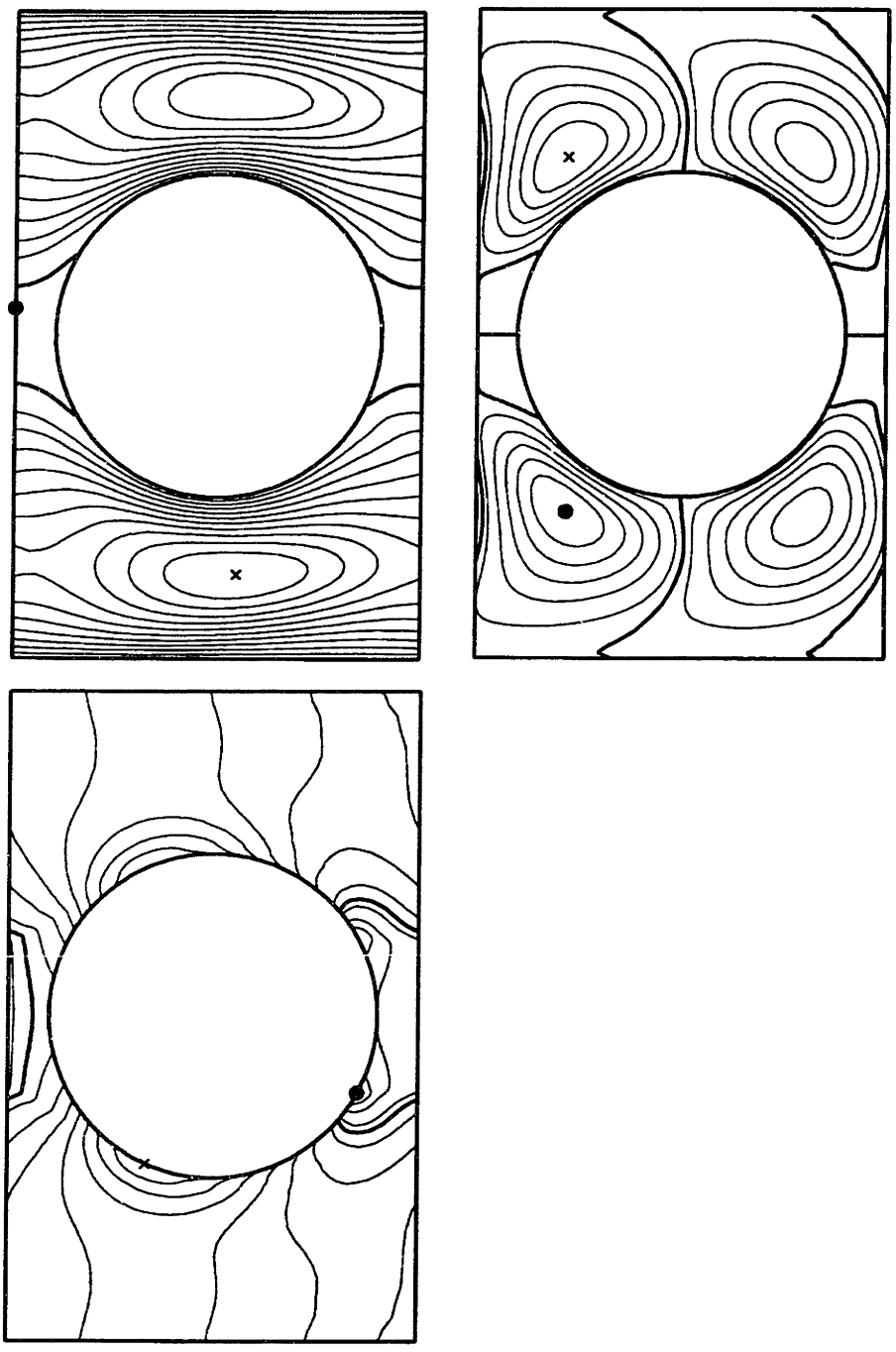

Figure 8-17: The contours of the (a) x-component of the velocity, (b) y-component of the velocity and (c) pressure computed with the DEVSS-G/FEM and the θ-method at $t = 3.0$ for a CR-FENE fluid in a periodic linear array of cylinders in a channel for $We = 3.0$

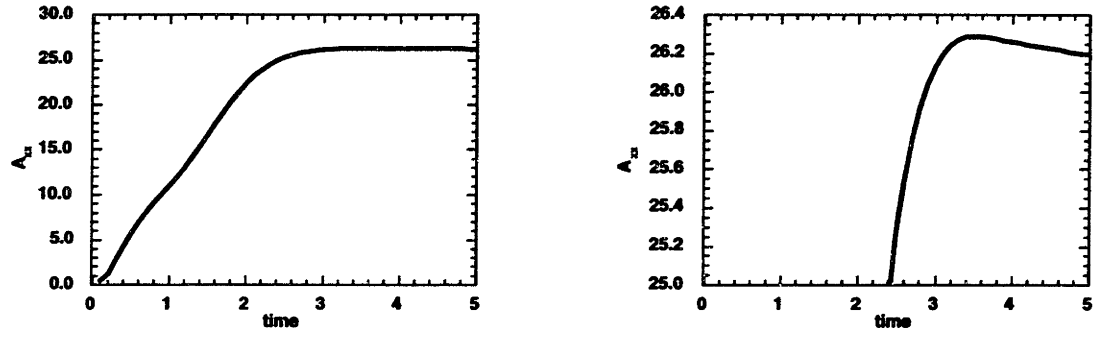

Figure 8-18: The time evolution of the x-component of velocity at the vertical mid-plane ($x = 0$) and about 1/6 of the distance between the cylinder and the top of the channel for $We = 0.5$. The value overshoots the final steady-state value. (a) The entire time history and (b) Focus on the overshoot.

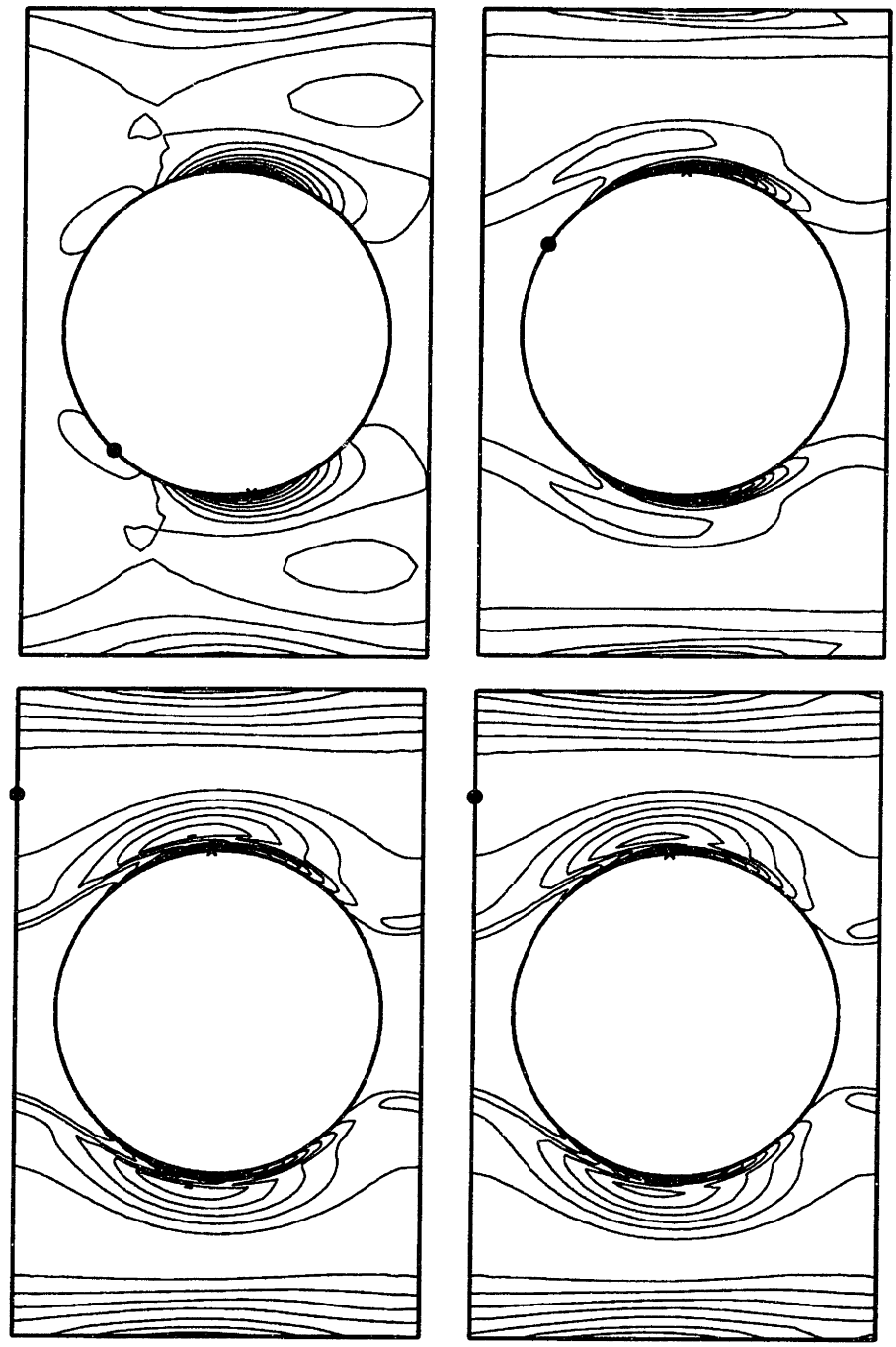

Figure 8-19: The contours of the xx-component of the configuration tensor as a function of time computed with the DEVSS-G/FEM and the θ-method at $We = 0.9$ and $\Delta t = 0.025$ for a CR-FENE fluid in a periodic linear array of cylinders in a channel. (a) $t = 0.1$, (b) $t = 1.0$, (c) $t = 3.0$, and (d) $t = 5.0$.

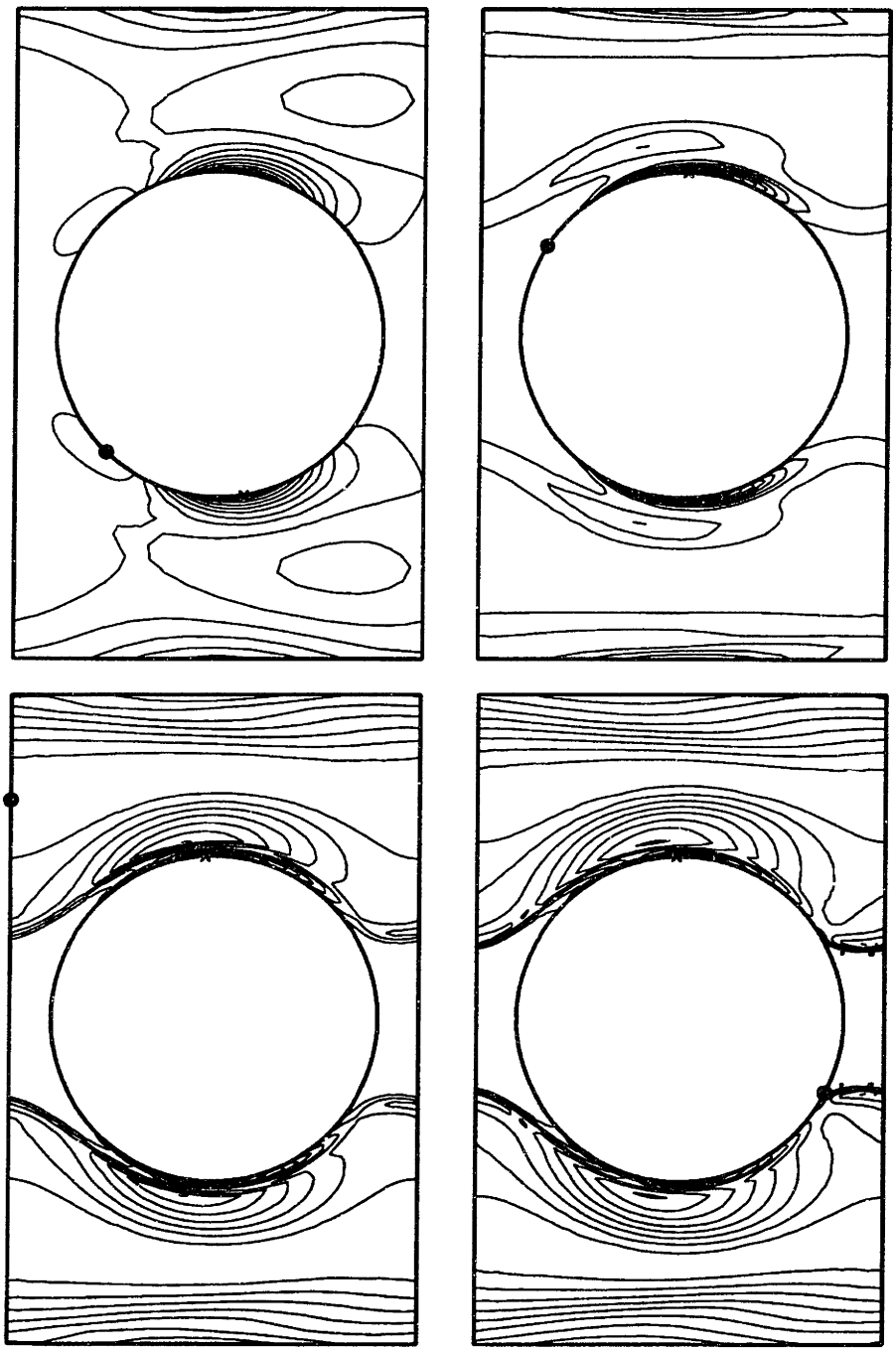

Figure 8-20: The contours of the xx-component of the configuration tensor as a function of time computed with the DEVSS-G/FEM and the θ-method at $We = 1.5$ and $\Delta t = 0.01$ for a CR-FENE fluid in a periodic linear array of cylinders in a channel. (a) $t = 0.1$, (b) $t = 1.0$, (c) $t = 3.0$, and (d) $t = 5.0$.

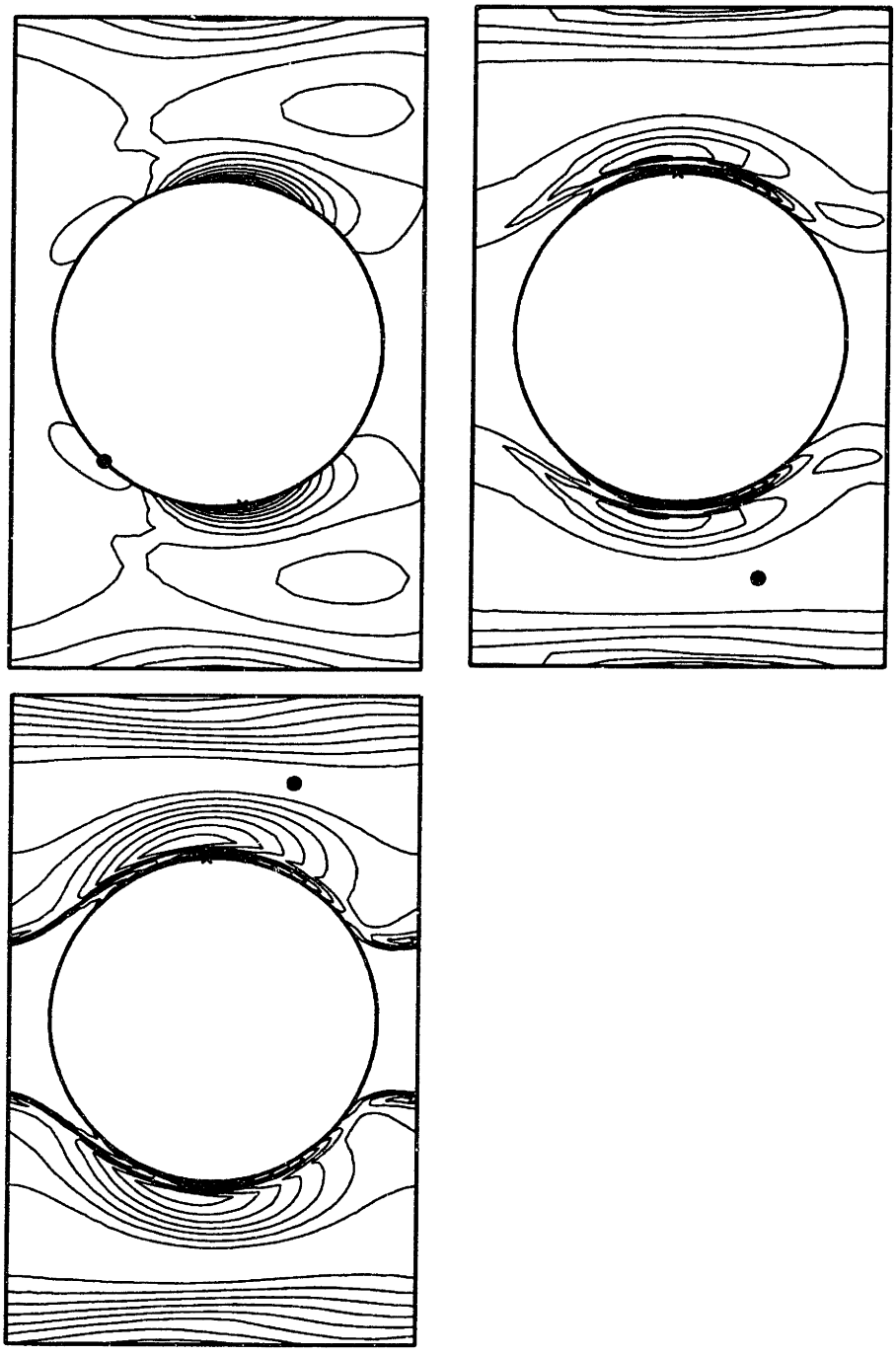

Figure 8-21: The contours of the xx-component of the configuration tensor as a function of time computed with the DEVSS-G/FEM and the θ-method at $We = 3.0$ and $\Delta t = 0.025$ for a CR-FENE fluid in a periodic linear array of cylinders in a channel. (a) $t = 0.1$, (b) $t = 1.0$, and (c) $t = 3.0$.

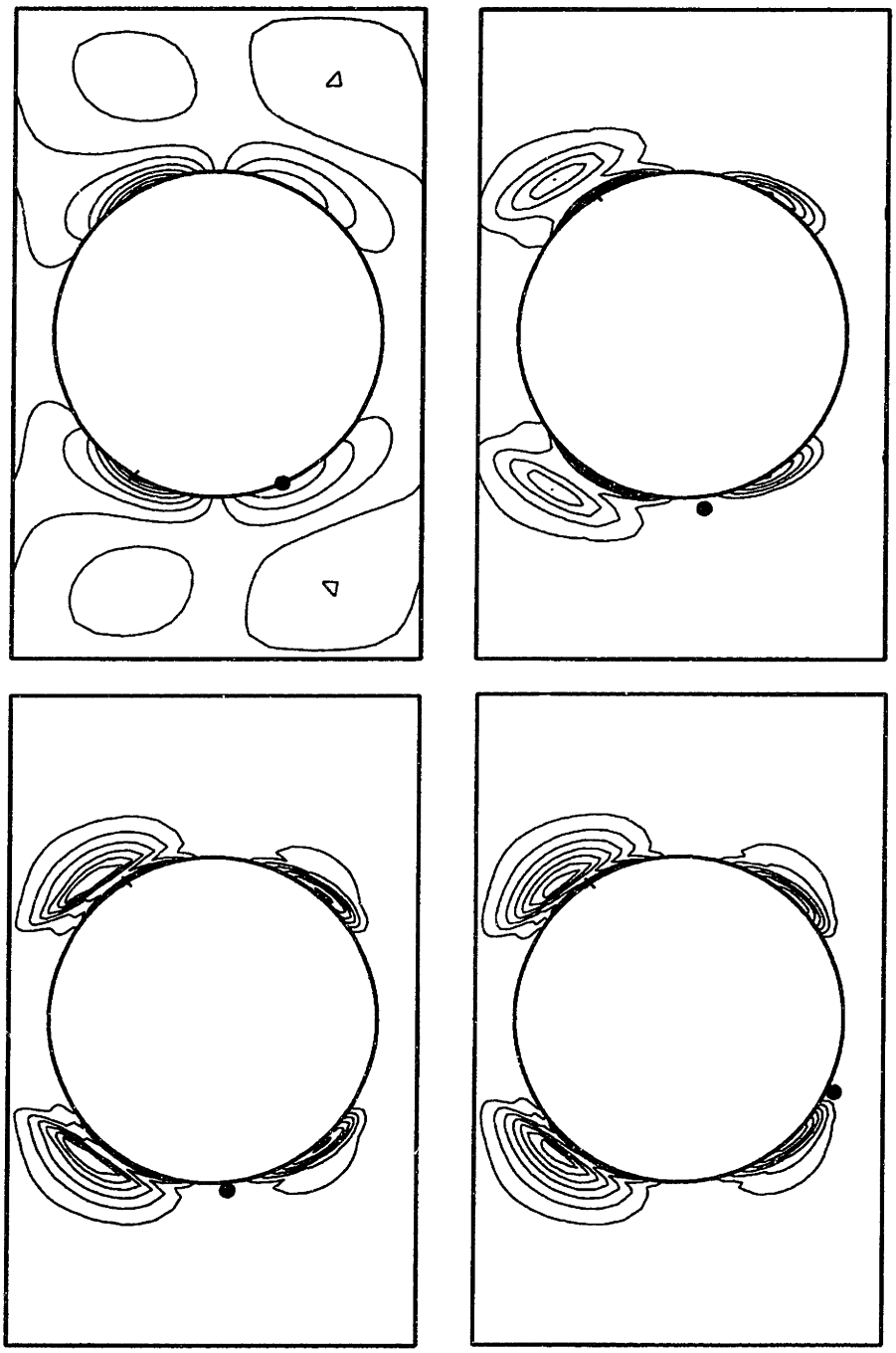

Figure 8-22: The contours of the yy-component of the configuration tensor as a function of time computed with the DEVSS-G/FEM and the θ-method at $We = 0.9$ and $\Delta t = 0.025$ for a CR-FENE fluid in a periodic linear array of cylinders in a channel. (a) $t = 0.1$, (b) $t = 1.0$, (c) $t = 3.0$, and (d) $t = 5.0$.

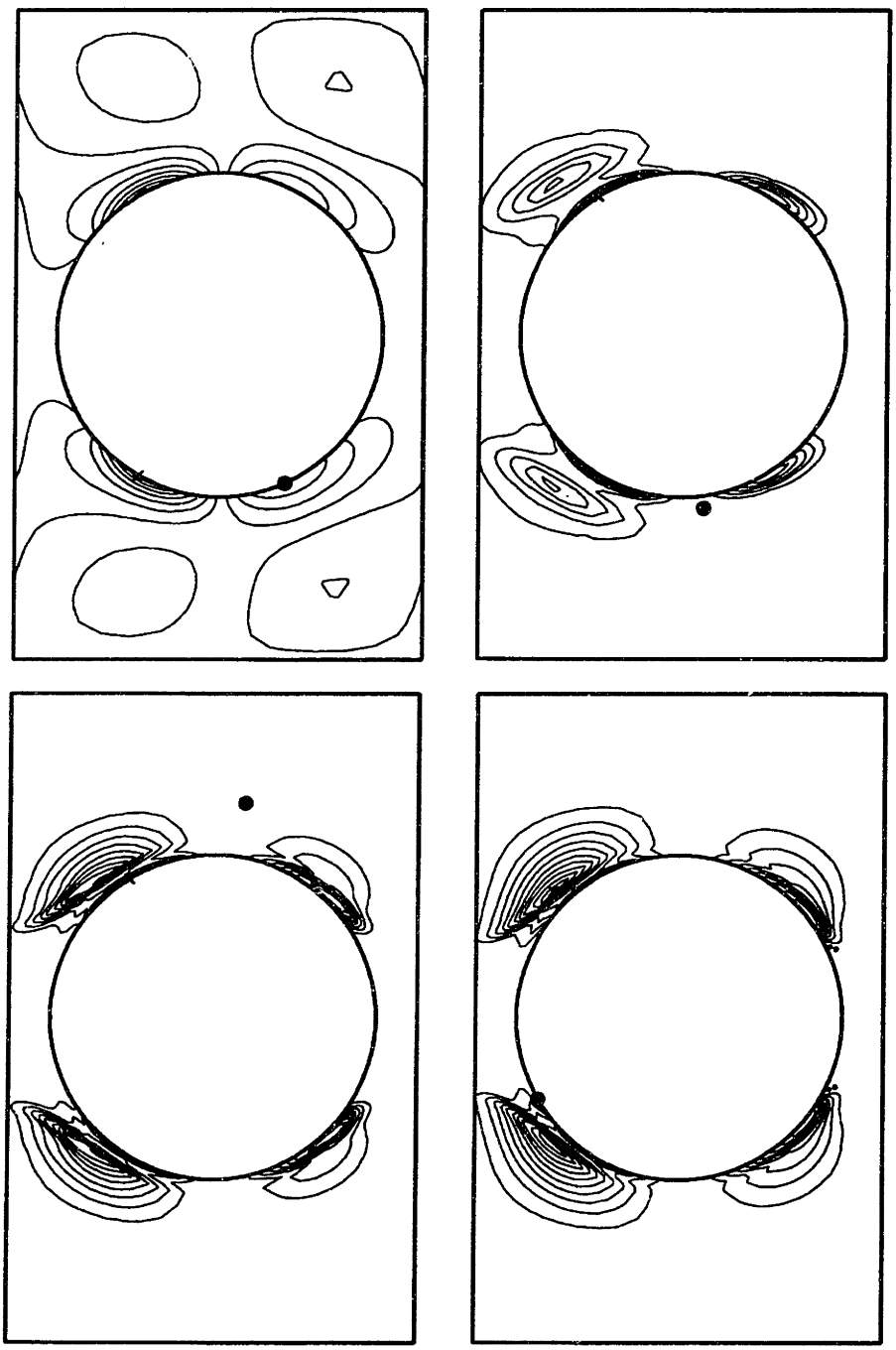

Figure 8-23: The contours of the yy-component of the configuration tensor as a function of time computed with the DEVSS-G/FEM and the θ-method at $We = 1.5$ and $\Delta t = 0.01$ for a CR-FENE fluid in a periodic linear array of cylinders in a channel. (a) $t = 0.1$, (b) $t = 1.0$, (c) $t = 3.0$, and (d) $t = 5.0$.

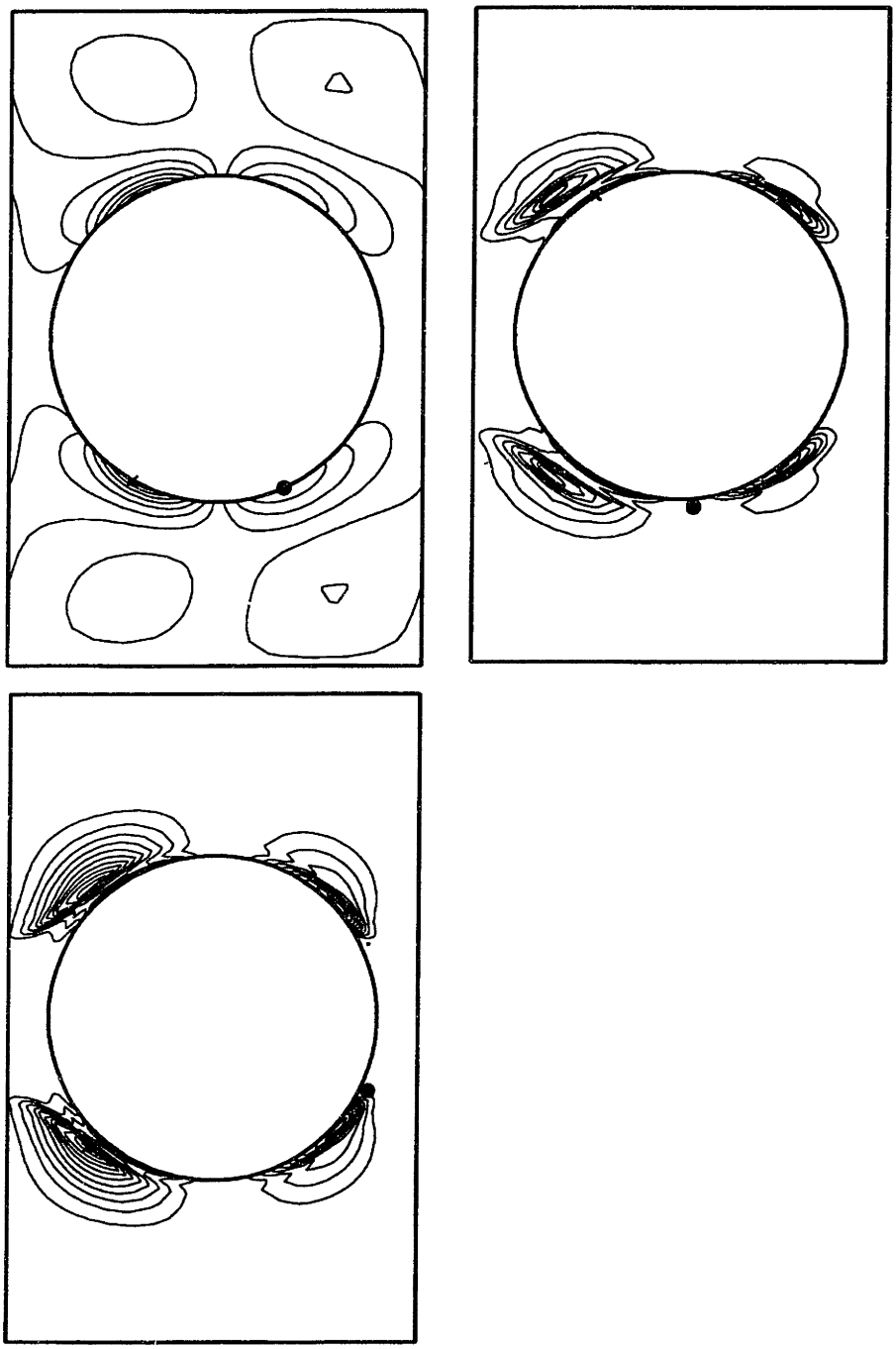

Figure 8-24: The contours of the yy-component of the configuration tensor as a function of time computed with the DEVSS-G/FEM and the θ-method at $We = 3.0$ and $\Delta t = 0.025$ for a CR-FENE fluid in a periodic linear array of cylinders in a channel. (a) $t = 0.1$, (b) $t = 1.0$, and (c) $t = 3.0$.

For A_{yx}, the structure begins similarly to A_{xx} in that a shear region is present near the walls of the channel and the region near the cylinder begins to extend so as to affect the downstream cylinders. However, this effect is not quite realized for any We (see Figures 8-25 - 8-27. At $We = 1.5$ and 3.0, the two lobes on each side of the cylinder almost interact with one another; it also appears that the separation between the shear region near the wall and the lobed structure near the cylinder is breaking down. The maximum and minimum values migrate along the cylinders toward the upstream stagnation point. Again, overshoots and undershoots are observed in regions of high gradients and the effects of convection become stronger with increasing We.

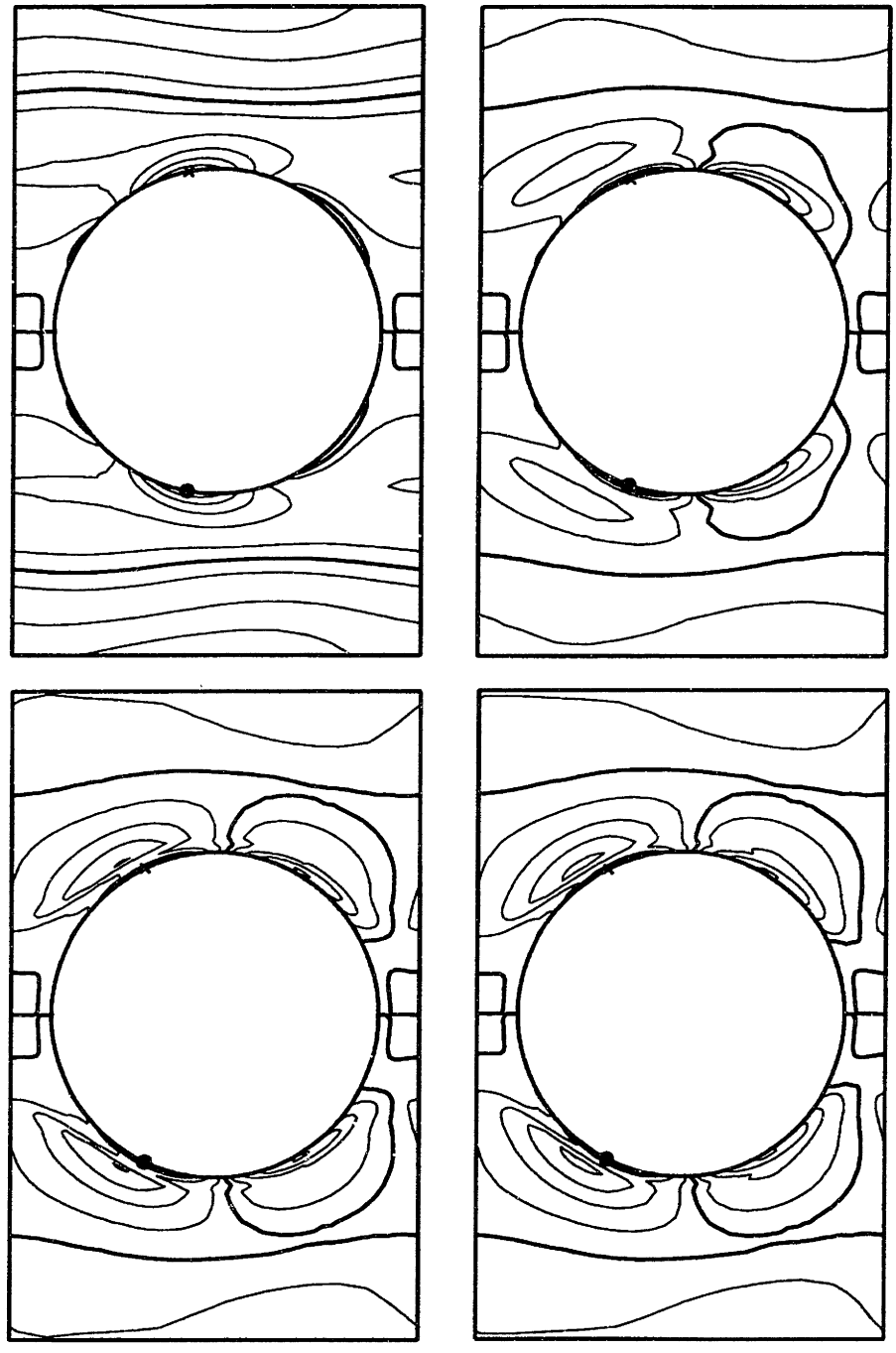

Figure 8-25: The contours of the yx-component of the configuration tensor as a function of time computed with the DEVSS-G/FEM and the θ-method at $We = 0.9$ and $\Delta t = 0.025$ for a CR-FENE fluid in a periodic linear array of cylinders in a channel. (a) $t = 0.1$, (b) $t = 1.0$, (c) $t = 3.0$, and (d) $t = 5.0$.

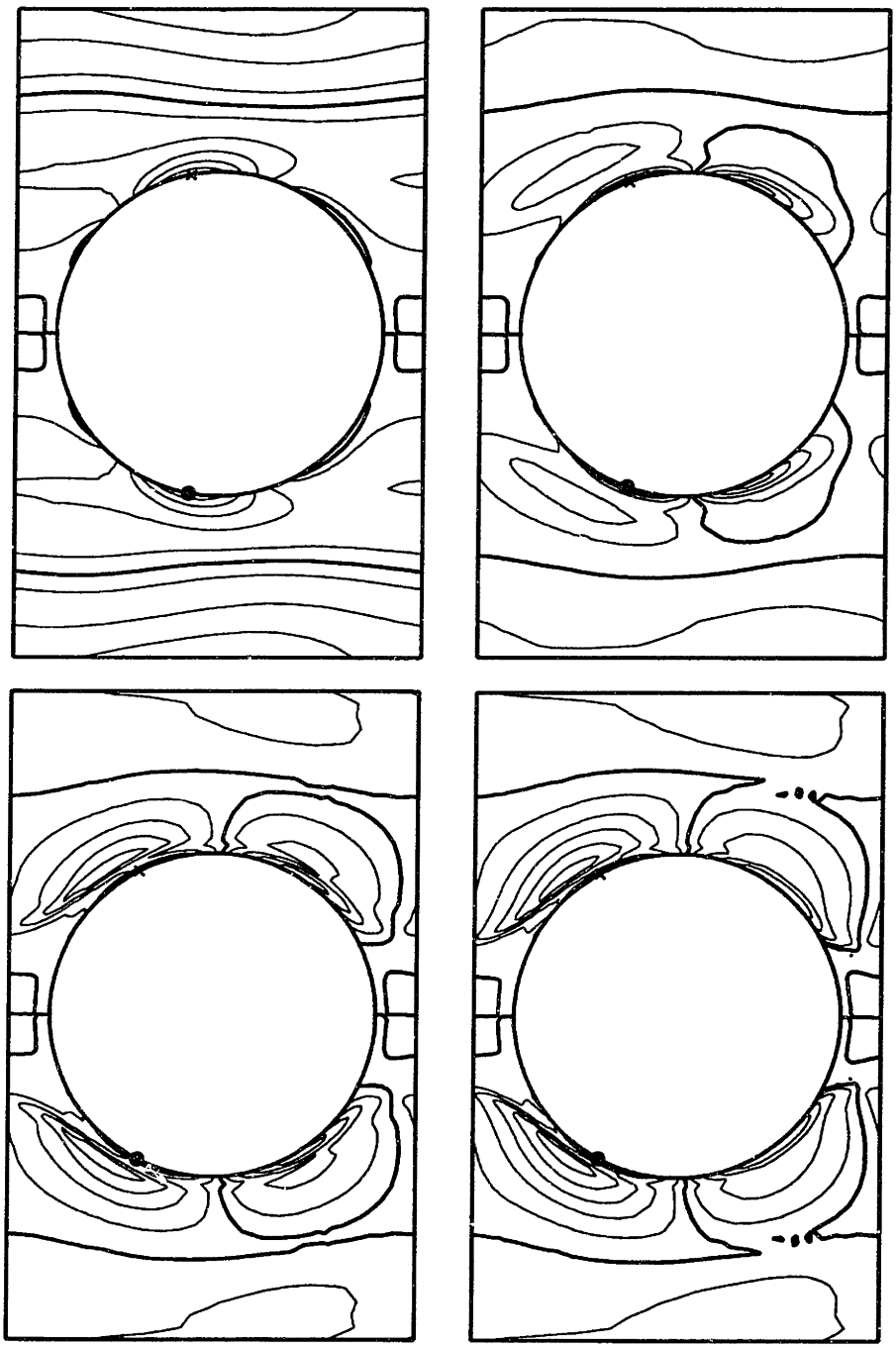

Figure 8-26: The contours of the yx-component of the configuration tensor as a function of time computed with the DEVSS-G/FEM and the θ-method at $We = 1.5$ and $\Delta t = 0.01$ for a CR-FENE fluid in a periodic linear array of cylinders in a channel. (a) $t = 0.1$, (b) $t = 1.0$, (c) $t = 3.0$, and (d) $t = 5.0$.

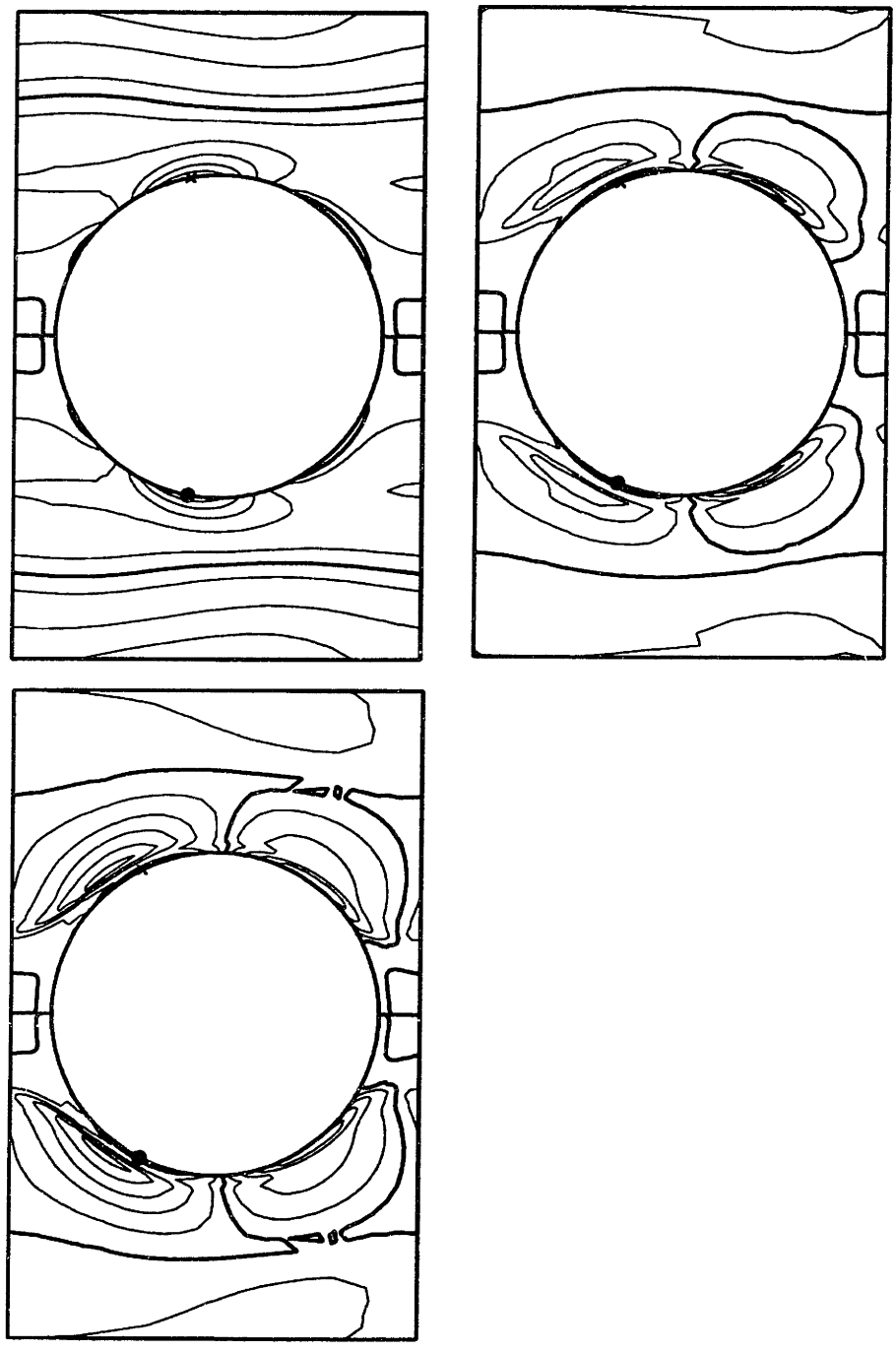

Figure 8-27: The contours of the yx-component of the configuration tensor as a function of time computed with the DEVSS-G/FEM and the θ-method at $We = 3.0$ and $\Delta t = 0.025$ for a CR-FENE fluid in a periodic linear array of cylinders in a channel. (a) $t = 0.1$, (b) $t = 1.0$, and (c) $t = 3.0$.

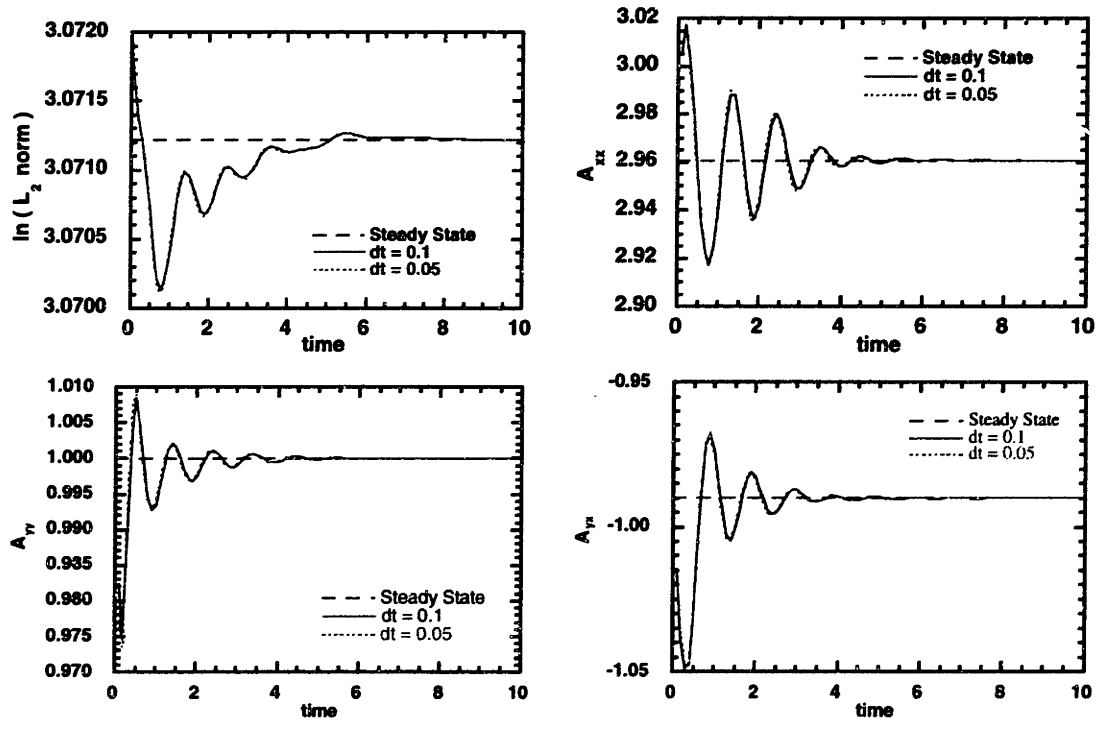

Figure 8-28: Nonlinear stability calculations for the planar Couette flow of a CR-FENE fluid at $De = 1.0$ and $\epsilon = 0.1$. (a) The L_2-norm of the solution vector as defined in eq. (5.15). The configuration tensor at the first interior node point in the mesh as a function of time is shown for (b) the xx-component, (c) the yy-component, and (d) the yx-component.

8.5 Nonlinear Stability of Planar Couette Flow

In order to confirm the results of the linear stability of the planar Couette flow of a CR-FENE fluid, a nonlinear stability analysis was conducted. In the nonlinear stability calculations, the steady-state was perturbed randomly and the nonlinear time dependent flow equations were integrated forward in time using the θ-method. The random perturbation was achieved by picking a random number between -1.0 and 1.0, multiplying it by a scaling factor ϵ, normalizing it by the maximum of the variable being perturbed and then adding the result to that variable. This was done for the configuration tensor at each node in the domain. The other variables are not perturbed because they do not satisfy a differential equation with respect to time.

The nonlinear stability results for $De = 1$ are shown in Figure 8-28 for $\epsilon = 0.1$ and in Figure 8-29 for $\epsilon = 0.001$. The results all show a simple linear response decaying

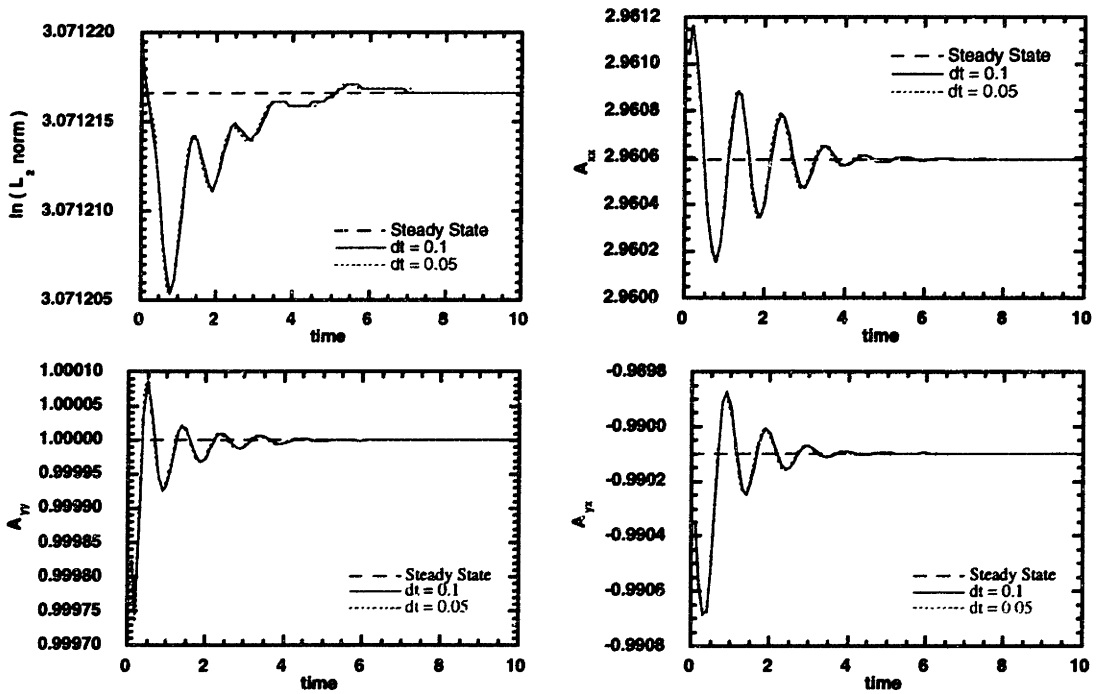

Figure 8-29: Nonlinear stability calculations for the planar Couette flow of a CR-FENE fluid at $De = 1.0$ and $\epsilon = 0.001$. (a) The L_2-norm of the solution vector as defined in eq. (5.15). The configuration tensor at the first interior node point in the mesh as a function of time is shown for (b) the xx-component, (c) the yy-component, and (d) the yx-component.

back to the steady state solution in less than ten relaxation times – the time is nondimensionalized with respect to the relaxation time. The response at $\epsilon = 0.1$ and $\epsilon = 0.001$ are virtually identical, the only difference is the magnitude of the initial perturbation. The identical type of results are seen at $De = 10.0$. The nonlinear stability analysis reduces to a linear stability analysis for $\epsilon \ll 1$. The stability of the nonlinear calculations at $\epsilon = 0.001$ should be approaching the calculations performed in Chapter 7. The nonlinear calculations confirm the linear calculations in that the flow is stable for both calculations.

8.6 Nonlinear Stability of Flow Through a // Periodic Array of Cylinders in a Channel

As a final attempt to calculate a time dependent solution for the flow of a CR-FENE fluid through a periodic linear array of cylinders in a channel. The disturbance was added to the steady-state solution in the same manner as for the planar Couette flow case with $\epsilon = 0.001$. The results are shown in Figure 8-30. At both We the flow converges back to the steady-state solution, which agrees with the linear stability calculations in Chapter 7 and the startup calculations in Section 8.4. The numerical solutions for $We = 0.5$ and 0.9 are very similar. For both numerical solutions, an upper limit on the time step is observed above which the solution begins to diverge and then the Newton iterations on the stress calculation step fails to converge. Saramito (1994) indicated that a step size bound, Δt_{crit}, does exist for the θ-method as applied to viscoelastic problems which scaled roughly as the maximum of the absolute value of $1/\nabla \boldsymbol{v}$. No step size limit was found for the planar Couette geometry, but for step sizes above the approximate bound given by Saramito, the calculations for the periodic array of cylinders failed. The dependence of Δt_{crit} on the We appears to be solely related to the effect of We on $\nabla \boldsymbol{v}$ in agreement with the work of Saramito (1994).

The transient response of the L_2 norm of the solution vector overshoots and un-

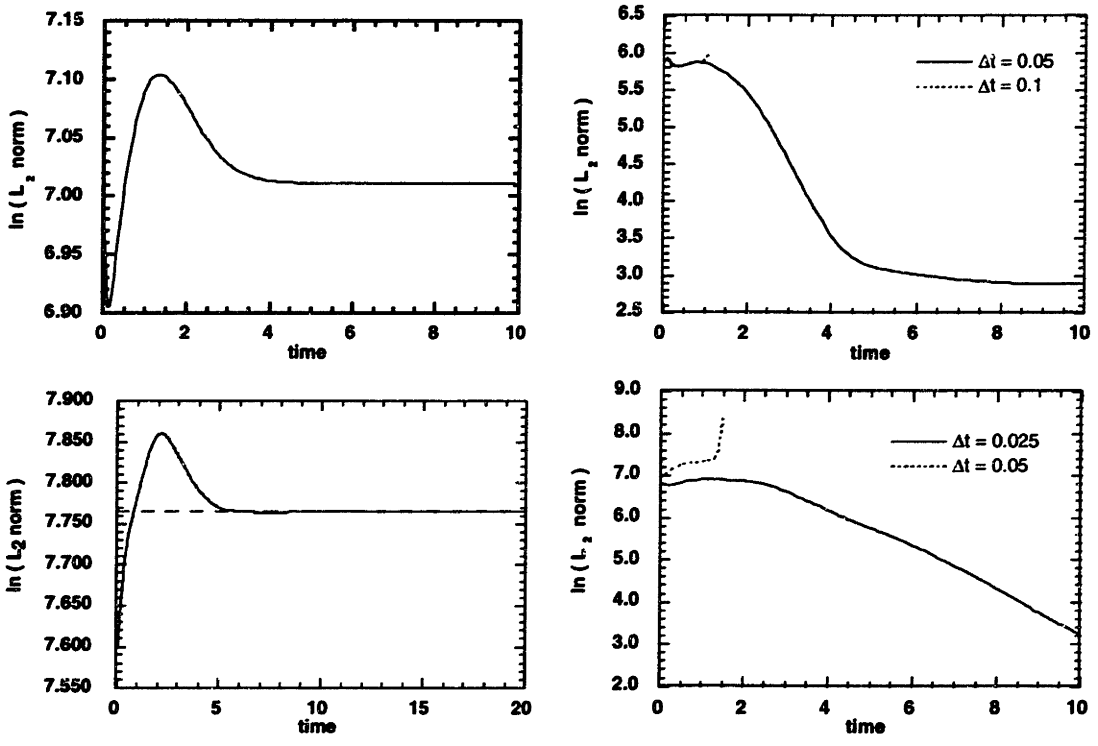

Figure 8-30: Nonlinear stability calculations for the flow of CR-FENE fluid in a linear periodic array of cylinders in a channel computed with the DEVSS-G/FEM and the θ-method. The transient response is shown as the L_2-norm of the solution vector as defined in eq. (5.15). (a) $We = 0.5$ and $\Delta t = 0.05$ and 0.1 for the response of the solution, (b) $We = 0.5$ and $\Delta t = 0.05$ for the response of the disturbance only, (c) $We = 0.9$ and $\Delta t = 0.025$ and 0.05 for the response of the solution, and (d) $We = 0.9$ and $\Delta t = 0.025$ for the response of the disturbance only.

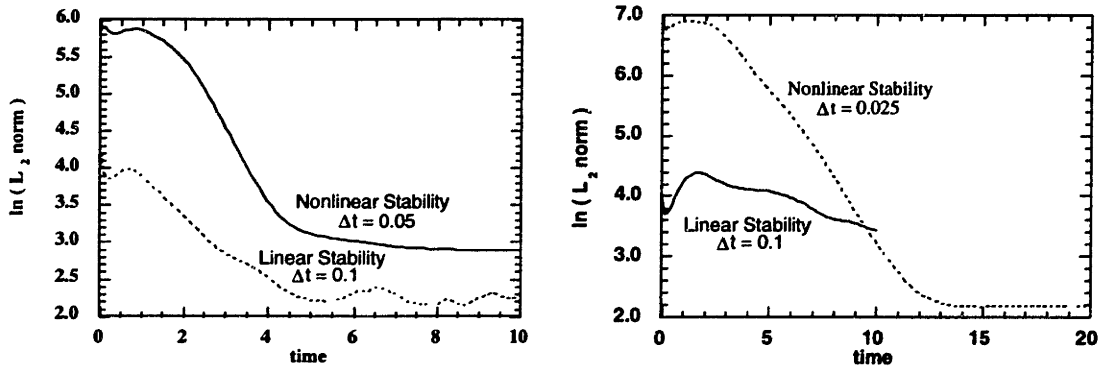

Figure 8-31: A comparison of the response of the disturbance as measured by the L_2-norm of the solution vector as defined in eq. (5.15) for the linear and nonlinear stability calculations for the flow of a CR-FENE fluid in a linear periodic array of cylinders in a channel computed with the DEVSS-G/FEM and the θ-method. (a) $We = 0.5$, (b) $We = 0.9$.

dershoots the final steady-state solution (see Figure 8-30a and c). Examination of only the disturbance results in a linear exponential decay similar to that observed in the linear stability analysis (see Figure 8-30b and d). The energy of the disturbance definitely decays over time.

In Figure 8-31 the response of the disturbance is compared between the nonlinear stability analysis and the linear stability analysis. The response of the nonlinear stability analysis decays as approximately $-1/(2De(\dot{\gamma}))$ which is the same as the planar Couette decay rate. The linear stability analysis decays slightly slower than this for $We = 0.5$ and significantly slower for $We = 0.9$. The time evolution of the flow and stress fields for $We = 0.9$ is shown in Figures 8-32 – 8-37. The initial condition is shown to give an idea of the magnitude of the perturbation compared to the steady-state solution. At $t = 2.0$, the L_2-norm of the solution vector is near its maximum value and $t = 15.0$ is the final time step computed. The time evolution of the solution at $We = 0.5$ does not differ significantly from that of $We = 0.9$ so only the final solution and the steady-state solution are shown in Figures 8-38 – 8-43. The steady-state solution and solution at the last time step computed are the same to within $\pm 2\%$.

The algebraic variables respond similarly to the startup flow where the variable quickly obtains the general structure of the steady-state solution and simply corrects

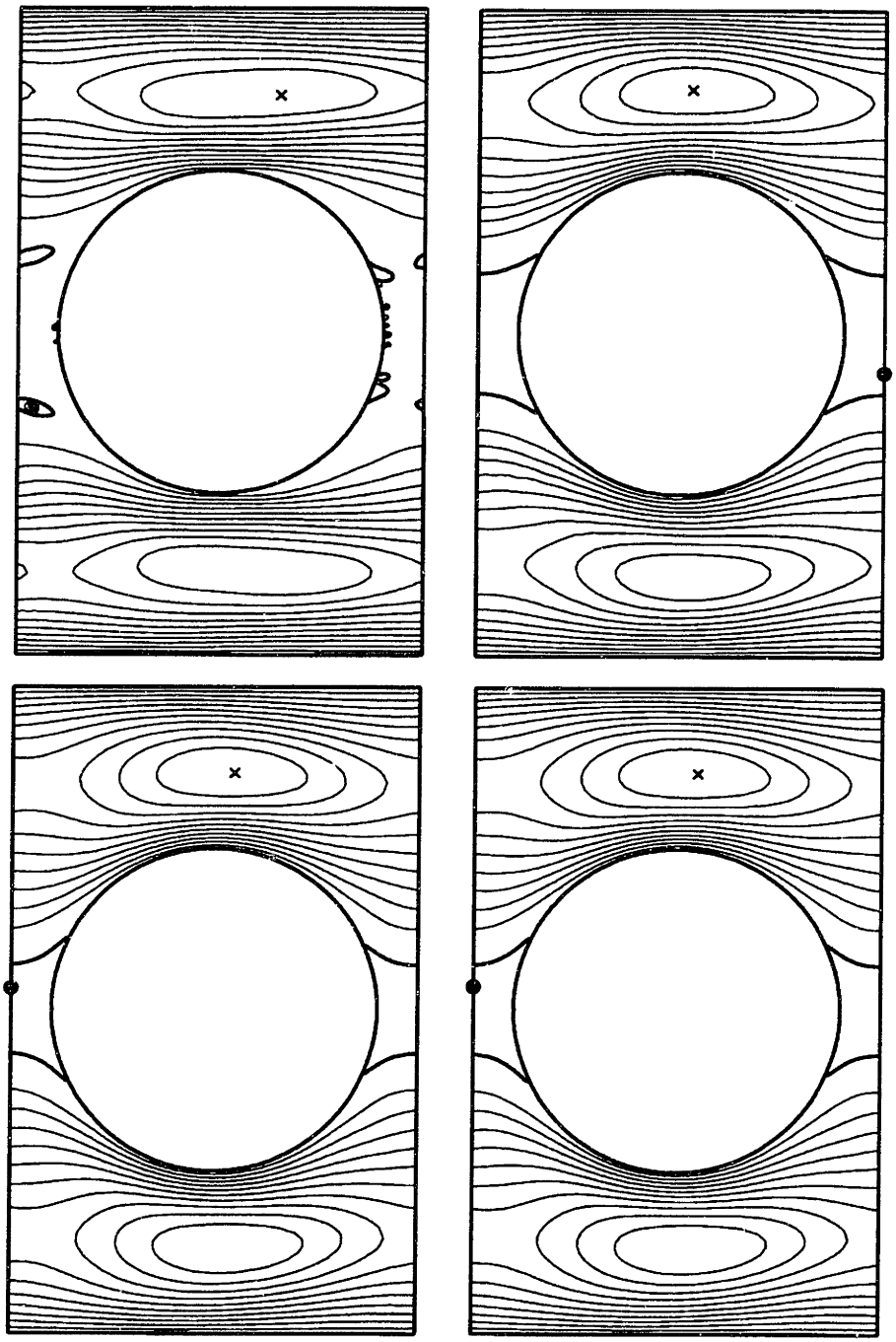

Figure 8-32: The contours of the x-component of the velocity for the nonlinear stability analysis as a function of time computed with the DEVSS-G/FEM and the θ-method at $We = 0.9$ and $\Delta t = 0.025$ for a CR-FENE fluid in a periodic linear array of cylinders in a channel. (a) $t = 0.025$, (b) $t = 2.0$, (c) $t = 15.0$, and (d) steady state.

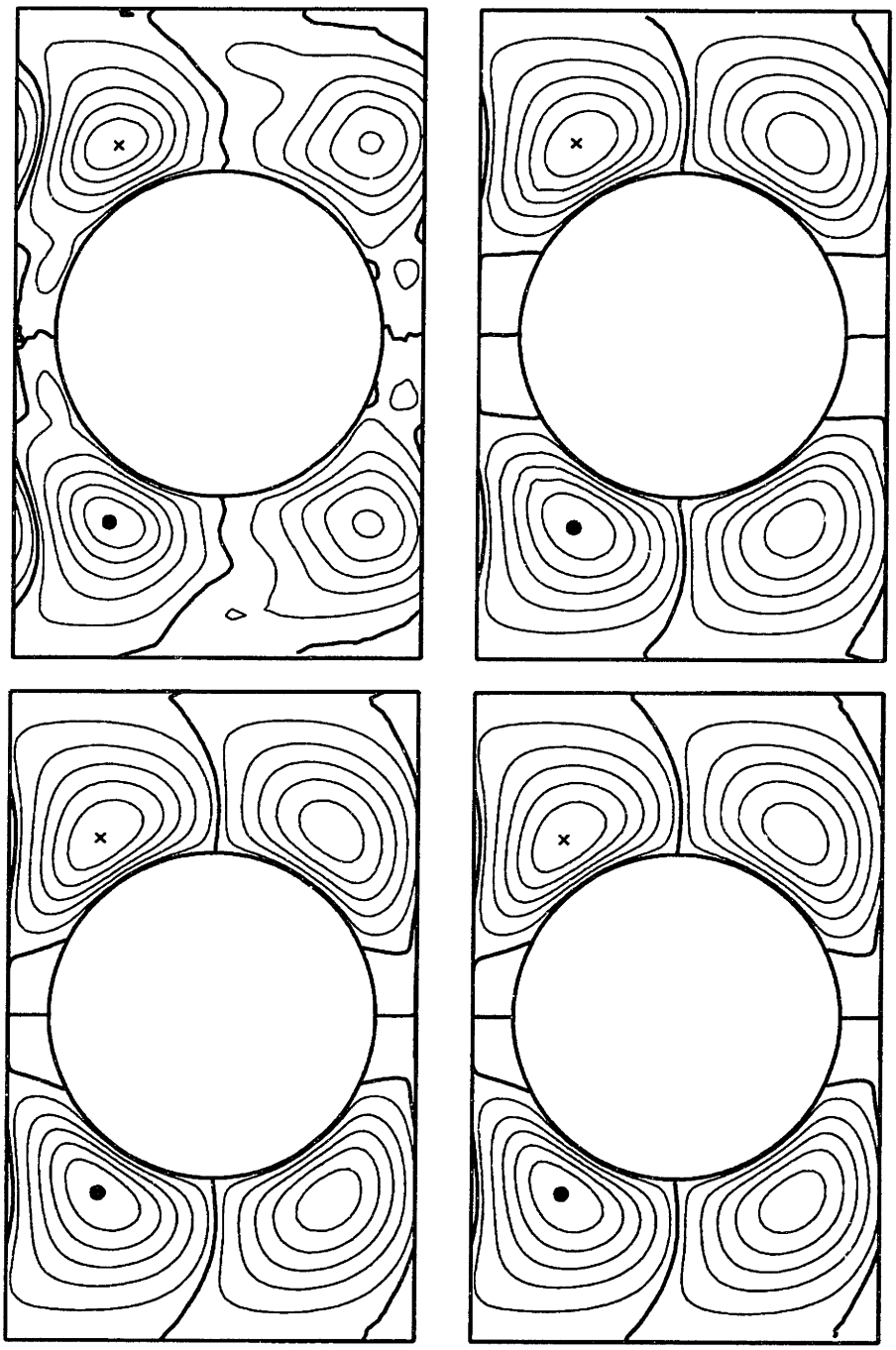

Figure 8-33: The contours of the y-component of the velocity for the nonlinear stability analysis as a function of time computed with the DEVSS-G/FEM and the θ-method at $We = 0.9$ and $\Delta t = 0.025$ for a CR-FENE fluid in a periodic linear array of cylinders in a channel. (a) $t = 0.025$, (b) $t = 2.0$, (c) $t = 15.0$, and (d) steady state.

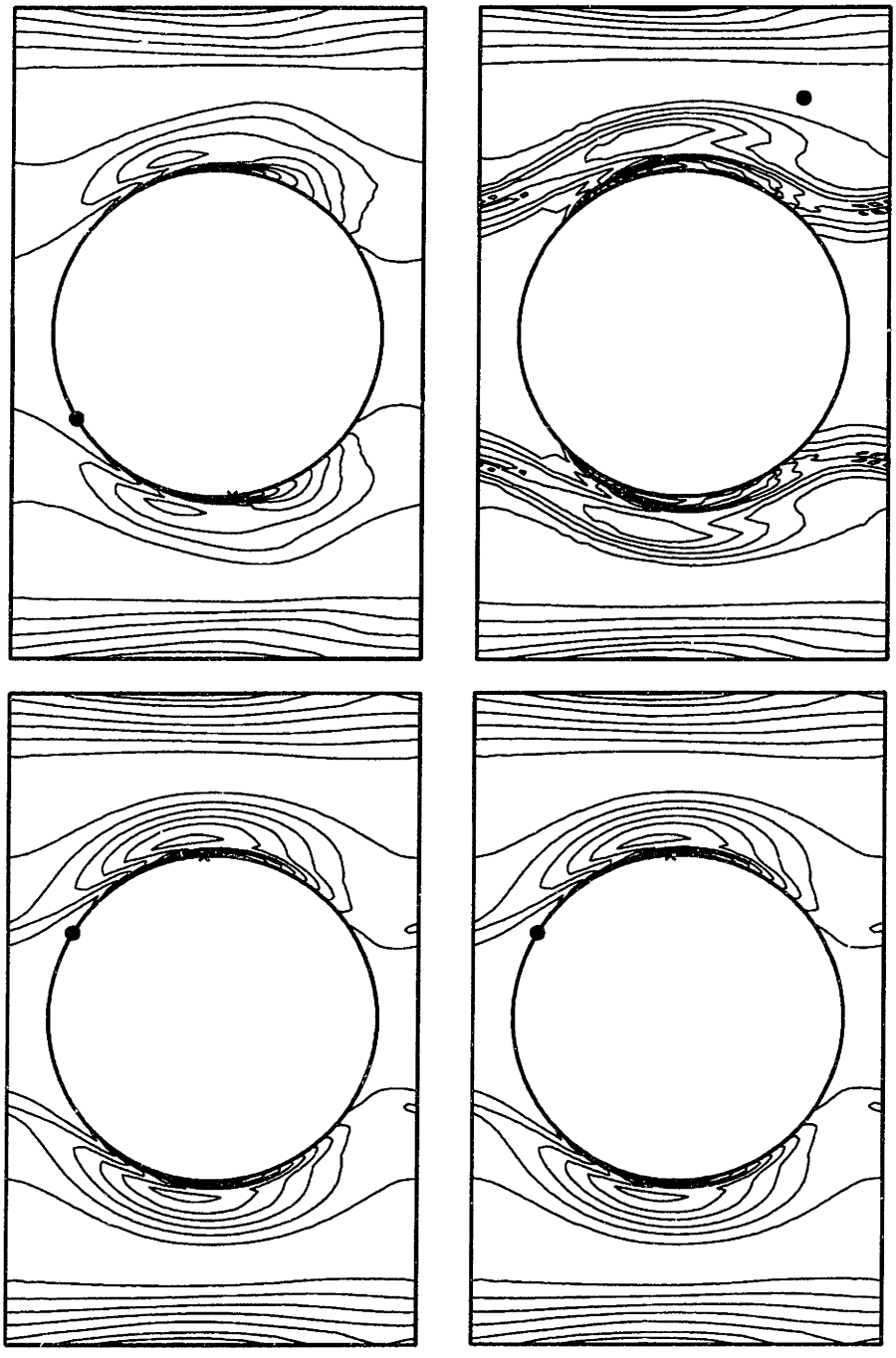

Figure 8-34: The contours of the xx-component of the configuration tensor for the nonlinear stability analysis as a function of time computed with the DEVSS-G/FEM and the θ-method at $We = 0.9$ and $\Delta t = 0.025$ for a CR-FENE fluid in a periodic linear array of cylinders in a channel. (a) $t = 0.025$, (b) $t = 2.0$, (c) $t = 15.0$, and (d) steady state.

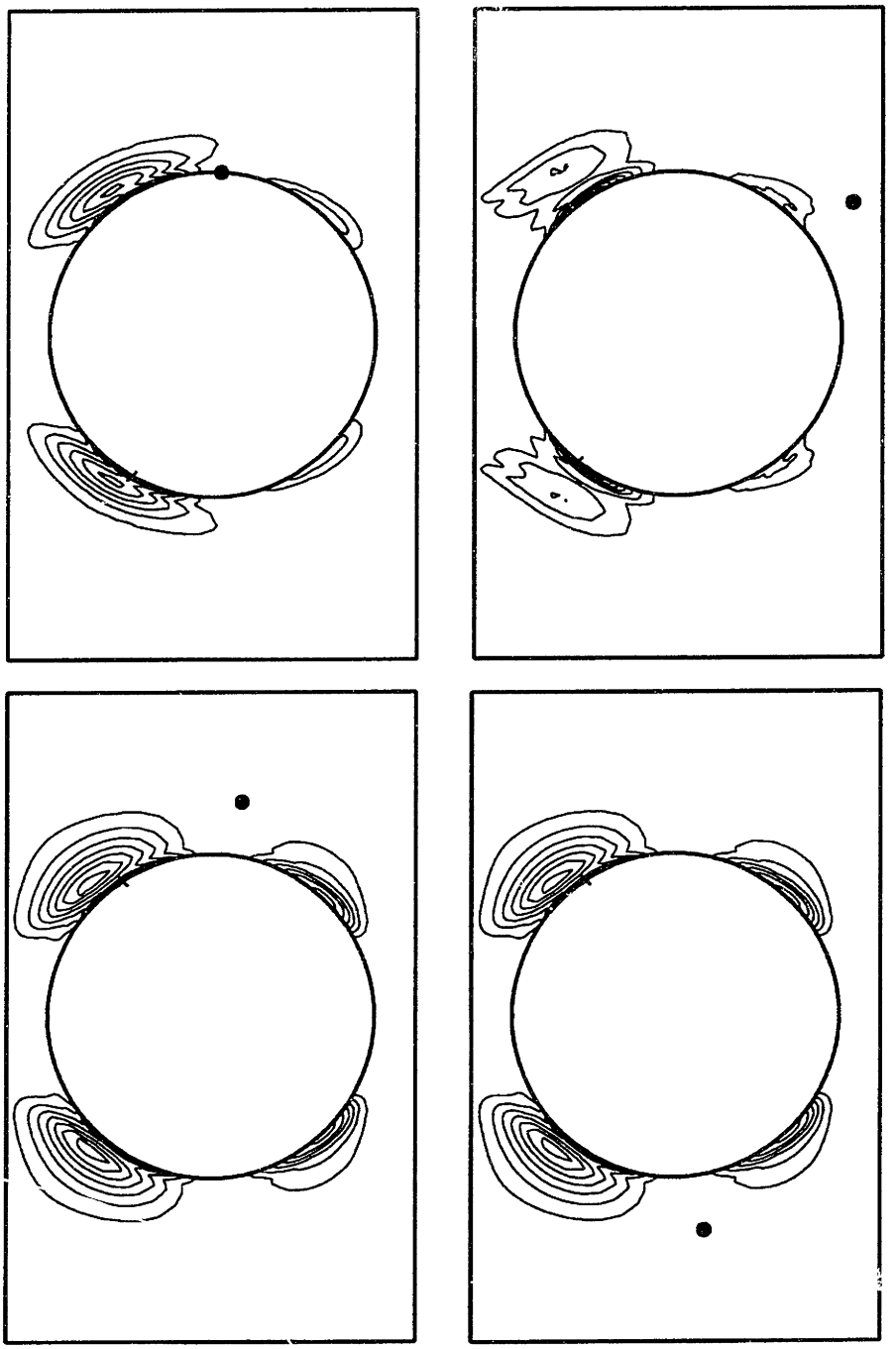

Figure 8-35: The contours of the yy-component of the configuration tensor for the nonlinear stability analysis as a function of time computed with the DEVSS-G/FEM and the θ-method at $We = 0.9$ and $\Delta t = 0.025$ for a CR-FENE fluid in a periodic linear array of cylinders in a channel. (a) $t = 0.025$, (b) $t = 2.0$, (c) $t = 15.0$, and (d) steady state.

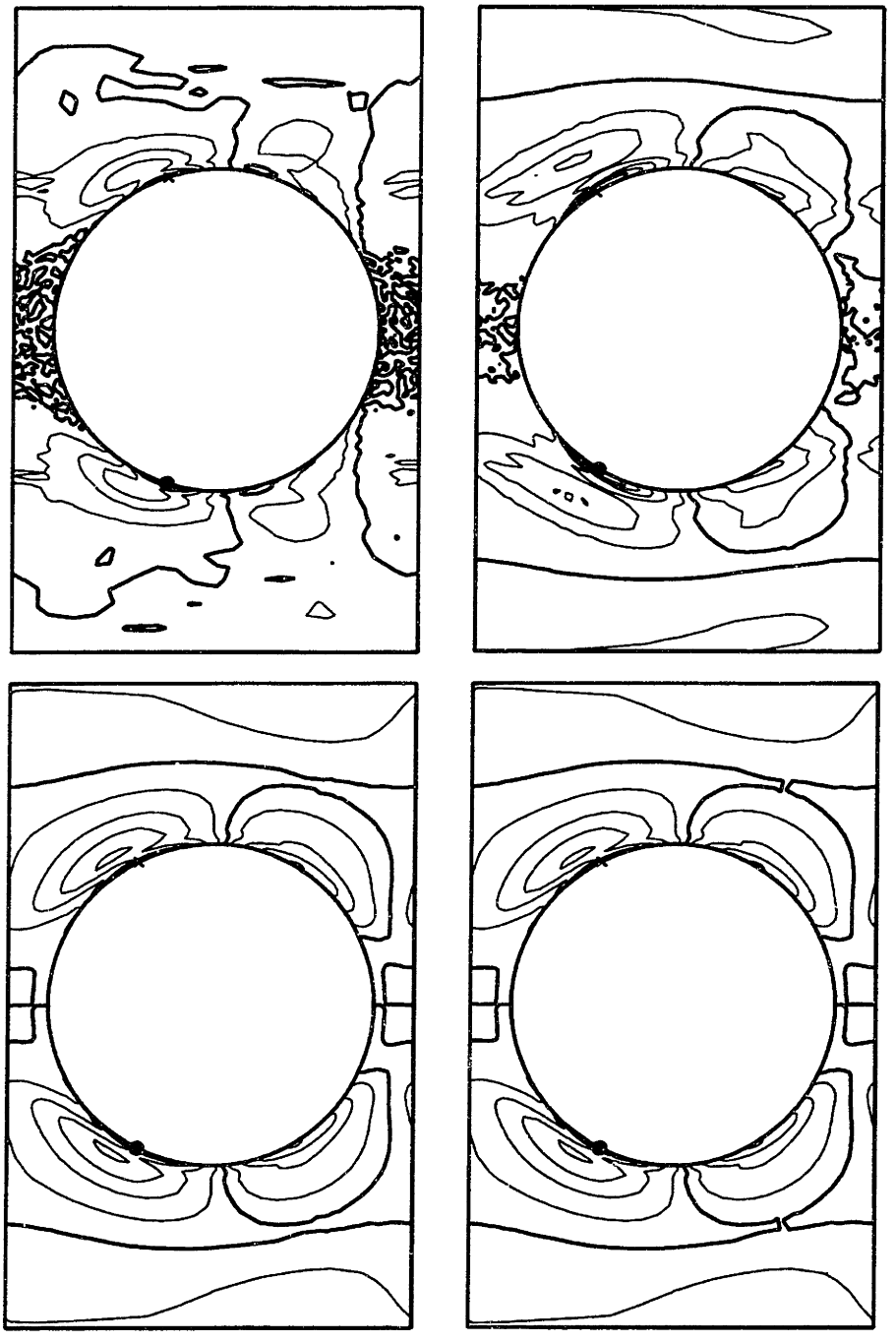

Figure 8-36: The contours of the yx-component of the configuration tensor for the nonlinear stability analysis as a function of time computed with the DEVSS-G/FEM and the θ-method at $We = 0.9$ and $\Delta t = 0.025$ for a CR-FENE fluid in a periodic linear array of cylinders in a channel. (a) $t = 0.025$, (b) $t = 2.0$, (c) $t = 15.0$, and (d) steady state.

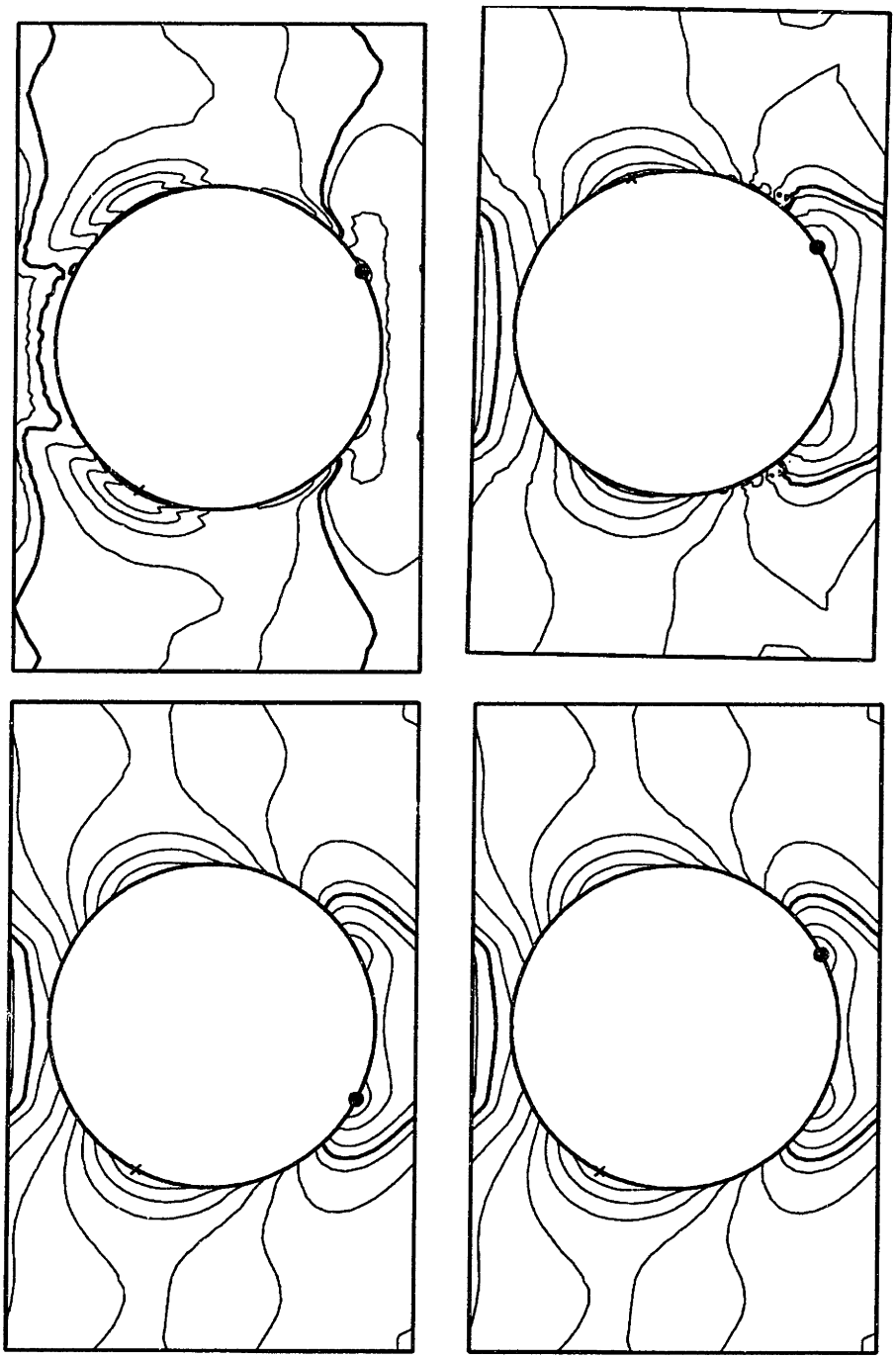

Figure 8-37: The contours of the pressure for the nonlinear stability analysis as a function of time computed with the DEVSS-G/FEM and the θ-method at $We = 0.9$ and $\Delta t = 0.025$ for a CR-FENE fluid in a periodic linear array of cylinders in a channel. (a) $t = 0.025$, (b) $t = 2.0$, (c) $t = 15.0$, and (d) steady state.

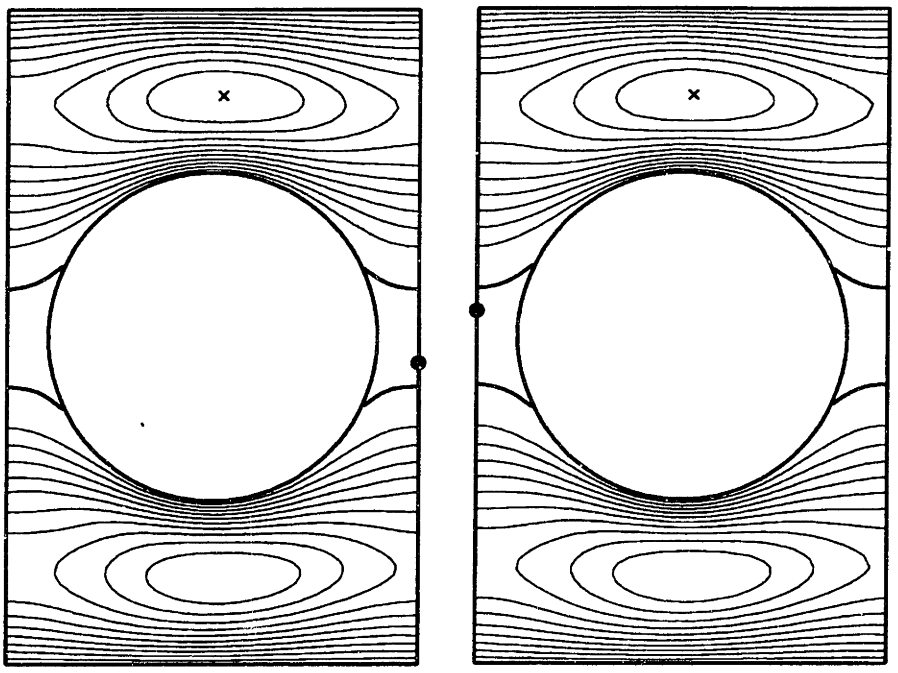

Figure 8-38: The contours of the x-component of the velocity for the nonlinear stability analysis as a function of time computed with the DEVSS-G/FEM and the θ-method at $We = 0.9$ and $\Delta t = 0.025$ for a CR-FENE fluid in a periodic linear array of cylinders in a channel. (a) $t = 9.9$ and (b) steady state.

slightly with increasing time (Figures 8-32, 8-33 and 8-37). The overall structure of the configuration tensor fields are not changed by the perturbation; this does not change at any time during the simulation (Figures 8-34, 8-35 and 8-36). The disturbance to the variables is asymmetric, but this dies out over time leaving the symmetric steady-state solution as a result.

These calculations were performed on an HP9000 Series 735 workstation. These nonlinear calculations used approximately 18 minutes of CPU time per time step (for step sizes on the order of $10^{-1} - 10^{-2}$ relaxation times) for $\sim 40,000$ unknowns. This results in a time savings of approximately twenty over the the fully implicit alternative. This is in line with the expected savings of fifteen estimated via operation counts. Furthermore, the startup calculations performed in the previous section were run on DuPont's Cray-C90; the CPU time per time step was approximately 85-90 seconds compared to an estimated 20 minutes for the fully implicit method. This is an increase of approximately twelve over the HP workstation which is the same

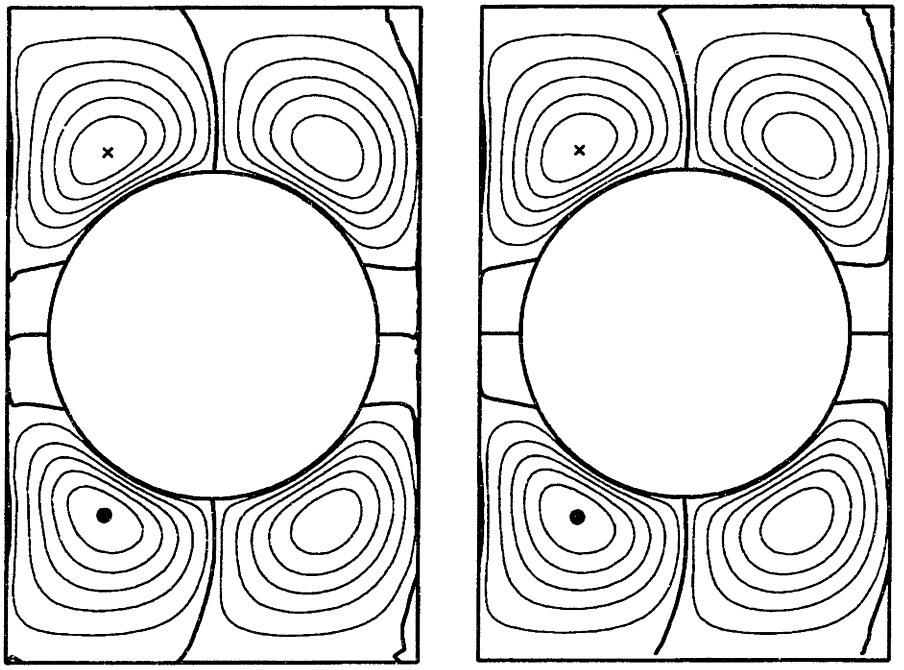

Figure 8-39: The contours of the y-component of the velocity for the nonlinear stability analysis as a function of time computed with the DEVSS-G/FEM and the θ-method at $We = 0.9$ and $\Delta t = 0.025$ for a CR-FENE fluid in a periodic linear array of cylinders in a channel. (a) $t = 9.9$ and (b) steady state.

order of magnitude of savings found for steady-state calculations (10-15). Additional savings can be expected if the code was optimized to run more efficiently on either the HP workstation or the Cray-C90.

8.7 Summary

The impetus for switching from fully implicit time integration to semi-implicit time integration methods such as the θ-Method is the ridiculously high CPU times necessary for moderate time dependent computations expected. In Section 8.1 it was estimated that approximately 3,600 hours (150 days) of CPU time would be necessary to take 600 time steps using an HP9000 Series 735 workstation for the periodic cylinder problem examined in this thesis. Switching to a Cray-C90 would not help much, since it is roughly an order of magnitude faster than the HP workstation.

The first attempt at using a semi-implicit method (a simple block decoupling

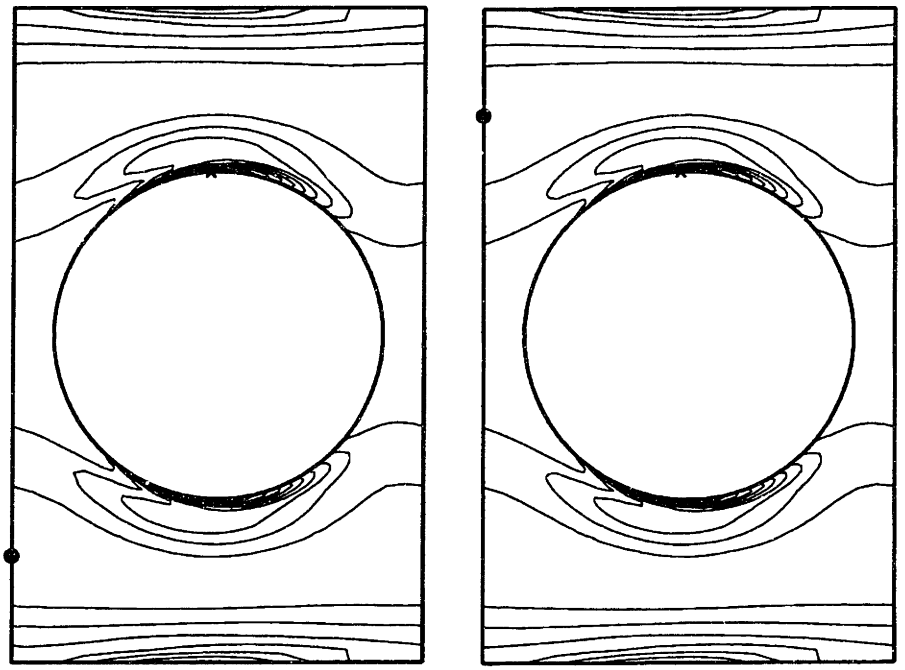

Figure 8-40: The contours of the xx-component of the configuration tensor for the nonlinear stability analysis as a function of time computed with the DEVSS-G/FEM and the θ-method at $We = 0.9$ and $\Delta t = 0.025$ for a CR-FENE fluid in a periodic linear array of cylinders in a channel. (a) $t = 9.9$ and (b) steady state.

method) failed due to the strong coupling between the velocity and the stress variables. After a search of the literature, operating splitting methods were pursued, specifically, the θ-method. This method is based on the initial alternating direction implicit ideas of Peaceman and Rachford (1955) used in finite difference methods.

The θ-method uses three substeps to march forward in time; the amount of work for all three substeps should be less than the amount necessary for one fully implicit step. The variables are divided into two groups(here, one set is elliptic while the other is hyperbolic) with one solved implicitly in the first step and the other explicitly. This order is reversed in the second step and, finally, the third step is repeats the first step. In attempting to apply this approach to the EVSS-G/FEM, it was found that the convected derivative of the rate-of-strain derivative found in the constitutive equation causes the failure of the application of this method. The DEVSS-G/FEM does not have this term and can be successfully formulated in the θ method. It is for this reason that the DEVSS-G/FEM is recommended for all further viscoelastic flow

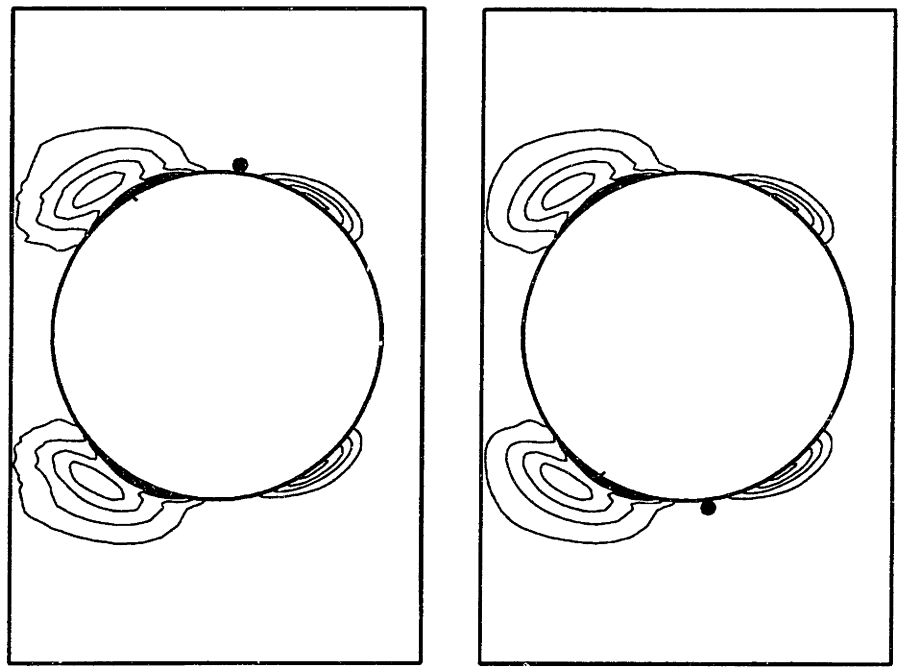

Figure 8-41: The contours of the yy-component of the configuration tensor for the nonlinear stability analysis as a function of time computed with the DEVSS-G/FEM and the θ-method at $We = 0.9$ and $\Delta t = 0.025$ for a CR-FENE fluid in a periodic linear array of cylinders in a channel. (a) $t = 9.9$ and (b) steady state.

calculations (Note: it is also easier to use complex viscoelastic constitutive equations in this formulation).

The θ-method was successfully implemented in this chapter to various nonlinear time dependent problems including startup flow calculations and nonlinear stability calculations for the CR-FENE constitutive equations. The startup of planar Couette flow gave the expected exponential form of the stress variables. The startup of flow through a linear periodic array of cylinders showed no time dependent solutions up to a $We = 3.0$; all calculations converged the steady-state solution found using the steady-state version of the DEVSS-G/FEM.

The nonlinear stability calculations of planar Couette flow confirmed the linear stability calculations of Chapter 7. The flow is stable up to at least a $De = 10.0$ and the results show a simple linear response decaying back to the steady-state solution. The nonlinear stability calculations for the flow through a linear periodic array of cylinders in a channel also confirmed the results of the linear stability calculations and

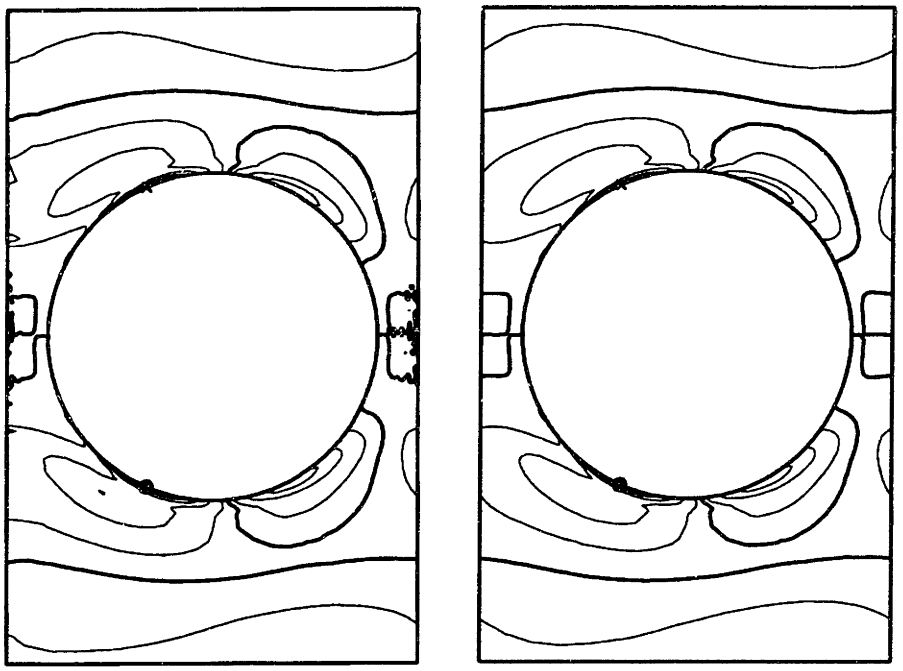

Figure 8-42: The contours of the yx-component of the configuration tensor for the nonlinear stability analysis as a function of time computed with the DEVSS-G/FEM and the θ-method at $We = 0.9$ and $\Delta t = 0.025$ for a CR-FENE fluid in a periodic linear array of cylinders in a channel. (a) $t = 9.9$ and (b) steady state.

the startup calculations. No time dependent solutions were found; the disturbance decays away leaving the original steady-state solution after approximately 10 -15 relaxation times.

This work represents the first successful implementation of a decoupled, iterative solver for viscoelastic flow calculations. The calculations for the flow through a linear periodic array of cylinders took roughly 18 minutes per time step (for time steps on the order 10^{-1}-10^{-2} relaxation times) on the HP9000 Series 735 workstation for approximately 40,000 unknowns. This is a reduction in the CPU time by a factor of approximately twenty over the fully implicit alternative. Furthermore, on DuPont's Cray-C90, the CPU time per time step was approximately 85-90 seconds, compared to an estimated 20 minutes for the fully implicit method. These timings on both the HP workstation and the Cray-C90 are approximately what is expected from operation count comparisons between the two methods and previous steady-state calculation experience with the two machines. Thus, this is a feasible method to calculate two-

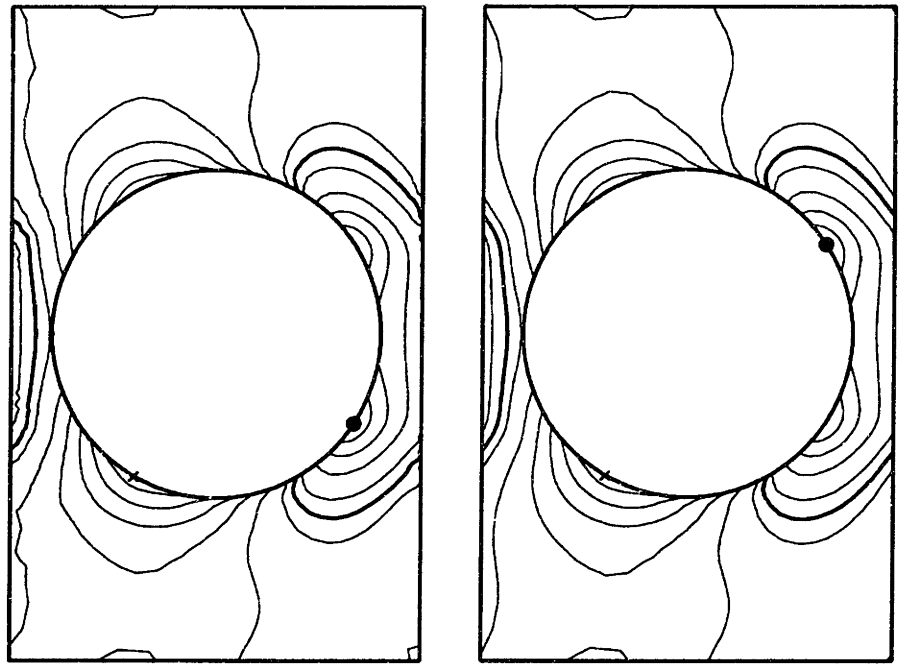

Figure 8-43: The contours of the pressure for the nonlinear stability analysis as a function of time computed with the DEVSS-G/FEM and the θ-method at $We = 0.9$ and $\Delta t = 0.025$ for a CR-FENE fluid in a periodic linear array of cylinders in a channel. (a) $t = 9.9$ and (b) steady state.

dimensional, time dependent viscoelastic flow calculations.

An upper time step limit for the convergence of the Newton iteration in the θ-method was found in agreement with Saramito (1994). This Δt_{crit} was found to be proportional to the maximum of the absolute value of the inverse of the velocity gradient ($\max \|1/\nabla \boldsymbol{v}\|$). For the calculations presented here, this time step limit was not critical since the required step sizes were still in the range of $10^{-1} - 10^{-2}$ relaxation times. However, if the gradient of the velocity became extremely large (for example at a singularity), then this limit might prohibitively decrease the time step required to solve the problem. This needs more study in the future both through numerical experimentation (implementation on a wider variety of problems) and theoretical work (what is the basis of this limit and can it be eliminated).

Chapter 9

Conclusions

"One of the most feared expressions in modern times is 'The Computer is down'. "

– Norman Augustine from Augustine's 94th Law, 1986

The goal of this thesis has been to simulate time dependent, two-dimensional viscoelastic flows accurately and in a feasible amount of computational time. This has required the use of a semi-implicit time integration method, the θ-method coupled with the DEVSS-G formulation of the governing viscoelastic flow equations.

The starting point for this thesis was the observations by Northey (1991) and Brown *et al.* (1993) that the time dependent formulations of the EEME/FEM and EVSS/FEM were linearly unstable. These two numerical methods had been previously shown by Brown and coworkers to be convergent with mesh refinement, numerically accurate and robust for the calculation of steady, two-dimensional viscoelastic flows for a number of benchmark geometries. steady-state calculations depend only on the real part of the eigenvalue governing the stability of the eigenvalue while time dependent simulations require both the real and imaginary parts to be stable. This is the reason the EEME/FEM and EVSS/FEM appeared to be stable algorithms for the simulation of viscoelastic flows when only the steady-state calculations were considered.

The linear stability of planar Couette flow with a UCM fluid was studied here because the behavior of the most dangerous eigenvalue and the structure of the eigenfunction are known in closed-form (Gorodtsov & Leonov, 1967). The calculation of the eigenvalue spectrum is a difficult numerical problem, since the most dangerous eigenvalue approaches neutral stability as De is increased and the eigenfunction develops a complex boundary layer structure in the cross-stream direction. This results in an excellent test problem for establishing the temporal stability of a numerical algorithm.

A fully implicit time integration scheme (first order Adams-Moulton) was used with the EEME/FEM and EVSS/FEM; therefore, any resulting instability is a result of the spatial discretization, not the temporal discretization of the numerical scheme employed. The numerical calculations revealed that the energy in the most dangerous disturbance is concentrated near the stationary streamline present in the flow geometry. At a stationary streamline, the zero velocity reduces the constitutive equation from a differential equation to an algebraic one. The algebraic equation consists of two variables, the elastic stress and the velocity gradient; this fact led to the conclusion that the numerical instability was related to the compatibility of the finite element spaces between these two variables. Both the EEME and EVSS algorithms used biquadratic Lagrangian elements for the stress variable and discontinuous bilinear Lagrangian elements for the velocity gradient. Obviously, these do not appear to be consistent.

Two new numerical methods were constructed based on the above observations: the EVSS-G and DEVSS-G methods. The EVSS-G formulation is similar to the EVSS formulation except that it uses an independent interpolation of the components of the velocity gradient tensor instead of the rate-of-strain tensor and bilinear basis functions for the stress tensor instead of biquadratic basis functions. This new construction gives compatible approximates for both the velocity gradient and the elastic stress on stationary streamlines. The DEVSS-G formulation begins similar to the EVSS-G formulation except the elastic stress is not substituted into the constitutive equations resulting in a much simpler formulation for complex, nonlinear constitutive models

such as the CR-FENE model; this formulation also eliminates the introduction of the upper convected derivative of the rate-of-strain tensor which will become important in the formulation of the θ-method. The same modifications to the EVSS formulation to result in the EVSS-G formulation are also made for this method to ensure the compatibility of the stress variable and the velocity gradient.

The linear stability of the EVSS-G/FEM was tested on the planar Couette geometry using the streamline upwind Petrov-Galerkin (SUPG), streamline upwinding (SU), and the Galerkin least squares (GLS) hyperbolic equation solvers. Each appears to improve the numerical stability compared to the original EVSS mixed finite element method. In the two cases, EVSS-G/SUPG and EVSS-G/SU, no upper bound was found for the loss of stability in the planar Couette flow analysis up to at least $De = 200.0$. The DEVSS-G/FEM with the SUPG method also had no loss of stability up to $De = 100.0$. There is little doubt the stability goes even higher; the calculations were stopped only due to the extremely long computational times required to show stability at very high De. Because no stability limit was identified with these methods, the idea of Keiller (1992) that the onset of numerical instability, as seen in his finite difference discretizations, was connected to the poor cross-stream resolution relative to the streamwise direction could not be tested in our calculations with the EVSS-G and DEVSS-G methods. It is possible the instability exists at higher values of De. Alternatively, the numerical results of Keiller (1992) may also be caused by the application of incompatible finite difference approximations between the velocity gradient and stress variables and would disappear with the proper discretization.

As briefly mentioned above, it is important to note at this point that two numerical methods, EEME/FEM and EVSS/FEM, which were believed to be well characterized for steady-state calculations in terms of convergence with mesh refinement, numerical accuracy and robustness, are *temporally unstable*! The positive eigenvalue is still present in the steady-state case, but its effect is not felt because it is complex. It is only in the time dependent problem that the impact of the discrete spectra is felt. The linear stability calculation is the main test to determine if a time dependent algorithm is numerically stable, although it is rarely performed. The EEME/FEM

and EVSS/FEM are two examples where this test is necessary because the formulation produces spurious results due to a problem in the spatial discretization which could not be found solely through the examination of steady-state calculations.

At this time, a mathematical proof pinpointing the reason for the failure of either the EEME/FEM or the EVSS/FEM or the apparent success of the EVSS-G/FEM and DEVSS-G/FEM does not exist. This thesis has relied on computational observations and heuristic arguments (e.g., the inconsistency of the stress variable and the velocity gradient at zero streamlines) to draw conclusions. Future work may lead to a deeper understanding of the exact reasons for these observations and will lead to the development of "better" and more optimal numerical methods to solve the time dependent viscoelastic flow equations.

After showing that the two new numerical formulations were linearly stable, the accuracy, convergence with mesh refinement and the robustness was demonstrated by the solution of various benchmark steady-state calculations in Chapter 6. These calculations were performed using both regular mesh refinement and local mesh refinement; the local mesh refinement allows the solution of problems where steep velocity and/or stress gradients would become too expensive if uniform refinement were utilized. The EVSS-G/FEM was extensively characterized using the flow of an UCM fluid in the eccentric cylinder geometry which is a well-established benchmark problem in viscoelastic flow simulation. The method was shown to be convergent with mesh refinement as well as accurate with respect to previous calculations, namely, the EVSS/FEM. The second test problem consisted of the flow of a CR-FENE fluid through an infinite periodic linear array of cylinders in a channel. The DEVSS-G/FEM was shown to give practically identical results to the EVSS-G/FEM. Some other steady-state problems used by various members of our research group at MIT were also summarized.

In the future, the DEVSS-G/FEM will be the preferred method due to its simplicity in the formulation with various, often complex rheological models. Also, flow problem which incorporate inflow and outflow boundaries will have to be examined, rather than the artificially simple periodic geometries examined in this thesis. This

incorporation of different boundary conditions does not affect the algorithm itself only the implementation of it to various flow geometries which are encountered.

Chapter 6 includes a comparison between calculations made with the SUPG and SU methods for solving hyperbolic differential equations. As has been found previously in the literature, the accuracy of the calculations using streamline upwinding diverged from the SUPG results beyond a critical critical value of De for a given mesh. Although the calculations converge, the results can become meaningless as further mesh refinement shows that the calculations approach those of the SUPG method for the smaller mesh. Thus, SU should be used with extreme caution.

Local mesh refinement can lead to highly irregular meshes which makes convergence with mesh refinement difficult to show; indeed for the periodic array of cylinders, no attempt was made to show convergence with mesh refinement. Uniformly increasing the discretization to uniformly change the characteristic mesh size would result in problems whose shear size would quickly become unmanageable even on today's supercomputers. An alternative approach that has much potential for solutions utilizing local mesh refinement is the use of local error indicators, such as elemental momentum and continuity balances. These would allow for a systematic assessment of the need for local mesh refinement of the solution with a given level of error on an elemental level. This technique has not received much attention in the viscoelastic flow simulation literature, but with the increasing use of local mesh refinement will become necessary to incorporate consistent standards of error management in different numerical algorithms.

To more accurately model real polymeric systems, multi-mode constitutive models are necessary. Due to the use of linear Lagrangian basis functions for the stress variable instead of the biquadratic basis functions used in the EVSS/FEM, the EVSS-G/FEM and DEVSS-G/FEM will enjoy a considerable savings in CPU time when multi-mode models are introduced.

The new methods will also extend fairly easily to three-dimensional flows, where the application of trilinear stress approximations will considerably simplify the calculations. The remaining problems with regards to three-dimensional simulations now

lie in the computational procedures used to solve the viscoelastic equations, not in the inherent problems with the formulation of the equations. Currently, the EVSS-G/FEM and the DEVSS-G/FEM are solved sequentially using a frontal method. Switching to block-preconditioned Krylov-based iterative methods will increase the size of the problems that can be handled while switching to a parallel implementation will significantly decrease the CPU time required to solve the equation set.

These new ways to solve the set of equations becomes extremely important for the time dependent problem which can be seen in its simplest form as the solution of n steady-state problems to advance from t_i to t_f in n steps of length Δt. This is especially true of the linear stability calculations of Chapter 7 for problems with no known solution. This fact made the similar solution of the nonlinear time dependent problem by a fully implicit problem computationally not feasible. In Section 8.1 it was estimated that approximately 1,800 hours (75 days) of CPU time would be necessary to take 600 time steps using an HP9000 Series 735 workstation for the periodic cylinder problem examined in this thesis. Switching to a Cray-C90 would not help much, since it is roughly an order-of-magnitude faster than the HP workstation. This led to a search for other possible methods to solve time dependent problems such as the implemented θ-method.

The θ-method was successfully implemented in Chapter 8 to various nonlinear time dependent problems including startup flow calculations and nonlinear stability calculations for the CR-FENE constitutive equations. Using this method it was shown that no time dependent solution exists for the problem up to a $We = 3.0$. This was a disappointing result because the numerical algorithm represents the first implementation of a decoupled, iterative solver for viscoelastic flow calculations. The calculations for the flow through a linear periodic array of cylinders took roughly 18 minutes per time step (for time steps on the order 10^{-1}-10^{-2} relaxation times) on the HP9000 Series 735 workstation for approximately 40,000 unknowns. This is a reduction in the CPU time by a factor of approximately twenty over the fully implicit alternative. Furthermore, on DuPont's Cray-C90, the CPU time per time step was approximately 85-90 seconds. These timings on both the HP workstation and the

Cray-C90 are approximately what is expected from operation count comparisons between the two methods (a savings of fifteen was expected) and previous steady-state calculation experience with the two machines (savings of 10-15 between the two machines). Thus, this is a feasible method to calculate two-dimensional, time dependent viscoelastic flow calculations.

An upper time step limit for the convergence of the Newton iteration in the θ-method was found for the calculations involving the flow through a periodic array of cylinders, but not for the planar Couette flow geometry calculations. This Δt_{crit} was discussed by Saramito (1994) and was found to be proportional to the maximum of the absolute value of the inverse of the velocity gradient ($\max \|1/\nabla \boldsymbol{v}\|$). For the calculations presented here, this time step limit was not critical, since the required step sizes were still in the range of $10^{-1} - 10^{-2}$ relaxation times. However, it is possible for this limit to become prohibitive if the gradient of the velocity became extremely large (for example at a singularity). Further numerical experimentation is needed with the θ-method to determine why the limit was found in the periodic array of cylinders geometry, but not for the simpler planar Couette geometry. It should be possible to examine the derivation of this Δt_{crit} and possibly eliminate it.

The time dependent finite element algorithm developed in this thesis using the DEVSS-G formulation of the viscoelastic flow equations and the θ-method to integrate forward in time can now be used with confidence that the resulting numerical solutions will be an accurate representation of the equations being solved. Recent experimental results have shown that there is a wide variety of instabilities that appear to be purely elastic in nature (i.e., they occur even when the Re is negligible). This numerical algorithm can be utilized to help develop an understanding of the causes of these instabilities. Several examples immediately come mind: the Taylor Couette problem, flow past a cylinder, flow past a sphere, flow past several cylinders or spheres and fiber spinning or extrusion flows.

The Taylor Couette problem has been examined in the literature and may be a good starting point to continue this research, since a well-characterized instability to time dependent flow exists. This would enable the algorithm to be further char-

acterized on a known instability problem. The cylinder and sphere problems may not be good problems to examine because the experimental evidence indicates that the instability is three-dimensional and/or time dependent; a two dimensional, time instability has not been observed. This brings us to the fiber spinning problem. Axisymmetric extrusion flows could be a perfect situation for the examination of two dimensional time dependent flows, as they are known to exist experimentally. Furthermore, with the characterization of the steady-state flow by Salamon (1995) with the use of 40,000-100,000 unknowns, this problem also fits into the size range at which the developed method should function well.

Bibliography

[1] F.P.T. Baaijens. Numerical analysis of start-up planar and axisymmetric flows using multi-mode differential constitutive models. *J. Non-Newtonian Fluid Mech.*, 48:147–180, 1993.

[2] F.P.T. Baaijens. Numerical experiments with a discontinuous galerkin method including monotonicity enforcement on the stick-slip problem. *J. Non-Newtonian Fluid Mech.*, 51:141–159, 1994a.

[3] F¿P¿T¿ Baaijens. Application of low-order discontinuous galerkin methods to the analysis of viscoelastic flows. *J. Non-Newtonian Fluid Mech.*, 52:37–57, 1994b.

[4] F.P.T. Baaijens. Application of Galerkin-Least-Squares related methods to the mixed formulation of steady viscoelastic flow. *J. Non-Newtonian Fluid Mech.*, submitted.

[5] I. Babuska. The finite element method with Lagrange multipliers. *Numer. Math.*, 35:179–192, 1973.

[6] J. Baranger and D. Sandri. Approximation par finis d'ecoulements de fluides viscoelastiques: Existence de solutions approchees er majoration d'erreur. I. Constraintes discontinues. *C.R. Acad. Sci. Paris, Serie I*, 312:541–544, 1991.

[7] J. Baranger and D. Sandri. Approximation par finis d'ecoulements de fluides viscoelastiques: Existence de solutions approchees er majoration d'erreur. II. Constraintes continues. *C.R. Acad. Sci. Paris, Serie I*, 313(111-114), 1991.

[8] J.T. Beale and A. Majda. Rates of convergence for viscous splitting of the navier-stokes equations. *Math. Comput.*, 37(156):243–259, 1981.

[9] E.B. Becker, G.F. Carey, and J.T. Oden. *Finite Elements: An Introduction*, volume I. Prentice-Hall, Inc., Englewood-Cliffs, NJ, 1981.

[10] L.E. Becker and G.H. McKinley. The unsteady motion of a sphere falling through a viscoelastic liquid. In *64th Annual Meeting of the Society of Rheology*, Santa Barbara, CA, February 1993.

[11] A.N. Beris, R.C. Armstrong, and R.A. Brown. *J. Non-Newtonian Fluid Mech.*, 13:109–148, 1983.

[12] A.N. Beris, R.C. Armstrong, and R.A. Brown. Finite-element/spectral calculations of the flow of a Maxwell fluid between eccentric rotating cylinders. *J. Non-Newtonian Fluid Mech.*, 22:129–167, 1987.

[13] A.N. Beris, M. Avgousti, and A. Souvaliotis. Spectral calculations of viscoelastic flows: Evaluation of the Giesekus constitutive equation in model flow problems. *J. Non-Newtonian Fluid Mech.*, 44:197–228, 1992.

[14] R.B. Bird and C.F. Curtiss. Fascinating polymeric liquids. *Physics Today*, 37:36–43, Jan. 1984.

[15] R.B. Bird, R.C.Armstrong, and O. Hassager. *Dynamics of Polymeric Liquids*, volume 1. John Wiley & Sons, New York, 1987.

[16] R.B. Bird, W.E. Stewart, and E.N. Lightfoot. *Transport Phenomena.* John Wiley & Sons, New York, 1960.

[17] C. Bisgaard. Velocity fields around spheres and bubbles investigated by laser-doppler anemometry. *J. Non-Newtonian Fluid Mech.*, 12:282–302, 1983.

[18] D.V. Boger. Viscoelastic flows through contractions. *Ann. Rev. Fluid Mech.*, 19:157–182, 1987.

[19] K.E. Brenan, S.L. Campbell, and L.R. Petzold. *Numerical Solution of Initial-Value Problems in Differential-Algebraic Equations.* North-Holland, New York, 1989.

[20] F. Brezzi. On the existence, uniqueness, and approximation of saddle-point problems arising from Lagrangian multipliers. *Revue Francaise d'Automatique, Informatique et Recherche Operationnelle*, 2:199–259, 1974.

[21] M.O. Bristeau, R. Glowinski, B. Mantel, J. Periaux, and P. Perrier. Numerical methods for incompressible and compressible navier-stokes problems. In R.H. Gallagher, G.F. Carey, J.T. Oden, and O.C. Zienkiewicz, editors, *Finite Elements in Fluids — Volume 6*, pages 1–40. John Wiley, Boston, 1985.

[22] M.O. Bristeau, R. Glowinski, and J. Periaux. Numerical methods for the navier-stokes equations. applications to the simulation of compressible and incompressible viscous flows. *Comput. Phys. Rep.*, 6:73–187, 1987.

[23] A.N. Brooks and T.J.R. Hughes. Streamline Upwind/Petrov Galerkin formulations. *Comp. Meths. Appl. Mech. Engng.*, 32:199–259, 1982.

[24] R.A. Brown, M.J. Szady, P.J. Northey, and R.C. Armstrong. On the numerical stability of mixed finite element methods for viscoelastic flows governed by differential constitutive equations. *Theor. and Comp. Fluid Dynamics*, 5:77–106, 1993.

[25] P. Brunn. Interaction of spheres in a viscoelastic fluid. *Rheol. Acta*, 16(5):461–475, 1977.

[26] S. Burdette, P.J. Coates, R.C. Armstrong, and R.A. Brown. lculations of viscoelastic flow through an axisymmetric corrugated tube using the explicitly elliptic momentume equation formulation (eeme). *J. Non-Newtonian Fluid Mech.*, 33:1–23, 1989.

[27] J.A. Byars, A. Oztekin, A.W. Liu, R.C. Armstrong, and R.A. Brown. in preparation.

[28] G.F. Carey and J.T. Oden. *Finite Elements: A Second Course*, volume II. Prentice-Hall, Inc., Englewood Cliffs, NJ, 1983.

[29] G.F. Carey and J.T. Oden. *Finite Elements: Computational Aspects*, volume III. Prentice-Hall, Inc., Englewood Cliffs, NJ, 1984.

[30] G.F. Carey and J.T. Oden. *Finite Elements: Fluid Mechanics*, volume VI. Prentice-Hall, Inc., Englewood Cliffs, NJ, 1986.

[31] G.F. Carrier and C.E. Pearson. *Partial Differential Equations: Theory and Tecchnique.* Academic Press, New York, 1976.

[32] M.D. Chilcott and J.M. Rallison. Creeping flow of dilute polymer solutions past cylinders and spheres. *J. Non-Newtonian Fluid Mech.*, 29:381–432, 1988.

[33] C. Chinnaswamy, B. Amadei, and T.H. Illangasekare. A new method for finite element transitional mesh generation. *Int. J. Numer. Methods Fluids*, 31:1253–1270, 1991.

[34] C. Chmielewski and K. Jayaraman. *J. Non-Newtonian Fluid Mech.*, 48:285–301, 1993.

[35] P.J. Coates. *Simulation of the Flow of Viscoelastic Fluids in Contraction Geometries.* PhD thesis, MIT, 1992a.

[36] P.J. Coates, R.C. Armstrong, and R.A. Brown. Calculation of steady-state viscoelastic flow through axisymmetric contractions with the EEME formulation. *J. Non-Newtonian Fluid Mech.*, 42:141–188, 1992b.

[37] P. Colella and P. Woodward. The piecewise-parabolic method (ppm) for gas-dynamical simulations. *J. Comput. Phys.*, 54:174–201, 1984.

[38] M. Crochet and V. Legat. The consistent streamline-upwind/petrov galerkin method for viscoelastic flow revisited. *J. Non-Newtonian Fluid Mech.*, 42:283–299, 1990.

[39] M.J. Crochet, A.R. Davies, and K. Walters. *Numerical Simulation of Non-Newtonian Flow.* Elsevier, Amsterdam, 1984.

[40] G. Dahlquist, A. Bjorck, and N. Anderson. *Numerical Methods.* Prentice-Hall, Inc., Englewood Cliffs, NJ, 1974.

[41] A.R. Davies and J. Devlin. On corner flows of oldroyd-b fluids. *J. Non-Newtonian Fluid Mech.*, 50:173–191, 1993.

[42] C.C. de Souza, R. Keunings, L.A. Wolsey, and O. Zone. A new approach to minimising the frontwidth in finite element calculations. *Comput. Methods Appl. Mech. Eng.*, 111:323–334, 1994.

[43] F. Debae, V. Legat, and M. Crochet. Practical evaluation of our mixed finite element methods for viscoelastic flow. *J. Rheol.*, 38:421–442, 1994.

[44] B. Debbaut and M.J. Crochet. Further results on the flow of a viscoelastic flow through an abrupt contraction. *J. Non-Newtonian Fluid Mech.*, 20:173–185, 1986.

[45] G.C. Everstine. A comparison of three resequencing algorithms for the reduction of matrix profile and wavefront. *Int. J. Numer. Methods Eng.*, 14:837–853, 1979.

[46] E. Fernandez-Cara and M.M. Beltran. The convergence of two numerical schemes for the navier-stokes equations. *Numer. Math.*, 55:33–60, 1989.

[47] M. Fortin and D. Esselaoui. A finite element procedure for viscoelastic flows. *Int. J. Numer. Meths. Fluids*, 7:1035–1052, 1987.

[48] M. Fortin and R. Glowinski. *Augmented Lagrangian Methods: Applications to the Numerical Solution of Boundary-Value Problems.* Elsevier Science, New York, 1983.

[49] M. Fortin and R. Pierre. On the convergence of the mixed method of crochet and marchal for viscoelastic flows. *Comp. Math. Appl. Mech. Eng.*, 73:341–350, 1989.

[50] M. Fortin and A. Zine. *J. Non-Newtonian Fluid Mech.*, 42:1–18, 1990.

[51] L.P. Franca and E.G. Dutra Do Carmo. The galerkin gradient least-squares method. *Comput. Meth. Appl. Mech. Eng.*, 74:41–54, 1989.

[52] L.P. Franca, S.L. Frey, and T.J.R. Hughes. Stabilized finite element methods: I. Application to the advective-diffusive model. *Comp. Meths. Appl. Mech. Engng.*, 95:253–276, 1992.

[53] C.W. Gear. *Numerical Initial Value Problems in Ordinary Differential Equations.* Prentice-Hall, Inc., Englewood Cliffs, NJ, 1971.

[54] G.C. Georgiou and M. Crochet. The simultaneous use of 4x4 and 2x2 bilinear stress elements for viscoelastic flows. *J. Comput. Mech.*, 11:341–354, 1993.

[55] N.E. Gibbs. Algorithm 509: A hybrid profile reduction algorithm. *ACM Trans. Mathe. Soft.*, 2(4):378–387, 1976.

[56] N.E. Gibbs, Jr. W.G. Poole, and P.K. Stockmayer. An algorithm for reducing the bandwidth and profile of a sparse matrix. *SIAM J. Numer. Anal.*, 13:236–250, 1976.

[57] N.E. Gibbs, Jr. W.G. Poole, and P.K. Stockmayer. A comparison of several bandwidth and profile reduction algorithms. *ACM Trans. Mathe. Soft.*, 2(4):322–330, 1976.

[58] R. Glowinski. Viscous flow simulation by finite element methods and related numerical techniques. In E.M. Murman and S.S. Arbanel, editors, *Progress and Supercomputing in Computational Fluid Dynamics*, pages 173–210. Birkhauser, Boston, 1984.

[59] R. Glowinski. Splitting methods for the numerical solution of the incompressible navier-stokes equations. In A.V. Balakrishnan, A.A. Dorodnitsyn, and J.L. Lions, editors, *Vistas in Applied Mathematics*, pages 57–95. Optimization Software, Inc., New York, 1986.

[60] R. Glowinski. Supercomputing and the finite element approximation of the navier-stokes equations for incompressible viscous fluids. In C.C. Chao and S.A. Orszag, editors, *Recent Advances in Computational Fluid Dynamics*, pages 277–315. Springer-Verlag, New York, 1988.

[61] R. Glowinski and P. LeTallec. *Augmented Lagrangian and Operator Splitting Methods in Nonlinear Mechanics.* SIAM, Philadelphia, 1989.

[62] R. Glowinski and O. Pironeau. Finite element methods for navier-stokes equations. *Annual Rev. Fluid Mech.*, 24:167–204, 1992.

[63] J.B. Goodman and R.J. LeVeque. On the accuracy of stable schemes for 2d scalar conservation laws. *Math. Comput.*, 45:15–21, 1985.

[64] J.B. Goodman and R.J. LeVeque. A geometric approach to high resolution tvd schemes. *SIAM J. Numer. Anal.*, 25(2):268–284, 1988.

[65] V.A. Gorodtsov and A.I. Leonov. On a linear instability of plane parallel Couette flow of viscoelastic fluid. *PNN*, 31:289–299, 1967.

[66] R. Guenette and M. Fortin. A new mixed finite element method for computing viscoelastic flows. *J. Non-Newtonian Fluid Mech.*, 60:27–52, 1995.

[67] C. Guillope and J.C. Saut. *Nonlinear Analysis, Theory, Meth. & Appl.*, 15:849–869, 1990.

[68] A.K. Gupta. A finite element for transition from a fine to a coarse grid. *Int. J. Numer. Methods Eng.*, 12:35–45, 1978.

[69] J. Happel and H. Brenner. *Low Reynolds Number Hydrodynamics.* Kluwer Academic Publishers, Boston, 1991.

[70] A. Harten, B. Engquist, S. Osher, and S.R. Chakravarthy. Uniformly high order accurate essentially non-oscillatory schemes, iii. *J. Comput. Phys.*, 71:231–303, 1987.

[71] A. Harten and S. Osher. Uniformly high-order accurate nonoscillatory schemes. i. *SIAM J. Num. Anal.*, 24:279–309, 1987.

[72] O. Hassager. Negative wake behind bubbles in non-Newtonian liquids. *Nature*, 279:402–403, 1979.

[73] O. Hassager. Working group on numerical techniques. *J. Non-Newtonian Fluid Mech.*, 29:2–5, 1988.

[74] P.C. Hiemenz. *Polymer Chemistry.* Marcel Dekker, Inc., New York, 1984.

[75] E.J. Hinch. The flow of an oldroyd fluid around a sharp corner. *J. Non-Newtonian Fluid Mech.*, 50:161–171, 1993.

[76] E. Hinton and J.S. Campbell. *Int. J. Numer. Meths. Eng.*, 8:461–480, 1974.

[77] Jr. H.L. Crane, N.E. Gibbs, Jr. W.G. Poole, and P.K. Stockmeyer. Algorithm 508: Matrix bandwidth and profile reduction. *ACM Trans. Mathe. Soft.*, 2(4):375–377, 1976.

[78] P. Hood. Frontal solution program for unsymmetric matrices. *Int. J. Numer. Meth. Eng.*, 10:379–399, 1976.

[79] T.J.R. Hughes and L.P. Franca. A new finite element formulation for computational fluid dynamics: VII. The Stokes problem with various well-posed boundary conditions: Symmetric formulations that converge for all velocity/pressure spaces. *Comp. Meths. Appl. Mech. Engng.*, 65:85–96, 1987.

[80] T.J.R. Hughes, L.P. Franca, and M. Balestra. A new finite element formulation for computational fluid dynamics: V. Circumventing the Babuska-Brezzi condition: A stable Petrov-Galerkin formulation of the Stokes problem accomodating equal-order interpolations. *Comp. Meths. Appl. Mech. Engng.*, 59:85–99, 1986.

[81] T.J.R. Hughes, L.P. Franca, and G.M. Hulbert. A new finite element formulation for computational fluid dynamics. VIII. The Galerkin least-squares method

for advective-diffusive equations. *Comp. Meths. Appl. Mech. Engng.*, 73:173–189, 1989.

[82] T.J.R. Hughes and M. Mallet. A new finite element formulation for computational fluid dynamics: IV. A discontinuity -capturing operator for multidimensional advective-difussive systems. *Comp. Meths. Appl. Mech. Engng.*, 58:329–336, 1986.

[83] G. Iooss and D.D. Joseph. *Elementary Stability and Bifurcation Theory.* Undergraduate Texts in Mathematics. Springer-Verlag, New York, second edition, 1990.

[84] Jr. J. Douglas and J. Wang. An absolutely stabilized finite element method for the Stokes problem. *Math. Comp.*, 52(186):495–508, April 1989.

[85] F. John. *Partial Differential Equations.* Applied Mathematical Sciences, vol. 1. Springer-Verlag, New York, fourth edition, 1982.

[86] C. Johnson. *Numerical Solution of Partial Differential Equations by the Finite Element Method.* Cambridge University Press, New York, 1987.

[87] C. Johnson, U. Navert, and J. Pitkaranta. Finite element methods for linear hyperbolic problems. *Comp. Meths. Appl. Mech. Engng.*, 45:285–312, 1984.

[88] D.D. Joseph, M. Renardy, and J.C. Saut. Hyperbolicity and change of type in the flow of viscoelastic fluids. *Arch. Rat. Mech.*, 87(213-251), 1985.

[89] R.A. Keiller. *Non-Newtonian Extensional Flows.* PhD thesis, University of Cambridge, 1991.

[90] R.A. Keiller. Numerical instability of time dependent flows. *J. Non-Newtonian Fluid Mech.*, 43:229–246, 1992.

[91] R. Keunings. On the high Weissenberg number problem. *J. Non-Newtonian Fluid Mech.*, 20:209–226, 1986.

[92] B. Khomami, K.K. Talwar, and H.K. Gupta. *J. Rheol.*, 38:255–289, 1994.

[93] R.C. King. *Stable and Convergent Finite Element Methods for the Calculation of Viscoelastic Flows in Smooth Geometries.* PhD thesis, MIT, 1987.

[94] R.C. King, M.R. Apelian, R.C. Armstrong, and R.A. Brown. Numerically stable finite-element methods for solution of steady viscoelastic flows. *J. Non-Newtonian Fluid Mech.*, 29:147–216, 1988.

[95] P. Kloucek and F.S. Rys. Stability of the fractional step θ-scheme for the nonstationary navier-stokes equations. *SIAM J. Numer. Anal.*, 31:1312–1335, 1994.

[96] L.G. Leal. The motion of small particles in non-Newtonian fluids. *J. Non-Newtonian Fluid Mech.*, 5:33–78, 1979.

[97] G. Leborgne. *Simulation numerique d'ecoulements de fluides viscoelastiques de type Oldroyd: Utilisation d'elements finis de degre 1.* PhD thesis, Ecole Polytechnique, 1992.

[98] G. Leborgne, 1993. private communication.

[99] K. Lee and B.A. Finlayson. Stability of plane Poiseuille flow and Couette flow of a Maxwell fluid. *J. Non-Newtonian Fluid Mech.*, 21:65–78, 1986.

[100] R.J. LeVeque and J. Oliger. Numerical methods based on additive splittings for hyperbolic partial differential equations. *Math. Comput.*, 40(162):469–497, 1983.

[101] J.G. Lewis. Algorithm 582: The gibbs-poole-stockmeyer and gibbs-king algorithms for reordering sparse matrices. *ACM Trans. Mathe. Soft.*, 8(2):190–194, 1982.

[102] J.G. Lewis. Implementation of the gibbs-poole-stockmeyer and gibbs-king algorithms. *ACM Trans. Mathe. Soft.*, 8(2):180–189, 1982.

[103] A.W. Liu, R.C. Armstrong, and R.A. Brown. *in preparation*, 1995.

[104] W.J. Lunsmann, L. Genieser, R.C. Armstrong, and R.A. Brown. Finite element analysis of steady viscoelastic flow around a sphere in a tube: Calculations with constant viscosity models. *J. Non-Newtonian Fluid Mech.*, 48:63–100, 1993.

[105] A. Maalouf and D. Sigli. Effects of body shape and viscoelasticity on the slow flow around an obstacle. *Rheol. Acta*, 23:497–507, 1984.

[106] J.M. Marchal and M.J. Crochet. A new mixed finite element method for calculating viscoelastic flow. *J. Non-Newtonian Fluid Mech.*, 26:77–114, 1987.

[107] G.I. Marchuk. *Methods of Numerical Mathematics.* Springer-Verlag, New York, 1975.

[108] G.H. McKinley. *Nonlinear Dynamics of Viscoelastic Flows in Complex Geometries.* PhD thesis, MIT, 1990.

[109] G.H. McKinley, R.A. Brown, and R.C. Armstrong. *Phil. Trans. Roy. Soc. Lond.*, 344A:265–304, 1993.

[110] G.H. McKinley, A. Oztekin, J.A. Byars, and R.A. Brown. Self-similar spiral instabilities in elastic flows between a cone and a plate. *J. Fluid Mech.*, 285:123–164, 1995.

[111] M.A. Mendelson, P.-W. Yeh, R.A. Brown, and R.C. Armstrong. Approximation error in finite element calculation of viscoelastic fluid flows. *J. Non-Newtonian Fluid Mech.*, 10:31–54, 1982.

[112] J. Michele, R. Patzold, and R. Donis. Alignment and aggregation effects in suspensions of spheres in non-Newtonian media. *Rheol. Acta*, 16:317–321, 1977.

[113] M.O.Bristeau, O. Pironneau, R. Glowinski, J. Periaux, and P. Perrier. On the numerical solution of nonlinear problems in fluid dynamics by least squares

and finite element methods: (i) least squares formulations and conjugate gradient solution of the continuous problems. *Comput. Meth. Appl. Mech. Eng.*, 17/18:619–657, 1979.

[114] S.J. Muller. *Experimental Analysis of Flow Through an Axisymmetric Sudden Contraction: Rheological Characterization and LDV Measurements.* PhD thesis, MIT, 1986.

[115] P.J. Northey. *Numerical Simulation of Time-Dependent, Two-Dimensional Viscoelastic Fluid Flows.* PhD thesis, MIT, 1991.

[116] P.J. Northey, R.C. Armstrong, and R.A. Brown. Finite element calculations of time-dependent flows of an Upper-Convected Maxwell fluid using the EEME formulation. *J. Non-Newtonian Fluid Mech.*, 36:109–134, 1990.

[117] P.J. Northey, R.C. Armstrong, and R.A. Brown. Finite amplitude time-periodic states in viscoelastic Taylor-Couette flow of a UCM fluid. *J. Non-Newtonian Fluid Mech.*, 42:117–140, 1992.

[118] J.T. Oden and H.J. Brauchli. *Int. J. Numer. Meth. Eng.*, 3:317–325, 1971.

[119] J.T. Oden and J.N. Reddy. Note on an approximate method for computing consistent conjugate stresses in elastic finite elements. *Int. J. Numer. Meth. Eng.*, 6:55–61, 1973.

[120] J.G. Oldroyd. An approach to Non-Newtonian fluid mechanics. *J. Non-Newtonian Fluid Mech.*, 14:9–46, 1984.

[121] S. Osher and S. Chakravarthy. High resolution schemes and the entropy condition. *SIAM J. Numer. Anal.*, 21:984–995, 1984.

[122] D. Peaceman and H. Rachford. The numerical solution of parabolic and elliptic differential equations. *J. SIAM*, 3:28–41, 1955.

[123] B. Perry, P. Bar-Yoseph, and G. Rosenhouse. Towards adaptive mesh refinement: application of new rectangular hybrid finite elements in 2d elasticity problems. *Int. J. Numer. Methods Eng.*, 30:473–489, 1990.

[124] N. Phan-Thien. Stagnation flows for the Oldroyd-B fluid. *Rheol. Acta*, 23:172–176, 1984.

[125] S. Pilitsis and A. N. Beris. Calculations of steady-state viscoelastic flow in an undulating tube. *J. Non-Newtonian Fluid Mech.*, 31:231–287, 1989.

[126] L.M. Quinzani, G.H. McKinley, R.A.Brown, and R.C.Armstrong. Modelling the rheology of polyisobutylene solutions. *J. Rheol.*, 34:705–748, 1989.

[127] W.P. Raiford. *Laser Doppler Velocimetry Measurements of Nonlinear Flow Transitions in the Axisymmetric Sudden Contraction.* PhD thesis, MIT, 1988.

[128] G.D. Raithby. Skew upstream differencing schemes for problems involving fluid flow. *Comp. Meths. Appl. Mech. Engng.*, 9:153–164, 1976.

[129] D. Rajagopalan. *Convergent Finite-Element Calculation of Steady, Viscoelastic Flow Using Nonlinear, Multimode Constitutive Models.* PhD thesis, MIT, 1991.

[130] D. Rajagopalan, R.C. Armstrong, and R.A. Brown. Finite element analysis of viscoelastic flow of a multi-mode Maxwell model: Application of EEME formulation. *J. Non-Newtonian Fluid Mech.*, 36:135–158, 1990a.

[131] D. Rajagopalan, R.C. Armstrong, and R.A. Brown. Finite element methods for calculations of steady, viscoelastic flow using constitutive equations with a Newtonian viscosity. *J. Non-Newtonian Fluid Mech.*, 36:159–192, 1990b.

[132] D. Rajagopalan, J.A. Byars, R.C. Armstrong, R.A. Brown, J.S. Lee, and G.G. Fuller. Comparison of numerical simulations and birefringence measurements in viscoelastic flow between eccentric rotating cylinders. *J. Rheol.*, 36:1349–1375, 1992a.

[133] D. Rajagopalan, R. Phillips, R.C. Armstrong, R.A. Brown, and A. Bose. The influence of viscoelasticity on the existence of steady solutions in two-dimensional rimming flow. *J. Fluid Mech.*, 235:611–642, 1992b.

[134] S.C. Reddy and D.S. Henningson. Energy growth in viscous channel flow. *J. Fluid Mech.*, 252:209–238, 1993.

[135] S.C. Reddy, P.J. Schmid, and D.S. Henningson. Pseudospectra of the orr-sommerfeld operator. submitted to *SIAM J. Appl. Mathe.*, 1992. preprint.

[136] S.C. Reddy and L.N. Trefethen. Pseudospectra of the convection-diffusion operator. *SIAM J. Appl. Mathe.*, 54(6):1634–1649, 1994.

[137] G. Rekers. *Numerical Simulation of Unsteady Viscoelastic Flow of Polymers.* PhD thesis, Universiteit Twente, 1995.

[138] M. Renardy. Existence of slow steady flows of viscoelastic fluids with differential constitutive equations. *Z. Angew. Math. u. Mech.*, 65:449–451, 1985.

[139] M. Renardy. Inflow boundary conditions for viscoelastic fluids with differential constitutive laws. *J. Non-Newtonian Fluid Mech.*, 29:11–24, 1988.

[140] M. Renardy. How to integrate the upper convected maxwell (ucm) stresses near a singularity (and maybe elsewhere, too). *J. Non-Newtonian Fluid Mech.*, 52:91–95, 1994.

[141] M. Renardy, W.J. Hrusa, and J.A. Nohel. *Mathematical Problems in Viscoelasticity.* Longmans Scientific and Technical Press, New York, 1987.

[142] M. Renardy and Y. Renardy. Linear stability of plane Couette flow of an upper convected Maxwell fluid. *J. Non-Newtonian Fluid Mech.*, 22:23–33, 1986.

[143] M. J. Riddle, C. Narvaez, and R.B. Bird. Interactions between two spheres falling along their line of centers in a viscoelastic fluid. *J. Non-Newtonian Fluid Mech.*, 2:23–35, 1977.

[144] P. Saramito. A new θ-scheme algorithm and incompressible fem for viscoelastic fluid flows. *Math. Modelling and Numer. Anal.*, 28:1–35, 1994a.

[145] P. Saramito and J.M. Piau. Flow characteristics of viscoelastic fluids in an abrupt contraction by using numerical modeling. *J. Non-Newtonian Fluid Mech.*, 52:263–288, 1994b.

[146] D.G. Scott and R.P.S. Han. Basis of an improved hybrid node renumbering algorithm for matrix bandwidth reduction. *Comput. Methods Appl. Mech. Eng.*, 118:309–318, 1994.

[147] J.A. Serdakowski and B. Caswell. Finite element Eulerian-Lagrangian method for time dependent flow of multimode fluids. *J. Non-Newtonian Fluid Mech.*, 29:217–244, 1988.

[148] P. Singh and L.G. Leal. Finite-element simulation of the start-up problem for a viscoelastic fluid in an eccentric rotating cylinder geometry using a third-order upwind scheme. *Theor. and Comput. Fluid Dynamics*, 5:107–137, 1993.

[149] S.W. Sloan. An algorithm for profile and wavefront reduction of sparse matrices. *Int. J. Numer. Methods Eng.*, 23:239–251, 1986.

[150] A. Souvaliotis and A. N. Beris. Applications of domain decomposition spectral collocation methods in viscoelastic flows through model porous media. *J. Rheol.*, 36(7):1417–1453, 1992.

[151] G. Strang. On the construction and comparison of difference schemes. *SIAM J. Numer. Anal.*, 5:506–517, 1968.

[152] G. Strang and G.J. Fix. *An Analysis of the Finite Element Method.* Prentice-Hall,Inc., Englewood Cliffs, NJ, 1973.

[153] P.K. Sweby. High resolution schemes using flux limiters for hyperbolic conservation laws. *SIAM J. Numer. Anal.*, 21:995–1011, 1984.

[154] M.J. Szady, A.W. Liu, R.C. Armstrong, and R.A. Brown. A new mixed finite element method for viscoelastic flows based on the discretized equations of motion. *J. Non-Newtonian Fluid Mech.*, submitted.

[155] M.J. Szady, T.R. Salamon, A.W. Liu, D.E. Bornside, R.C. Armstrong, and R.A. Brown. A new mixed finite element method for viscoelastic flows goverend by differential constitutive equations. *J. Non-Newtonian Fluid Mech.*, 59(215-243), 1995.

[156] K.K. Talwar and B. Khomami. Applications of higher order finite element methods to viscoelastic flow in porous media. *J. Rheol.*, 36(7):1377–1416, 1992.

[157] C. Taylor and P. Hood. A numerical solution of the navier-stokes equations using the finite element technique. *Comput. Fluids*, 1(1):73–100, 1973.

[158] L.N. Trefethen, A.E. Trefethen, S.C. Reddy, and T.A. Driscoll. Hydrodynamic stability without eigenvalues. *Science*, 261:578–584, 1993.

[159] K. Tsiveriotis. *Morphology and dynamics of highly deformed interfaces during directional solidification.* PhD thesis, MIT, 1992.

[160] K. Tsiveriotis and R.A. Brown. *Int. J. Numer. Meth. Fluid*, 16:827–843, 1993.

[161] L.H. Ungar, N. Ramprasad, and R.A. Brown. Finite element methods for unsteady solidification problems arising in prediction of morphological structure. *J. Sci. Comput.*, 3:77–108, 1988.

[162] B. van Leer. Towards the ultimate conservative difference scheme ii. monotonicity and conservation combined in a second order scheme. *J. Comput. Phys.*, 14:361–370, 1974.

[163] B. van Leer. Towards the ultimate conservative difference scheme iii. upstream-centered finite-difference schemes for ideal compressible flow. *J. Comput. Phys.*, 23:263–275, 1977.

[164] B. van Leer. Towards the ultimate conservative difference scheme iv. a new approach to numerical convection. *J. Comput. Phys.*, 23:276–299, 1977.

[165] B. van Leer. Towards the ultimate conservative difference scheme v. a second order sequel to godunov's method. *J. Comput. Phys.*, 32:101–136, 1979.

[166] N.N. Yanenko. *The Method of Fractional Steps.* Springer-Verlag, New York, 1971.

[167] C.-T. Yang and S. Atluri. An 'assumed deviatoric stress-pressure-velocity' mixed finite element method for unsteady, convective, incompressible viscous flow, part1: Theoretical development. *Int. J. Numer. Meths. Fluids*, 3:377–398, 1983.

[168] C.-T. Yang and S. Atluri. An 'assumed deviatoric stress-pressure-velocity' mixed finite element method for unsteady, convective, incompressible viscous flow, part1: Computational studies. *Int. J. Numer. Meths. Fluids*, 4:43–69, 1984.

[169] D.P. Young, R.G. Melvin, M.B. Bieterman, F.Y. Johnson, S.S. Samant, and J.E Busoletti. *J. Comput. Physics*, 92:1–66, 1991.

[170] R. Zheng, N. Phan-Thien, and R.I. Tanner. On the flow past a sphere in a cylindrical tube: Limiting Weissenberg number. *J. Non-Newtonian Fluid Mech.*, 36:27–49, 1990.

THESIS PROCESSING SLIP

FIXED FIELD: ill _____ name _____

index _____ biblio _____

▶ COPIES: (Archives) Aero Dewey Eng Hum

Lindgren Music Rotch (Science)

TITLE VARIES ▶☐ _____

_____

_____

NAME VARIES: ▶☐ _____

_____

IMPRINT: (COPYRIGHT) _____

▶COLLATION: 312 l

_____

▶ADD. DEGREE: _____ ▶DEPT.: _____

SUPERVISORS: _____

_____

_____ _____

_____ _____

_____ _____

_____ _____

_____ _____

_____ _____

_____ _____

NOTES:

cat'r: date:

page: ▶J151

▶DEPT: Chem. Eng

▶YEAR: 1996 ▶DEGREE: Ph.D.

▶NAME: SZADY, Michael Joseph

_____